

Michael Drass

# Constitutive Modelling and Failure Prediction for Silicone Adhesives in Façade Design

---

# **Mechanik, Werkstoffe und Konstruktion im Bauwesen**

Band 55

**Reihe herausgegeben von**

Ulrich Knaack, Darmstadt, Deutschland

Jens Schneider, Darmstadt, Deutschland

Johann-Dietrich Wörner, Darmstadt, Deutschland

Stefan Kolling, Gießen, Deutschland

Institutsreihe zu Fortschritten bei Mechanik, Werkstoffen, Konstruktionen, Gebäudehüllen und Tragwerken. Das Institut für Statik und Konstruktion der TU Darmstadt sowie das Institut für Mechanik und Materialforschung der TH Mittelhessen in Gießen bündeln die Forschungs- und Lehraktivitäten in den Bereichen Mechanik, Werkstoffe im Bauwesen, Statik und Dynamik, Glasbau und Fassadentechnik, um einheitliche Grundlagen für werkstoffgerechtes Entwerfen und Konstruieren zu erreichen. Die Institute sind national und international sehr gut vernetzt und kooperieren bei grundlegenden theoretischen Arbeiten und angewandten Forschungsprojekten mit Partnern aus Wissenschaft, Industrie und Verwaltung. Die Forschungsaktivitäten finden sich im gesamten Ingenieurbereich wieder. Sie umfassen die Modellierung von Tragstrukturen zur Erfassung des statischen und dynamischen Verhaltens, die mechanische Modellierung und Computersimulation des Deformations-, Schädigungs- und Versagensverhaltens von Werkstoffen, Bauteilen und Tragstrukturen, die Entwicklung neuer Materialien, Produktionsverfahren und Gebäudetechnologien sowie deren Anwendung im Bauwesen unter Berücksichtigung sicherheitstheoretischer Überlegungen und der Energieeffizienz, konstruktive Aspekte des Umweltschutzes sowie numerische Simulationen von komplexen Stoßvorgängen und Kontaktproblemen in Statik und Dynamik.

Weitere Bände in der Reihe <http://www.springer.com/series/13824>

---

Michael Drass

# Constitutive Modelling and Failure Prediction for Silicone Adhesives in Façade Design

 Springer Vieweg

@Seismicisolation

Michael Drass  
FB 13 Bauingenieurwesen  
Technical University of Darmstadt  
Mainz, Germany

ISSN 2512-3238                    ISSN 2512-3246 (electronic)  
Mechanik, Werkstoffe und Konstruktion im Bauwesen  
ISBN 978-3-658-29254-6        ISBN 978-3-658-29255-3 (eBook)  
<https://doi.org/10.1007/978-3-658-29255-3>

© The Editor(s) (if applicable) and The Author(s), under exclusive license to Springer Fachmedien Wiesbaden GmbH, part of Springer Nature 2020

This work is subject to copyright. All rights are solely and exclusively licensed by the Publisher, whether the whole or part of the material is concerned, specifically the rights of translation, reprinting, reuse of illustrations, recitation, broadcasting, reproduction on microfilms or in any other physical way, and transmission or information storage and retrieval, electronic adaptation, computer software, or by similar or dissimilar methodology now known or hereafter developed.

The use of general descriptive names, registered names, trademarks, service marks, etc. in this publication does not imply, even in the absence of a specific statement, that such names are exempt from the relevant protective laws and regulations and therefore free for general use.

The publisher, the authors and the editors are safe to assume that the advice and information in this book are believed to be true and accurate at the date of publication. Neither the publisher nor the authors or the editors give a warranty, expressed or implied, with respect to the material contained herein or for any errors or omissions that may have been made. The publisher remains neutral with regard to jurisdictional claims in published maps and institutional affiliations.

This Springer Vieweg imprint is published by the registered company Springer Fachmedien Wiesbaden GmbH part of Springer Nature.

The registered company address is: Abraham-Lincoln-Str. 46, 65189 Wiesbaden, Germany



# Acknowledgement

This dissertation was written as part of my work as a scientific assistant at the Institute for Statics and Design at the Technical University Darmstadt between 2014 and 2019. It is the intention of these lines to thank those who have supported and encouraged me on this long journey. I apologize very much in advance if I have forgotten someone.

My greatest thanks go to Professor Jens Schneider for the trust placed in me and for giving me the opportunity to begin and complete my dissertation at the Technical University Darmstadt. His dedication to the institute, motivation of staff and openness to new research ideas is unique and enabled me to work freely and creatively. These thanks also go to Professor Knaack, whose declared goal is to train young scientists on their hopefully long path in science in such a way that they are better than their teachers and form the next generation of professors and scientists of the highest level. I am also very grateful to Professor Stefan Kolling. The way in which Professor Kolling gives lectures and communicates very complex facts in the simplest way has led me to dedicate my dissertation to polymer materials. Further thanks go to Professor Christian Louter, who has always been very interested in my work and invited me to a research stay at the TU Delft.

I would like to thank my colleagues at the Institute of Structural Mechanics and Design for the many interesting discussions and the friendly interaction, which contributed to a very pleasant working atmosphere. Special thanks go to my colleagues Sascha Hickert M.A., Carina Kisker M.A., Alimir Mohsen M.Eng., Miriam Schuster M.Sc., Gregor Schwind M.Sc., Hagen Berthold M.Sc. and Marcel Hörbert B.Sc. Daily discussions on important as well as unimportant nonsense topics characterized an excellent working atmosphere. Furthermore, I would like to thank the former members of the institute, Dr.-Ing. Sebastian Schula and Mr. Dr.-Ing. Jonas Hilcken, for stimulating technical discussions and the joint work on exciting projects. I would also like to thank Dr.-Ing. Vladimir Kolupaev for his dedication and expertise in the field of strength hypotheses and limit state analyses. The discussions with him have contributed significantly to the success of the thesis. In addition, I would like to thank the students of the Technical University Darmstadt who supported me through their enthusiasm for research and interest in complex issues - in the form that they wrote their theses with me.

For me personally, it was always important to network beyond the institute's boundaries and to have a lively scientific exchange. Therefore, I would like to express my special thanks to my colleagues and friends Philipp Rosendahl M.Sc. and Dr.-Ing. Michael Kraus, with whom not only an intensive and very fruitful research and publication activity has taken place in the past, but also in the future joint projects are planned to start together - *TRIO INTEGRAL*.

Furthermore, I would like to thank Mr. Julian Felger M.Sc. and Mr. Alex Großmann M.Sc. for the very funny meetings in the Mensa, where you could always leave the stressful everyday life behind you.

I would also like to thank numerous industrial partners with whom I have carried out numerous projects in the past. Above all, I would like to thank DOW - in particular Sigurd Sitte, Dr. phil. Andreas Wolf, Valérie Hayez PhD. Loriane Tachon Parisot and Enrico Cutri, who have always supported my research work. Furthermore, I would like to thank Mr. Dipl.-Ing. Bruno Kassnel-Henneberg and Dr.-Ing. Ali Hamdan from Glas Trösch Group, who have always shown great interest in my work and supported me in the production of samples. I would also like to thank Michael Elstner from AGC Interpane, who supported my research from the absolute beginning.

The preparation of a dissertation requires family support. Therefore, I would like to especially thank my parents, Donate and Waldemar Drass, who are always at my side and have supported me in every situation.

My sincere personal thanks go to my beloved wife Anne-Sophie Drass for bringing happiness, wisdom and tenderness into my life. Her love, her blind trust and her support in all kind of situations - in good and hard times - made it possible to write my dissertation. I thank her with all my heart and dedicate this work to her in love.

Finally I wish to thank to whoever is responsible of placing all the above mentioned people on my way.

Mainz, October 2019

*Michael Drass*

# Abstract

The general aim of the present work is to improve the understanding about the elementary material behaviour of flat bonded structural silicones in the façade area. Therefore, extensive experimental investigations are carried out on a transparent structural silicone adhesive (TSSA) and evaluated using the latest methods of optical measurements in order to be able to explain the material behaviour, failure and microscopic effects such as stress whitening, cavitation failure and the Mullins effect. Based on the experimental data novel hyperelastic material models are developed to account for the strong non-linear material behaviour under isochoric as well as volumetric deformations. Due to the development of a physically-motivated, volumetric hyperelastic model, it is possible for the first time to approximate the structural behaviour of TSSA under constrained tensile loading, where the cavitation effect (void growth) is present. The developed material models are also implemented in a finite element software in order to be able to calculate any flat-bonded structures. The quality of the model is verified by three-dimensional numerical simulations of validation experiments. Another goal is the transfer of the model to the cyclic behaviour of TSSA not only in case of volume-constant deformations but also in case of volumetric-cyclic loading. Here, too, the validity of the developed models is proven by comparing numerical calculations with experimental results. Additionally, a novel stretch-based failure criterion is developed generally and applied to the experimental data of TSSA to predict failure of the material in Finite Element calculations. Furthermore, the novel stretch-based failure criterion is combined with a safety concept to ensure and calculate the structural integrity of bonded components in façade application. The aim is to show that the classical approaches for describing the strength of flat-bonded silicone adhesive joints in accordance to the manufacturer specifications lead to conservative results. If, however, newly developed models and failure formulations are used for the design and dimensioning of such non-standardized bonded joints, a significant increase in structural strength can be adduced without reducing the global safety level.

# Zusammenfassung

Generelles Ziel der vorliegenden Arbeit ist es, das Verständnis für das Materialverhalten von flachverklebten Struktursilikonen im Fassadenbereich zu verbessern. Darauf werden umfangreiche experimentelle Untersuchungen an einem transparenten Struktursilikon (TSSA) durchgeführt und mit modernsten optischen Messmethoden ausgewertet, um das Materialverhalten, das Versagen und mikroskopische Effekte wie stress whitening, Kavitationsversagen und den Mullins-Effekt erklären zu können. Basierend auf den experimentellen Daten werden neuartige hyperelastische Materialmodelle entwickelt, um das stark nichtlineare Materialverhalten unter isochoren sowie volumetrischen Verformungen zu berücksichtigen. Durch die Entwicklung eines physikalisch motivierten, volumetrischen hyperelastischen Modells ist es erstmals möglich, das Strukturverhalten von TSSA unter eingeschränkter Zugbelastung, bei der der Kavitationseffekt (Hohlraumwachstum) eintritt, zu approximieren. Die entwickelten Materialmodelle werden auch in einer Finite-Elemente-Software implementiert, um beliebige flachverklebte Strukturen berechnen zu können. Die Qualität des Modells wird durch dreidimensionale numerische Simulationen von Validierungsexperimenten verifiziert. Ein weiteres Ziel ist die Übertragung des Modells auf das zyklische Verhalten von TSSA - nicht nur bei volumenkonstanten Verformungen, sondern auch bei volumetrisch-zyklischer Belastung. Auch hier wird die Validität der entwickelten Modelle durch den Vergleich von numerischen Berechnungen mit experimentellen Ergebnissen nachgewiesen. Zusätzlich wird ein neuartiges Versagenskriterium entwickelt und auf die experimentellen Daten von TSSA angewendet, um das Versagen des Materials in Finite-Elemente-Berechnungen vorherzusagen. Darüber hinaus wird das neuartige Versagenskriterium mit einem Sicherheitskonzept kombiniert, um die strukturelle Integrität von verklebten Bauteilen in der Fassadenanwendung zu gewährleisten und zu berechnen. Es soll gezeigt werden, dass die klassischen Ansätze zur Beschreibung der Festigkeit von flachverklebten Silikonklebeverbindungen nach Hersteller-vorgaben zu konservativen Ergebnissen führen. Werden jedoch für die Auslegung und Dimensionierung solcher nicht genormter Klebverbindungen neu entwickelte Modelle und Versagensformulierungen verwendet, kann eine deutliche Erhöhung der Strukturfestigkeit erreicht werden, ohne das globale Sicherheitsniveau zu reduzieren.

# Résumé

L'objectif général du présent travail est d'améliorer la compréhension du comportement des matériaux élémentaires des silicones de construction à liant plat dans la zone de la façade. C'est pourquoi des études expérimentales approfondies sont menées sur un adhésif de silicone structurel transparent (TSSA) et évaluées à l'aide des dernières méthodes de mesure optique afin de pouvoir expliquer le comportement du matériau, la défaillance et les effets microscopiques tels que le blanchiment sous contrainte, la défaillance par cavitation et l'effet Mullins. Sur la base des données expérimentales, de nouveaux modèles de matériaux hyperélastiques sont développés pour tenir compte du fort comportement non linéaire des matériaux sous des déformations isochoriques ainsi que volumétriques. Grâce au développement d'un modèle hyperélastique volumétrique hyperélastique à motivation physique, il est possible pour la première fois d'approcher le comportement structurel de la TSSA sous une charge de traction limitée, où l'effet de cavitation (croissance de vide) est présent. Les modèles de matériaux développés sont également implantés dans un logiciel d'éléments finis afin de pouvoir calculer toute structure à liant plat. La qualité du modèle est vérifiée par des simulations numériques tridimensionnelles d'expériences de validation. Un autre objectif est le transfert du modèle au comportement cyclique de la TSSA non seulement en cas de déformations constantes en volume mais aussi en cas de charge volumétrique cyclique. Ici aussi, la validité des modèles développés est prouvée en comparant les calculs numériques aux résultats expérimentaux. De plus, un nouveau critère de rupture basé sur l'étirement est généralement élaboré et appliqué aux données expérimentales de la TSSA pour prédire la rupture du matériau dans les calculs par éléments finis. De plus, le nouveau critère de rupture basé sur l'étirement est combiné avec un concept de sécurité pour assurer et calculer l'intégrité structurelle des composants collés dans l'application de façade. L'objectif est de montrer que les méthodes classiques de description de la résistance des joints adhésifs en silicium à liant plat conformément aux spécifications du fabricant conduisent à des résultats prudents. Cependant, si, pour la conception et le dimensionnement de ces assemblages collés non normalisés, on utilise des modèles et des formulations de rupture nouvellement développés, on peut obtenir une augmentation significative de la résistance structurale sans réduire le niveau de sécurité global.

# Contents

<b>Glossaries</b>	xvii
<b>1 Introduction</b>	1
1.1 Motivation and Problem Statement .....	1
1.2 Objectives and Limitations .....	6
1.3 Concept and Structure .....	7
1.4 Author's Publications Prior to this Thesis .....	9
<b>2 Theoretical Principles on Mechanics</b>	11
2.1 Aspects on Continuum Mechanics.....	11
2.1.1 Continua, Material Bodies and Motion of Continuous Bodies ..	11
2.1.2 Deformations and Strain Measures .....	13
2.1.3 Stress Measures.....	16
2.1.4 Balance Principles in Continuum Mechanics .....	17
2.2 Failure Criteria and Limit State Analyses .....	22
2.2.1 Basics of Failure Criteria .....	22
2.2.2 Visualization Methods .....	23
2.2.3 Convexity Constraints .....	24
2.3 Micromechanics and Homogenization .....	28
2.3.1 Concept of Representative Volume Elements .....	29
2.3.2 Micromechanical Homogenization.....	30
2.3.3 Approximate Solutions and Bounds in Micromechanics .....	33
<b>3 Elastomers and their Mechanical Behaviour</b>	37
3.1 Classification of Polymers .....	37
3.1.1 General Polymer Structures and Properties.....	37
3.1.2 Mechanical Behaviour and Emergent Effects of Rubbers ..	40
3.2 Hyperelastic Material Modelling .....	47
3.2.1 Incompressible Hyperelasticity .....	48
3.2.2 Compressible Hyperelasticity .....	49
3.2.3 Remarks on Volumetric-Isochoric Split .....	51
3.2.4 Isochoric Hyperelastic Constitutive Models .....	55
3.2.5 Volumetric Hyperelastic Constitutive Models .....	58

3.3	Hyperelasticity for Porous Continua .....	60
3.4	Concept of Pseudo-Elasticity .....	61
<b>4</b>	<b>Experiments on Transparent Structural Silicone Adhesive</b>	<b>65</b>
4.1	Transparent Structural Silicone Adhesive - TSSA .....	65
4.2	Homogeneous Experimental Tests .....	66
4.2.1	Uniaxial Tension .....	66
4.2.2	Cyclic Uniaxial Tension .....	69
4.2.3	Uniaxial Compression .....	71
4.2.4	Biaxial Tension .....	73
4.2.5	Shear-Pancake .....	77
4.3	Inhomogeneous Experimental Tests .....	79
4.3.1	Pancake Tension Tension .....	80
4.3.2	Cyclic Pancake Tension Test .....	85
4.4	Micro-Structure Analyses .....	88
4.4.1	Studies on Porosity .....	88
4.4.2	Stress Whitening Effect .....	90
4.5	Conclusions .....	94
<b>5</b>	<b>Development of Constitutive Models for Poro-Hyperelastic Materials</b>	<b>95</b>
5.1	Isochoric Helmholtz Free Energy Function .....	95
5.1.1	Classification of Isochoric Hyperelastic Material Model .....	96
5.1.2	New Isochoric Hyperelastic Material Model .....	96
5.1.3	Proof of Polyconvexity .....	100
5.1.4	Proof of Convexity vs. Drucker's Stability Postulate .....	104
5.1.5	Reconciling Phenomenological and Molecular-Statistical Theory .....	106
5.2	Novel Volumetric Helmholtz Free Energy Function .....	116
5.2.1	Single and Multi-Voided Representative Volume Elements .....	117
5.2.2	Homogenization Concepts at Finite Strains .....	125
5.2.3	RVE vs. EHM - Numerical Homogenization .....	131
5.2.4	Bounds in Micro-Mechanics .....	131
5.2.5	Remarks on Volumetric Helmholtz Free Energy Functions .....	133
5.3	Pseudo-Elastic Cavitation Model .....	136
5.3.1	General Concept .....	136
5.3.2	Isoperimetric Inequality .....	141
5.3.3	Equivalent Void Growth Measure .....	143
5.3.4	Constitutive Modelling and Algorithmic Settings .....	145
5.3.5	Parameter Studies of Isoperimetric Extension of Volumetric Helmholtz Free Energy Function .....	146
5.4	Extension of Pseudo-Elastic Cavitation Model for Cyclic Loading .....	149

5.4.1	Motivation .....	149
5.4.2	General Concept .....	151
5.4.3	Isochoric Mullins Damage under Cyclic Loading .....	151
5.4.4	Volumetric Damage and Healing under Cyclic Loading .....	153
5.4.5	Parameter Studies on Cyclic Pseudo-Elastic Cavitation Model	158
5.5	Numerical Validation of Constitutive Models .....	160
5.5.1	Approximation of Different Hyperelastic Materials .....	161
5.5.2	Simulation of ETAG H-shaped Test Sample .....	163
5.5.3	Simulation of Dumbbell-Shaped Tensile Test .....	165
5.5.4	Simulation of Bulge-Test .....	168
5.5.5	Simulation of Pancake Tension Tests .....	170
5.5.6	Simulation of Cyclic Uniaxial and Constrained Tensile Test .....	174
5.6	Conclusions .....	177
<b>6</b>	<b>Development of Failure Criteria for Poro-Hyperelastic Materials</b>	<b>179</b>
6.1	Isochoric Failure Criteria .....	180
6.2	Classical Cavitation Criteria .....	183
6.2.1	Gent & Lindley Criterion .....	183
6.2.2	Hou & Abeyaratne Criterion .....	184
6.2.3	Lopez-Pamies et al. Criterion .....	185
6.3	Generalized Cavitation Criterion .....	187
6.3.1	Extended Podgórski Criterion Accounting for Cavitation .....	187
6.3.2	Parameter Studies on Extended Podgórski Criterion .....	189
6.3.3	Virtual Data For Cavitation Failure at Finite Porosity .....	191
6.3.4	Approximation of Cavitation Failure in Stress Space .....	193
6.3.5	Approximation of Cavitation Failure in Stretch Space .....	197
6.4	Coupled Distortional-Dilatational Failure Criterion .....	200
6.4.1	Concept of Coupled Distortional-Dilatational Failure Criterion	201
6.4.2	Coupled Failure Surface in Section Planes .....	204
6.4.3	Novel Failure Criterion for DOWSIL™ TSSA .....	205
6.5	Numerical Validation of Failure Criteria .....	206
6.5.1	Limit State Analysis - Uniaxial Tensile Test .....	207
6.5.2	Limit State Analysis - Bulge Test .....	209
6.5.3	Limit State Analysis - Pancake Tension Test .....	209
6.6	Conclusions .....	212
<b>7</b>	<b>Design Methods for Structural Silicone Adhesives</b>	<b>213</b>
7.1	Normative Concepts on Structural Sealant Glazing Systems .....	213
7.1.1	ETAG 002 Concept .....	213
7.1.2	DIBt Concept .....	216
7.2	Logical Experimental Testing Program .....	217

7.3	Material Parameter Identification .....	221
7.4	Modelling of Silicone Adhesive Joints .....	228
7.4.1	Classification of Adhesive Joints .....	228
7.4.2	Classification of Material Models .....	234
7.5	Safety Concept and Limit State Analyses .....	236
7.6	Conclusions .....	244
<b>8</b>	<b>Conclusion and Outlook</b>	<b>247</b>
8.1	Conclusions .....	247
8.2	Future Research .....	250
<b>Bibliography</b>		<b>253</b>
<b>A</b>	<b>Triaxiality in 3D Stress Space</b>	<b>275</b>
A.1	Numerical Examples of Modified Triaxiality .....	275
A.2	Numerical Examples.....	275
<b>B</b>	<b>Pancake Tension Test under Temperature</b>	<b>277</b>
<b>C</b>	<b>Porosity of TSSA</b>	<b>279</b>
<b>D</b>	<b>Engineering Approach Determining Experimental Testing Speed</b>	<b>281</b>
<b>E</b>	<b>Molecular-Statistical Approaches</b>	<b>283</b>
E.1	Gaussian Statistics .....	283
E.2	Non-Gaussian Statistics (Langevin Approach) .....	284
E.3	Relaxed Langevin Approach .....	285
E.4	Tube Statistics .....	286
<b>F</b>	<b>User-Defined Material Models in ANSYS FE-Code</b>	<b>287</b>

# Glossaries

## Abbreviations

### General

BT	Biaxial Tension
BVP	Boundary Value Problem
DIC	Digital image correlation
EHM	Equivalent Homogeneous Material
FE code	Finite Element code
FEA	Finite Element Analysis
FEM	Finite Element Method
HT	Hydrostatic Tension
PC	Pancake
PDE	Partial Differential Equation
RVE	Representative Volume Element
SEM	Scanning electron microscope
SPC	Shear Pancake
ST	Shear Test
UT	Uniaxial Tension

### Materials

EPDM	Ethylen-Propylene-Diene-Monomer
LSG	Laminated Safety Glass
NR	Natural Rubber
PDMS	polydimethylsiloxane
PP	Polypropylene
PVB	Polyvinylbutyral
TSSA	Transparent Structural Silicone Adhesive

## Symbols

### Continuum Mechanics

$D_V$	dilatation
$J$	Jacobian determinant / relative volume
$\mathbf{C} / \mathbf{b}$	right / left Cauchy-Green tensor
$\mathbf{D}$	rate-of-deformation tensor
$\mathbf{E}$	Green-Lagrange strain tensor
$\mathbf{H}$	material displacement gradient tensor
$\mathbf{P} / \mathbf{S}$	1. Piola-Kirchhoff / 2. Piola-Kirchhoff stress tensor
$\mathbf{R}$	orthogonal rotation tensor
$\mathbf{U} / \mathbf{v}$	right / left stretch tensor
$\mathbf{e}$	Euler-Almansi strain tensor
$\boldsymbol{\sigma}$	Cauchy stress tensor
$\boldsymbol{\varepsilon}$	Hencky strain tensor
$\lambda_i$	principal stretch
$\rho_0 / \rho$	mass density in reference / current configuration
$\mathbf{F}$	deformation gradient
$\vec{\mathbf{B}} / \vec{\mathbf{b}}$	body forces in reference / current configuration
$\vec{\mathbf{X}} / \vec{\mathbf{x}}$	position vectors in reference / current configuration
$\vec{\mathbf{u}}$	displacement vector
$\vec{\mathbf{A}} / \vec{\mathbf{a}}$	Lagrangian / Eulerian acceleration field
$\vec{\mathbf{t}}$	stress / traction vector
$dV / dv$	differential volume element in reference / current configuration
$d\vec{\mathbf{A}} / d\vec{\mathbf{a}}$	differential area element in reference / current configuration
$I_{1,\bullet} / I_{2,\bullet} / I_{3,\bullet}$	principal invariants of argument ( $\bullet$ )
$\Gamma_{0,\vec{\mathbf{t}}} / \Gamma_{0,\vec{\mathbf{u}}}$	traction / displacement boundary conditions
$\mathcal{B}_0 / \mathcal{B}$	material body in reference / current configuration
$\hat{\mathbf{N}} / \hat{\mathbf{n}}$	surface element's normal in reference and current configuration
$\mathcal{P}_0 / \mathcal{P}$	material points in reference / current configuration
$\vec{\mathbf{N}}_i / \vec{\mathbf{n}}_i$	eigenvectors of $\mathbf{U} / \mathbf{v}$
$w^{\text{int}} / \dot{w}^{\text{int}}$	internal work / rate of internal work

### Failure Criteria

$\Phi(\bullet)$	general failure criterion
$\mathbf{M}$	orthogonal transformation matrix

$\sigma''$	principal Cauchy stress tensor
$\mathcal{K}$	Gaussian curvature
$\mathcal{R}$	safe region without failure
$\rho$	radius of $\pi$ -plane
$\theta$	stress angle in $\pi$ -plane
$\sigma_{\text{vM}}$	von Mises equivalent stress
$\xi_1, \xi_2, \xi_3$	new axes of transformed orthogonal coordinate system

## Hyperelasticity

$K$	bulk modulus
$\Psi$	Helmholtz free energy function
$\Psi_{\text{iso}}$	isochoric Helmholtz free energy function
$\Psi_{\text{vol}}$	volumetric Helmholtz free energy function
$\eta$	internal variable for pseudo-elastic formulation
$\gamma$	Lagrange multiplier
$\mu$	initial shear modulus
$\phi(\eta)$	damage function for pseudo-elastic formulation
$p$	hydrostatic pressure

## Mathematical Operators

:	double scalar product
$\times$	tensor cross product
.	scalar product
$\otimes$	tensorial product
$\det(\bullet)$	determinant of argument ( $\bullet$ )
$(\bullet) = \frac{D}{Dt} (\bullet)$	time derivative of argument
$[\bullet]$	Hessian operator applied on argument
$\nabla \cdot (\bullet) = \text{div}(\bullet)$	divergence of argument
$\nabla(\bullet)$	gradient of argument
$\text{tr}(\bullet)$	trace of argument

## Micro-Mechanics

$K_\bullet^\Delta$	approximate solution for the initial bulk modulus
$\mathbb{S}$	compliance stiffness tensor
$(\bullet)^\Delta$	effective property of argument
$(\bullet)^*$	identities of EHM
$\mathbb{A}$	influence tensor accordingly to Eshelby's solution
$l_\bullet$	micromechanical length scale of argument
$(\bullet)^\circ$	identities of RVE

$\mathbb{C}$	elastic stiffness tensor
$\langle \bullet \rangle$	volume-average of argument

## Statistical Mechanics

$E_b$	bonding stiffness
$L$	contour length of polymer chain
$N$	number of chain segments
$T$	absolute temperature
$\Lambda$	macro-stretch acting on single polymer chain
$\Lambda_m$	macro-locking stretch acting on polymer network
$\lambda$	micro-stretch acting on single polymer chain
$\lambda_b$	bond micro-strech relaxing Langevin approach
$\lambda_m$	micro-locking stretch acting on single polymer chain
$\lambda_r$	relative micro-stretch acting on single polymer chain
$\mathcal{V}$	macro-tube contraction
$\nu$	micro-tube contraction
$\psi_s$	free energy of single polymer chain
$\psi_t$	free energy from topological constraints
$d$	tube diameter
$f_s$	axial micro-force acting on single polymer chain
$f_t$	radial micro-force contracting tube
$k$	Boltzmann's constant
$l$	Kuhn segment length
$p$	joint probability density
$r$	end-to-end distance of polymer chain
$r_0$	initial length of single polymer chain
$s$	entropy of a single polymer chain confined by a tube
$\hat{\varepsilon}_b$	change in internal energy related to segment stretching
$\mathcal{L}^{-1}$	inverse Langevin function



# 1 Introduction

## 1.1 Motivation and Problem Statement

Glass is a popular building material in construction industry with which monumental buildings made of large-format glass with almost complete transparency can be realized today (Bedon and Santarsiero, 2018; Staudt, 2017; Drass et al., 2018d). In order to meet the demand for almost complete transparency, very filigree fasteners were developed especially for façade constructions. These fasteners are ranging from button and countersunk fittings, undercut anchors and clamped fittings to adhesive joints (Tibolt, 2015).

When focusing on adhesive joints in façade design, structural silicones in particular have become established as they can withstand large deformations due to wind and temperature loads and / or differential displacements between the glass pane and the secondary supporting structure without failing. Silicone-based adhesive joints have excellent resistance to external influences such as temperature, UV, water and even recently have enabled almost completely transparent structures to be created which are of great interest today for façade architecture (Bedon and Santarsiero, 2018). In addition, silicone adhesives hardly creep and creep is virtually independent of temperature for a wide temperature range (Kłosowski and Wolf, 2016:p.317). The mechanical behaviour of silicones, which are assigned to the group of polymers in general, can be classified as hyperelastic. By using strain energy potentials, it is possible to calculate the stress-strain behaviour of hyperelastic materials at large deformations (Treloar, 1975:p.64). Furthermore, silicones show an almost incompressible material behaviour so that the Poisson's ratio is  $\nu \approx 0.5$  (Wolf and Descamps, 2003). This means that the material deforms almost constant in volume. In addition, polymers exhibit a time- and temperature-dependent behaviour with respect to stiffness, which can be more or less pronounced depending on the material under investigation (M. A. Kraus et al., 2017).

Classical adhesive joints in façade constructions typically use double or quadrilateral bonded glass elements to provide homogeneous force transmission without weakening the glass by drilling or penetration, which is desired due to the brittle failure behaviour of glass (Schneider et al., 2016). Hence, adhesive joints are particularly well suited due to the homogeneous force transmission, the possibil-

ity of large adhesive surfaces and no penetration of the glass or building envelope (Staudt, 2017).

Linear adhesive joints are frequently used in façade systems (Kłosowski and Wolf, 2016; Staudt et al., 2018), which means bonding along the right-angled glass edges and frame profiles made of aluminium, stainless steel or timber. The adhesion between the adhesive and the adherent is limited to two sides in order to prevent a lateral contraction limitation of the material. Although the limitation of lateral contraction leads to an enormous increase in stiffness (Kłosowski and Wolf, 2016:p.316), which is particularly useful for insulating glass edge seals, the amount of movement of the edge seal is also greatly reduced, which can lead to micro-defects and cracks in the adhesive (Buddenberg et al., 2016). A similar effect may occur in very flat silicone adhesive joints, where the lateral contraction is hindered (Silvestru et al., 2018b; Drass et al., 2018b), which means that the height-width ratio becomes very small. To prevent the discussed deformation disability, the above-mentioned linear adhesive joints must comply with geometric boundary conditions accordingly to requirements of ETAG 002 (2012) or ASTM C1401 (2002). A prerequisite for this is that the width of the bonded joint must be less than or equal to three times the height of the bonded joint (ETAG 002, 2012). In summary, a soft adhesive capable of absorbing large deformations without failure should be used for linear joints in façade systems, and constructive precautions must be taken to prevent the silicone sealant from being hindered in its lateral contraction.

In contrast to classic linear adhesive bonds, modern adhesive joints only envisage local bonding via so-called adhesive point fixings or embedded thick or thin inserts over which large loads can be transferred as a result of the thin design of the adhesive (Sitte et al., 2011; Santarsiero et al., 2018a). Since façade elements are now only bonded locally, higher demands are placed on the silicone adhesive and its performance of higher stiffness and strength in order to guarantee the structural integrity of the bonded construction. Flat-bonded adhesive joints are typically achieved by directly bonding glass to metal with thin silicone adhesives, which is designated as a laminated connection due to the special production process applied (Santarsiero, 2015). The full-glass exhibition stand produced by Glas Trösch Holding AG is an attractive building project, which impresses with its maximum transparency and minimisation of connecting elements, here laminated point fixings and inserts (see Fig 1.1 a-b). The laminated joints are manufactured using, for example, a 1 mm thin transparent structural silicone (DOWSIL™ TSSA), which is characterized by its transparency, high stiffness and strength as well as resistance to external environmental influences. Furthermore, TSSA exhibits only low viscous effects so that it is virtually independent of rates or load duration. As a result of the flat geometric shape of the adhesive joint and the almost incompressible ma-

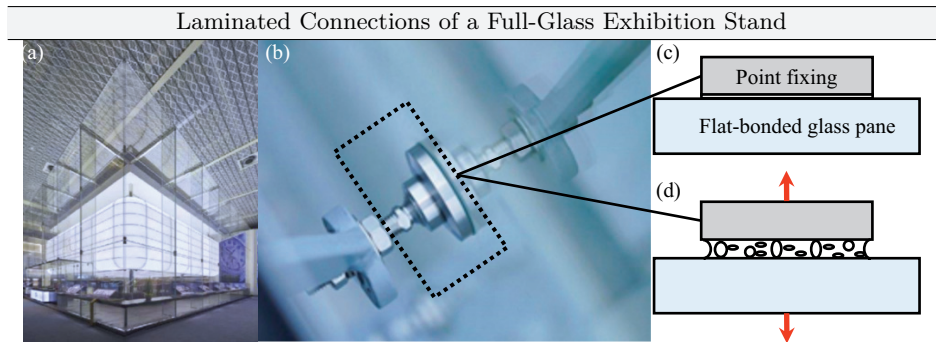


**Figure 1.1** (a) Full-glass exhibition stand produced by Glas Trösch, (b) laminated connection to a glass pane with DOWSIL™ TSSA - Permission of DOWSIL and (c-d) schematic representation of a flat bonded point fixing under axial load, where the cavitation effect occurs in the form of void growth in the material

terial behaviour of silicone (Wolf and Descamps, 2003), this special type of joint has a high stiffness under axial load, which, however, may lead to stress softening and a pronounced whitening in the material when subjected to too high stresses (Hagl et al., 2012a; Hagl et al., 2012b; Hagl, 2016; Drass et al., 2017a). The design of the flat adhesive joint therefore leads to significantly different stress states (hydrostatic stresses) in the silicone adhesive than in linear joints, since the lateral contraction in the material is impeded. Thus, when an adhesive joint is subjected to an axial load, the disability of lateral strains may cause abrupt cavity growth in the silicone (see Fig 1.1 c). This behaviour is called cavitation and leads to a significant increase in the ductility of the connection before final distortional failure occurs (Gent and Lindley, 1959; Hamdi et al., 2014; Drass et al., 2018b; Drass et al., 2018c). The effect of increasing ductility manifests itself through a pronounced effective stress softening causing large deformations in the material without significantly increasing the load. Since cavitation in polymers has not yet been fully understood (Fond, 2001), the following questions in accordance to Tab. 1.1 arise. These postulated questions are endeavoured to be answered within the framework of this work.

Returning to adhesive joints in general, thin adhesive bondings do not meet the geometric requirements of ETAG 002 (2012). Hence, it is only possible to proof the structural integrity and therefore the static load bearing capacity by means of an increased experimental and numerical effort (Hagl, 2016). Unfortunately, there are so far no comprehensible material models to describe the non-linear structural behaviour including the stress softening due to cavitation as well as the final failure of heavily constrained silicone adhesive joints. Hence, if it would be possible to characterise the structural behaviour and failure of the material experimentally

**Table 1.1** Open questions on the cavitation effect in structural silicones to be answered in this thesis

- What influence does cavitation have on the global structural behaviour of silicones adhesives?
- Which material properties affect the cavitation effect (shear modulus, bulk modulus, micro-structure, porosity etc.)?
- Is the effect of cavitation in terms of void growth a real material damage or a reversible process?
- Can cavitation be associated with stress whitening, which occurs especially in transparent silicone adhesives under load?
- How can the cavitation effect be mechanically represented by material models?
- Is it possible to consider the cavitation effect in numerical calculations to make the flat-bonded adhesive joint system more predictable?
- How can the cavitation effect be used in the dimensioning of flat-bonded adhesives joints in order to guarantee an efficient and material-specific design of the bond?

on the material rather than on the component level and to approximate it with improved mechanical models that take into account the non-linearities of TSSA, new design possibilities could be offered to structural engineers working with flat or laminated adhesive joints.

Due to the limited knowledge about the physical processes occurring in flat-bonded silicone adhesive joints, the damage mechanisms and the ultimate failure description, easily accessible mechanical models have been developed in order to approximate the structural behaviour as well as to conduct a dimensioning of the adhesive joint (Descamps et al., 2017). These mechanical models are based on the assumption of a linear elastic material, whereby failure is evaluated by a simple engineering stress-based failure criterion. The above-mentioned approach and model is well suited for a first approximation to describe the stiffness and the stress state in the silicone adhesive. Nevertheless, it is clear that due to the underlying assumptions an efficient dimensioning of flat-bonded adhesive joints cannot take place. This can only be achieved by an increased understanding of the material and its micro-structure, the exact description of the material behaviour under load and its final failure. Since there is hardly any research on this topic so far, it is not surpris-

ing that the load-bearing capacity of TSSA is severely limited or at a very low load level respectively. Thus, the design leads to conservative results. Typical design strengths for TSSA for dynamic and permanent loads read  $\sigma_{\text{des}} = \tau_{\text{des}} = 1.33 \text{ MPa}$  and  $\sigma_{\infty} = \tau_{\infty} = 0.66 \text{ MPa}$ , which are specified by the manufacturer in order to design and dimension flat-bonded adhesive joints (Kłosowski and Wolf, 2016:p.346). Here, it should be mentioned again that the proposed design strengths are defined by means of a linear elastic material behaviour and the assumptions of engineering stresses to determine the limit state, which refer to the loaded initial cross-section of the adhesive joint. Keeping in mind that silicones can withstand large deformations and show a strong non-linear material behaviour, these assumption are not justified but sufficient for a first approximation of the structural behaviour. Returning to the conservative design strengths for TSSA, they were determined by defining the stress whitening effect occurring at approximately 2.0 MPa in axial tension as final failure. The actual origin and background of stress whitening has not yet been clarified. As a result, the design strength under short-term load was determined by dividing the engineering stress of 2.0 MPa by a global safety factor of 1.5, which corresponds to a global safety factor of approximately three with regard to the ultimate failure stress observed in the experiments. In contrast, the determination of the design strengths under permanent load was determined on the basis of long-term tests, assuming a time to failure of over 100 years, for which a global safety factor of three was assumed. Looking at the design failure strengths of other structural silicones used in façade construction, such as DOWSIL™ 993 ( $\sigma_{\text{des}} = 0.14 \text{ MPa}$ ,  $\tau_{\text{des}} = 0.11 \text{ MPa}$  and  $\tau_{\infty} = 0.011 \text{ MPa}$ ), the design strengths for TSSA are magnitudes greater than in comparison to DOWSIL™ 993. This results in greater opportunities for the application of novel design principles in façade construction and joining of façade elements.

However, since conservative approaches have been generally used in the past to determine the design strengths for TSSA and structural silicones in general under the assumption of a linear elastic material behaviour, stress-based failure criteria and dimensioning of these adhesive joints using simple manual calculations, the question remains whether the assumptions made are justified. In addition, the question arises whether it is possible to increase the load bearing capacity with improved physically motivated material models and enhanced models for describing the failure of silicones without reducing an existing safety level. To answer this question, the present work deals with the experimental characterization, the constitutive modelling considering the whitening, cavitation and Mullins effect as well as the description of failure via novel stretch-based failure criteria for TSSA.

## 1.2 Objectives and Limitations

The general aim of the present work is to improve the understanding about the elementary material behaviour of flat bonded structural silicones in the façade area. To this end, extensive experimental investigations are carried out on the material TSSA and evaluated using the latest methods of optical measurements in order to be able to explain the material behaviour, failure and microscopic effects such as stress whitening, cavitation failure and the Mullins effect.

A further goal is to predict the structural behaviour of TSSA observed in the experimental investigations, using new developed physically-motivated material models. For this purpose, theoretical models are compared with the experimental results of TSSA and transferred into novel constitutive relationships. The developed material models are then to be implemented in a finite element software in order to be able to calculate any flat-bonded structures. On the one hand, the focus is on approximating the isochoric, i.e. volume constant, material behaviour of TSSA and basically of elastomers for any deformation as best as possible. On the other hand, a mechanical model is to be developed which is able to reproduce the cavitation effect of axially pulled heavily constrained adhesive joints. The quality of the model will be verified by three-dimensional numerical simulations of validation experiments. Another goal is the transfer of the model to the cyclic behaviour of TSSA not only in case of volume-constant deformations but also in case of volumetric-cyclic loading. Here, too, the validity of the developed models is to be proven by comparing numerical calculations with experimental results.

Typically, it is not sufficient just to describe the structural behaviour of any material but it is also important to describe the final failure of it. Therefore, adaptive failure criteria for TSSA have to be developed which on the one hand should be able to approximate the isochoric failure and on the other hand should predict the occurrence of cavitation. Since the stretch measure has been shown to be well suited for the failure description of polymer materials (Rosendahl et al., 2019), both distortional and dilatational failure criterion are defined in three-dimensional stretch space. Furthermore, both criteria will be coupled in order to have one failure criterion for arbitrary deformation situations. Finally, the coupled improved, novel stretch-based failure criterion shall be combined with a safety concept to ensure and calculate the structural integrity of bonded components in façade application. The aim is to show that the classical approaches for describing the strength of flat-bonded silicone adhesive joints according to ETAG 002 (2012) or manufacturer specifications lead to conservative results. If, however, newly developed models and failure formulations are used for the design and dimensioning of such non-standardized bonded joints, a significant increase in structural strength should be made possible without reducing the global safety level. The present work

excludes the time- and temperature-dependent material behaviour of polymeric materials. Furthermore, the work disregards the evaluation of failure criteria in relation to the dependence of the results on the finite element mesh. Mesh studies are shown but not considered in the evaluation of failure criteria. As has often been discussed, the evaluation of failure criteria via finite element calculations always shows a mesh dependency. This is especially true when bi-material notches occur at which so-called stress singularities arise. The special investigation of mesh-independent failure models is deliberately excluded but the developed models are prepared in such a way that they can be transferred, for example, to the concept of finite fracture mechanics, with which mesh-independent failure loads can be calculated.

## 1.3 Concept and Structure

The structure of the present dissertation is first divided into a short introduction designated as **Chap. 1**, in which the motivation and problem statement are described and defined. In **Chap. 2**, the theoretical foundations of continuum mechanics, the homogenization of micro-structural behaviour and the failure description and limit state analyses on materials are presented concisely. This gives the reader the necessary tools to follow the developments in the further course of the work. Since the present thesis investigates a transparent structural silicone, which can be described mechanically by hyperelasticity, **Chap. 3** presents the field of hyperelasticity and its mathematical description as well as essential hyperelastic material models. **Chap. 4** proposes the experimental investigations carried out on TSSA and summarises the main results. In addition to the experiments for the description of the structural behaviour, experiments for a better understanding of the micro-structural behaviour of TSSA are also described. Based on the experimental investigations and the discovered material effects, such as the Mullins effect, stress whitening and cavitation, **Chap. 5** presents novel physically motivated material models to describe the structural behaviour of TSSA. Furthermore, the presented material models are transferred into a commercial FE code and validated by the simulation of three different experiments. In **Chap. 6**, theoretical considerations are given for the description of the distortional and dilatational failure of polymeric materials and two novel stretch-based failure criteria are presented and validated on the basis of the experimentally measured data. The validation is done by three-dimensional FE calculations in which the novel failure criteria are evaluated. A roadmap is presented in **Chap. 7**, which is dedicated to the design of silicone-bonded constructions in glass and façade systems. The main findings of the present work are summarized and essential remarks and limits are given for the experimental characterization, the material parameter identification, the material

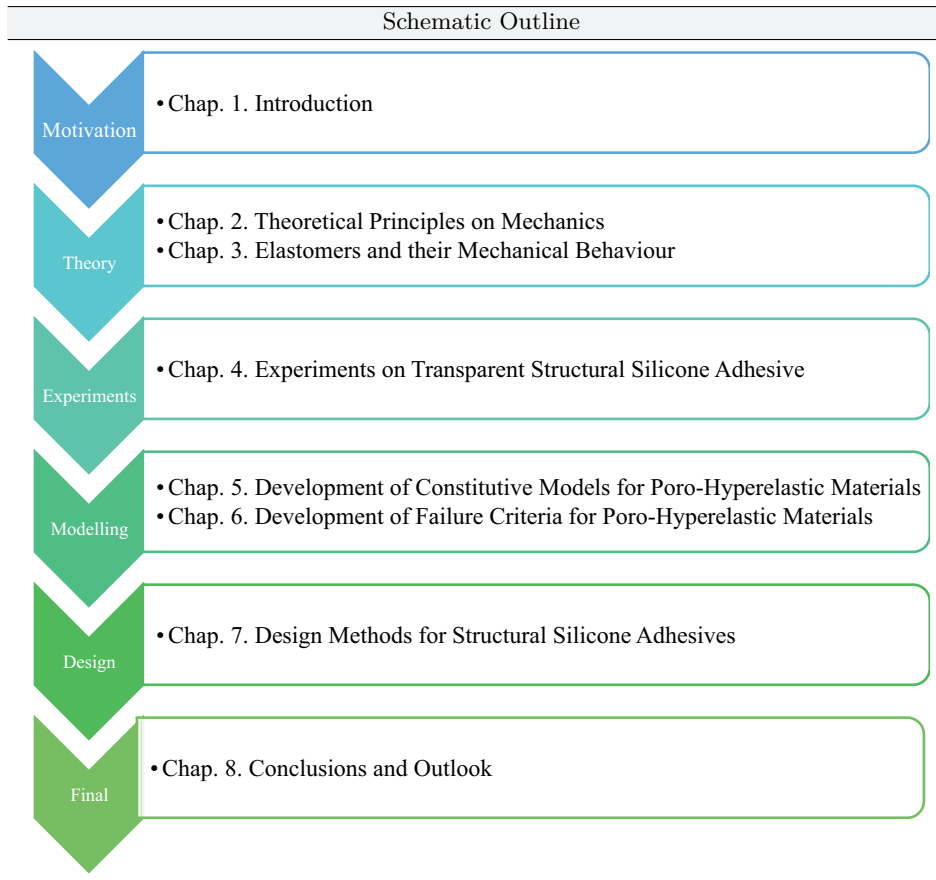


**Figure 1.2** Schematic overview of the outline of the present thesis

modelling as well as the limit state analyses for structural sealant glazing systems. **Chap. 8** summarizes the most important conclusions and gives an outlook on further research work. In order to understand the structure of the work visually, the reader is referred to Fig 1.2, in which the structure and the individual chapters of this work are presented. A detailed description of the state of the art is given separately in the corresponding chapters.

## 1.4 Author's Publications Prior to this Thesis

The following list contains publications, which are related to this thesis, but were published prior to it by the author of this thesis:

- Drass, M., V. A. Kolupaev, P. L. Rosendahl, J. Schneider, and W. Becker (2018a). "Generalized cavitation criterion for poro-hyperelastic materials". In: *Forschungskolloquium 2018 Grasellenbach*. Ed. by J. Schneider and N. Kiziltoprak. Wiesbaden: Springer Fachmedien Wiesbaden, pp. 20–23.
- Drass, M., J. Schneider, and S. Kolling (2018b). "Novel volumetric Helmholtz free energy function accounting for isotropic cavitation at finite strains". In: *Materials & Design* 138, pp. 71–89.
- Drass, M., N. Bartels, J. Schneider, and D. Klein (2019a). "Pseudo-Elastic Cavitation Model - Part II: Extension to Cyclic Behavior of Transparent Silicone Adhesives". In: *Glass Structures & Engineering*.
- Drass, M., P. A. Du Bois, J. Schneider, and S. Kolling (2019b). "Pseudo-Elastic Cavitation Model - Part I: Finite Element Analyses on Thin Silicone Adhesives in Façades". In: *Glass Structures & Engineering*.
- Drass, M., V. A. Kolupaev, J. Schneider, and S. Kolling (2018c). "On cavitation in transparent structural silicone adhesive: TSSA". In: *Glass Structures & Engineering* 3.2, pp. 237–256.
- Drass, M., J. Muth, J. Schneider, and C. Louter (2019c). "Stress Whitening Effects in Transparent Structural Silicone Adhesives". In: *Glass Structures & Engineering*.
- Drass, M., J. Schneider, and U. Knaack (2018d). "New Technologies and the Future of Glass in Building Constructions". In: ed. by U. Knaack and B. Horn. Messe Düsseldorf GmbH. Chap. Visions - Glass Technology Live: The Hub @ Glasstec 2018, pp. 10–23.
- Drass, M., J. Schneider, and S. Kolling (2017a). "Damage effects of adhesives in modern glass façades: a micro-mechanically motivated volumetric damage model for poro-hyperelastic materials". In: *International Journal of Mechanics and Materials in Design*.
- Drass, M., K.-U. Schober, and M. Kuechler (2014). "Advancement of glued-in rods using polymer concrete as composite material". In: *Proceedings of the 13th World Conference on Timber Engineering (WCTE 2014)*.
- Drass, M., M. Schuster, and J. Schneider (2017b). "Comparison of unconventional testing methods for mechanical characterization of polymeric materials in modern glass structures". In: *IABSE Symposium Report*. Vol. 109. 27. International Association for Bridge and Structural Engineering, pp. 2370–2377.

- Drass, M., G. Schwind, J. Schneider, and S. Kolling (2018e). “Adhesive connections in glass structures—part I: experiments and analytics on thin structural silicone”. In: *Glass Structures & Engineering* 3.1, pp. 39–54.
- Drass, M., G. Schwind, J. Schneider, and S. Kolling (2018f). “Adhesive connections in glass structures—part II: material parameter identification on thin structural silicone”. In: *Glass Structures & Engineering* 3.1, pp. 55–74.
- Gade, J., R. Kemmler, M. Drass, and J. Schneider (2018). “Enhancement of a meso-scale material model for nonlinear elastic finite element computations of plain-woven fabric membrane structures”. In: *Engineering Structures* 177, pp. 668–681.
- Kelleter, C., M. Drass, W. Haase, and J. Schneider (2016). “Aspekte experimenteller und numerischer Untersuchungen von Klemmhalterungen im Glasbau”. In: *Stahlbau* 85.1, pp. 183–195.
- Lübke, J., M. Wetzlaufer, N. Kiziltoprak, M. Drass, J. Schneider, and U. Knaack (2018). “Honeycomb-Paperboard Glass Composite Beams”. In: *Engineered Transparency* 2.5-6, pp. 57–69.
- Rosendahl, P. L., M. Drass, J. Felger, J. Schneider, and W. Becker (2019). “Equivalent strain failure criterion for multiaxially loaded incompressible hyperelastic elastomers”. In: *International Journal of Solids and Structures* 166, pp. 32–46.
- Rosendahl, P. L., M. Drass, J. Schneider, and W. Becker (2018). “Crack nucleation in hyperelastic adhesive bonds”. In: *Engineered Transparency* 2.5-6, pp. 409–425.
- Schober, K.-U., W. Becker, and M. Drass (2012). “Advanced interface interaction in timber engineering joints with dowel-type fasteners embedded in high-performance ceramic fillers”. In: *Proceedings of the 12th World Conference on Timber Engineering (WCTE 2012)*.
- Schober, K.-U., W. Becker, M. Drass, and J. Weber (2014). “High-performance timber composite joints for spatial round wood truss structures”. In: *Proceedings of the 13th World Conference on Timber Engineering (WCTE 2014)*.
- Schober, K.-U., M. Drass, and W. Becker (2013). “Adhesive strength of timber joints with unconventional glued-in steel rods”. In: *Proceedings of Wood Adhesives*.
- Silvestru, V. A., M. Drass, O. Englhardt, and J. Schneider (2018a). “Performance of a structural acrylic adhesive for linear glass-metal connections under shear and tensile loading”. In: *International Journal of Adhesion and Adhesives* 85, pp. 322–336.



## 2 Theoretical Principles on Mechanics

This chapter gives an introduction into mechanical principles of continuum mechanics, limit state analysis and failure criteria in general mechanics and a brief introduction into the field of micromechanics and homogenization. The essential equations are presented, but the reader is also referred to advanced literature, in which the strongly summarized contents are explained much more extensively.

### 2.1 Aspects on Continuum Mechanics

#### 2.1.1 Continua, Material Bodies and Motion of Continuous Bodies

All physical objects consist of molecules formed by atomic and subatomic particles. To describe physical phenomena under neglecting the microscopic scale, the method of continuum mechanics was developed as a powerful tool to characterize the macroscopic scale of materials by a few quantities. More detailed information on the development of continuum mechanics can be found in the classic monographs of Truesdell and Noll (2004); Chaves (2013); Altenbach (2015).

Continuum mechanics studies the motion of solids, fluids and gases of a continuous medium consisting of matter that is exposed to forces (e.g. displacements). The aim is to describe the movement of a material body from the reference configuration  $\mathcal{B}_0$  to the current, deformed configuration  $\mathcal{B}$  and thus to obtain information about the evolution of the material body over time. The subscript  $(\bullet)_0$  denotes the reference configuration, where all physical values are given in capital letter. The material body  $\mathcal{B}_0$  is defined as the manifold of all material points  $\mathbb{M} \subseteq \mathbb{E}^3$ , which are delimited through its boundary  $\partial\mathcal{B}_0$ . The manifoldness of all material points is described in three-dimensional Euclidean space  $\mathbb{E}^3$ , where the positions of material points  $\mathcal{P}_0 \in \mathbb{M}$  are characterized by the position vector  $\vec{\mathbf{X}} \in \mathbb{M}$  in the reference configuration. Deforming the body  $\mathcal{B}_0$  to  $\mathcal{B}$ , the material points  $\mathcal{P}_0$  of

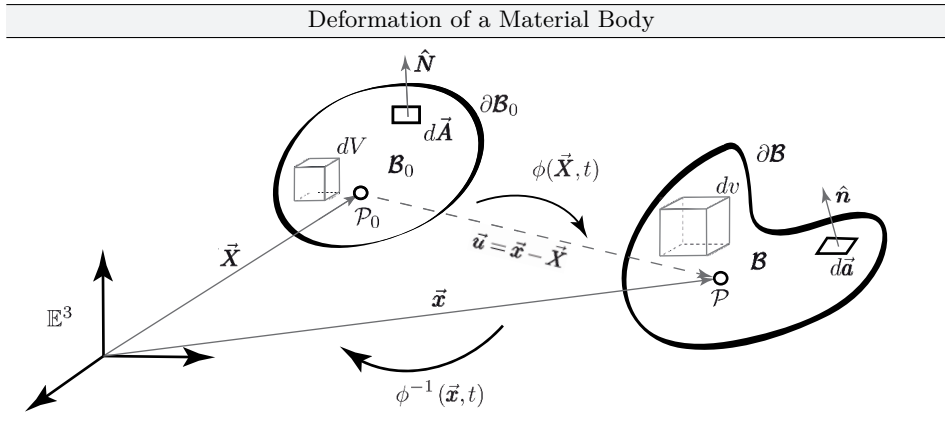


**Figure 2.1** Exemplary representation of a material body in the reference and current configuration

the reference configuration are mapped to the current configuration and denoted with  $\mathcal{P}$ . The position vector of the current configuration is defined by

$$\vec{x} = \phi(\vec{X}, t), \quad (2.1)$$

where the scalar field  $\phi$  describes the motion of bodies from the reference to the current configuration. Eq. (2.1) is also called Lagrangian or material description of motion. The inverse description of motion is given by

$$\vec{X} = \phi^{-1}(\vec{x}, t). \quad (2.2)$$

Thus, the motion of bodies can be explained by the continuous series of configurations  $\vec{x} = \phi(\vec{X}, t)$  over time, where  $\vec{X}$  describes the array-parameter and  $t$  the curve-parameter of motion trajectories. The difference between the above-mentioned two configurations can be described through the displacement vector  $\vec{u} = \vec{u}(\vec{X}, t)$ , which is defined through the difference of the position vectors  $\vec{x}$  and  $\vec{X}$  by

$$\vec{u} = \vec{x} - \vec{X}. \quad (2.3)$$

To complete the typical representation of the kinematic relationship between the two configurations, additional variables must be introduced. An arbitrary body in the reference configuration consists of differential volume elements  $dV$  and differential area elements  $d\vec{A}$ , which is identified by its normal  $\hat{n}$ . The same relationships apply for the current configuration, where these quantities are written in small letters (see Fig. 2.1).

## 2.1.2 Deformations and Strain Measures

To characterize the kinematics of continua, the deformation gradient  $\mathbf{F}$  is introduced, which maps a material line element  $d\vec{\mathbf{X}}$  from the reference configuration to the current configuration. By building the total differential of an infinitesimal position vector  $d\vec{\mathbf{x}}$  with respect to  $d\vec{\mathbf{X}}$

$$d\vec{\mathbf{x}} = \frac{\partial \phi(\vec{\mathbf{X}}, t)}{\partial \vec{\mathbf{X}}} \cdot d\vec{\mathbf{X}} = \frac{\partial \vec{\mathbf{x}}}{\partial \vec{\mathbf{X}}} \cdot d\vec{\mathbf{X}} = \mathbf{F} \cdot d\vec{\mathbf{X}}, \quad (2.4)$$

the deformation gradient is defined as

$$\mathbf{F} = \frac{\partial \vec{\mathbf{x}}}{\partial \vec{\mathbf{X}}} = \nabla_{\vec{\mathbf{X}}} \vec{\mathbf{x}}. \quad (2.5)$$

This second-order tensor is defined as a two-point tensor because it refers to the reference and the current configuration. Defining the inverse deformation gradient  $\mathbf{F}^{-1}$  as the spatial deformation gradient, the inverse motion can be described through the following equations:

$$d\vec{\mathbf{X}} = \mathbf{F}^{-1} \cdot d\vec{\mathbf{x}} \quad (2.6)$$

with

$$\mathbf{F}^{-1} = \frac{\partial \vec{\mathbf{X}}}{\partial \vec{\mathbf{x}}} = \nabla_{\vec{\mathbf{x}}} \vec{\mathbf{X}}. \quad (2.7)$$

The motion must be uniquely invertible at all times to form the reverse transformation. The necessary and sufficient condition is

$$J = \det \mathbf{F} \neq 0, \quad (2.8)$$

where  $J$  is called Jacobian determinant. If  $J > 0$  is guaranteed, two material points can never be in the same place at the same time, which is also called the axiom of impenetrability. The constraint of incompressibility is guaranteed for  $J = 1$  for any deformation so that the volume does not change.

With the definition of the displacement vector  $\vec{\mathbf{u}} = \vec{\mathbf{x}} - \vec{\mathbf{X}}$  and the deformation gradient  $\mathbf{F}$ , the material displacement gradient tensor  $\mathbf{H}$  is given by

$$\mathbf{H} = \nabla_{\vec{\mathbf{X}}} \vec{\mathbf{u}}(\vec{\mathbf{X}}, t) = \mathbf{F} - \mathbf{1} \quad (2.9)$$

Since the mapping of a material line element has already been described by Eq. (2.5), the following describes the linear mapping of a differential area and volume element

from the reference to the current configuration. The mapping of a differential area element is described by Nanson's formula, which reads

$$d\vec{\mathbf{a}} = J d\vec{\mathbf{A}} \cdot \mathbf{F}^{-1} = J \mathbf{F}^{-T} \cdot d\vec{\mathbf{A}}. \quad (2.10)$$

The relation between the volume of the reference and current configuration reads

$$dv = \det \mathbf{F} dV = J dV, \quad (2.11)$$

where  $J$  can also be described as the relative volume. The relative change of a volume element is often referred to as dilatation (Chaves, 2013:p.220) and is described by

$$D_V(\vec{\mathbf{X}}, t) = \frac{dV(\vec{\mathbf{x}}, t) - dV(\vec{\mathbf{X}}, 0)}{dV(\vec{\mathbf{X}}, 0)} = J - 1. \quad (2.12)$$

To split the deformation gradient into a rotation tensor and a stretch tensor, the theorem of polar decomposition is used, which leads to

$$\mathbf{F} = \underbrace{\mathbf{R} \cdot \mathbf{U}}_{\text{right polar decomposition}} = \overbrace{\mathbf{v} \cdot \mathbf{R}}^{\text{left polar decomposition}} \quad (2.13)$$

with

$$\mathbf{v} = \mathbf{R} \cdot \mathbf{U} \cdot \mathbf{R}^T. \quad (2.14)$$

This gives an orthogonal rotation tensor  $\mathbf{R} = \mathbf{R}^T$  and a symmetrical and positive definite right stretch tensor  $\mathbf{U} = \mathbf{U}^T$  or a left stretch tensor  $\mathbf{v} = \mathbf{v}^T$ . The right stretch tensor  $\mathbf{U}$  is also often called Lagrangian stretch tensor, whereas the left stretch tensor  $\mathbf{v}$  is called Eulerian stretch tensor based on the underlying configuration. Both stretch tensors can be also given in spectral representation reading

$$\mathbf{U} = \sum_{i=1}^3 \lambda_i \vec{\mathbf{N}}_i \otimes \vec{\mathbf{N}}_i \quad (2.15)$$

and

$$\mathbf{v} = \sum_{i=1}^3 \lambda_i \vec{\mathbf{n}}_i \otimes \vec{\mathbf{n}}_i, \quad (2.16)$$

where  $\lambda_i$  with  $i \in [1, 2, 3]$  represent the principal stretches (eigenvalues) and  $\vec{\mathbf{N}}_i$  and  $\vec{\mathbf{n}}_i$  define the eigenvectors of  $\mathbf{U}$  and  $\mathbf{v}$ . The eigenvalues and eigenvectors can

be obtained by solving a set of homogeneous algebraic equations for the unknown eigenvalues and the unknown eigenvectors, which reads

$$(\mathbf{U} - \lambda_i \mathbf{1}) \vec{\mathbf{N}}_i = \mathbf{0} \quad (2.17)$$

or

$$(\mathbf{v} - \lambda_i \mathbf{1}) \vec{\mathbf{n}}_i = \mathbf{0}. \quad (2.18)$$

The principal scalar invariants can be determined by solving, for instance, Eq. (2.18). To have solutions  $\vec{\mathbf{n}}_i \neq \mathbf{0}$ , the determinant must vanish. Thus,

$$\det(\mathbf{v} - \lambda_i \mathbf{1}) = \mathbf{0} \quad (2.19)$$

with

$$\det(\mathbf{v} - \lambda_i \mathbf{1}) = -\lambda_i^3 + I_{1,\mathbf{v}} \lambda_i^2 - I_{2,\mathbf{v}} \lambda_i + I_{3,\mathbf{v}} \quad (2.20)$$

By solving this cubic equation (characteristic polynomial) in  $\lambda$ , which can be re-expressed as

$$\lambda^3 - I_{1,\mathbf{v}} \lambda^2 + I_{2,\mathbf{v}} \lambda - I_{3,\mathbf{v}} = 0 \quad (2.21)$$

one obtains eigenvalues the  $\lambda_i$ . The principal invariants of a general tensor, e.g.  $\mathbf{b}$ , read

$$I_{1,\mathbf{b}} = \text{tr}(\mathbf{b}), \quad I_{2,\mathbf{b}} = \frac{1}{2} [I_{\mathbf{b}}^2 - \text{tr}(\mathbf{b}^2)], \quad I_{3,\mathbf{b}} = \det(\mathbf{b}), \quad (2.22)$$

where  $\mathbf{b}$  represents the second order left Cauchy-Green deformation tensor. It is defined by

$$\mathbf{b} = \mathbf{v}^2 = \mathbf{F} \cdot \mathbf{F}^T, \quad (2.23)$$

whereas the right Cauchy-Green deformation tensor reads

$$\mathbf{C} = \mathbf{U}^2 = \mathbf{F}^T \cdot \mathbf{F}. \quad (2.24)$$

Based on the deformation tensors defined above, important strain measures are summarized in the following. The Green-Lagrange strain tensor can be derived by

$$\mathbf{E} = \frac{1}{2} (\mathbf{C} - \mathbf{1}) = \frac{1}{2} (\mathbf{U}^2 - \mathbf{1}) = \frac{1}{2} (\mathbf{F}^T \cdot \mathbf{F} - \mathbf{1}), \quad (2.25)$$

whereas the spatial Euler-Almansi strain tensor is defined by

$$\mathbf{e} = \mathbf{F}^{-T} \cdot \mathbf{E} \cdot \mathbf{F}^{-1} = \frac{1}{2} (\mathbf{1} - \mathbf{b}^{-1}) = \frac{1}{2} (\mathbf{1} - \mathbf{v}^{-2}) = \frac{1}{2} \left( \mathbf{1} - (\mathbf{F} \cdot \mathbf{F}^T)^{-1} \right). \quad (2.26)$$

Inserting the material displacement gradient tensor  $\mathbf{H}$  in Eq. (2.25), the Green-Lagrange strain tensor can be split into a linear and non-linear part reading

$$\mathbf{E} = \frac{1}{2} \underbrace{\left( \mathbf{H} + \mathbf{H}^T \right)}_{\text{linear}} + \frac{1}{2} \underbrace{\left( \mathbf{H}^T \cdot \mathbf{H} \right)}_{\text{nonlinear}}. \quad (2.27)$$

Under consideration of small deformations the difference between the reference and current configuration vanishes so that the non-linear behaviour is disregarded. The main disadvantage of the Green-Lagrange or Euler-Almansi strain tensors is that both are not suitable to solve problems incrementally because they do not allow any additive superposition of motion increments (Chaves, 2013:p.240). In contrast, the logarithmic strain tensor or Hencky strain tensor allows the addition of strain increments. The Hencky strain tensor is defined by

$$\boldsymbol{\varepsilon} = \ln(\mathbf{U}) = \ln(\mathbf{v}). \quad (2.28)$$

### 2.1.3 Stress Measures

In continuum mechanics it is important to define stress measures in order to analyse classically the structural behaviour and its failure. Regarding the current configuration  $\mathcal{B}$  in Fig. 2.1, the stress vector  $\vec{t}$  can be derived by Cauchy's theorem as

$$\vec{t} = \boldsymbol{\sigma} \cdot \hat{\mathbf{n}}, \quad (2.29)$$

where the linear map between the stress vector  $\vec{t}$  and the surface element's normal  $\hat{\mathbf{n}}$  in the current configuration is described by the Cauchy stress tensor  $\boldsymbol{\sigma}$ . The second order symmetrical Cauchy stress tensor  $\boldsymbol{\sigma}$  consists of nine components and refers to the current configuration, making it often referred to as a true stress tensor. The same can also be derived for the reference configuration, which results in the relationship

$$\vec{t}_0 = \mathbf{P} \cdot \hat{\mathbf{N}}, \quad (2.30)$$

where  $\mathbf{P}$  describes the first Piola-Kirchhoff stress tensor or nominal / engineering stress tensor, respectively. The relation between the stress tensors of the reference and current configuration results in

$$\mathbf{P} = J \boldsymbol{\sigma} \cdot \mathbf{F}^{-T}. \quad (2.31)$$

Since the first Piola-Kirchhoff stress tensor  $\mathbf{P}$  is an unsymmetrical tensor, the second Piola-Kirchhoff stress tensor  $\mathbf{S}$  will be introduced as a pure operand without physical meaning. It reads

$$\mathbf{S} = \mathbf{F}^{-1} \cdot \mathbf{P} = J\mathbf{F}^{-1} \cdot \boldsymbol{\sigma} \cdot \mathbf{F}^{-T}. \quad (2.32)$$

### 2.1.4 Balance Principles in Continuum Mechanics

In continuum mechanics there are four fundamental equations for the description of boundary value problems (BVP) based on conservation principles of physical quantities. A conservation principle implies that no physical quantity (mass density, energy density, etc.) per unit volume in a part of a domain can be created or destroyed, but only changes from one place to another. These conservations principles can be summarized through:

- principle of conversation of mass
- principle of conversation of linear momentum
- principle of conversation of angular momentum
- principle of conversation of energy

These principles are not sufficient to solve a BVP, hence the constitutive model must be additionally considered in order to fully describe the physical problem.

#### Conservation of Mass

Starting with the conservation of mass, it must be the same for the reference and the current configuration. The conservation principle reads in an integral form

$$\int_{V_0} \rho_0(\vec{\mathbf{X}}) dV_0 = \int_V \rho(\vec{\mathbf{x}}, t) dV = \int_{V_0} \underbrace{\rho(\vec{\mathbf{x}}, t) J}_{f(\vec{\mathbf{X}})} dV_0, \quad (2.33)$$

where  $\rho_0$  and  $\rho$  characterize the mass density in the reference respectively the current configuration. Since equation Eq. (2.33) must be valid at every material point, it must also be locally fulfilled, which leads to

$$\rho_0(\vec{\mathbf{X}}) = J\rho. \quad (2.34)$$

Additionally, since  $\rho_0$  and  $J\rho$  are independent of time, the Lagrangian description of the mass continuity equation can be obtained by

$$\frac{D}{Dt}(J\rho) = 0 \quad (2.35)$$

whereas for the Eulerian description it becomes

$$\frac{\partial \rho}{\partial t} + \nabla_{\vec{x}} \cdot (\rho \vec{v}) = 0. \quad (2.36)$$

The Eulerian velocity is characterized by  $\vec{v}$ . Analysing incompressible materials, the mass density field for all particles is independent on time, therefore the following applies

$$\frac{D J}{Dt} \equiv \dot{J} = 0 ; \quad \frac{D \rho}{Dt} \equiv \dot{\rho} = 0 ; \quad \rho = \rho_0 ; \quad J = 1, \quad (2.37)$$

which results in

$$\nabla_{\vec{x}} \cdot \vec{v} = 0 \quad (2.38)$$

for the mass continuity equation in the Eulerian description.

### Conservation of Linear Momentum

The principle of conservation of linear momentum is based on Newton's second law, which states that the rate of change of the linear momentum of any part of a continuous medium is equivalent to the resulting force (body and surface forces) acting on the mentioned part (Chaves, 2013:p.297). Renouncing an explicit derivation, Cauchy's first equation of motion in the Eulerian description reads

$$\nabla_{\vec{x}} \cdot \boldsymbol{\sigma} + \rho \vec{b} = \rho \vec{a}, \quad (2.39)$$

where  $\vec{a}$  represents the Eulerian acceleration field. The local form in the material or Lagrangian description results in

$$\nabla_{\vec{x}} \cdot \mathbf{P} + \rho_0 \vec{B} = \rho_0 \vec{A}, \quad (2.40)$$

where  $\vec{A}$  represents the Lagrangian acceleration field. In the case that the acceleration forces are zero, we have a static or quasi-static scenario, whereby the equilibrium conditions are reduced to

$$\nabla_{\vec{x}} \cdot \boldsymbol{\sigma} + \rho \vec{b} = \vec{0} \quad (2.41)$$

and

$$\nabla_{\vec{x}} \cdot \mathbf{P} + \rho_0 \vec{B} = \vec{0}, \quad (2.42)$$

which represents classical equilibrium conditions in continuum mechanics.

### Conservation of Angular Momentum

According to Chaves (2013):p.303, the principle of conservation of angular momentum describes that the rate of change of the angular momentum with respect to a point is equal to the resulting momentum (with respect to that point) generated by all the forces acting on the body under consideration. Skipping the explicit derivation, the principle of angular momentum states that

$$\boldsymbol{\sigma} = \boldsymbol{\sigma}^T \quad \text{and} \quad \mathbf{P} \cdot \mathbf{F}^T = \mathbf{F} \cdot \mathbf{P}^T. \quad (2.43)$$

Thus the conversation of angular momentum requires that the Cauchy stress tensor is symmetric.

### Conservation of Energy

The conservation of energy in a closed system can be described by

$$\rho \frac{Dw^{\text{int}}}{Dt} = \boldsymbol{\sigma} : \mathbf{D} - \nabla_{\vec{x}} \cdot \vec{q} + \rho r, \quad (2.44)$$

which gives us the energy equation in the current configuration. In this context  $\mathbf{D}$  is the rate-of-deformation tensor,  $\vec{q}$  characterizes the thermal flux vector and  $r$  is the radiant heat constant. For pure mechanical problems with no internal heat production and / or heat flux, Eq. (2.44) degenerates to

$$\dot{w}^{\text{int}} = \frac{1}{\rho} \boldsymbol{\sigma} : \mathbf{D}, \quad (2.45)$$

or in the Lagrangian description

$$\dot{w}^{\text{int}} = \frac{1}{\rho_0} \mathbf{P} : \dot{\mathbf{F}}. \quad (2.46)$$

Summarizing, the governing equations for a total Lagrangian formulation are presented in Tab 2.1. As already mentioned, the balance principles alone are not sufficient to fully describe a BVP. Hence further equations must be given for reasons of completeness. The additional equations describe the constitutive model, strain measurement, boundary conditions and initial conditions. Although this thesis deals with the constitutive description of materials and the solution of BVP using the finite element method, no detailed description of this method is given below. Reference is made to secondary literature such as the monograph of Belytschko et al. (2013). The momentum equations are given in terms of the stress tensor  $\mathbf{P}$

due to reasons of simplicity. In contrast, the constitutive equation is evaluated by the second Piola-Kirchhoff stress tensor  $\mathbf{S}$  because it is symmetric. The transformation from  $\mathbf{S}$  to stress tensor  $\mathbf{P}$  can be done over the double scalar product with the transposed deformations gradient. Regarding the boundary conditions (stress boundary conditions) of an arbitrary BVP defined in the total Lagrangian formulation, Cauchy's theorem must be re-expressed for the reference configuration. The relationship between stress tensor and stress vector results through the extension with the scalar product between stress tensor  $\mathbf{P}$ , the surface element's normal  $\hat{\mathbf{n}}$  and the stress vector  $\vec{\mathbf{t}}$  respectively with the unit base vectors  $\vec{\mathbf{e}}_i$ . Traction boundary conditions are called  $\Gamma_{0,\vec{\mathbf{t}}}$ , whereas displacement boundary conditions are referred to as  $\Gamma_{0,\vec{\mathbf{u}}}$ . The value for the displacement vector  $\vec{\mathbf{u}}$  is given by  $\vec{\mathbf{u}}^*$ . In general BVP's it is possible to have initial traction or velocity conditions such as temperature residual stresses. These must also be considered in the solution. In general, the initial conditions apply for the event  $t = 0$ .

**Table 2.1** Governing equations for total Lagrangian formulation for pure mechanical, quasi-static problems disregarding internal heat production and / or heat flux

(1) Conservation of mass

$$\rho J = \rho_0 J_0 = \rho_0$$

(2) Conservation of linear momentum

$$\nabla_{\vec{X}} \cdot \mathbf{P} + \rho_0 \vec{\mathbf{B}} = \vec{0}$$

(3) Conservation of angular momentum

$$\mathbf{P} \cdot \mathbf{F}^T = \mathbf{F} \cdot \mathbf{P}^T$$

(4) Conservation of energy

$$\dot{w}^{\text{int}} = \frac{1}{\rho_0} \mathbf{P} : \dot{\mathbf{F}}$$

(5) Constitutive equation

$$\mathbf{S} = \mathbf{S}(\mathbf{E}, \dots, \text{etc.}) \text{ or } \mathbf{P} = \mathbf{S} \cdot \mathbf{F}^T$$

(6) Measure of Strain

$$\mathbf{E} = \frac{1}{2} (\mathbf{F}^T \cdot \mathbf{F} - \mathbf{I})$$

(7) Boundary conditions

$$\vec{\mathbf{e}}_i \cdot \hat{\mathbf{n}} \cdot \mathbf{P} = \vec{\mathbf{e}}_i \cdot \vec{\mathbf{t}}_0 \quad \text{on } \Gamma_{0,\vec{t}}$$

$$\vec{\mathbf{u}} = \vec{\mathbf{u}}^* \quad \text{on } \Gamma_{0,\vec{u}}$$

(8) Initial conditions

$$\mathbf{P}(\vec{X}, 0) = \mathbf{P}_0(\vec{X})$$

$$\dot{\mathbf{u}}(\vec{X}, 0) = \dot{\mathbf{u}}_0(\vec{X})$$

## 2.2 Failure Criteria and Limit State Analyses

### 2.2.1 Basics of Failure Criteria

The formulation of failure criteria has been a popular topic of mechanics for more than a hundred years in order to be able to describe failure for any load scenarios over a scalar quantity. An overview of the history of failure criteria, which were developed in the past, is given by Timoshenko (1953), Kolupaev (2018) and Yu (2018). A common method in limit state analyses is the equivalent stress or strain concept, which assumes the equivalence of different stress and strain states. Describing the surface, which represents the boundary between an intact and a damaged material with  $\Phi$ , a general phenomenological failure criterion

$$\Phi(\boldsymbol{\sigma}, \boldsymbol{\varepsilon}) = 0 \quad (2.47)$$

can be formulated. Describing the failure formulation of materials with words, an intact material exists for  $\Phi(\boldsymbol{\sigma}, \boldsymbol{\varepsilon}) < 0$ , but if  $\Phi(\boldsymbol{\sigma}, \boldsymbol{\varepsilon}) \geq 0$  applies, the material will fail. In this context it is important to note that material failure includes the start of yielding phenomena and also softening effects, which, however, do not represent the final failure of the material. Nevertheless, in limit state analyses it is common to use this terminology although the material exhibits internal capacities to withstand further loading.

Returning back to the general form of a failure criterion presented in Eq. (2.47), it depends on tensorial quantities, which must be expressed by invariants of them to obtain scalar quantities as an evaluation criterion for failure. A commonly used stress-based invariant in the field of limit state analyses is formulated by the trace of the Cauchy stress tensor, which reads

$$I_{1,\boldsymbol{\sigma}} = \text{tr}(\boldsymbol{\sigma}) = \sigma_1 + \sigma_2 + \sigma_3. \quad (2.48)$$

The first invariant is related to the hydrostatic stress and is therefore important for dilatational failure. In contrast, considering distortional failure, the second and third invariant of the stress deviator is often used. The second invariant is given by

$$I'_{2,\boldsymbol{\sigma}} = \frac{1}{6} [(\sigma_1 - \sigma_2)^2 + (\sigma_2 - \sigma_3)^2 + (\sigma_3 - \sigma_1)^2], \quad (2.49)$$

whereas the third invariant of the stress deviator can be expressed as

$$I'_{3,\boldsymbol{\sigma}} = \left( \sigma_1 - \frac{I_{1,\boldsymbol{\sigma}}}{3} \right) \left( \sigma_2 - \frac{I_{1,\boldsymbol{\sigma}}}{3} \right) \left( \sigma_3 - \frac{I_{1,\boldsymbol{\sigma}}}{3} \right). \quad (2.50)$$

To make it clear that both invariants represent distortional failure or depend on the stress deviator, respectively, they are additionally indicated with an apostrophe. In Eqs. (2.48)-(2.50), the components  $\sigma_1, \sigma_2, \sigma_3$  of the principal stress tensor  $\boldsymbol{\sigma}''$  are applied, which can be obtained by multiplication of the Cauchy stress tensor with an orthogonal matrix  $\mathbf{M}$  based on the eigenvectors of the right stretch tensor  $\mathbf{U}$ , which reads

$$\boldsymbol{\sigma}'' = \mathbf{M}\boldsymbol{\sigma}\mathbf{M}^T. \quad (2.51)$$

### 2.2.2 Visualization Methods

Failure criteria can be visualized using three-dimensional or two-dimensional implicit plots. Focusing on three-dimensional, non-closed failure criteria (Drass et al., 2018c), these can generally be represented in stress or strain space. The sectional plane of the failure surface with the deviator or  $\pi$ -plane is often of great interest, especially with regard to the verification of convexity. Introducing a new orthogonal coordinate system with the coordinates  $\xi_1, \xi_2$  and  $\xi_3$ , the deviator plane is characterized by  $\xi_2$  and  $\xi_3$ , whereas the third coordinate  $\xi_1$  is perpendicular to that plane (Schreyer, 1989). The orthogonal transformed coordinates read

$$\xi_1 = \frac{I_{1,\boldsymbol{\sigma}}}{\sqrt{3}} = \frac{\sigma_1 + \sigma_2 + \sigma_3}{\sqrt{3}}, \quad (2.52)$$

$$\xi_2 = \frac{\sigma_1 - \sigma_3}{\sqrt{2}} \quad (2.53)$$

and

$$\xi_3 = \frac{2\sigma_2 - \sigma_1 - \sigma_3}{\sqrt{6}}, \quad (2.54)$$

whereas the coordinate transformation between the principal stresses and the transformed coordinates reads

$$\begin{pmatrix} \sigma_1 \\ \sigma_2 \\ \sigma_3 \end{pmatrix} = \begin{pmatrix} \frac{1}{\sqrt{3}} & \frac{1}{\sqrt{2}} & -\frac{1}{\sqrt{6}} \\ \frac{1}{\sqrt{3}} & 0 & \frac{2}{\sqrt{6}} \\ \frac{1}{\sqrt{3}} & -\frac{1}{\sqrt{2}} & -\frac{1}{\sqrt{6}} \end{pmatrix} \begin{pmatrix} \xi_1 \\ \xi_2 \\ \xi_3 \end{pmatrix}. \quad (2.55)$$

A generic example for an illustration of a non-closed failure criterion in three-dimensional stress space is given in Fig. 2.2. For a better understanding, the transformed coordinate system and three  $\pi$ -planes at different sectional planes are also illustrated. Additionally, important meridians for stress angles of  $\theta = 0, 30, 60^\circ$  are shown, which are of great importance to determine parameters for three-dimensional failure criteria based on experimental or virtual datasets (Fahlbusch

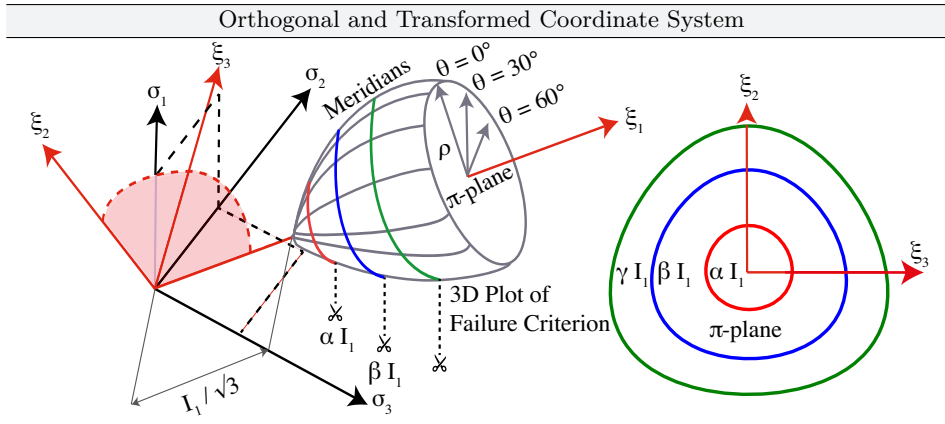


**Figure 2.2** Haigh & Westergaard-space of arbitrary cavitation criterion in terms of principal Cauchy stresses ( $\sigma_1, \sigma_2, \sigma_3$ ), the transformed coordinates  $\xi_1, \xi_2$  and  $\xi_3$  and the  $\pi$ -plane at different sectional planes ( $\alpha I_1, \beta I_1, \gamma I_1$ )

et al., 2016). In contrast to the classical proposed invariants of Eqs. (2.48)-(2.50), more descriptive invariants with geometrical meaning were introduced by Novozhilov (Kolupaev, 2018:p. 6), which are defined by the scaled hydrostatic axis  $\xi_1$ , the distance between the failure surface to the hydrostatic axis  $\rho$  and the stress angle  $\theta$ . The radius  $\rho$  and the argument  $\theta$  of the stress angle  $\cos 3\theta$  are defined by

$$\rho = \sqrt{\xi_2^2 + \xi_3^2} = \sqrt{2I'_2} \quad (2.56)$$

and

$$\theta = \frac{1}{3} \arccos \left( \frac{3\sqrt{3}}{2} \frac{I'_3}{(I'_2)^{3/2}} \right) \quad \text{with } \theta \in [0, \pi/3]. \quad (2.57)$$

The so-called Burzyński-plane, in which different meridians are represented in the coordinates  $\xi_1 - \rho$ , is often used to illustrate three-dimensional failure criteria in a vivid and descriptive manner (Zyczkowski, 1981). In Kolupaev (2018):p.75, it is recommended to scale the axis of the Burzyński-plane with respect to the von Mises criterion with the result that the scaled Burzyński-plane is formulated in  $I_1 - \sqrt{3I'_2}$  coordinates. For all following studies, the definition in accordance to Kolupaev (2018) will be applied for illustrating the scaled Burzyński-plane.

### 2.2.3 Convexity Constraints

The demand for convex yield or failure surfaces is often a strict mathematical requirement that is met by almost all formulations (Kolupaev, 2018). The require-

ment for convex yield or failure surfaces arose from history of plasticity modelling to ensure a positive plastic dissipation, when a material begins to yield. A discussion about non-convex yield surfaces, which nevertheless guarantee a positive plastic dissipation, was conducted in Glüge and Bucci (2017). Nevertheless, different methods for proving convexity of failure surfaces are presented in the following, since the requirement for convexity has become established in literature. Three different criteria for checking convexity are introduced and their applicability is presented with the help of an example.

### Drucker's Material Stability Postulate

A widely used criterion for checking convexity is the material stability postulate of Drucker (1957), which states that the strain energy at any plastic deformation is not negative. This means for a work-hardening material that the yield surface is convex and the plastic strain increment is normal to the yield surface. A material that does not meet this criterion is often perceived as unstable in the sense that any load acting at one single material point can lead to arbitrary deformations at that material point. Summarizing, the associated flow rule, the normality rule, the principle of maximum plastic work and the convexity of the yield surface can be subsumed with the postulate of Drucker (Stoughton and Yoon, 2006). A concise derivation of the inequality is given in Ganczarski and Skrzypek (2015). The postulate of Drucker reads

$$\begin{aligned} (\boldsymbol{\sigma} - \boldsymbol{\sigma}^*) : d\boldsymbol{\varepsilon}^P &\geq 0 \\ d\boldsymbol{\sigma} : d\boldsymbol{\varepsilon}^P &\geq 0, \end{aligned} \tag{2.58}$$

where  $\boldsymbol{\sigma}^*$  describes the initial stress state inside a current yield surface and  $\boldsymbol{\sigma}$  represents the current stress state belonging to the yield surface with  $\Phi(\boldsymbol{\sigma}) = 0$ .  $d\boldsymbol{\varepsilon}^P$  represents the irreversible incremental plastic strain tensor, which is defined as the vector normal of the yield surface. Eq. (2.58) can be interpreted geometrically as convexity constraint for a yield surface.

A schematic example for a convex and a non-convex yield surface in two-dimensional space is shown in Fig. 2.3. Since the double scalar product between the tensors  $(\boldsymbol{\sigma} - \boldsymbol{\sigma}^*)$  and  $d\boldsymbol{\varepsilon}^P$  must be non-negative. Thus, the angle between the corresponding vectors must be either acute or right-angled. In order to still have a plastic process with increasing deformation, only such virtual stresses  $d\boldsymbol{\sigma}$  are permissible, which point out of the yield surface. Consequently, the flow surface must be convex. Satisfying Drucker's postulate, the materials and their constitutive models are generally well suited for linear and non-linear numerical analyses using the finite element method, while materials that do not meet this criterion may exhibit difficulties (i.e. non-uniqueness or singularity) during the solution process.

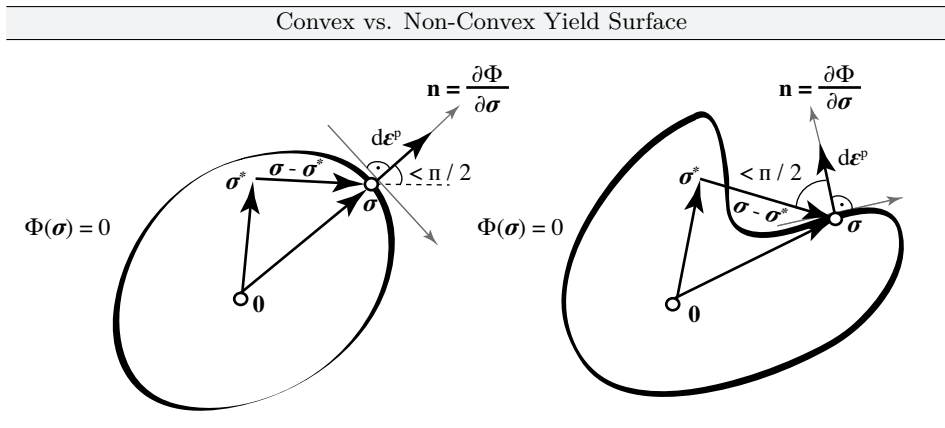


**Figure 2.3** Generic example for Drucker's stability postulate, which is satisfied (convexity and normality condition hold) and is not satisfied (non-convex yield surface is present)

### Sylvester's Stability Condition

Chen and Han (2007):p.168 ff. proposed a stability criterion, where the convexity of a hyper-surface of constant strain energy  $\hat{\Psi} = \text{const.}$  is proved by analysing the definiteness of the Hessian matrix  $[\mathbb{H}_{\hat{\Psi}}]$  of  $\hat{\Psi}$ . This stability criterion is also called convexity postulate of surfaces of constant strain energy. Formulating a general incremental material model in Voigt notation, such as

$$d\{\sigma\} = [\mathbb{H}_{\hat{\Psi}}] d\{\varepsilon\}, \quad (2.59)$$

the Hessian matrix  $[\mathbb{H}_{\hat{\Psi}}] = \partial^2 \Psi / \partial \varepsilon^2$  must be positive definite to ensure a convex surface. Substituting Eq. (2.59) into Eq. (2.58) (Kuna-Ciskał and Skrzypek, 2004), the stability criterion reads

$$[\mathbb{H}_{\hat{\Psi}}] d\{\varepsilon\} d\{\varepsilon\} > 0. \quad (2.60)$$

This means that the quadratic form (Eq. (2.60)) must be positive definite for any  $d\varepsilon$  to ensure convexity.

### Proof of Gaussian Curvature

Since both criteria, Drucker's material stability postulate and Sylvester's stability condition, imply restrictions with respect to a convex and closed yield or failure surface (Ganczarski and Skrzypek, 2015), a more general approach is given by analysing the Gaussian curvature of an arbitrary yield or failure surface. The

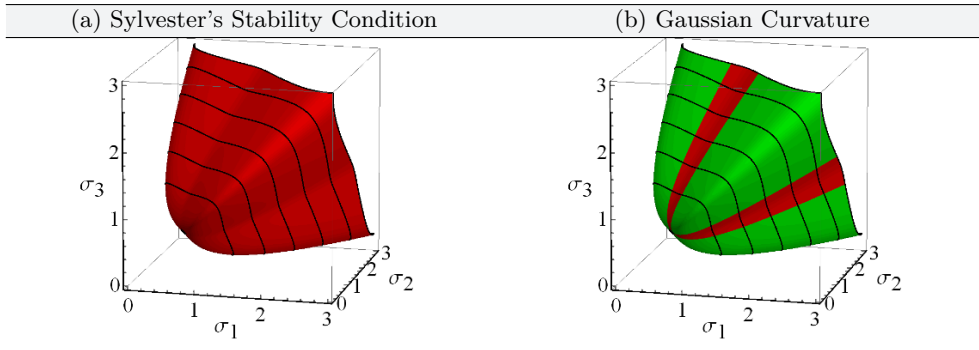


**Figure 2.4** Generic example of three-dimensional failure surfaces formulated in Cauchy stress space: (a) Visualisation of Sylvester's stability condition and (b) Gaussian curvature, where the green colouring (■) represents a convex / positive curvature and the red colouring (■) the opposite

Gaussian curvature  $\mathcal{K}$  is defined as the product of the principal curvatures  $\kappa_1, \kappa_2$  of a local point on a surface with

$$\mathcal{K} = \kappa_1 \kappa_2. \quad (2.61)$$

To calculate the Gaussian curvature of an arbitrary yield or failure criterion / surface  $\Phi(\boldsymbol{\sigma}, \boldsymbol{\varepsilon})$ , the Hessian matrix and the gradient of  $\Phi(\boldsymbol{\sigma}, \boldsymbol{\varepsilon})$  must be calculated. For an implicitly defined failure surface, the Gaussian curvature reads

$$\mathcal{K} = \frac{\begin{vmatrix} \mathbb{H}_\Phi & \nabla \Phi^T \\ \nabla \Phi & 0 \end{vmatrix}}{|\nabla \Phi|^4}, \quad (2.62)$$

where  $\mathbb{H}_\Phi$  is the Hessian operator applied to  $\Phi$  and  $\nabla \Phi$  describes the gradient of the yield or failure criterion. To ensure a convex (concave) surface the Gaussian curvature must be  $\mathcal{K} \geq 0$ , while a saddle point show a curvature of  $\mathcal{K} \leq 0$  (Gromov, 1991).

The advantage of the evaluation of the Gaussian curvature lies on the one hand in the direct geometric analysis of failure surfaces independent of a constitutive model. On the other hand, convexity testing can also be performed for non-closed failure surfaces using the Gaussian curvature. This can be convincingly demonstrated on a pressure-sensitive non-closed failure surface formulated in three-dimensional Cauchy stress space. Looking at Fig. 2.4, it is obvious that Sylvester's stability condition postulates a non-convex failure surface (red colouring). In contrast, the Gaussian curvature shows exactly these areas that are convex (green colouring). Therefore, especially for non-closed failure surfaces, the evaluation of

the Gaussian curvature is useful to provide information about convexity with an exact localization of convex and non-convex areas.

## 2.3 Micromechanics and Homogenization

Micromechanics focuses on the microstructure of any material. Using homogenization techniques, the microstructural material behaviour is mapped to a macroscopic constitutive model (Zohdi and Wriggers, 2011). Hill (1972) divided the field of homogenization into two sub-areas: (i) continuum-mechanically motivated determination of the effective material parameters and (ii) a rational micro-macro transition of the mechanical fields.

On the condition that the effective overall properties of heterogeneous materials have been determined, three essential homogenization procedures have found access in professional circles:

- Mathematical Homogenization
- Numerical Homogenization
- Micromechanical Homogenization

### **Mathematical Homogenization**

Within the framework of mathematical homogenization a mechanical problem is analysed in terms of mathematical formalism, where the underlying equations and boundary conditions have to be solved with the help of functional spaces and operators. For this formalized problem concepts of convergence and limit processes have been developed with the help of which a homogenized compensatory problem can be solved. In this context, the classical method of asymptotic evolution, two-scale convergence and gamma, G and H convergence should be mentioned. Since the mathematical homogenization will not be addressed in this work, the interesting reader is referred to Sanden (2013).

### **Numerical Homogenization**

The numerical homogenization is a method within the context of micromechanics, which has no restrictions towards the micromechanically-motivated representative volume elements (RVE), boundary conditions, linear or non-linear material behaviour and damage processes including dissipative mechanism. Hereby, a macroscopic structure is modelled with a relative coarse mesh using the Finite-Element-Method, where the (effective) material parameters are initially unknown, and has to be determined and transitioned by solving simultaneously a boundary value

problem on the microscale in every Gaussian point. This procedural method was applied first by Ghosh et al. (1995); Ghosh and Moorthy (1995); Ghosh et al. (1996) solving the differential equations of a BVP with the help of the so-called Voronoi-Cell-Finite-Element-Method (VCFEM). Based on the solution of the microscale the effective material parameters and stiffnesses are passed to the macrostructure by homogenization, where the scale transition can be achieved through diverse methods. In Miehe and Koch (2002), different boundary conditions (stress, displacement or periodic boundary conditions) have been analysed more in detail, where the stress boundary conditions are equal to the infimum and the displacement boundary conditions represent the supremum of the stress response of any material. Considering periodic boundary conditions, the solution lies between the upper and lower bounds of the stress response. The method to solve a multi-scale problem via FEM is also known as the FE<sup>2</sup>-method Feyel (1999); Feyel and Chaboche (2000); Feyel (2003), which is in terms of computational power very time consuming, but good for parallelisation.

### Micromechanical Homogenization

Micromechanical homogenization has been of interest in research for 50 years (Pindera et al., 2009), whereby almost all analytical solutions developed are based on Eshelby's solution (Eshelby, 1957) and the Eshelby tensor is the basis for almost all solutions for determining effective stiffnesses.

From Eshelby's solution different theories have been developed, like scheme of Mori and Tanaka (1973) and the self-consistent scheme in accordance to Hill (1965). As result the micromechanical homogenization provides approximate solutions and bounds for the effective material properties, which will be briefly described in Section 2.3.3.

#### 2.3.1 Concept of Representative Volume Elements

Within the theory of micromechanics RVE's are introduced, which account for the microstructure of the analysed material. In general RVE's can be composed of periodic or non-periodic microstructures. In the case of periodic microstructures, the RVE should contain an integer multiple of the repetitive microstructure in all spatial directions with the result that the periodic RVE works as a unit cell (cf. Fig. 2.5). In the case of non-periodic microstructures the RVE represents a segment of the nano-/ micro-structure of a material, where the inhomogeneities of it are statistically, homogeneously distributed with the result that the effective material properties are independent of the size and the shape of the RVE. Furthermore the RVE should contain a sufficient quantity of inhomogeneities and be sufficiently small so that it can be understood as a single material point on the macro-scale.

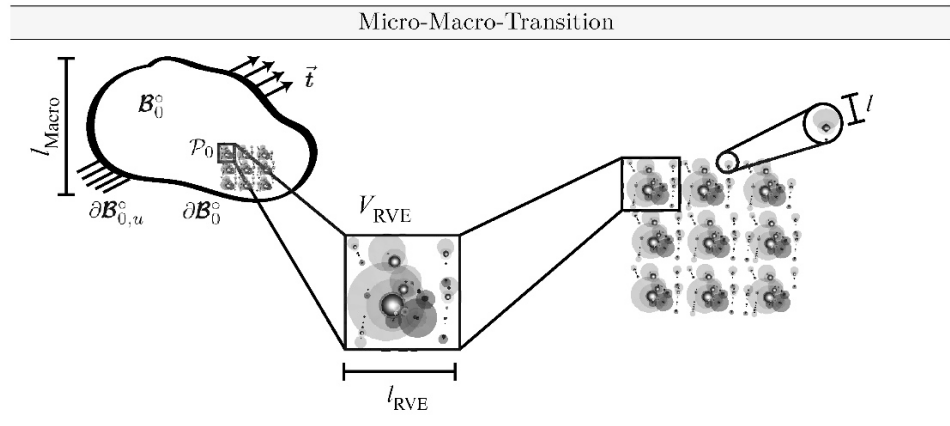


**Figure 2.5** Illustration of the micro-macro-transition of a global, heterogeneous structure, a RVE and the size of inhomogeneities of the RVE (Gade et al., 2018)

Therefore the length of the RVE must be larger than a characteristic length on a nano- / micro-scale and smaller than the length on a macro-scale with the result that

$$l_{\text{Nano}} \ll l_{\text{RVE}} \ll l_{\text{Macro}} \quad (2.63)$$

should be satisfied (Hohe and W. Becker, 2003; Gade et al., 2018). It has to be noted that the total dimension of periodic and non-periodic RVE's, which is influenced by the geometry of the bulk material and the distribution and orientation of the inhomogeneities, is not of interest because if the relative dimensions between RVE and the inherent inhomogeneities are reasonably chosen, the total size of the RVE is scalable (Nakamura and Lopez-Pamies, 2012).

### 2.3.2 Micromechanical Homogenization

In this section, the theoretical basics of micromechanical homogenization are introduced, since this is of importance in the further course of the present work.

Considering the average field theory for obtaining the overall response of a heterogeneous medium, the objective of homogenization is formulated as the representation of the material response, kinematics, strain energy and deformations of the RVE, which should be equivalent to those of an equivalent homogeneous material (EHM) (Zohdi and Wriggers, 2011). In the following all identities of the RVE are marked with  $(\bullet)^o$  and of the EHM with  $(\bullet)^*$ . To obtain relationships for the micro-macro-transition, the material response of every single material point  $\mathcal{P}^o$  /  $\mathcal{P}^*$  of the RVE / EHM on the macro-scale should correlate with a volume-average

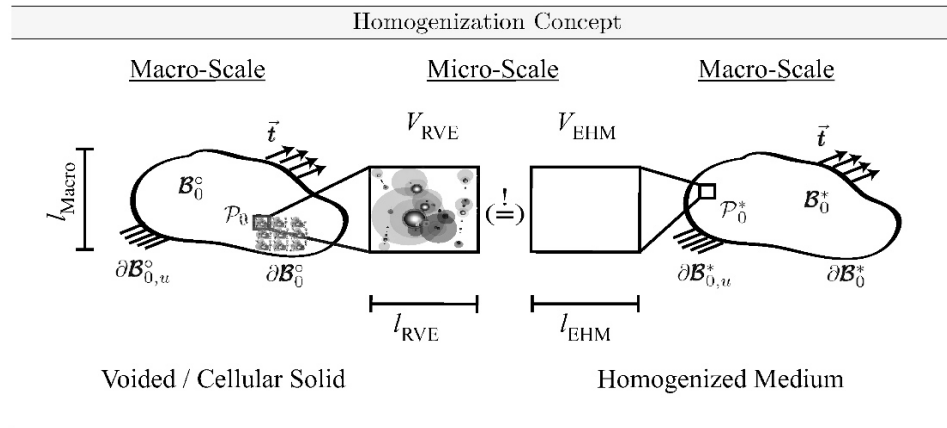


**Figure 2.6** Illustration of homogenization concept between RVE and EHM

value on the micro-scale (see Fig. 2.6). This can be expressed in terms of stresses and infinitesimal strains by

$$\langle \sigma_{ij}^o \rangle = \frac{1}{V^{\text{RVE}}} \int_{V^{\text{RVE}}} \sigma_{ij}^o dV = \frac{1}{V^{\text{EHM}}} \int_{V^{\text{EHM}}} \sigma_{ij}^* dV = \langle \sigma_{ij}^* \rangle \quad (2.64)$$

respectively

$$\langle \varepsilon_{kl}^o \rangle = \frac{1}{V^{\text{RVE}}} \int_{V^{\text{RVE}}} \varepsilon_{kl}^o dV = \frac{1}{V^{\text{EHM}}} \int_{V^{\text{EHM}}} \varepsilon_{kl}^* dV = \langle \varepsilon_{kl}^* \rangle. \quad (2.65)$$

To get a better differentiation between the hierarchical variables, Macaulay brackets are introduced for  $\langle \sigma_{ij}^o \rangle$  and  $\langle \varepsilon_{kl}^o \rangle$  describing the volume-average macro-stresses and macro-strains of the RVE. In contrast, the volume-average macro-stresses and macro-strains of the EHM are defined by  $\langle \sigma_{ij}^* \rangle$  and  $\langle \varepsilon_{kl}^* \rangle$ . Considering the micro-scale, the stresses and strains are characterized by  $\sigma_{ij}$  and  $\varepsilon_{kl}$ .

This classical theory is often utilized in the field of linear continuum mechanics at infinitesimal strains, however it has the opportunity to widen itself to finite strains. The relationship between the macro-stresses and macro-strains of an RVE is given in indicial notation by

$$\langle \sigma_{ij}^o \rangle = C_{ijkl} \langle \varepsilon_{kl}^o \rangle, \quad (2.66)$$

respectively in tensorial notation by

$$\langle \boldsymbol{\sigma}^o \rangle = \mathbb{C} : \langle \boldsymbol{\varepsilon}^o \rangle, \quad (2.67)$$

where  $C_{ijkl}$  respectively  $\mathbb{C}$  represent the elastic stiffness tensor of the material components of the RVE. The EHM is equipped with an effective elastic stiffness tensor  $C_{ijkl}^\Delta$  respectively  $\mathbb{C}^\Delta$ , which is modified in a way that Eq. (2.64) and Eq. (2.65) are satisfied. Based on the following equations,

$$\langle \sigma_{ij}^* \rangle = C_{ijkl}^\Delta \langle \varepsilon_{kl}^* \rangle \quad (2.68)$$

and

$$\langle \boldsymbol{\sigma}^* \rangle = \mathbb{C}^\Delta : \langle \boldsymbol{\varepsilon}^* \rangle, \quad (2.69)$$

Hill's lemma can also be derived (Bishop and Hill, 1951), which is a fundamental requirement in micro-mechanics. It ensures that the distribution of the strain energy density on the macro-scale is correctly reproduced under consideration of the effective properties. In other words, the average of the performed work, which the micro-stresses contribute on the micro-strains, must be equal to the performed work of the average stresses on the average strains with

$$\langle \boldsymbol{\sigma}^o : \boldsymbol{\varepsilon}^o \rangle = \langle \boldsymbol{\sigma}^o \rangle : \langle \boldsymbol{\varepsilon}^o \rangle. \quad (2.70)$$

To generalize the proposed linear average field theory a so-called strain-energy homogenization concept can be adduced, which is well suited to account for finite strains problems and micro-heterogeneous materials with non-orthotropic material behaviour (Hohe and W. Becker, 2003). Originally proposed by Hill (1952) and Ponte Castañeda and Suquet (1995), this special form of homogenization scheme has the advantage that Hill's principle (cf. Eq. (2.70)) is directly fulfilled as equivalence criterion. Thus, stresses are afterwards calculated as energy complement to the chosen strain measure.

Under consideration of non-dissipative processes, the strain energy equivalence between an RVE and EHM can be formulated in a non-incremental form with

$$\langle \Psi^o \rangle = \frac{1}{V^{\text{RVE}}} \int_{V^{\text{RVE}}} \Psi^o dV = \frac{1}{V^{\text{EHM}}} \int_{V^{\text{EHM}}} \Psi^* dV = \langle \Psi^* \rangle. \quad (2.71)$$

The equivalence of the deformation gradient, which is also formulated as a volume-average on the effective hierarchical level, can be written as

$$\langle F_{ij}^o \rangle = \frac{1}{V^{\text{RVE}}} \int_{V^{\text{RVE}}} F_{ij}^o dV = \frac{1}{V^{\text{EHM}}} \int_{V^{\text{EHM}}} F_{ij}^* dV = \langle F_{ij}^* \rangle. \quad (2.72)$$

In this context  $\langle \Psi_{ij}^{\circ} \rangle$  and  $\langle F_{ij}^{\circ} \rangle$  describe the volume-average strain energy density respectively the volume-average deformation gradient of the RVE. In contrast, the volume-average strain energy density function and deformation gradient of the EHM are defined by  $\langle \Psi_{ij}^* \rangle$  and  $\langle F_{ij}^* \rangle$ . From Eq. (5.52), a special requirement follows that the deformation gradient for the RVE and EHM must be macroscopically equivalent. In summary, the mechanical equivalence between an RVE and an EHM can be achieved by an equivalence of stress, strain, strain energy density and deformation (cf. Eq. (2.64)-(2.65) and Eq. (5.51)-(5.52)).

### 2.3.3 Approximate Solutions and Bounds in Micromechanics

In literature there exist several analytical approaches to identify initial stiffness parameters, like the shear modulus, bulk modulus or the elastic stiffness tensor. The first practical solutions to determine effective material parameters were proposed by Voigt (1889) and Reuss (1929), which represent the infimum and supremum of the material stiffness parameters. Accordingly to Voigt (1889), the supremum bound in terms of the elastic stiffness tensor can be determined by

$$\mathbb{C}_{\text{Voigt}}^{\Delta} = \langle \mathbb{C} \rangle = \sum_{\alpha=1}^n c_{\alpha} \mathbb{C}_{\alpha}, \quad (2.73)$$

where the strain field is assumed to be constant. It is composed additively of the effective stiffnesses of the individual phases. In this notation, the index  $\alpha$  represents the material number of the individual phases, where  $\alpha = i$  represents an inhomogeneity like a void and  $\alpha = m$  characterizes the matrix under consideration of a two-phase material, e.g. a material consisting of a matrix and a singular void. This means that  $c_i$  stands for the so-called void fraction  $f_0$ , which is the ratio of the volume of the pores to the total volume. The ratio of the volume of the matrix to the total volume is denoted as  $c_m$ . Both ratios are given through

$$c_i = f_0 = \frac{V_{\text{void}}}{V_{\text{total}}} \quad \text{and} \quad c_m = 1 - f_0 = 1 - \frac{V_{\text{void}}}{V_{\text{total}}}. \quad (2.74)$$

Since the initial bulk modulus is important for the present work, different approximations are given in the following. Accordingly to Voigt (1889), Eq. (2.73) can be rewritten for a two-phase material by

$$K_{\text{Voigt}}^{\Delta} = \underbrace{c_i K_i}_{=0} + c_m K_m = \left( \frac{V_m}{V_i + V_m} \right) K_m, \quad (2.75)$$

which gives the upper bound for effective bulk modulus. In contrast, the infimum bound in accordance to Reuss (1929), which assumes a constant stress field, is defined as the average compliance

$$\mathbb{C}_{\text{Reuss}}^{\Delta} = \langle \mathbb{C}^{-1} \rangle = \sum_{\alpha=1}^n c_{\alpha} \mathbb{C}_{\alpha}^{-1}. \quad (2.76)$$

With regard of a voided material the solution for the effective bulk modulus reads

$$K_{\text{Reuss}}^{\Delta} = \frac{K_i K_m}{c_i K_i + c_m K_m} = 0. \quad (2.77)$$

Since the pore stiffness is zero, the total effective stiffness according to Reuss (1929) is also zero, so that it becomes clear that it describes the lower limit bound. The most general solution for effective material properties in the field of micromechanics was proposed by Eshelby (1957), who studied analytically ellipsoidal elastic inclusions in an infinite elastic body. Considering an inclusion under a constant inelastic eigenstrain  $\varepsilon_{kl}^*$ , the total strain  $\varepsilon_{ij}$  can be determined by

$$\varepsilon_{ij} = S_{ijkl} \varepsilon_{kl}^*, \quad (2.78)$$

where  $S_{ijkl}$  is a symmetric fourth order tensor, which is strictly speaking only symmetric towards the first two and the last indices, however there exist no symmetry for permutations. On the basis of this solution a direct approximation for the bulk modulus of a voided material can be given by

$$K_{\text{Eshelby}}^{\Delta} = K_m - \frac{c_i K_m (3K_m + 4\mu_m)}{4\mu_m}. \quad (2.79)$$

Regarding the Mori and Tanaka (1973) homogenization scheme, it is a specialization of the dilute distribution of voids and inclusions, where the far-field strain  $\varepsilon^0$  is replaced by the average matrix strain  $\langle \varepsilon_{\text{matrix}} \rangle$ . With the help of Eshelby's solution, the average defect strain can be calculated by

$$\langle \varepsilon_i \rangle = \mathbb{A}_i^{\infty} : \langle \varepsilon_m \rangle \quad (2.80)$$

Eliminating the average matrix strain by  $\langle \varepsilon \rangle = c_i \langle \varepsilon_i \rangle + c_m \langle \varepsilon_m \rangle$  the influence tensor  $\mathbb{A}$  can be determined by

$$\mathbb{A}_{\text{MT}} = [\mathbb{I} + c_m \mathbb{S}_m : \mathbb{C}_m^{-1} : (\mathbb{C}_i - \mathbb{C}_m)]^{-1} \quad (2.81)$$

with the result that the effective stiffness can be calculated by

$$\mathbb{C}_{MT}^{\Delta} = \mathbb{C}_m + c_i (\mathbb{C}_i - \mathbb{C}_m) : \mathbb{A}_{i,MT}. \quad (2.82)$$

An approximation of the Mori and Tanaka (1973) scheme in terms of the initial bulk modulus of a voided material is given by

$$K_{MT}^{\Delta} = K_m - \frac{c_i K_m (3K_m + 4\mu_m)}{3K_m + 4\mu_m - 3(1 - c_i) K_m}. \quad (2.83)$$

In contrast to the previously described solutions, the upper bound gives the results in accordance to Mori and Tanaka (1973). The calculation of the lower and upper bounds for the approximate solution in accordance to Hashin and Shtrikman (1963) reads

$$K_{HS+}^{\Delta} = K_m + c_i \left( \frac{1}{K_i - K_m} + \frac{3c_m}{3K_m + 4\mu_m} \right)^{-1} \quad (2.84)$$

and

$$K_{HS-}^{\Delta} = K_i + c_m \left( \frac{1}{K_m - K_i} + \frac{3c_i}{3K_i + 4\mu_i} \right)^{-1}. \quad (2.85)$$

With the help of the approximate solutions given for the initial bulk modulus of a two-phase voided material, the stiffness behaviour can be estimated well. However, it can be seen that the analytical solutions do not lead to a consensus, so experiments are necessary to correctly estimate the initial stiffness.

A comparison of the proposed bounds of the effective, normalized bulk moduli dependent on the void fraction is illustrated in Fig. 2.7. This clearly shows that

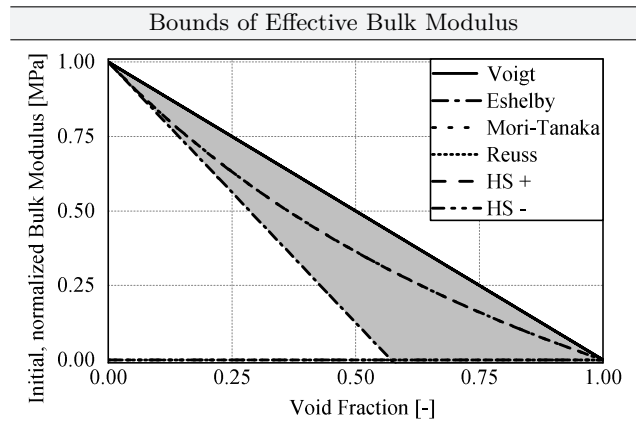


**Figure 2.7** Illustration of bounds of effective, normalized bulk moduli dependent on void fraction in accordance to Voigt (1889) and Reuss (1929), which determine the supremum and infimum as well as bounds in accordance to Eshelby (1957), Mori and Tanaka (1973) and Hashin and Shtrikman (1963)

Voigt's solution represents the upper limit. The solutions from Eshelby (1957), Mori and Tanaka (1973) and Hashin and Shtrikman (1963) provide a physically reasonable solution as they are below the Voigt solution but are not equal to zero. The lower bound in accordance to Hashin and Shtrikman (1963) corresponds to the result of Reuss (1929). However, since a solution of  $K = 0$  is obtained here independently of the void fraction, these solutions do not seem to be physically correct. Therefore, the range of physical solutions is greyed out to describe a range of approximated bulk moduli dependent on void fraction.

Summarizing this chapter, the main principles of continuum mechanics, limit state analyses and micromechanics have been presented, which will be applied in the further course of the work to describe the material behaviour of a structural silicone adhesive up to failure. In terms of content, the chapter was strongly summarized, so that interested readers are referred to the relevant literature in the individual sections.



# 3 Elastomers and their Mechanical Behaviour

This chapter deals with an introduction in the general mechanical behaviour of polymers and their classification into material groups depended on their structural behaviour. After the general characterization of polymer materials, special features such as softening, the Mullins effect and cavitation are discussed. Finally, with reference to continuum mechanics and material modelling, classical material modelling approaches are presented. The aim of this chapter is to understand the behaviour of polymers and their classical material modelling. The main features of material modelling will be used later (Chap. 5) to develop novel improved material models.

## 3.1 Classification of Polymers

In industrial applications there is a large variety of polymeric materials with different material properties, designs, constituents and applications forms, so that a categorization of polymers into defined material classes appears to be reasonable. To do so, a general description of polymeric materials is described in the following under characterization of the mechanical behaviour as well as the description of general physical dependencies and effects, which influence the behaviour of the polymers substantially. Since this thesis deals in particular with structural silicones in façade applications, which are generally assigned to the material class of elastomers, the material behaviour and typical phenomena including softening effects and failure mechanism of this class of polymers are described more in detail.

### 3.1.1 General Polymer Structures and Properties

A polymer is a large macromolecule with a low relative molecular mass consisting of repeating sub-structures and sub-networks. The individual components are typically organic molecules based on carbon or hydrogen, which are also called monomers. During the chemical process of polymer production, large groups of monomers are formed, which combine to form long polymer chains (macromolecules). Depending on the type of process and production, narrow or wide

meshed, strongly or not at all cross-linked, linear or strongly branched as well as more or less intertwined molecule chains can be formed.

In general, polymers can be roughly classified by their type of occurrence (natural or synthetic) and the monomer used for polymer production. Natural polymers are, for example, shellac, amber, wool and natural rubber, while the list of synthetic polymers is almost endless, since synthetic polymers are constantly adapted and modified due to the changing requirements of manufacturers, processors and users from industry as well as users for private use. To name a few synthetic polymers, one can refer to neoprene, synthetic rubber, polyvinylbutyral (PVB) and silicones. The second classification is based on the monomer used in polymer production, which essentially characterizes the material properties. Hence, the type of microstructure of the polymer significantly determines the macroscopic mechanical properties. Looking at the type of monomer used, a distinction is made between polymers that have only one type of repeating unit. These polymers are called homopolymers. An example of this is polystyrene, which is composed entirely of styrene monomers. In contrast, if a polymer consists of two or more types of repeating units, it is termed copolymer. An example of this is ethylene-vinyl acetate (EVA), which is often used as a polymer interlayer in laminated safety glass (Drass et al., 2017b).

As already mentioned, the microstructure of the polymer has a decisive influence on the physical bulk properties at the macro level. In literature, polymers are mostly classified into the main groups of thermosets (duroplasts), thermoplastics and elastomers, each of which has typical material characteristics (see Fig. 3.1).

**Thermosets** are highly cross-linked polymers with close meshes and are therefore amorphous and non-meltable. It follows from this that viscous effects play only a minor role due to the high degree of cross-linking. The decomposition temperature is usually in the range of the glass transition temperature or even below. Therefore, thermosets show almost exclusively a stiff, elastic behaviour followed by a brittle fracture in the energy-elastic range.

**Thermoplastics** are characterized by the fact that linear macromolecules are not cross-linked and the polymers are therefore plastically deformable. Plastic deformations occur when, for example, the secondary valence forces between the polymer chains are not sufficient to permanently withstand the external stress during loading. As a result, the connections rupture, the polymer chains slide past each other, resulting in plastic deformation of the material. Thermoplastics can be amorphous or semi-crystalline, whereby the stiffness behaviour changes significantly with increasing deformation speed and / or temperature.

**Elastomers** are wide-meshed, chemically cross-linked polymers, which, in contrast to thermosets, have a much lower degree of cross-linking. In contrast to thermoplastics, the partial cross-linking of elastomers leads to almost no plastic deformation

of the material in the course of external loading. In addition, cross-linking prevents melting, so that the polymer decomposes only at high temperatures. The glass transition temperature is typically far below 0°C. In the service temperature range, elastomers therefore behave entropically elastic, show no irreversible deformations and may exhibit a slight increase in stiffness with increasing temperature due to higher entropy (Kuntsche, 2015). In order to distinguish between elastomers, they are divided into the main categories of a filled or an unfilled elastomer. Carbon black or silica particles are often used as fillers, which in most cases lead to a reinforcement of the polymer. This is the reason why we often speak of reinforced elastomers. By the addition of fillers, the polymer can thus achieve a higher stiffness, but the extensibility of the polymer chains is frequently reduced as a result, since their conformations (permissible deformations) are limited by the rigid fillers. As is typical for every material, elastic constants must also be specified for elastomers, but these generally only apply to small deformations, since it is known that elastomers can withstand large deformations. Typically, not the Young's modulus but the shear modulus for elastomers is specified, since this remains almost constant even at large deformations, which does not apply to the Young's modulus.

In order to gain a better understanding of the micro-structure of the proposed general classes of polymers, Fig. 3.1 shows schematic drawings of thermosets, thermoplastics and filled elastomers. The schematic representation quickly shows that thermosets are densely cross-linked with a close-meshed network of macromolecules, whereas thermoplastics show no cross-linking. Looking at the schematic illustration of the filled elastomers, it can be seen that the polymer network is wide-meshed with various cross-links. Since the material behaviour of rubber is particularly analysed in this thesis, the micro-structural description of the filled elastomer is also depicted on the micro- and nano-scale. Looking at the nano-scale of a filled rubber, the material is composed of polymer chains, aggregates consisting of filler particles and so-called vacuoles, which can form on and between the aggregates during the production of the material. Vacuoles are vacuum cavities that can occur during production as well as during deformation due to weak filler-matrix interactions. This is especially the case for dispersions of silica in rubber vulcanizates without adding silane coupling agents (Sarkawi et al., 2015). The so-called cross-links occur during vulcanization, in which an uncured elastomer material is heated. Cross-links represent a real chemical bond between the molecules, which are decisive for the later micro-structural form as well as macroscopic material characteristics. Since the final cured elastomer is often called rubber after curing, this term as well as the term rubber-like materials is used in the following. The final shape of the elastomer network can change over the course of its service life due to influences from temperature, mechanical stresses / strains and chemical diffusion processes.

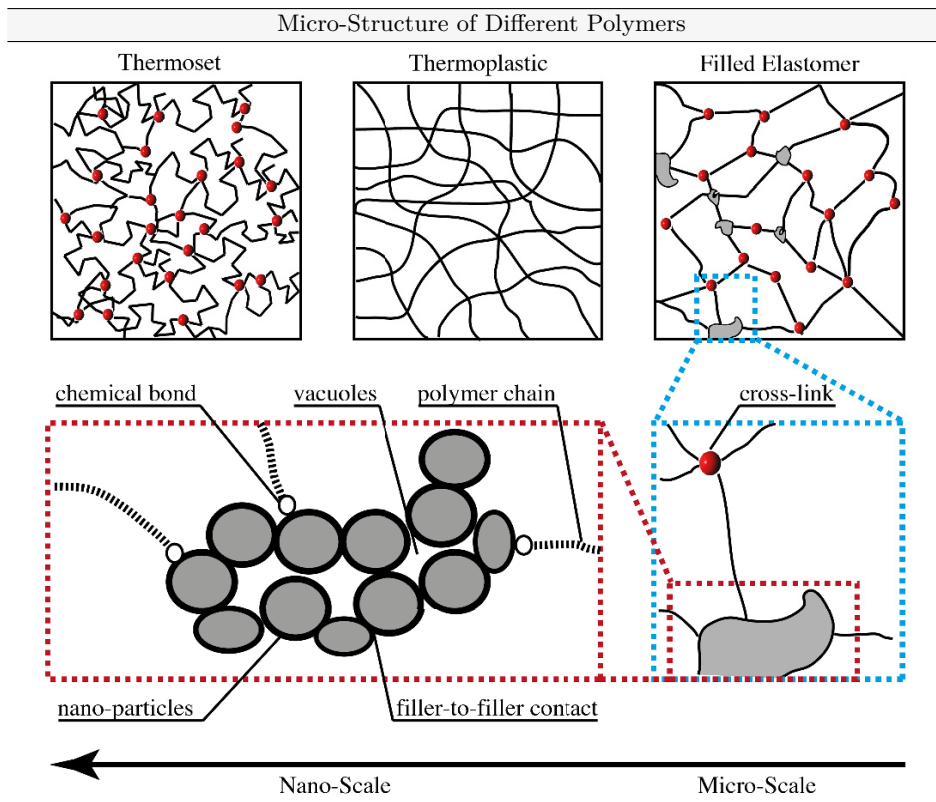


**Figure 3.1** Schematic illustration of different microstructures for polymers: (a) thermosets, (b) thermoplastics and (c) filled elastomer, which is also depicted schematically on the micro- and nano-scale

### 3.1.2 Mechanical Behaviour and Emergent Effects of Rubbers

In this section, the mechanical behaviour and typical effects of elastomers are briefly described and schematically explained. In order to get an overview of the physical effects of elastomers, these are documented and briefly explained with numerous sources from the current literature. Thus, this section deals in particular with the description of the general behaviour of rubbers and rubber-like materials without describing them mechanically via constitutive models. The constitutive description takes place in a separate chapter (see Section 3.2), since this is an essential element of the present work.

## Mechanical Behaviour

The typical mechanical behaviour of polymeric materials, here elastomers or rubber-like materials, shows a strong non-linear characteristic, especially in the case of large deformations (Treloar, 1975). The strong non-linear elastic material behaviour is often characterized or approximated respectively by the approach of hyperelasticity. In this context hyperelasticity describes the elastomer in the ground state or the equilibrium or long-term response respectively (Behnke, 2015). Green elastic materials are characterized by hyperelastic constitutive models to describe pure elastic processes for small and large deformations, where the stress-strain relationship is derived from a strain-energy density function, often also known as the Helmholtz free energy function. The descriptions of these free energy functions to characterize the mechanical behaviour of elastomers in the ground state are deliberately described in a separate section for reasons of clarity (see Section 3.2). In general, hyperelastic material models are divided into the class of phenomenological or molecular-statistical models, depending on how they were derived. An overview of different models and their applicability is given by Marckmann and Vernon (2006) and Steinmann et al. (2012). Large deformations can occur in stressed elastomers even at comparatively low loads, which can be explained by the low isochoric stiffness of the material. In contrast to the very low isochoric stiffness, the bulk modulus  $K$  is orders of magnitude higher than the shear modulus  $\mu$  leading to

$$\mu \ll K. \quad (3.1)$$

This is due to the fact that elastomers exhibit a Poisson's ratio of almost  $\nu \approx 0.5$ , so that an almost volume-constant behaviour is assumed. This is why elastomers, especially rubbers, are often associated with an incompressible material behaviour. In addition to the strongly non-linear behaviour, elastomers also exhibit rate- and temperature-dependent behaviour, which is attributable to viscous effects in the material. This behaviour is similar to that of thermoplastics and must be considered in a visco-elastic mechanical model via external state variables (e.g. strain field, temperature) to describe the status of a material point and its associated irreversible thermodynamics (Behnke, 2015). Since visco-elasticity and its experimental and numerical characterization are not part of the present work, it is not discussed here, but referred to the relevant literature (Wineman, 2009; M. A. Kraus et al., 2017).

A schematic representation of the stress-strain behaviour of an elastomer at different strain rates and ambient temperatures is shown in Fig. 3.2, where it can be clearly seen that the stiffness of the material increases with increasing strain rate. In contrast, the stiffness decreases significantly with increasing temperature. In addition, Fig. 3.2 shows the final fracture at different temperatures and strain

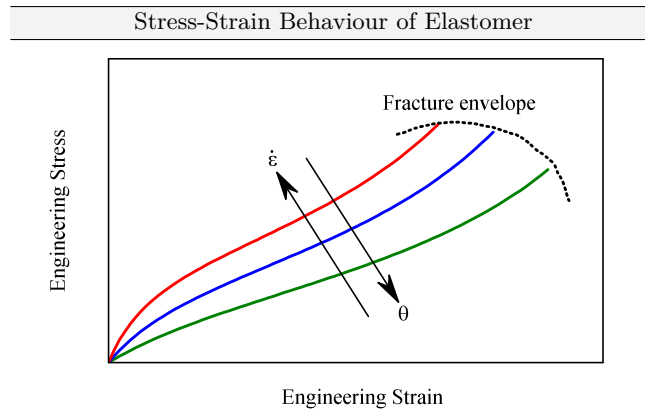


**Figure 3.2** Schematic stress-strain behaviour of an elastomer at different strain rates and ambient temperatures

rates. It becomes clear that as the strain rate increases, the allowable strain in the material decreases until the final failure occurs. In contrast, the allowable strain until final failure occurs may be increased by applying higher temperatures. However, this does not always have to be the case and must be evaluated experimentally. Looking at the failure of the polymer, this example shows that failure can be expressed in terms of strains or stresses. From this example it becomes clear that the failure stresses are very similar, but the strains differ significantly from each other. Therefore, a discussion between stress and strain based failure criteria takes place in Section 6 to highlight the advantages and disadvantages of both failure formulations.

### Mullins Effect

Loading filled elastomers cyclically, Bouasse and Carrière (1903) already discovered a distinct difference in the stress-strain behaviour between virgin, unloading and reloading path in the experiments carried out, which manifests itself with a distinct **softening effect** in the structural response of the elastomers. This phenomenon was further investigated by Mullins (1949) and Mullins and Tobin (1965), whereby this effect was designated as Mullins effect. In these studies, the softening effect for unfilled and filled elastomers was experimentally investigated. It was found that in both types of elastomers a softening in the structural response could be detected during the unloading. Since the criterion for softening could better be described by means of stresses and not by stretches or strains, the Mullins effect is often associated with the notion of stress softening (Harwood et al., 1965).

Diani et al. (2009) compared numerous studies on **strain-induced crystallisation** in polymers with the Mullins effect. In this context, strain crystallization means that an initially amorphous solid material is phase-transformed by the application of strains (Rastak and Linder, 2018). Based on their results, it was postulated that the presence of crystallites is necessary for the occurrence of Mullins softening in unfilled rubbers and that Mullins softening does not influence the strain-induced crystallization.

The **permanent set** refers to the residual strain that remains after a material sample has been stretched and unloaded. Analysing cyclic loading in unfilled elastomers, stresses and strains reduce to zero, generally leaving no permanent residual deformations within the material. In contrast, this behaviour is not recognizable for filled elastomers. Here also a distinct stress softening in the structural behaviour between the virgin and unloading path could be observed, which is additionally followed by permanent set or permanent deformations in the material (Diani et al., 2006). Dorfmann and Ogden (2004) found that with increasing content of carbon black fillers and with increasing strain amplitude, which is acting on the material, the residual strains increase. This was also confirmed in uniaxial compression tests on an EPDM-PP thermoplastic rubber, where the permanent set increases with increasing load (Boyce et al., 2001).

In the numerous experimental studies performed by Mullins (1948), it was also observed that stretching a reinforced rubber causes an irregular softening in all directions, so that one speaks of the effect of **induced anisotropy** due to cyclic loading. This effect was confirmed by the studies of Diani et al. (2006), who analysed a carbon-black filled EPDM experimentally. Additionally to these studies, Hanson et al. (2005) investigated a silica filled PDMS, where also the effect of induced anisotropy due to cyclic loading could be observed. Furthermore, in the investigations of Itskov et al. (2006), anisotropic stress softening was also experimentally analysed in successive tensile tests, which were conducted in different stretch-directions.

Another interesting effect in cyclic experiments on elastomers is **healing** or **recovery**, where the stiffness on the reloading path may be greater than in comparison to the unloading path, i.e. the material has experienced healing (D'Ambrosio et al., 2008). A second definition of healing or recovery of elastomers exposed to cyclic loading is described when the residual strains or the permanent set can be reduced by temperature storage or by the removal of specimens with long relaxation times, so that the residual strains almost drop to zero. The test sample is then not exposed to external loads during the relaxation time or temperature storage, so that it can deform free of constraint. Different experiments to describe the healing effect in rubbers were carried out, for example, by Mullins (1948), who investigated stress-recovery of a filled NR under temperature influence and sample

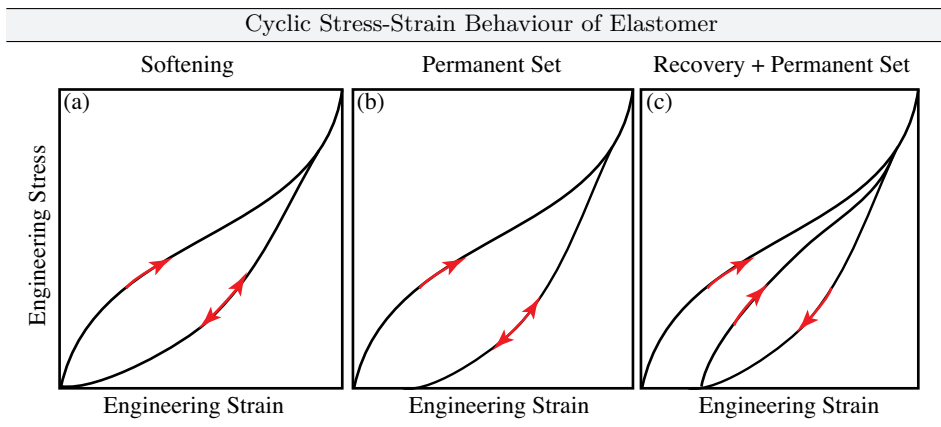


**Figure 3.3** Schematic stress-strain behaviour of an elastomer under cyclic loading: (a) idealised Mullins effect, (b) Mullins effect with residual strains and (c) Mullins effect with residual strains and healing effects during reloading

storage for a certain period of time. He found that with increasing temperature or storage time the healing effect in the form of reduction of residual strains in the material increased significantly. In contrast, for a carbon black filled NR only a small amount of healing was observed even during a relaxation period of four weeks (Mullins, 1948). During the studies on healing of Hanson et al. (2005) on a silica-filled PDMS, it was found that even at the relaxation period of six months no recovery took place, so it is not surprising that Diani et al. (2009) state that this effect can be neglected with standard application in indoor climate. Looking at cyclic constrained tensile test of a transparent structural silicone adhesive, in which an almost hydrostatic tensile stress prevails in the material, it was experimentally proven that the healing effect (recovery of stiffness) can be clearly seen on a kN scale - without exposing the test samples to temperature storage or relaxation times to make healing effects visible (Bartels, 2018). Therefore, in particular with this type of loading - cyclic loading in room climate under quasi-static experimental boundary conditions - the healing effect for the experimental and mechanical evaluation or description should not be waived.

A schematic representation of the described effects of an elastomer subjected to cyclic loading is shown in Fig 3.3. Here, the idealized Mullins effect is shown without the effects of permanent set, induced anisotropy or healing. Furthermore, the effect of the residual strains as well as the residuals strain combined with healing during re-exertion can be seen schematically.

A unified theory for the **physical interpretation** of the Mullins effect does not yet exist. Therefore, three descriptive models for the characterization of the Mullins

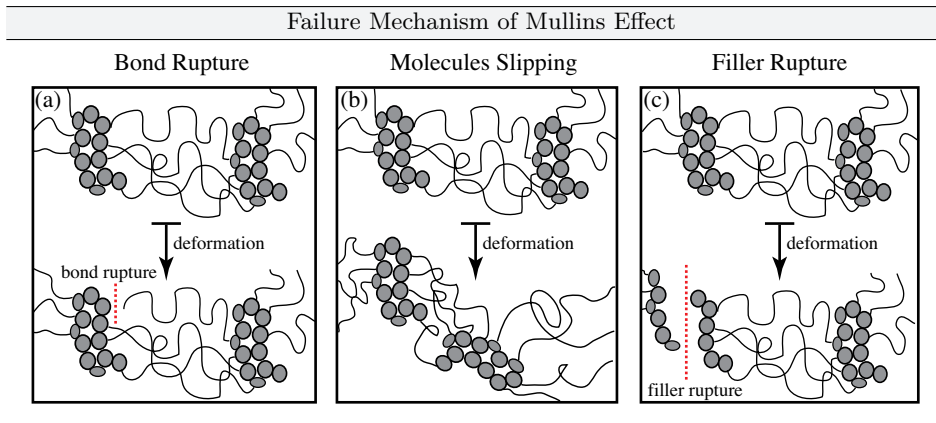


**Figure 3.4** Schematic rupture mechanism to describe Mullins effect of an elastomer under cyclic loading: (a) bond rupture (Blanchard and Parkinson, 1952; Bueche, 1960), (b) molecules slipping (Houwink, 1956) and (c) filler ruptures (G. Kraus et al., 1966; Klüppel and Schramm, 2010)

effect are briefly discussed below. In the early investigations of Blanchard and Parkinson (1952), it is assumed that stress softening occurs as a result of the Mullins effect by so-called bond rupture between polymer chain and filler. This idea was taken up by Bueche (1960) and further explained by the fact that the physical bond between polymer and filler is weaker than the chemical bond between the Kuhn segments of the polymer chain. When the polymer chain between two filler particles is completely stretched, fracture must take place at the filler-matrix-interaction according to that model, since on the one hand the weaker bond is present and on the other hand it is assumed that the Kuhn segments are rigid and therefore cannot be further stretched. Another theory on the Mullins effect states that during the initial loading molecules slip over the surface of the fillers and new bonds are formed along the chains (Houwink, 1956). The model conception of molecules slipping is equivalent to the change of entropy in the material, which may be restored to the almost original dimension by temperature input, which corresponds to the experimental results of Mullins (1948). The third model assumes a rupture of the filler agglomerates or aggregates, since in the experimental investigations of G. Kraus et al. (1966) neither the theory of bond rupture, molecule slipping nor the formation of vacuoles at the matrix-filler-interaction were sufficient to explain the observed Mullins effect. However, this approach has the disadvantage that filler rupture is an irreversible process (Klüppel and Schramm, 2010), which has not been experimentally confirmed. All three model concepts are schematically shown in Fig. 3.4, where a polymer network containing several filler particles are illustrated in the undeformed and deformed configuration.

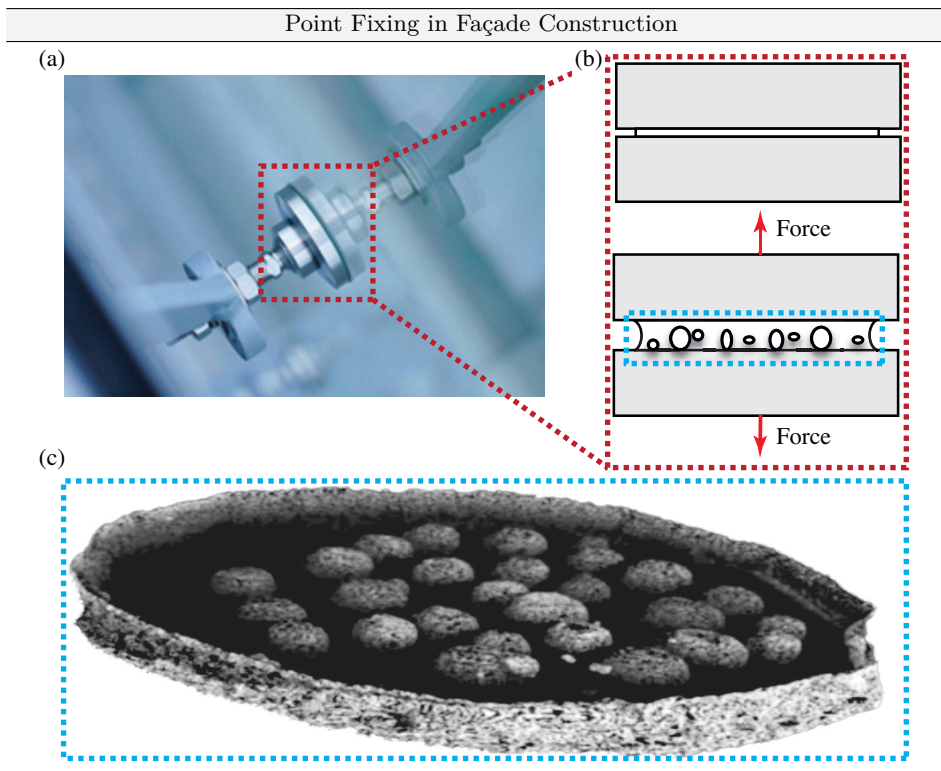


**Figure 3.5** (a) Flat bonded point holder in a glass façade under axial wind load, (b) schematic representation of a flat bonded silicone adhesive joint in a glass façade under axial load with formation of pore growth due to the cavitation effect and (c) scanning electron image of a flat bonded point holder in axially deformed state with formation of many cavities due to disability of lateral contraction (Euchler et al., 2018)

### Cavitation Effect

In order to introduce the cavitation effect in rubbers not only theoretically, it is motivated by a simple application example of a point-bonded glass façade which is exposed to an external wind load. When constructing conventional glass façades, a critical design element is the connection between the glass pane and the supporting secondary load bearing members. To avoid stress peaks in the glass, the joint must be ductile and be able to withstand environmental influences (wind, rain, sun, etc.), while also being architecturally appealing. In modern construction, this connection is typically achieved by directly bonding glass to metal with thin silicone adhesives (see Fig. 3.5 a). When such an adhesive joint is then subjected to a lateral load, the disability of lateral strains within the bondline may cause abrupt cavity growth in the silicone (see Fig. 3.5 b). This behaviour is known

as cavitation (Drass et al., 2017a) and under its effects the connection experiences significant increases in ductility before final dilatational failure occurs (see Chap. 6). The cavitation effect and the formation of voids is a well-known observation when rubber or rubber-like materials are hydrostatically loaded. This can be demonstrated by the SEM image in Fig. 3.5 c, in which the formation of cavities in bulk material under axial load could be observed (Euchler et al., 2018). Based on the pioneering experimental work of Busse (1938), Yerzley (1939) and Gent and Lindley (1959), where flat rubber cylinders were vulcanized to plane metal end pieces and afterwards tensioned, a yield point in the load displacement behaviour was observed due to internal rupture, e.g. void nucleation Busse (1938); Yerzley (1939). Gent and Lindley (1959) interpreted the discontinuity in the load displacement response as sudden appearance of internal flaws, which was determined by (i) audible popping and (ii) cutting open the so-called pancake (PC) test specimen before and after reaching the breaking point. The audible popping was also analysed experimentally by Kakavas and Chang (1991), where via acoustic emission a correlation between the total number of events and counts of void nucleation was given. The experimental test set-up of Gent and Lindley (1959) was improved by Lindsey (1967), where the plane metal end pieces were exchanged by transparent polymethylmethacrylate. Furthermore, to obtain more insight in the formation of internal voids, a transparent polyurethane was applied as bonding material. Lindsey (1967) observed the appearance of a single void at the centre, which rapidly grows spherically and finally interacts with the boundary. The critical load under hydrostatic tension was determined to  $p_{cr} = 5/2\mu$ , which corresponds to the results of Gent and Lindley (1959). In this context  $\mu$  represents the initial shear modulus. Recent experimental investigations proposed a new methodology to investigate cavitation using a confined geometry (Cristiano et al., 2010). Cristiano et al. (2010) proposed a testing set-up, where the bondline thickness increased with an increase of the radius in the lateral direction. To quantify illustratively cavitation, a transparent PU sample was fixed between a glass plate and a glass lens. Hereby during the testing a single cavity was detected, which started to grow very close to the centre. A brief summary for experimental investigations on cavitation in elastomers is given in Hamdi et al. (2014), where the critical hydrostatic load of  $p_{cr} = 5/2\mu$  was confirmed by several authors. In contrast to the established results from literature, the work of Cristiano et al. (2010) did not confirm that cavitation strength increases linearly with the initial shear modulus (Gent and Lindley, 1959).

## 3.2 Hyperelastic Material Modelling

Since the material behaviour and typical physical effects of elastomers and rubbers were addressed schematically in the previous chapter, the material theory and the

constitutive description are briefly presented in this section. In general hyperelastic or Green-elastic materials are defined by a Helmholtz free energy function  $\Psi$ , which is characterized per unit reference volume and depends solely on a deformation measure, such as the deformation gradient  $\mathbf{F}$ . The Helmholtz free energy describes a thermodynamic potential from a closed thermodynamic system at constant temperature and volume, which measures the useful or available work of this system. Hyperelastic materials are therefore independent of the deformation history, so that they can only be described by the current value of the state variables. By setting the Helmholtz free energy in dependence to the deformation gradient with  $\Psi = \Psi(\mathbf{F})$ , a so-called strain energy density function can be defined (Holzapfel, 2000). In order to limit the field of hyperelasticity and its rate-dependent elastic or inelastic extension, only homogeneous and isotropic materials will be examined in the following, ignoring viscosity and plasticity. Softening effects due to the Mullins and cavitation effect are included in the following descriptions.

### 3.2.1 Incompressible Hyperelasticity

Since many polymeric materials show nearly no change in volume at finite strains, the assumption of incompressibility is an adequate and often utilized working hypothesis to characterize hyperelastic materials. Therefore, the incompressibility constraint of

$$\det \mathbf{F} = J = 1 \quad (3.2)$$

is used to define so-called constrained hyperelastic materials. From the incompressibility constraint, it follows that the strain energy density is unaffected by the volumetric part since

$$\Psi(\mathbf{F}^{\text{vol}}) = \Psi(\mathbf{1}) = 0 \quad (3.3)$$

applies. Based on the proposed incompressibility constraint and the demand that the volumetric Helmholtz free energy is always zero, the strain energy density function can be described by

$$\Psi = \Psi(\mathbf{F}) + \gamma(J - 1), \quad (3.4)$$

where  $\gamma$  defines a scalar, indeterminate Lagrange multiplier, which must be calculated by the incompressibility constraint. Between the Lagrange multiplier and the hydrostatic pressure the relationship of  $\gamma = -p$  is also valid. Thus, the hydrostatic pressure  $p$  represents a workless reaction and may be determined by equilibrium

equations and boundary conditions. On the basis of the strain energy density function, the first Piola-Kirchhoff stress tensor  $\mathbf{P}$  can be derived by

$$\mathbf{P} = \frac{\partial \Psi(\mathbf{F})}{\partial \mathbf{F}} - p \mathbf{F}^{-T}. \quad (3.5)$$

The second Piola-Kirchhoff stress tensor  $\mathbf{S}$  can be calculated by multiplying Eq. (3.5) from the left-hand side with  $\mathbf{F}^{-1}$  with the result of

$$\mathbf{S} = \mathbf{F}^{-1} \cdot \frac{\partial \Psi(\mathbf{F})}{\partial \mathbf{F}} - p \mathbf{F}^{-1} \cdot \mathbf{F}^T = 2 \frac{\partial \Psi(\mathbf{C})}{\partial \mathbf{C}} - p \mathbf{C}^{-1}. \quad (3.6)$$

By multiplying Eq. (3.6) with  $\mathbf{F}^T$  from the right-hand side, one obtains the symmetric Cauchy stress tensor  $\boldsymbol{\sigma}$  as

$$\boldsymbol{\sigma} = \frac{\partial \Psi(\mathbf{F})}{\partial \mathbf{F}} \cdot \mathbf{F}^T - p \mathbf{I} = \mathbf{F} \cdot \left( \frac{\partial \Psi(\mathbf{F})}{\partial \mathbf{F}} \right)^T - p \mathbf{I}, \quad (3.7)$$

which is a fundamental equation in hyperelasticity. To obtain explicit derivations of the above equations, the author refers to the classical monographs of Holzapfel (2000) and Chaves (2013).

### 3.2.2 Compressible Hyperelasticity

Nonetheless, the assumption of incompressibility only arose from mathematical convenience, but polymeric materials generally exhibit a dependence on the hydrostatic pressure (Bischoff et al., 2001). To account for volume changes at finite strains, a volumetric-isochoric split of the deformation gradient  $\mathbf{F}$ , originally proposed by Flory (1961), can be utilized, which is reasonable when materials have large differences between the shear and bulk modulus. The deformation gradient  $\mathbf{F}$  is therefore split into a volume-preserving part  $\mathbf{F}^{\text{iso}}$  and a dilatational part  $\mathbf{F}^{\text{vol}}$  by

$$\mathbf{F} = \mathbf{F}^{\text{iso}} \cdot \mathbf{F}^{\text{vol}}, \quad (3.8)$$

which is illustratively represented in Fig. 3.6. To obtain a brief summary of the proposed relation in terms of the left and right Cauchy-Green deformation tensors, the following equation can be utilized:

$$\mathbf{F}^{\text{iso}} = J^{-\frac{1}{3}} \mathbf{F}; \quad \mathbf{F}^{\text{vol}} = J^{\frac{1}{3}} \mathbf{I} \quad \Rightarrow \begin{cases} \mathbf{C}^{\text{iso}} = J^{-\frac{2}{3}} \mathbf{C}; & \mathbf{C}^{\text{vol}} = J^{\frac{2}{3}} \mathbf{I} \\ \mathbf{b}^{\text{iso}} = J^{-\frac{2}{3}} \mathbf{b}; & \mathbf{b}^{\text{vol}} = J^{\frac{2}{3}} \mathbf{I} \end{cases}. \quad (3.9)$$

In this context the modified deformation gradient  $\bar{\mathbf{F}}$  and the modified left and right Cauchy-Green tensors  $\bar{\mathbf{b}}$ ,  $\bar{\mathbf{C}}$  are introduced and denoted by an overbar as

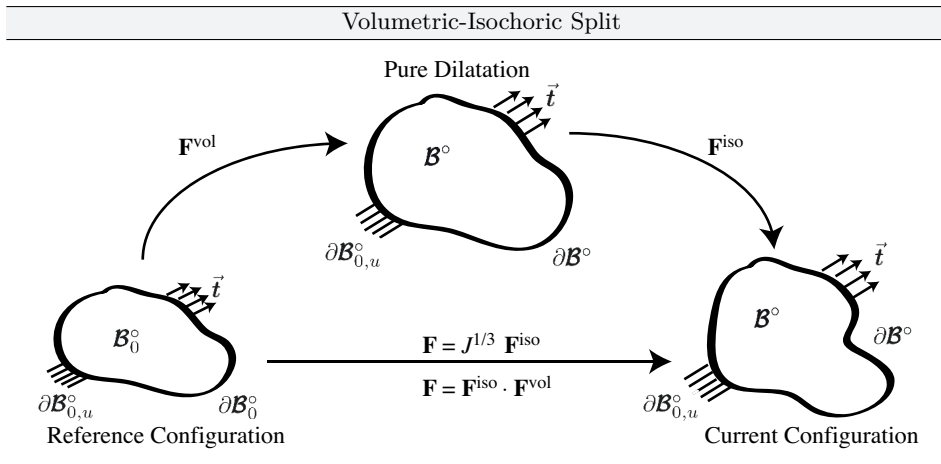


**Figure 3.6** Illustration of motion of a material body split into a dilatational and volume-preserving (isochoric) part

$(\bullet^{\text{iso}}) \equiv (\bullet)$  to represent the isochoric parts of its argument. This notation now applies to all of the following considerations.

To account for volume changes in Finite Element Analysis (FEA) compressibility has to be introduced, which can be achieved by adding volumetric part or component in the constitutive equations. Especially during hydrostatically loading conditions of hyperelastic materials, a certain amount of compressibility is required in numerical analysis to obtain physical results under a stable numerical calculation (Peng and Landel, 1975; Fried and A. R. Johnson, 1988; Bischoff et al., 2001).

Generally, the volumetric component of strain energy density functions can be described based on two principles (Ehlers and Eipper, 1998). The first principle is formulated by a coupled strain energy density function, where the volumetric and isochoric parts are not separated from each other with regard to the deformation gradient as well as the corresponding strain measure. Hence the complete Helmholtz free energy function reads

$$\Psi(\mathbf{b}) = \Psi_{\text{iso}}(\mathbf{b}) + \Psi_{\text{vol}}(J), \quad (3.10)$$

where  $\mathbf{b}$  represents the unmodified left Cauchy-Green deformation tensor, which is now dependent on volume changes. This special formulation is called Simo-Pister-type, which will be explicitly explained later.

In contrast, the second principle makes use of the modified or isochoric left Cauchy-Green deformation tensor  $\bar{\mathbf{b}}$ , which clearly separate isochoric from volumetric deformations by means of

$$\Psi(\mathbf{b}) = \Psi_{\text{iso}}(\bar{\mathbf{b}}) + \Psi_{\text{vol}}(J). \quad (3.11)$$

As previously mentioned, this type of formulation is called Flory-type constitutive model, which has the advantage of separating the deformations. Hence, the advantages lie in the complete separation of isochoric and volumetric deformations, whereby effects triggered by these deformations, such as cavitation caused by volumetric loading, can be described by separate model approaches and parameters. Furthermore, these effects can be observed decoupled by skilful execution of experiments, whereby material parameters can be read directly derived from experiments (Bartels, 2018).

### 3.2.3 Remarks on Volumetric-Isochoric Split

The volumetric-isochoric split is a common approach modelling hyperelastic materials (Flory, 1961). However, a physical background was never given to split the deformation gradient into a purely volumetric and isochoric deformation (Li et al., 2007). Following the studies of Ehlers and Eipper (1998), who analysed different types of volumetric Helmholtz free energy functions as well as different approaches for the volumetric-isochoric split, anomalies in the structural behaviour for simple tension problems were observed when not restricting to a nearly incompressible material behaviour. Ehlers and Eipper (1998) categorized the volumetric-isochoric split into a Flory-type split, which is dependent on the relative volume  $J$  and the modified first invariant  $I_{1,\bar{\mathbf{b}}}$  of the left Cauchy-Green deformation tensor  $\bar{\mathbf{b}}$ . Hence, the additively split volumetric and isochoric strain energy functions are clearly separated from each other. The alternative volumetric-isochoric split makes use of the relative volume  $J$  and the first invariant  $I_{1,\mathbf{b}}$  of the left Cauchy-Green deformation tensor  $\mathbf{b}$ .

To point out the alleged problem of the Flory-type split, the compressible stress response of a Neo-Hookean material will be analysed in the following, where a simple tension problem is analysed with different volumetric-isochoric splits and volumetric Helmholtz free energy functions. Based on the classical, pure isochoric Neo-Hookean Helmholtz free energy function reading

$$\Psi_{\text{iso,NH}}(\bar{\mathbf{b}}) = \frac{\mu}{2} \left( I_{1,\bar{\mathbf{b}}} - 3 \right) \text{ with } I_{1,\bar{\mathbf{b}}} = \frac{I_{1,\mathbf{b}}}{J^{\frac{2}{3}}} \quad (3.12)$$

or the counterpart, which also depends on volume changes,

$$\Psi_{\text{iso}, \text{NH}}(\mathbf{b}) = \frac{\mu}{2} (I_{1,\mathbf{b}} - 3), \quad (3.13)$$

the Cauchy stress in the principal stretch direction can be generally calculated accordingly to Pence and Gou (2015) by

$$\sigma_1 = \frac{2}{J} \frac{\partial \Psi}{\partial I_{1,\mathbf{b}}} \lambda_1^2 + \frac{\partial \Psi}{\partial J} \quad (3.14)$$

or more general by

$$\boldsymbol{\sigma} = \frac{2}{J} \frac{\partial \Psi}{\partial I_{1,\mathbf{b}}} \mathbf{b} + \frac{\partial \Psi}{\partial J} \mathbf{I}. \quad (3.15)$$

In the case of a compressible material, the relative volume is implicitly dependent on the applied stretch. Hence, the implicit function

$$0 = \frac{2}{J} \frac{\partial \Psi}{\partial I_{1,\mathbf{b}}} \lambda_2^2 + \frac{\partial \Psi}{\partial J} \quad (3.16)$$

must be solved by root-finding method. In accordance to Ehlers and Eipper (1998) and Pence and Gou (2015), it is straight-forward to analyse the compressible response of uniaxial tension problems by plotting the implicit relationship with respect to  $\lambda_1 - \lambda_2$ . In this context,  $\lambda_1$  denotes the stretch in which the traction takes place, whereas  $\lambda_2$  denotes the lateral stretch. This representation is ideal to investigate potential anomalies within the structural response as well as the constitutive model. To obtain a relation purely described by principal stretches, the relative volume  $J$  must be replaced by  $J = \lambda_1 \lambda_2^2$ . For the sake of completeness, the longitudinal stretch  $\lambda_1$  dependent on the relative volume  $J$  is also illustrated for the uniaxial tension problem. Regarding Fig. 3.7, the results for three volumetric strain energy functions are illustrated. As it is obvious from Fig. 3.7 a,b, the Flory-type approach for the classical Helmholtz free energy function, which reads

$$\Psi_{(a-b)} = \frac{\mu}{2} \left( \frac{I_{1,\mathbf{b}}}{J^{\frac{2}{3}}} - 3 \right) + \frac{K}{2} (J - 1)^2, \quad (3.17)$$

leads to an abnormal structural behaviour for large compression stretches. After reaching a maximum for the lateral strain  $\lambda_2$ , it decreases with an increasing longitudinal compression stretch. This means that the cross-sectional area of a specimen would become smaller with increasing compression. Due to this abnormal structural behaviour, Ehlers and Eipper (1998) argue that the Flory-type volumetric-isochoric split leads to non-physical material behaviour in general. Furthermore, Ehlers and Eipper (1998) argue that in the case of uniaxial tension

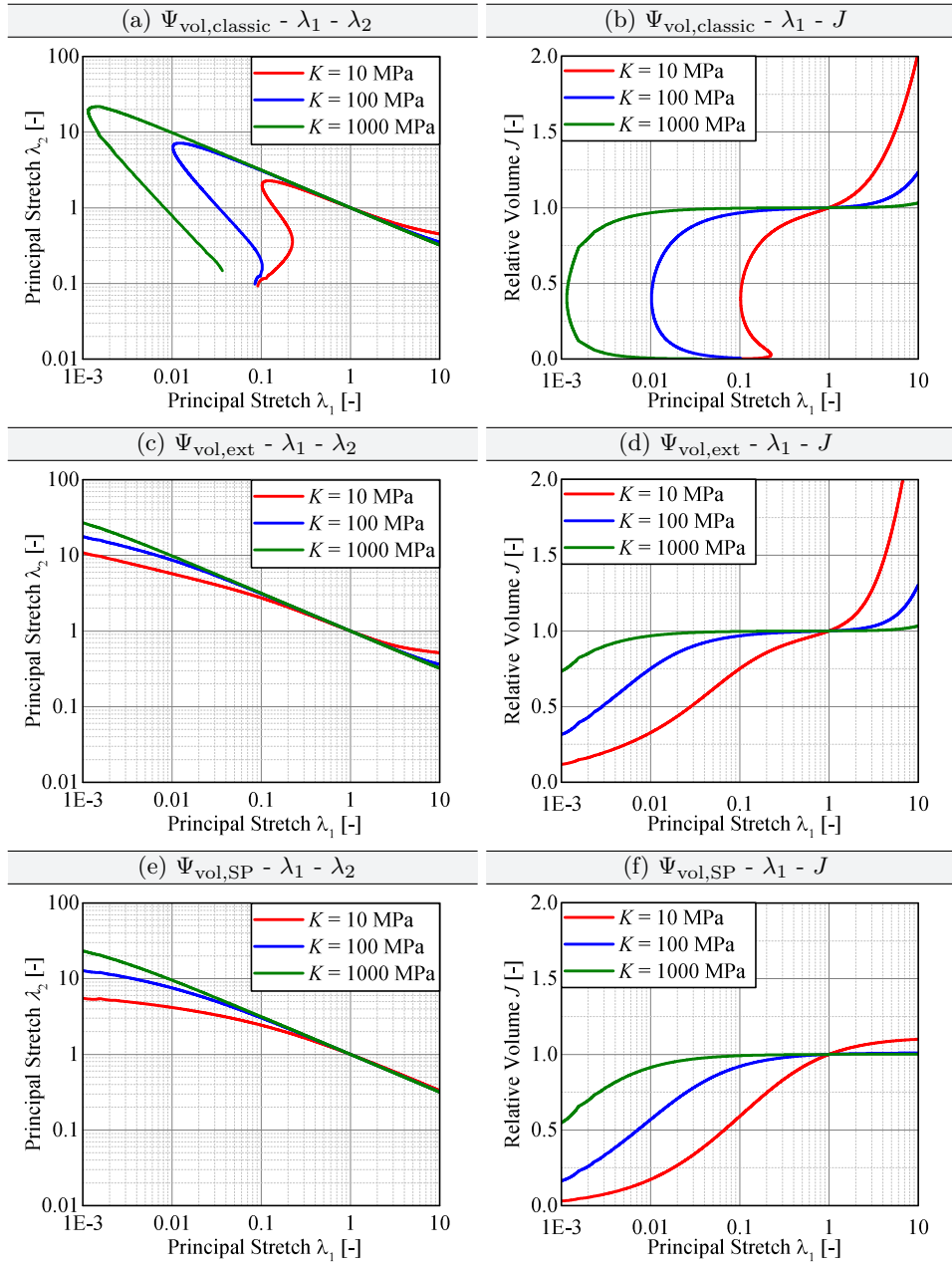


**Figure 3.7** Comparison of different volumetric Helmholtz free energies in the uniaxial tensile test under consideration of the  $\lambda_1-\lambda_2$  and  $\lambda_1-J$  relationship: (a) classical, volumetric Helmholtz free energy function with Flory-type split (see Eq. (3.17)), (b) extension of classical, volumetric Helmholtz free energy function with Flory-type split in accordance to Pence and Gou (2015) (see Eq. (3.18)) and (c) Simo-Pister-type volumetric-isochoric split (see Eq. (3.20))

the cross-sectional area increases by increasing the longitudinal stretch  $\lambda_1$ , which represents for them also an abnormal structural behaviour. Summarizing, the Flory-type volumetric isochoric split leads to non-physical results for the uniaxial tension / compression problem accordingly to Ehlers and Eipper (1998). However, Le Cam (2010) and Kazina et al. (2011) showed that an increase in volume for uniaxial tensile tests is physically and should be taken into account. Therefore, the author is of the opinion that only the abnormal behaviour for the uniaxial compression tests has to be eliminated in order to get a physical motivation for the Flory-like split. To do so, Pence and Gou (2015) showed that even for a Flory-type split an abnormal structural behaviour can be avoided by choosing an extension of the classical volumetric Helmholtz free energy function, which reads

$$\Psi_{(c-d)} = \frac{\mu}{2} \left( \frac{I_{1,b}}{J^{\frac{2}{3}}} - 3 \right) + \frac{K}{8} \left( J^2 + \frac{1}{J^2} - 2 \right). \quad (3.18)$$

With regard to Fig. 3.7 c,d the structural behaviour is illustrated for Eq. (3.18), which clearly shows that a physical behaviour can be also guaranteed for a Flory-type volumetric-isochoric split.

In contrast to Eq. (3.18), where the advantages of a strict separation between volumetric and isochoric deformations are obvious, the Simo-Pister-type split loses these advantages. However, accordingly to Ehlers and Eipper (1998) this split provides a physical material behaviour for the uniaxial tension problem. Since the advantages of the Flory-type split are no longer given, the material parameters, i.e. the initial shear modulus  $\mu$  and the bulk modulus  $K$  must be chosen carefully to obtain a stress-free reference configuration. This can be achieved by interrelating the initial shear modulus  $\mu$  and the bulk modulus  $K$  via first Lamé constant reading

$$\Lambda = K - \frac{2}{3}\mu. \quad (3.19)$$

Based on this, the results for the Simo-Pister-type volumetric-isochoric split, which reads

$$\Psi_{(e-f)} = \frac{\mu}{2} (I_{1,b} - 3) + \frac{\Lambda}{2} \ln(J)^2 - \mu \ln(J), \quad (3.20)$$

are illustrated in Fig. 3.7 e,f. From this, it is obvious that a physical structural behaviour is apparent. Nevertheless, since the volumetric-isochoric split can also demonstrably lead to physical material behaviour and at the same time offers the advantages of a strict distinction between volumetric and isochoric deformations, the Flory-type split is used for all further developments.

### 3.2.4 Isochoric Hyperelastic Constitutive Models

This section presents isochoric hyperelastic material formulations, which on the one hand have a molecular-statistical foundation and on the other hand are purely phenomenological in nature. Since there is a large amount of hyperelastic formulations in literature (Marckmann and Verron, 2006; Steinmann et al., 2012), only those models are described which will be used in the further course of the dissertation. However, to give a brief overview of the classification and important hyperelastic material formulations from literature, the state of the art is outlined below.

Looking at the mathematical description of hyperelastic constitutive models, they are divided into first-invariant ( $I_1$ ) based models (Treloar, 1943; Yeoh, 1990; Yeoh and Fleming, 1997; Zúñiga and Beatty, 2002; Beatty, 2008; Lopez-Pamies, 2010; Khajehsaeid et al., 2013), two invariant ( $I_1$  and  $I_2$ ) based models (Mooney, 1940; Rivlin, 1948; Hart-Smith, 1966; Alexander, 1968; Pucci and Saccomandi, 2002; Horgan and Saccomandi, 2006; Beda, 2007), material formulations depending on the principal stretches (Valanis and Landel, 1967; Ogden, 1972; Kaliske and Heinrich, 1999; Shariff, 2000; Mansouri and Darijani, 2014) and models based on logarithmic strain invariants (Hencky, 1933; Ogden, 1972; Shariff, 2000; Neff et al., 2015). Furthermore, molecular-statistically motivated models exist which derive macroscopic constitutive relationships from the statistical mechanics of polymer chains (James and Guth, 1943; Arruda and Boyce, 1993; Zúñiga and Beatty, 2002; Miehe et al., 2004a; Beatty, 2008). As reported in the studies of Marckmann and Verron (2006) and Khiêm and Itsakov (2016), only four models exist, namely the Ogden model (Ogden, 1972), the Extended Tube model (Kaliske and Heinrich, 1999), the Shariff model (Shariff, 2000) and the tube-like microsphere model (Miehe et al., 2004a), which are able to represent the non-linear stress-strain relationships for rubber in diverse deformation states. In the course of this dissertation, this hypothesis will be verified using an isochoric Helmholtz free energy function developed within the framework of this dissertation (see Section 5.1).

## Molecular-Statistical Constitutive Laws for Hyperelasticity

Hyperelasticity can be characterized based on so-called molecular-statistical models, which analyse the deformation behaviour of rubbers on a micro-scale level deriving the stress-strain relationship from idealized macro-molecular models. The elementary statistical theory on polymers was founded by Kuhn (1934); Kuhn (1936), Kuhn and Grün (1942) and James and Guth (1943), where rubbers and rubber-like materials are understood as flexible long-chain molecules with weak intermolecular forces and partial cross linkings between the molecules forming networks.

Considering the classical Gaussian statistic applied on a single polymer chain according to Kuhn (1934) and Kuhn (1936), the free energy of it can be calculated by

$$\psi_s(\bar{\lambda}) = \frac{3}{2}kT\lambda^2 + \psi_0, \quad (3.21)$$

where the micro-stretch  $\lambda$  acts on a single chain as deformation.  $N$  characterizes the number of statistical links per polymer chain and is therefore a real material constant (Treloar, 1975). Now it still needs a relationship between the response of a single polymer chain and the macroscopic deformation at the continuum level. The simplest network model for this is the three-chain model of Kuhn and Grün (1942) and James and Guth (1943), in which the arrangement of the three idealized polymer chains along the Cartesian axes of the macroscopic coordinate system causes an affine deformation. Hence, the macroscopic isochoric free energy  $\Psi_{\text{iso}}$  can be calculated by the arithmetic average of the free energies  $\psi_s$  for three principal directions, which reads

$$\Psi_{\text{iso}} = N \langle \psi_s \rangle \text{ with } \langle \psi_s \rangle = \frac{1}{3} [\psi_s(\lambda_1) + \psi_s(\lambda_2) + \psi_s(\lambda_3)]. \quad (3.22)$$

Inserting the free energy of a single chain described by Eq. (3.21), one obtains the macroscopic isochoric Neo-Hookean free energy attributed with a molecular-statistical background, which reads

$$\Psi_{\text{iso}} = \frac{\mu}{2} (\lambda_1 + \lambda_2 + \lambda_3) \text{ with } \mu := NkT. \quad (3.23)$$

Keeping in mind that the first invariant of the left Cauchy-Green deformation tensor is given by  $I_{1,\mathbf{b}} = \lambda_1 + \lambda_2 + \lambda_3$ , the molecular-statistically motivated Neo-Hookean material can be reformulated to  $\Psi_{\text{iso}} = \frac{\mu}{2} I_{1,\mathbf{b}}$ . Since no free energy should be available in the undeformed condition, which manifest itself with  $I_{1,\mathbf{b}}^{\text{ref}} = 3$ , the originally proposed form of the micro-mechanically motivated Neo-Hookean constitutive law is modified by

$$\Psi_{\text{iso}} = \frac{\mu}{2} (I_{1,\mathbf{b}} - 3). \quad (3.24)$$

For well-known reasons, the proposed affine deformation assumption remains contrary to experimental results as it only covers moderate deformations without considering the limit of stretch of the polymer chains. Consequently, more complex chain models were developed, such as the eight-chain model of Arruda and Boyce (1993) or the micro-sphere model of Miehe et al. (2004a), in order to be able to represent also non-affine deformations and thus also the behaviour of polymers at large deformations. Further models with molecular-statistical background, where not only elasticity but also softening and strain-induced crystallization due to the Mullins effect can be modelled, were presented by Khiêm and Itskov (2018).

However, the proposed molecular-statistical models do not consider topological constraints due to polymer network interactions, since the idealized polymer networks are free in their motion and furthermore consider only a single polymer chain. Hence, the constrained segment and constrained junction theories have been additionally developed (Deam and Edwards, 1976; Edwards and Vilgis, 1988; Kaliske and Heinrich, 1999). In this thesis the constrained segment theory plays an important role, so that it is presented in more detail with regard to the extended tube model of Kaliske and Heinrich (1999). The extended tube model accounts for the above-mentioned topological constraints as well as the limited chain extensibility of network chains. It is described by four material parameters with physical meaning. The strain energy density function of this model is given by

$$\Psi_{\text{iso}}(\bar{\mathbf{b}}) = \frac{G_c}{2} \left[ \frac{(1-\delta^2)(I_{1,\bar{\mathbf{b}}}-3)}{1-\delta^2(I_{1,\bar{\mathbf{b}}}-3)} + \ln(1-\delta^2(I_{1,\bar{\mathbf{b}}}-3)) \right] + \frac{2G_e}{\beta^2} \sum_{A=1}^3 (\lambda_A^{-\beta} - 1). \quad (3.25)$$

In this hyperelastic material model the parameter  $G_c$  describes the cross-link distribution of the shear modulus, whereas  $G_e$  represents the constrained distribution of the shear modulus. The total shear modulus is the sum of both parts. The parameter  $\beta$  describes the rearrangement of cross-links upon deformations and  $\delta$  stands for the maximal extensibility of a polymer chain.

## Phenomenological Constitutive Laws for Hyperelasticity

An important phenomenological model was developed by Mooney (1940), where an incompressible, homogeneous and isotropic material obeys Hooke's law in simple shear considering two material parameters. This model was generalized by Rivlin (1948) expressing the Helmholtz free energy as an infinite power series, which yields

$$\Psi(\bar{\mathbf{b}}) = \sum_{i,j=0}^{\infty} C_{ij} (I_{1,\bar{\mathbf{b}}}-3)^i (I_{2,\bar{\mathbf{b}}}-3)^j. \quad (3.26)$$

Considering the originally proposed form with two parameters, the Mooney-Rivlin material model can be described by

$$\Psi(\bar{\mathbf{b}}) = C_{10} (I_{1,\bar{\mathbf{b}}}-3) + C_{01} (I_{2,\bar{\mathbf{b}}}-3), \quad (3.27)$$

which represents a fundamental hyperelastic material model. In contrast to the micro-mechanically motivated Neo-Hookean and extended tube material models,

this model is purely phenomenologically motivated and includes the second invariant of the left Cauchy-Green tensor combined with an additional material parameter.

### 3.2.5 Volumetric Hyperelastic Constitutive Models

In contrast to the brief description of isochoric hyperelastic models and the restriction of the detailed description to only three essential models due to the enormous number of isochoric models, almost all volumetric energy functions occurring in the literature are presented in detail in the following, since only few approaches exist here. An overview of the various volumetric Helmholtz free energy functions for hyperelastic materials is given by Hartmann and Neff (2003). The simplest form of a volumetric Helmholtz free energy is dependent on the bulk modulus  $K$  and the relative volume  $J$  only. Due to its simple form, the functional is denoted as the classical volumetric Helmholtz free energy function, which reads

$$\Psi_{\text{vol,classic}} = \frac{K}{2}(J - 1)^2. \quad (3.28)$$

Since the classical volumetric Helmholtz free energy function violates the postulate of convexity for  $J \rightarrow 0$ , which reads

$$\lim_{J \rightarrow +\infty} \Psi_{\text{vol}} = \lim_{J \rightarrow 0} \Psi_{\text{vol}} = \infty, \quad (3.29)$$

Pence and Gou (2015) suggested a volumetric strain energy function that does not exhibit this disadvantage resulting in

$$\Psi_{\text{vol,ext}} = \frac{K}{8}(J^2 + \frac{1}{J^2} - 2). \quad (3.30)$$

Simo and Taylor (1982) also proposed an improvement of the classical volumetric Helmholtz free energy function by adding the natural logarithm to the power of two. The enhanced volumetric strain energy function reads

$$\Psi_{\text{vol,ST}} = \frac{K}{4} \left[ (J - 1)^2 + \ln(J)^2 \right]. \quad (3.31)$$

Regarding variational methods for the volume-constraint in finite deformation elasto-plasticity, Simo et al. (1985) proposed a variation of Eq. (3.31) by considering the natural logarithm only, i.e.

$$\Psi_{\text{vol,STP}} = \frac{K}{2} \left[ \ln(J)^2 \right]. \quad (3.32)$$

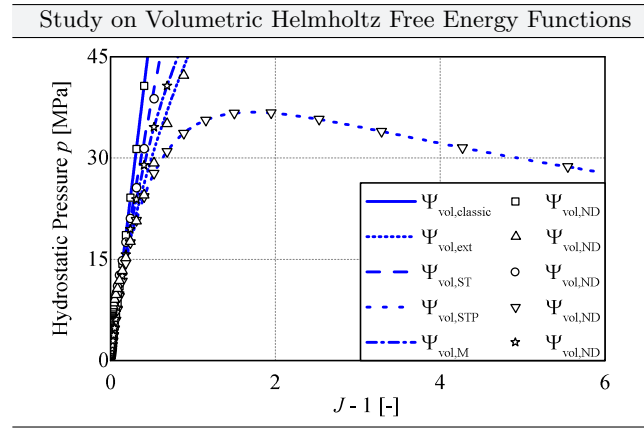


**Figure 3.8** Approximation of conventional volumetric Helmholtz free energy functions via  $\Psi_{\text{vol,ND}}$  with  $K = 100 \text{ MPa}$  and  $\mu = 1 \text{ MPa}$

Miehe (1994) proposed also an alteration of the above-mentioned volumetric Helmholtz free energies, which reads

$$\Psi_{\text{vol,M}} = K [J - \ln(J) - 1]. \quad (3.33)$$

Following Hartmann and Neff (2003) and Li et al. (2007), most of the models were developed without a physical background. The main focus was set on enforcing the incompressibility constraint under ensuring the element stability, (Bonet and Wood, 2008:p.171). In contrast, Drass et al. (2018b) proposed a micro-mechanically motivated volumetric Helmholtz free energy function accounting for cavitation in structural silicones. The novel approach reads in a generalized form

$$\Psi_{\text{vol,ND}} = \int_J \frac{(J-1)}{\sum_{i=0}^m \kappa_i (J-1)^i} dJ \quad \text{with } i \in \mathbb{N}. \quad (3.34)$$

In Fig. 5.15, the hydrostatic pressure  $p$  depended on the relative volume  $J$  is illustrated with respect to all proposed volumetric Helmholtz free energy functions. In addition,  $\Psi_{\text{vol,ND}}$  is presented as a fitting result of all conventional volumetric strain energy functions to demonstrate its flexibility. From Fig. 3.8 is obvious that  $\Psi_{\text{vol,ND}}$  includes all classical energy functions, since  $\Psi_{\text{vol,ND}}$  adequately approximates the structural responses of all classical models. Regarding Fig. 3.8, all proposed models show a similar structural response. The classic Helmholtz free energy function shows a linear dependence between  $p$  and  $J$ , while all other strain energy functions show a moderate to a strong non-linearity. Regarding hydrostatic tensile

loading ( $J > 1$ ), moderate softening of structural behaviour for  $\Psi_{\text{vol,ext}}$ ,  $\Psi_{\text{vol,ST}}$  and  $\Psi_{\text{vol,M}}$  can be observed. In contrast,  $\Psi_{\text{vol,STP}}$  shows a distinct softening of the structural behaviour, which is not due to the cavity growth under hydrostatic loading and the associated macroscopic material softening, but only due to the chosen mathematical approach. In summary, the classical volumetric approaches are good in the sense of a stable finite element calculation, but processes such as stress softening due to the cavitation effect in rubbers under hydrostatic tensile loading cannot be reproduced. However, with the micro-mechanical approach of Drass et al. (2017a) and Drass et al. (2018b) void growth due to cavitation can be modelled.

### 3.3 Hyperelasticity for Porous Continua

Danielsson et al. (2004) presented a method for deriving a homogenized strain energy density function for porous continua based on a kinematically permissible deformation field, which was originally proposed by Hou and Abeyaratne (1992). The limitations of the model can be summarized with (i) incompressible material behaviour on the meso-scale and (ii) a spherical, vacuous cavity at the centre of a sphere resulting in isotropic macroscopic behaviour. The kinematically admissible deformation field for void growth reads

$$x_i = \psi_i X_i \quad (\text{no sum on } i). \quad (3.35)$$

Without going into the derivation in detail, a system of differential equations was calculated, whereby a deformation gradient for a porous continuum is obtained when solving it. The components of the deformation gradient read

$$F_{ij} = \frac{\lambda_i}{J^{\frac{2}{3}}} \left( \frac{1 - \psi^3}{\psi^2 R^2} X_i X_j + \psi \delta_{ij} \right), \quad (3.36)$$

with

$$\psi = \left( 1 + (J - 1) \left( \frac{B}{R} \right)^3 \right)^{\frac{1}{3}}. \quad (3.37)$$

In this context, the parameter  $R$  describes the radial distance of a voided sphere in the reference configuration, whereas  $B$  characterizes the radius in the current configuration. On this basis, modified strain invariants on the meso-scale were derived based on Eq. (3.36), which read

$$I_1^\circ = \frac{1}{J^{\frac{2}{3}}} \left[ I_1 \psi^2 + \frac{1}{R^2} (\lambda_1^2 X_1^2 + \lambda_2^2 X_2^2 + \lambda_3^2 X_3^2) \left( \frac{1}{\psi^4} - \psi^2 \right) \right] \quad (3.38)$$

and

$$I_2^\circ = J^{\frac{2}{3}} \left[ \frac{I_2}{J^2 \psi^2} + \frac{1}{R^2} \left( \frac{X_1^2}{\lambda_1^2} + \frac{X_2^2}{\lambda_2^2} + \frac{X_3^2}{\lambda_3^2} \right) \left( \psi^4 - \frac{1}{\psi^2} \right) \right] \quad (3.39)$$

where  $I_1$  and  $I_2$  represent the first and second invariant of a general left Cauchy Green stretch tensor. Based on these modified strain invariants defined at the meso-scale, Danielsson et al. (2004) proposed a homogenized strain energy  $\Psi^*$ , which can be obtained by

$$\Psi^* = \frac{1}{V_0} \int_{Bf_0^{1/3}}^B \int_0^{2\pi} \int_0^\pi \Psi^\circ(I_1^\circ, I_2^\circ) R^2 \sin \Theta d\Theta d\Phi dR. \quad (3.40)$$

In the case of a Neo-Hookean matrix, the homogenized strain energy function reads

$$\Psi^* = \frac{\mu}{2} \left[ I_1 \left( 2 - \frac{1}{J} - \frac{f_0 + 2(J-1)}{J^{\frac{2}{3}} \eta^{\frac{1}{3}}} \right) - 3(1-f_0) \right] \text{ with } \eta = 1 + \frac{J-1}{f_0}, \quad (3.41)$$

which is an extended representation of the Neo-Hooke model by the porosity  $f_0$ . At this point it should be noted that this is no longer a Flory-type material model, since no separation between isochoric and volumetric deformations could be maintained.

## 3.4 Concept of Pseudo-Elasticity

In the investigations of Fung (1980) on living tissues, it was found that the loading and unloading paths under cyclic loading differ significantly. Each can be described separately by a unique relationship between stresses and strains. Since both load paths were represented independently by two single classical hyperelastic material models or with different material parameters for one hyperelastic material model, but the unloading path is strictly speaking inelastic, this phenomenological concept was termed pseudo-elasticity. Lazopoulos and Ogden (1998) proposed the general concept of pseudo-elasticity by introducing a Helmholtz free energy function  $\Psi(\mathbf{F}, \eta)$  that is additionally dependent on an internal scalar variable  $\eta$ . The extension of  $\Psi$  by a continuous or discontinuous internal variable  $\eta$  additionally motivates the designation of this theory as pseudo-elasticity.

For the extended functional  $\Psi(\mathbf{F}, \eta)$ , the first Piola-Kirchhoff stress tensor  $\mathbf{P}$  can be calculated through

$$\mathbf{P} = \frac{\partial \Psi}{\partial \mathbf{F}}(\mathbf{F}, \eta) + \frac{\partial \Psi}{\partial \eta}(\mathbf{F}, \eta) \frac{\partial \eta}{\partial \mathbf{F}}(\mathbf{F}) \quad (3.42)$$

assuming an elastic body, which is mapped from the reference to the current configuration by the deformation gradient  $\mathbf{F}$ . Since the internal variable depends additionally on  $\mathbf{F}$ , the functional must be differentiated according to  $\eta$ , whereby  $\eta$  must be subsequently differentiated according to  $\mathbf{F}$ . In the absence of body forces the first and at the same time also usual equilibrium equation in the Lagrangian description reads

$$\nabla_{\vec{\mathbf{X}}} \cdot \mathbf{P} = \vec{\mathbf{0}} \quad (3.43)$$

where  $\nabla_{\vec{\mathbf{X}}} \cdot (\bullet)$  represents the divergence operator with respect to the reference configuration. Lazopoulos and Ogden (1998) formulated an additional equilibrium condition derived from a variational principle (stationary energy principle), which reads

$$\frac{\partial \Psi}{\partial \eta} (\mathbf{F}, \eta) = 0. \quad (3.44)$$

This equilibrium equation implicitly relates the internal variable  $\eta$  to  $\mathbf{F}$  and thus continuously modifies the strain energy density function with progressing deformation. Based on these basic equations, Ogden and Roxburgh (1999) defined a pseudo-elastic energy function of type

$$\Psi(\mathbf{F}, \eta) = \eta \hat{\Psi}(\mathbf{F}) + \phi(\eta), \quad (3.45)$$

where  $\phi(\eta)$  describes a damage function to describe the Mullins effect. The inclusion of  $\eta$  and  $\phi(\eta)$  offers the possibility to change the form of the energy function during deformation.

According to Dorfmann and Ogden (2003), the damage parameter was assumed to be inactive during loading conditions and active for unloading with  $\eta \in [0, 1]$ . The internal variable was explicitly derived by inserting Eq. (3.45) in Eq. (3.44), which reads

$$-\phi'(\eta) = \hat{\Psi}(\mathbf{F}). \quad (3.46)$$

Since the damage function  $\phi(\eta)$  is intended to determine  $\eta$  depending on the state of deformation,  $\phi(\eta)$  was chosen so that

$$-\phi'(\eta) = m \tanh^{-1}[r(\eta - 1)] + \hat{\Psi}_{\max} \quad (3.47)$$

applies. In this context  $r \geq 0$  and  $m \geq 0$  are parameters to calibrate the amount of the Mullins damage during unloading, whereas  $\hat{\Psi}_{\max}$  characterizes the maximum reached strain energy during loading. By equating Eq. (3.46) with Eq. (3.47), the damage variable is fully described by

$$\eta = 1 - \frac{1}{r} \tanh \left[ \frac{1}{m} \left( \hat{\Psi}_{\max}(\mathbf{F}) - \hat{\Psi}(\mathbf{F}) \right) \right]. \quad (3.48)$$

The damage function  $\phi(\eta)$  can be obtained by integrating Eq. (3.47) with respect to  $\eta$ , which reads

$$\phi(\eta) = -m(\eta-1)\tanh^{-1}[r(\eta-1)] - (\eta-1)\hat{\Psi}_{\max}(\mathbf{F}) - \frac{m}{2r}\ln\left[1-r^2(\eta-1)^2\right]. \quad (3.49)$$

The theory of pseudo-elasticity has been successfully applied to the description of rubbers and polymer foams with stress softening and residual strain effects (Gracia et al., 2009; Zhang et al., 2011).

In summary, this chapter has presented the structural behaviour of polymers and described failure mechanisms. Since the present work is intended to contribute to the novel material modelling of a transparent silicone adhesive, classical forms of material modelling of rubber-like materials with reference to continuum mechanics have been presented. These provide the basis for the new development of various material models, which will be developed and presented in Chap. 5.



# 4 Experiments on Transparent Structural Silicone Adhesive

The aim of the work is the material characterization and failure modelling of a transparent structural silicone adhesive. This requires experimental tests, which are briefly described in this chapter and the main results are summarized. The performed experimental tests are categorized into homogeneous and inhomogeneous test. With the results of the homogeneous tests it is possible to analytically determine material parameters, whereas inverse numerical methods have to be applied to calculate material parameters based on the inhomogeneous tests. A homogeneous experiment is present, when the test sample is homogeneously deformed within the applied test set-up. Based on the experimental results not only new material models (Chap. 5) but also failure criteria are developed based on the determined failure modes seen in the experiment (Chap. 6).

## 4.1 Transparent Structural Silicone Adhesive - TSSA

The material to be investigated in this work is a transparent structural silicone adhesive - TSSA, which is used as an adhesive in point fixed supports in façade construction to bond large-format glass to the secondary load-bearing structure (see Fig. 4.1). TSSA is notable for its ease of use, as it is easy to cut and apply. The one-part material has a heat-activated cross-linking mechanism, which gives it its final material properties. The adhesive film is cured at temperatures of  $120 - 130^{\circ}\text{C}$  for a period of  $20 - 30$  min under a pressure of typically  $0.15 - 1.3 \text{ MPa}$  to ensure efficient wetting of the substrate and thus an optimum adhesion. The best results for this so-called laminated connection are achieved in the autoclave process, but a strong connection can also be obtained via laminators or vacuum bagging during the curing process. The fully cured material is characterized by its high transparency, high tensile strength, strong adhesion, good thermal stability and high weather resistance (Sitte et al., 2011).

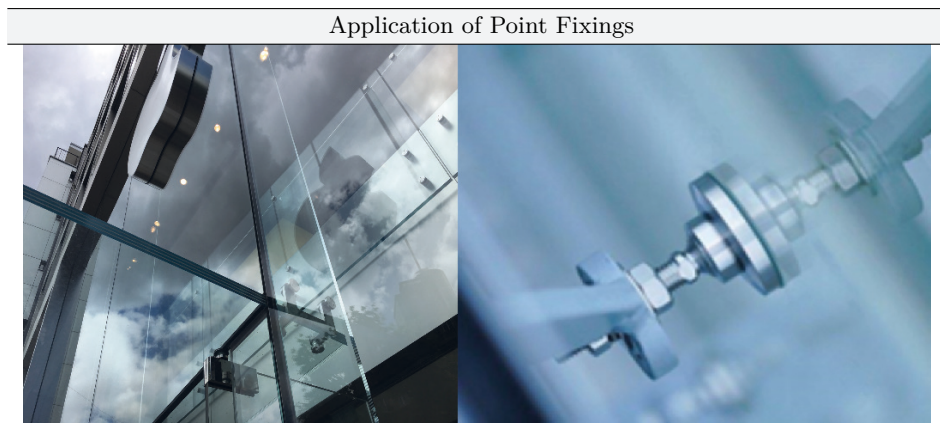


**Figure 4.1** Metal button of large-format glass panes in broken and intact condition made with TSSA

## 4.2 Homogeneous Experimental Tests

In order to identify reliable material parameters for hyperelastic material models analytically (semi-analytically), it is necessary to perform a range of different experimental tests in which a homogeneous stress and strain state is guaranteed (Drass et al., 2018e; Drass et al., 2018f). The following is a brief summary of all experimental tests carried out with TSSA with regard to structural behaviour and failure loads and stretches. In addition, the test set-ups, the test speeds used, experimental boundary conditions and test sequence are briefly presented in order to make experimental characterization of the material comprehensible. It is to note that all experimental data are prepared in such a way that each individual test curve, the mean value and the standard deviation are presented. This representation is helpful for later numerical simulations of the experimental investigations.

### 4.2.1 Uniaxial Tension

Uniaxial tensile tests for rubber-like materials are standardized in ASTM D638 - 02a (2003) and ISO 37 (2011). Typical test specimens are dumbbell-shaped with a large edge-parallel area in order to perform measurements on them. To achieve a homogeneous stress and strain field in the edge-parallel area, the clamped ends are connected to the edge-parallel area by rounding the connecting segments. The stressed cross-section, in which optical strain measurements are typically carried out, is small for standardized specimens, so that a measurement of the Poisson's ratio is not easily possible. For this reason the geometry of the tensile specimen according to F. Becker (2009) is used, which is wider in the edge-parallel area than

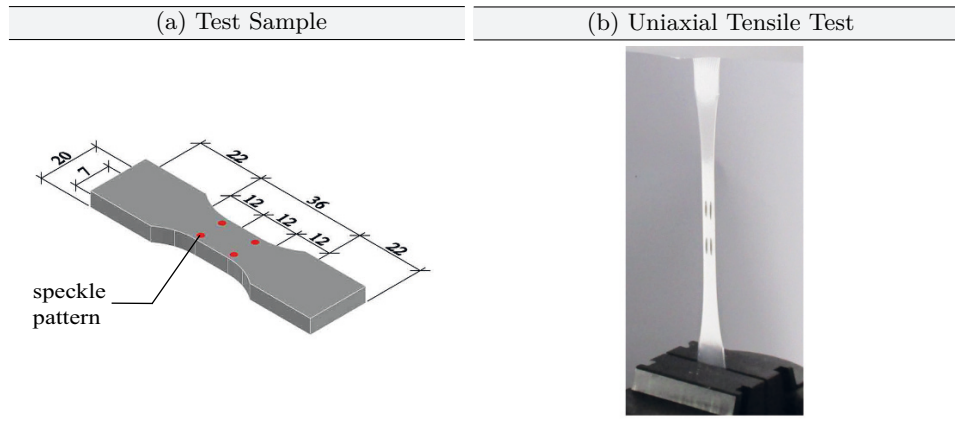


**Figure 4.2** (a) Geometry of uniaxial tensile test specimens; (b) test set-up of uniaxial tensile tests during testing

standardized specimens (see Fig. 4.2). This specimen describes an ideal shape for measurements at low and high strain rates while guaranteeing a homogeneous stress and strain field in the edge-parallel region. This can be easily visualized by examining the modified triaxiality of the test specimen. The modified triaxiality  $\eta_{\text{mod}}$  describes the magnitude of the ratio of hydrostatic pressure  $p = \text{tr}(\boldsymbol{\sigma})$  to von Mises equivalent stress  $\sigma_{\text{vM}} = \sqrt{3I'_{2,\sigma}}$ . An explanation can be found in Appendix A. Drass et al. (2018e) demonstrated that a homogeneous stress condition prevails for a hyperelastic material under uniaxial tensile loading.

F. Becker (2009) showed for thermoplastics, which exhibit a linear elastic behaviour followed by a distinctive yield behaviour, that the shape of the test specimen has a remarkable influence on the triaxiality. This does not apply to rubber-like materials, as their material behaviour is completely different from that of thermoplastics. Hyperelastic materials behave elastically up to breakage, whereas thermoplastics show a pressure-dependent flow behaviour, so that this has a great influence on the triaxiality. In addition, the stress concentrations at free corners do not develop as strongly due to the low stiffness of the rubber.

Returning to the uniaxial tensile tests, the experimental test matrix consists of ten test samples, where the specimens were punched out of a cured TSSA sheet with a punching tool (Drass et al., 2018e). The uniaxial tensile tests were performed in a standard atmosphere with a testing speed of  $v_{\text{UT}} = 5.0 \text{ mm/s}$ . Standard atmosphere is also defined in this context as a standard climate for testing plastics in non-tropical countries, where an air temperature of  $23^{\circ}\text{C}$  and a relative humidity of 50% are required (DIN EN ISO 291, 2008). The so-called Digital Image Correlation (DIC) was used to determine the local strains due to an external loading based

on optical measurements. During the deformation, images of the specimen were recorded with two cameras. The object surface to be measured is provided with a random speckle pattern. Here a dot pattern was applied by hand ( $d \leq 2$  mm) with a black touch-up pencil and then evaluated. An exact evaluation of a finer dot pattern was not possible or necessary for two reasons. On the one hand, with the existing equipment and the resolution of the cameras, no finer dot pattern could be evaluated for the analysis of large deformations. This is due to the fact that the assessable or evaluable image window, the size of the speckle pattern and the distance between the cameras and the sample are interrelated. The smaller the speckle pattern, the higher the resolution, but the distance between sample and cameras must be minimized. Therefore, the evaluable image window is then very small. So if large deformations occur in the experiment, which is generally the case when rubber is pulled uniaxially, the experiment can no longer be evaluated to failure because the speckle pattern is pulled out of the measuring range of the cameras. On the other hand, it is not necessary to evaluate the local strains using a fine speckle pattern in the uniaxial tensile test, since a smeared strain information is already sufficient to approximate material models, for example. Returning to the DIC in general, the measured pixel coordinates of the pattern were used to calculate displacements and strains on the specimen. Since large deformations occur in the uniaxial tensile test, virtual measuring marks were generated on the specimen, which were used to determine the engineering strain. Again, local measurements of Hencky strain at such large deformations were not possible or insufficient with the installed set-up, as the resolution of the system is limited.

Fig. 4.3 a shows all test results individually as well as the mean value curve and the simple standard deviation. In Fig. 4.3 b the failure engineering stresses and the failure stretches are shown. In addition, all failure points are shown individually. Furthermore, the mean value, the standard deviation and the min. / max. values can be observed. From Fig. 4.3 a it is obvious that a slight non-linear behaviour is apparent as well as large strains can be sustained by TSSA. The maximum engineering strain that can appear has approximately a value of 1.8. The experimental results for the uniaxial tensile load correspond to the results proposed by Hagl (2016) and Santarsiero et al. (2016), while the classical structural behaviour known from natural rubbers in the form of an S-shape is not apparent (Treloar, 1975). It is interesting to note that with increasing deformation a so-called whitening of the sample occurs (see Fig. 4.2 b). By pure visual observation the white colouration could be observed at discrete places, which intensifies with increasing deformation. The spot-wise white colouration in uniaxial tensile test was also confirmed by the investigations of Sitte et al. (2011) and Santarsiero et al. (2016). The origin of the whitening effect and a possible physical explanation is presented in Section 4.4.2. Nevertheless, it can already be stated at this point

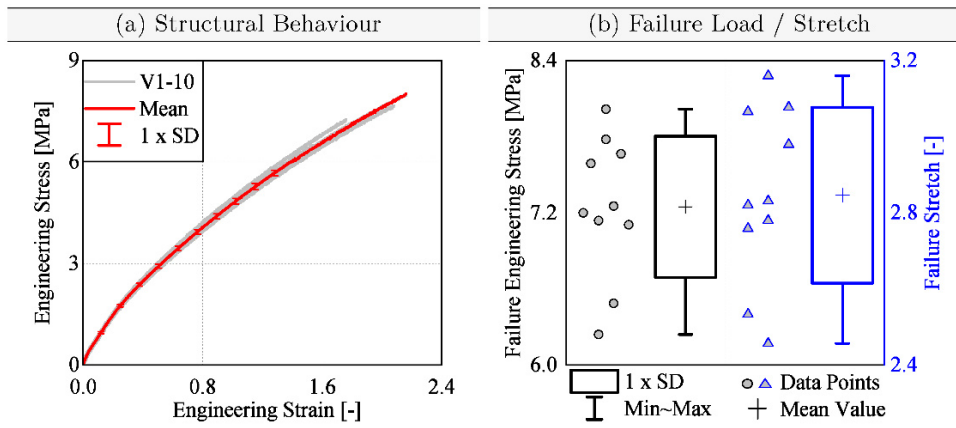


**Figure 4.3** Experimental test results for TSSA under uniaxial tensile loading: (a) engineering stress-strain behaviour (b) failure stresses and stretches

that spot-wise whitening only occurred locally on the surface of the dumbbell test sample, which became apparent during the experiment.

In addition to the description of the uniaxial tensile test and their results, the present deformation state of the experiment is briefly described below. Hence, for the subsequent determination of material parameters, the deformation gradient  $\mathbf{F}$  and the left Cauchy-Green stretch tensor  $\mathbf{b}$  of a compressible hyperelastic material are given in matrix notation by

$$\mathbf{F} = \begin{bmatrix} \lambda & 0 & 0 \\ 0 & \sqrt{\frac{J}{\lambda}} & 0 \\ 0 & 0 & \sqrt{\frac{J}{\lambda}} \end{bmatrix} \quad \text{and} \quad \mathbf{b} = \begin{bmatrix} \lambda^2 & 0 & 0 \\ 0 & \frac{J}{\lambda} & 0 \\ 0 & 0 & \frac{J}{\lambda} \end{bmatrix}, \quad (4.1)$$

where  $\lambda$  describes the stretch in tensile direction. Setting  $J = 1$ , the incompressibility assumption applies so that the volume does not change during any deformation.

### 4.2.2 Cyclic Uniaxial Tension

Special cyclic uniaxial tensile tests were performed to experimentally characterize the cyclic behaviour of TSSA and to observe the effect of stretch-induced whitening of the test sample. Therefore, miniature tensile tests were carried out under the light microscope in order to assign high-resolution images of the surface of each test sample and the evolution of the spot-wise whitening to the structural response of the tests. The test set-up therefore consists of a miniature tensile module of the company Kammrath & Weiss GmbH, which was installed in a light microscope

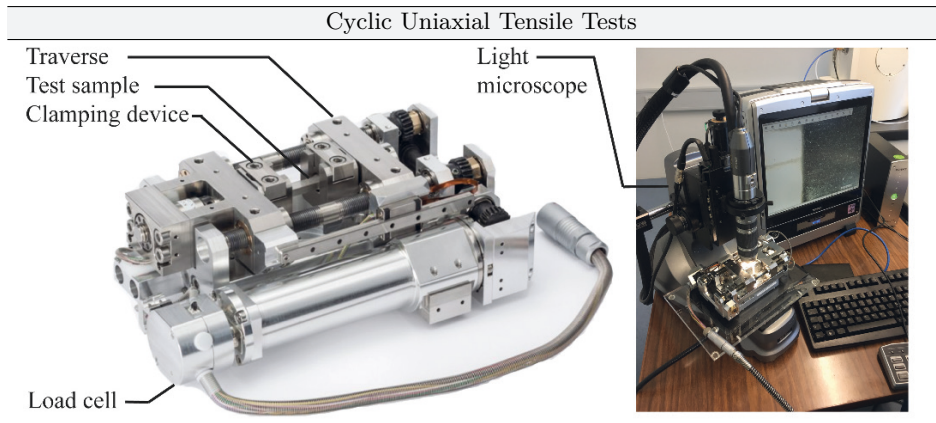


**Figure 4.4** Experimental set-up of the cyclic uniaxial tensile tests in the miniature tensile module installed in a light microscope © Kammerath & Weiss GmbH

(Keyence Model VHX-600 Digital Microscope). The corresponding test set-up is shown in Fig. 4.4. Muth (2018) presented the geometry and manufacturing of the test samples as well as the testing procedure in great detail in his work. Nevertheless, it should be mentioned at this point that, on the one hand, a special cutting die was produced in order to be able to produce miniature tensile specimens at all. The shape was chosen according to the available space within the miniature tensile testing machine. Basically, however, it can be said that the miniaturized test sample is only a scaling of the dumbbell tensile test specimen developed by F. Becker (2009), which has already been presented in Section 4.2.1. On the other hand, the base material was placed in a climatic chamber at 140°C and pressurized to obtain the typical material properties of TSSA. This procedure is the same as that proposed by Sitte et al. (2011).

The cyclic uniaxial tensile tests were performed in standard climate with a constant displacement rate of  $v_{CUT} = 3.75 \text{ mm/min}$ , which is the fastest displacement rate of the tensile module. The force was measured with a 5,000 N load cell. The specimen was clamped using a mechanical screw-clamping system, so that a slight slipping out of the specimen could be detected during testing. Since a local measurement of Hencky strains using DIC was not possible, the results of five test samples are shown in Fig. 4.5 in the form of global force-displacement curves. Additionally, the load history is presented for reasons of clarity.

The results show the Mullins effect clearly, in which a pronounced softening of the material can be seen for the unloading paths. Looking at the reloading paths, they follow the unloading paths up to the maximum stretch applied so far. Exceeding this point, the so-called virgin path is followed again, which corresponds

to the material response of a non-cyclic loaded uniaxial tensile test. The material behaviour to be seen corresponds to the classical definition of the Mullins effect (Diani et al., 2009) without exhibiting healing effects. Furthermore, it is noticeable that the structural responses scatter strongly, especially at small deformations, which is due to the slipping out of the specimens due to the mechanical clamping. Nevertheless, the structural responses show a typical behaviour under cyclic loading. Finally, it should be mentioned that the effect of whitening, especially in the virgin loading paths, could also be clearly seen in the cyclical experiments. During the unloading and reloading paths, the described whitening remains at approximately the same level until one again loads beyond the point of maximum achieved elongation. A detailed evaluation of the light microscope images and the analysis of the evolution of whitening for cyclic tensile tests is provided separately (see Section 4.4.2).

Finally it is to note that for the identification of material parameters, the deformation gradient  $\mathbf{F}$  and the left Cauchy-Green stretch tensor  $\mathbf{b}$  correspond to Eq. (4.1).

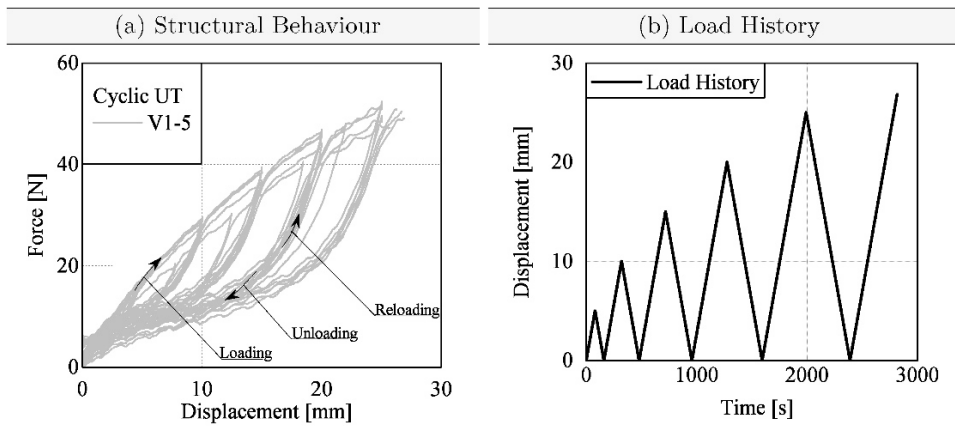


**Figure 4.5** Experimental test results for TSSA under cyclic uniaxial tensile loading: (a) force-displacement curves (b) load history

### 4.2.3 Uniaxial Compression

Uniaxial compression tests on rubber-like materials can be carried out by compressing a test sample with perfect slippage or by compressing bonded specimens (ISO 7743, 2011). Considering the first testing procedure, it is important to test lubricated specimens to guarantee a frictionless support, which is conterminous with a homogeneous stress and strain field within the specimen (Staudt et al., 2018; Drass et al., 2018e). In ISO 7743 (2011), the ratio between the height of the specimen

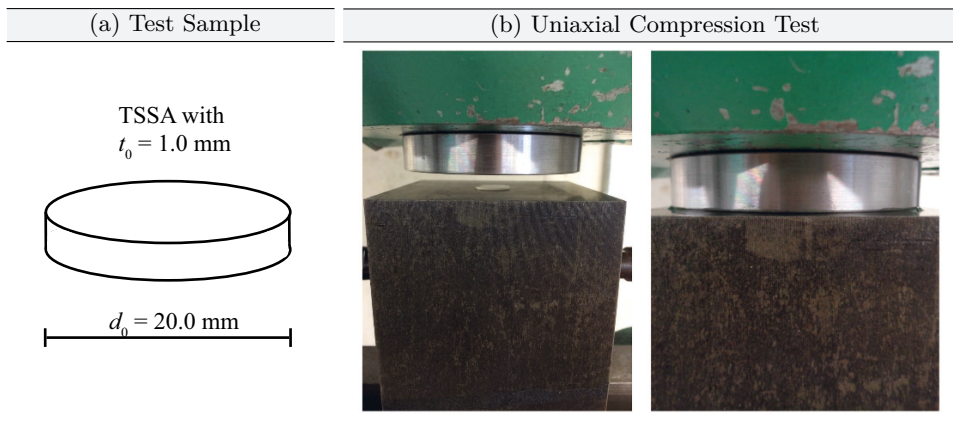


**Figure 4.6** (a) Geometry of uniaxial compression test specimens; (b) test set-up of uniaxial compression tests during testing

$t_0$  and the diameter  $d_0$  is proposed to be greater than or equal to one. Since the analysed material TSSA is produced with a fixed thickness of  $t_0 = 1.0 \text{ mm}$  and the diameter of the compression test specimen was chosen to  $d_0 = 20.0 \text{ mm}$  (see Fig. 4.6), the ratio can be determined by  $t_0/d_0 = 0.05$ .

Due to the large deviation of the aspect ratio, small frictional effects have a strong influence on the stress-strain behaviour of the compression tests. For this reason, both the test specimens and the compression plates were accurately lubricated with saBesto HHS 5000 produced by Würth and then tested with a constant testing speed of  $v_{UC} = \text{const.} = 0.174 \text{ mm/min}$  in a standard climate. The testing speed was calculated on the basis of an engineering approach proposed in Appendix D. The basic idea of this approach is to ensure equivalent strain energies between arbitrary and reference test specimens during testing. Since the reference experiment is the uniaxial tensile test, for all further tests the loading speed shall be calculated according to the approach given in Appendix D. Since the contact between lubrication and TSSA only existed during the test, no significant influence of lubrication on material properties could be observed. Assuming a frictionless support, the homogeneous stress state in the uniaxial compression test can be confirmed by visualizing the modified triaxiality. However, if friction effects occur, this homogeneous stress state changes according to the prevailing friction coefficient into a strongly non-homogeneous stress state (Appendix A). However, it should also be noted that an almost homogeneous stress state always prevails for small compressive strains, which however gains in multi-axiality with increasing deformation.

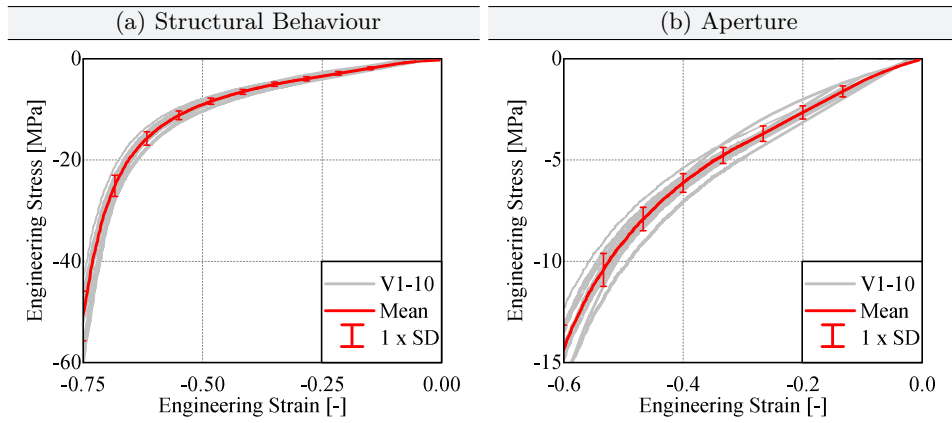


**Figure 4.7** Experimental test results for TSSA under uniaxial compression loading: (a) engineering stress strain behaviour (b) aperture of engineering stress-strain behaviour

The engineering stress-strain behaviour of ten test specimens is shown in Fig. 4.7. All tests were stopped reaching an engineering strain of  $\varepsilon = 0.75$ . The uniaxial compression tests were consciously aborted because the standard deviation was too large for strains greater than  $\varepsilon > 0.75$ . No failure in the material could be identified after the test specimens were unloaded, so that the representation of the failure stresses and stretches are omitted. Instead, an additional representation of the experimental results is shown in Fig. 4.7 b in order to analyse the material behaviour even at small strains. The experimental results show a typical behaviour for rubber-like materials under uniaxial compression load. Starting with a very soft structural response, a material stiffening follows due to strongly stretched molecular chains. During the tests, it was not possible to analyse the whitening effect due to the geometric boundary conditions of the test set-up. With regard to the identification of material parameters, the deformation gradient  $\mathbf{F}$  and the left Cauchy-Green stretch tensor  $\mathbf{b}$  corresponds to Eq. (4.1). Finally, it is worth mentioning that the uniaxial compression test leads to a biaxial deformation condition under the assumption of a completely friction-free support, since the specimen is compressed in the main direction, but it can expand freely in the lateral direction at the same time.

#### 4.2.4 Biaxial Tension

In order to experimentally investigate a biaxial deformation and stress state in polymeric materials, the so-called bulge test can be used, in which a thin polymer layer is inflated in the form of a balloon by means of air or water pressure (Sasso et al., 2008; Machado et al., 2012; Selvadurai and Shi, 2012). Comparing the bulge

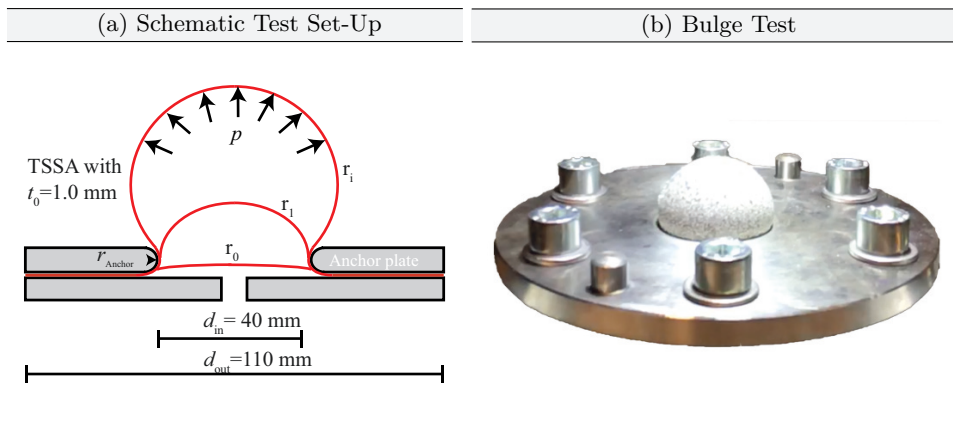


**Figure 4.8** (a) Schematic illustration of test set-up of bulge tests under different applied loads; (b) test set-up of BT tests during testing

test with conventional biaxial tests, where a cross-shaped sample is generally pulled simultaneously in x- and y-direction, the conventional test set-up is much simpler in the experimental application, whereas the bulge test offers the advantage of a uniform load with exclusion of edge influences, so that a purely biaxial stress and strain state can be ensured until failure occurs. A disadvantage of the bulge test is the use of the additional medium water. Some polymers, such as PVB, which is the most common interlayer for laminated safety glass, react very sensitive to temperature and moisture changes. The inflation test presented here is therefore not suitable for all polymeric materials. For a detailed comparison of the classical biaxial tests with the current bulge test, please refer to the publication of Drass et al. (2017b).

To determine the biaxial material behaviour of TSSA, corresponding inflation tests were carried out with a special test device consisting of a cylindrical anchor plate made of stainless steel, a foil made of TSSA and a cylindrical base plate. Since this special test method is not standardized, the dimensions of the test set-up were chosen on the basis of the works of Sasso et al. (2008), Machado et al. (2012) and Selvadurai and Shi (2012). The specific dimensions of the test set-up are shown schematically in Fig. 4.8. To avoid stress singularities induced by sharp edges, the anchor plate was smoothed with a radius of  $r_{\text{Anchor}} = 5 \text{ mm}$ . When the test specimen and the anchor plate were attached, the anchor plate was then fastened with six M 12 screws and afterwards loaded. All tests were carried out in a standard climate, which corresponds to an air temperature of  $23 \text{ }^{\circ}\text{C}$  and a relative humidity of 50 %.

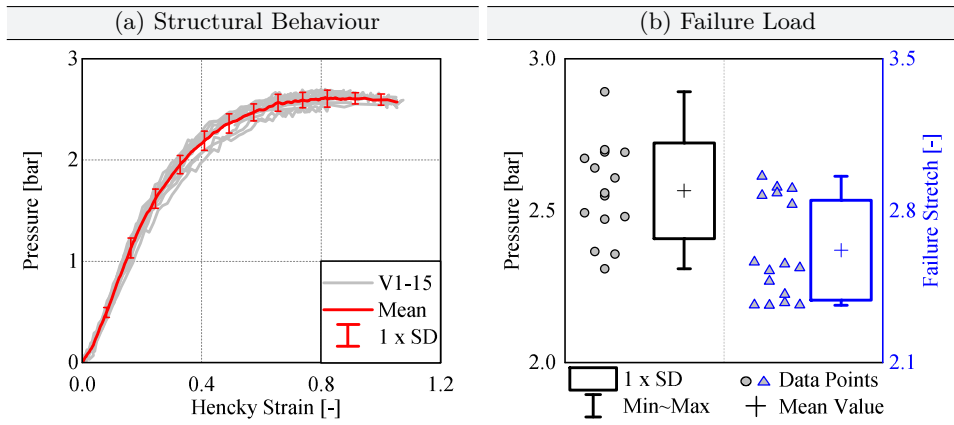


**Figure 4.9** Experimental test results for TSSA under biaxial tensile loading (a) pressure vs. Hencky strain (b) failure stresses and stretches

A total of 15 cured TSSA foils were produced in accordance to Section 4.1. Subsequently, circular test samples with an outer radius of  $d_{\text{out}}=110$  mm were cut out. Since the area to be inflated has a radius of only  $d_{\text{in}}=40$  mm, an optimal clamping between the anchor plates and test sample could be guaranteed. Before testing the material, a stochastically distributed speckle pattern was applied on the test samples to measure locally Hencky strains via DIC. A penny shape was not provided with the speckle pattern to qualitatively observe the effect of stress whitening during the experiment. Additionally, in order to obtain test results that can be evaluated until failure, the inner diameter was limited to  $d_{\text{in}}=40$  mm to ensure sufficient depth of field for the optical measurements. The thickness of the materials varied between  $t_0 = 1.00 - 1.08$  mm. This was measured with a caliper gauge at three different positions, bearing in mind that the thickness in the middle of the sample was never measured to avoid damage in the centre. In order to analyse a possible anisotropic material behaviour, all samples were placed in the same position in the test device. Subsequently, water pressure was applied to inflate TSSA, which is a common method for testing polymers under biaxial tension (Selvadurai and Shi, 2012). Since the experiments were conducted force (pressure) controlled, the engineering approach to determine the displacement rate from Appendix D is not applicable.

Regarding Fig. 4.9 a, the pressure in relation to the Hencky strain is shown for a constant pressure rate. In addition, Fig. 4.9 b shows the failure pressure and stretches for the tests carried out. The structural behaviour to be seen is typical for rubber-like materials under biaxial deformation. Since TSSA was only in contact with water for a short time, precisely when the load was applied, no negative

influence on the material behaviour could be determined. The scattering of the measurement curves is greater than in uniaxial tensile and compression tests, for example. This might be due to the more complex test set-up and measurement technology. During the tests, no anisotropy was observed, as the material inflated uniformly and the local strain measurement in the two main directions also provided approximately the same results. The spot-wise stress whitening, which intensifies with increasing deformation, was also seen according to the uniaxial tensile tests. The failure stresses could be evaluated for all 15 tests, whereas the measurement of the failure stretches could only be successfully carried out on six samples. This is due to the fact that during the test the speckle pattern has flaked off and thus a strain measurement until failure was no longer possible. Nevertheless, the failure stretches for six specimens are shown in x- and y-direction. As a result, a total of 12 measuring points can be evaluated

The deformation gradient  $\mathbf{F}$  and the left Cauchy-Green stretch tensor  $\mathbf{b}$  for biaxial loading conditions can be described through

$$\mathbf{F} = \begin{bmatrix} \lambda & 0 & 0 \\ 0 & \lambda & 0 \\ 0 & 0 & \frac{J}{\lambda^2} \end{bmatrix} \quad \text{and} \quad \mathbf{b} = \begin{bmatrix} \lambda^2 & 0 & 0 \\ 0 & \lambda^2 & 0 \\ 0 & 0 & \frac{J^2}{\lambda^4} \end{bmatrix}. \quad (4.2)$$

The assumption of an incompressible material is pertained by setting the relative volume constant to  $J = 1$ . To determine material parameters, the applied pressure  $p$  must be recalculated in engineering or Cauchy stresses. Following Sasso et al. (2008), the relation between the Cauchy stress and the applied pressure is given by

$$\sigma_1 = \sigma_2 = \frac{pr_i}{2t} = \frac{pr_i}{2t_0\lambda_3}, \quad (4.3)$$

where  $r_i$  characterizes the measured radii during the inflation process. Since the initial thickness  $t_0$  is much smaller than the lateral dimensions of the test sample, the stresses in thickness direction can be set to  $\sigma_3 \approx 0$ . Keeping in mind that  $\lambda_3 = 1/\lambda^2$ , Eq.(4.3) can be re-expressed by

$$\sigma_1 = \sigma_2 = \frac{pr_i\lambda^2}{2t_0}. \quad (4.4)$$

It follows that the above assumptions lead to an almost perfect biaxial stress state, which can be confirmed by visualising the modified triaxiality according to Appendix A.

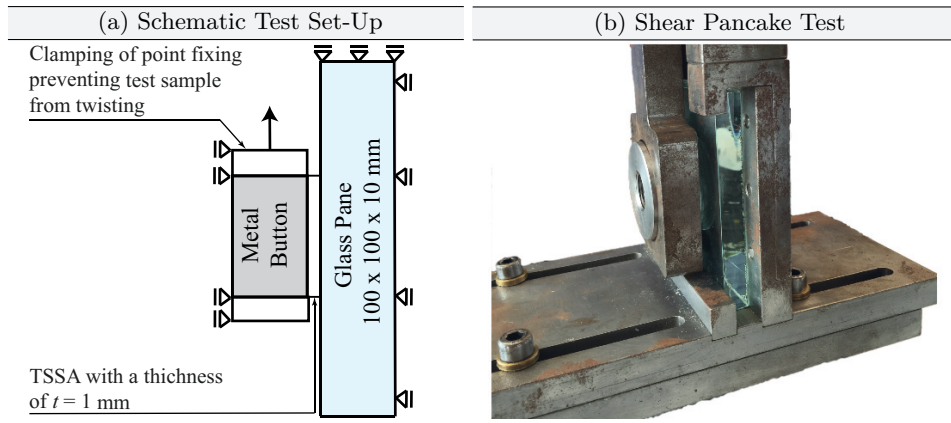


**Figure 4.10** (a) Schematic illustration of geometry of shear pancake test specimens, in which the rotation of the test specimen is hindered by a precise fitting connection; (b) test set-up of shear pancake tests during testing

#### 4.2.5 Shear-Pancake

Testing rubber-like materials under shear is a common method to describe the material behaviour, not least because the initial shear modulus is a material parameter of great importance in many hyperelastic constitutive laws (Treloar, 1975; Gent, 1996; Kaliske and Heinrich, 1999; Lopez-Pamies, 2010).

In general, shear tests for polymers are standardized in ASTM D732 - 10 (2010), ISO 1827 (2011) and BS903-A14 (1992). In ASTM D732 - 10 (2010), it is suggested that a specimen be clamped and loaded with a punch located between two metal fixtures. With a male punch a force is applied, which results in a shear loading in the specimen. The tests result is a scalar value of the shear strength disregarding the structural response of the material. Considering ISO 1827 (2011) and BS903-A14 (1992), shear tests are conducted using a quadruple block test sample. This test set-up is also known as the non-homogeneous shear test according to Van den Bogert and De Borst (1994).

Due to the limited thickness of TSSA, a test sample deviating from the standard-compliant test specimens was analysed. A so-called shear pancake, which consists of a glass pane bonded to a metal button or point fixing with a thin layer of TSSA, was tested under simple shear (see Fig. 4.10). The adhesive joint has a diameter of  $d_0 = 50.0 \text{ mm}$  and a thickness of  $t_0 = 1.0 \text{ mm}$ . Since the simple shear deformation condition is not easy to achieve when testing rubber-like materials under large deformations, the proposed test device has some special features. Regarding Fig. 4.10 more precisely, it looks like a standard shear application, similar to the proposed testing device of Santarsiero et al. (2016). Both testing devices are guided

in line in the z-direction with the result that rotations are minimized. A special feature of the present testing device is that the metal button can undergo deformations in out-of-plane direction with the result that compression strains due to the so-called Poynting-effect are minimized (see Fig. 4.10 a). The Poynting effect describes developing axial stresses which occur perpendicular to two sheared surfaces in the case of large deformations. Therefore, simple shear can be maintained for large deformations, which is, in fact, not the case, if the lateral deformation is constrained. At this point, the author refers to the works of Poynting (1909); Gent et al. (2007); Horgan and Murphy (2010); Mihai and Goriely (2011), where the above-mentioned Poynting-effect is discussed more in detail. In addition, the selected test set-up prevents the test piece from twisting due to a precise fitting connection, which also maintains the deformation state of a simple shear test. The test matrix consists of five test samples with a calculated testing speed based on the engineering approach proposed in Appendix D of vSPC = 0.21 mm/min. To analyse the material response, optical measurements were conducted accordingly to the proposed method of Section 4.2.1. Based on the chosen testing speed, the strain energies for the uniaxial tensile test and shear pancake test correspond to each other.

The engineering values for shear stress  $\tau$  were calculated by dividing the measured force by the cross-sectional area of the test sample. The amount of shear  $\gamma$  can be easily calculated by dividing the longitudinal deformation by the thickness of the adhesive. Shear test results for TSSA are shown in Fig. 4.11. In accordance with the experimental investigations described above, the structural behaviour as well as the individual failure loads and stretches are presented. The shear behaviour is described by an almost linear relationship between the amount of shear and shear stress, which corresponds to the results of Hagl (2016) and Santarsiero et al. (2016).

Regarding the deformation gradient  $\mathbf{F}$  and the left Cauchy-Green tensor  $\mathbf{b}$ , the deformation measures for simple shear can be written as

$$\mathbf{F} = \begin{bmatrix} 1 & \gamma & 0 \\ 0 & 1 & 0 \\ 0 & 0 & 1 \end{bmatrix} \quad \text{and} \quad \mathbf{b} = \begin{bmatrix} 1 & \gamma & 0 \\ \gamma & 1 + \gamma^2 & 0 \\ 0 & 0 & 1 \end{bmatrix}. \quad (4.5)$$

Following Moreira and Nunes (2013) and Nunes and Moreira (2013), simple shear can be expressed in terms of principal stretches  $\lambda_i$  utilizing the amount of shear  $\gamma$ .

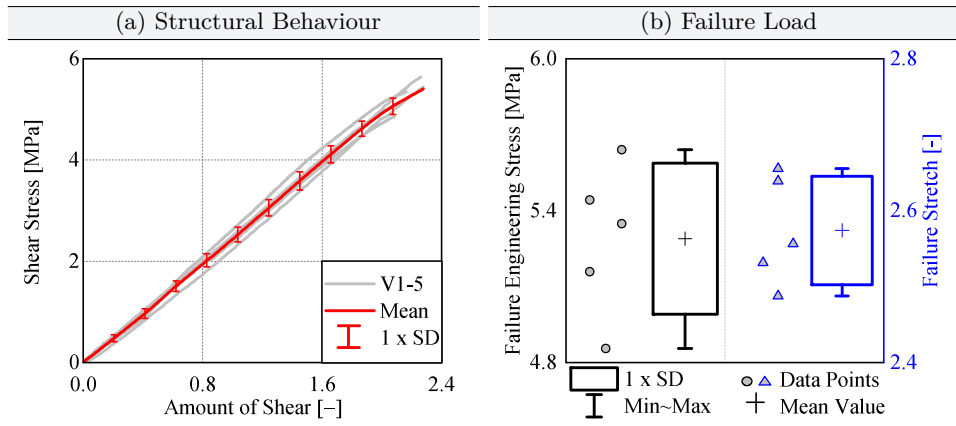


**Figure 4.11** Experimental test results for TSSA under simple shear loading (a) shear stress vs. amount of shear; (b) failure stresses and stretches

Determining the eigenvalues of  $\mathbf{b}$ , which are the squares of the principal stretches, the deformation gradient can be rewritten by

$$\mathbf{F} = \begin{bmatrix} \sqrt{1 + \frac{\gamma^2}{2}} + \gamma\sqrt{1 + \frac{\gamma^2}{4}} & 0 & 0 \\ 0 & \sqrt{1 + \frac{\gamma^2}{2}} - \gamma\sqrt{1 + \frac{\gamma^2}{4}} & 0 \\ 0 & 0 & 1 \end{bmatrix}, \quad (4.6)$$

which is advantageous for identifying hyperelastic material parameters under simple shear loading. Therefore, the principal stretches of the material can be determined by re-formulating the simple shear deformation state in main directions.

### 4.3 Inhomogeneous Experimental Tests

Experimental tests are inhomogeneous if the applied deformation state leads to non-homogeneous stresses and strain in the material. The evaluation of the triaxiality of inhomogeneous experimental tests therefore leads to different colour ranges (see Appendix A). This is an indicator that on the one hand there is no analytical relationship to describe uniquely the stress-strain behaviour and that material parameters can only be determined using inverse numerical methods (Drass et al., 2018f). Furthermore, inhomogeneous experimental tests serve to validate material models, since full-scale numerical simulations of the test set-up must accurately reproduce the structural behaviour.

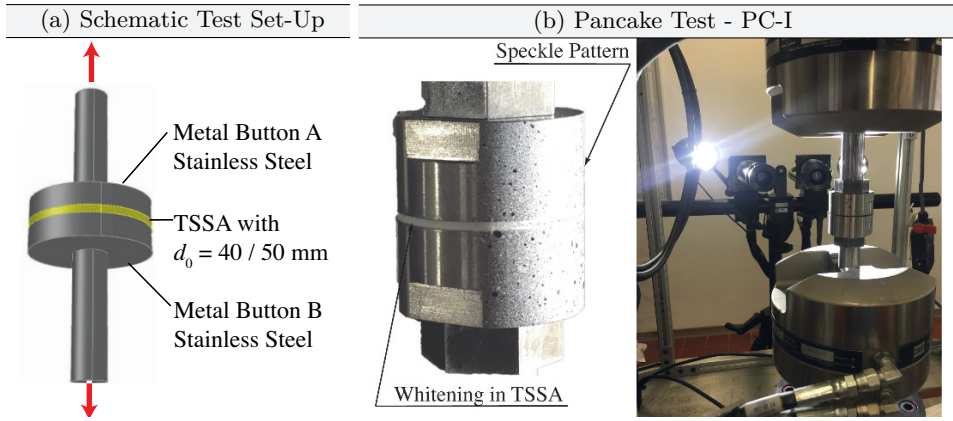


**Figure 4.12** (a) Geometry of pancake tension test PC-I specimens; (b) test set-up of pancake tension tests (PC-I) during testing

### 4.3.1 Pancake Tension Tension

The so-called pancake tension test was first conducted by Busse (1938), Yerzley (1939) and Gent and Lindley (1959), where flat rubber cylinders were tested under tension. The analysed materials were bonded between two metal plates and afterwards axially loaded, which led to a disability of lateral strains. Hence, high hydrostatic stresses occurred in the centre of the test sample. Due to high hydrostatic stresses, all stress-strain diagrams exhibit a breaking point, at which cavities start to grow excessively. Since the performed experiments did not provide the ability to study cavitation during testing, all specimens were cut open after testing to see cavities within the rubber matrix.

In order to experimentally investigate TSSA under an almost triaxial deformation condition, classical pancake tests were carried out according to the tests of Gent and Lindley (1959), in which two steel cylinders were bonded with TSSA and then axially pulled. Since this test set-up corresponds to the classic pancake tension test, it is denoted as PC-I. In order to generate a large experimental data base, the pancake tests were tested with a diameter of  $d_0 = 40.0 / 50.0$  mm. The pancake tension test specimens were produced in an autoclave according to the specifications of Sitte et al. (2011). The schematic test set-up and a demonstration of the experiment is shown in Fig. 4.12 a. In the test series of the classical pancake tension tests, ten specimens with a diameter of  $d_0 = 40.0$  mm and six specimens with a diameter of  $d_0 = 50.0$  mm were tested in a standard climate under axial loading. The local deformations of the adhesive were recorded utilizing the DIC. For this purpose, the specimen was first coated with a white primer in the area of the measuring field and then a black speckle pattern was applied to carry out

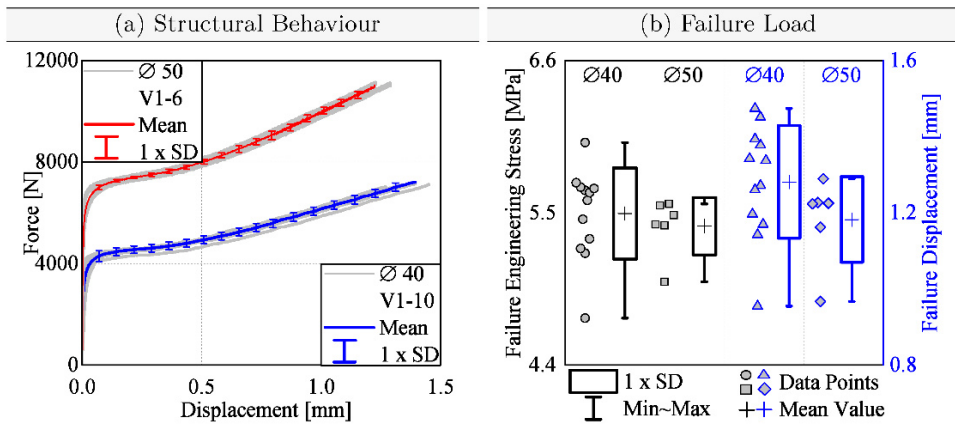


**Figure 4.13** Experimental pancake tension test results for TSSA (a) force vs. local displacement; (b) failure stresses and displacements

the local strain measurement (see Fig. 4.12 b). In contrast to the uniaxial tensile tests (see section 4.2.1), the pancake tension tests show only small deformations in the axial direction, so that these must be recorded very precisely by means of optical measuring methods in order to be able to correctly determine the stiffness behaviour of the material. This is also the reason why the speckle pattern for these tests could be applied by spraying. The displacement rate was constantly set to  $v_{PC} = 0.1 \text{ mm/min}$  for all performed pancake tension tests to ensure quasi-static loading conditions. Since this is a non-homogeneous test in which very divergent stress states occur in the material, the approach for calculating the displacement rate according to Appendix D is not applicable. A representation of the different stress states is shown in Appendix A under visualization of the modified triaxiality.

The obtained experimental data were prepared in such a way that the force signal is compared to the local axial deformation for each tested diameter (see Fig. 4.13 a). In addition, the engineering failure stresses and the corresponding axial deformations are shown in Fig. 4.13 b. The engineering stress was determined by dividing the failure load by the pulled area. As was to be assumed, more load can be transferred when the adhesive joint has a larger diameter. Nonetheless, the structural behaviour of both experiments is very similar. The course of the curves is typical for rubber-like material in the pancake tension test. Starting with an enormously high initial stiffness, the cavitation effect then begins, so that a strong stress softening takes place. The initially high stiffness can be explained by the fact that in pancake tension testing the bulk modulus is predominantly active, whereas in isochoric deformations the initial shear modulus represents the intrinsic

material stiffness. Since the bulk modulus of rubber-like materials is larger than the shear modulus by orders of magnitude, it is clear that a high initial stiffness is present, which is extremely reduced by the onset of cavitation. By softening the material in the form of excessively void growth, the stresses are transferred to the peripheral areas so that a further increase in load is possible. If the limit value of extensibility of the material in the border area is reached, crack growth from the outside to the inside begins, whereby the material completely fails. Looking at the failure stresses, it is noticeable that they are almost independent of the investigated adhesive joint diameter. This also applies to the local axial deformation that leads to the failure of the adhesive joint. The experiments described were also carried out at an ambient temperature of 80°C, whereby a detailed description is given in Appendix B.

Furthermore, the effect of the whitening in the classical pancake tension test or the silicone adhesive respectively could also be observed qualitatively. As can be seen from Fig. 4.12 b, the initially transparent adhesive joint is coloured white due to the axial load, which is clearly visible at the edge of the silicone. It should also be noted that the white colouring in the pancake tension test does not correspond to the white colouring of the uniaxial tensile tests (cf. Section 4.2.1). In the pancake tension test, a much denser uniform whitening occurs over the entire cross-sectional thickness of the silicone, which is presumably due to the hydrostatic stress state in the specimen (Drass et al., 2019c; Drass et al., 2018b; Santarsiero, 2015). Whether this effect starts from the inside of the sample and moves outwards to the edge of it must be clarified by additional tests. Hence, to avoid the drawback of the classical pancake tension tests that the effect of the whitening cannot be analysed during the loading, an unconventional testing device was developed to study the cavitation effect in structural silicones. Since TSSA has a maximum thickness of 1 mm, it is not possible to cut open the specimens after testing to see cavities as it was done by Gent and Lindley (1959). The second reason why the development of a special test device is necessary to observe cavitation during the test is that it is unclear whether cavitation is a reversible or irreversible phenomenon for rubbery materials. In order to answer this question, it is therefore crucial to qualitatively observe the cavitation effect during the execution of the test.

In Fig. 4.14 a,b, the test set-up for an unconventional testing device of the pancake tension test, PC-II, is illustrated. The design of the testing device was inspired by the work of Cristiano et al. (2010), who analysed transparent adhesives, which were bonded between a glass plate and glass lens and afterwards tensioned. Since this application can be expensive due to the bonding of glass lenses, an alternative is presented, which also allows a quantification of the cavitation effect during the test. In order to do this, PC-II was provided with an opening on the lower support of the test sample, which makes it possible to visually analyse

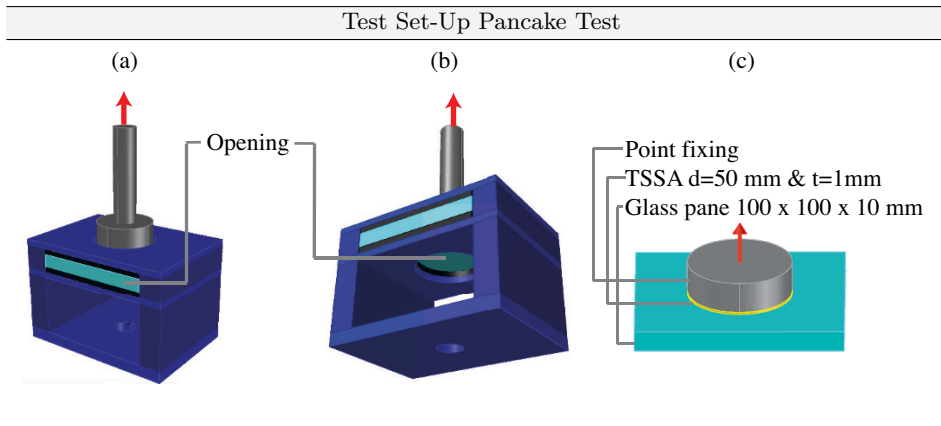


**Figure 4.14** Illustration of test set-ups for PC tests: (a) / (b) PC-II test set-up to visualize qualitatively cavitation during experimental testing Hippe (2015) and (c) test specimens for PC-II tests

the behaviour of the adhesive joint during the test. Hence, cavitation can be observed by filming through the opening. Since the transparent structural silicone is bonded to transparent glass, no special issues occurred to determine qualitatively the cavitation effect within the matrix of the structural silicone. The test sample for PC-II, which consists of a metal button, a glass pane and structural silicone, is shown in the Fig 4.14 c. The diameter was set constant to  $d_0 = 50.0$  mm within the series PC-II.

Seven test samples of the PC-II series were experimentally analysed at standard climate conditions. In general, the same test conditions were applied as for the classical pancake tension tests of the PC-I series. In Fig. 4.15 a, the force-displacement curves of the unconventional pancake tension tests are illustrated. Looking at the structural behaviour of the PC-II experiments, one notices the greater scatter of the measurement curves compared to the measurement results of the PC-I series. The scattering of the test curves can be traced back to the compliance of the test set-up. Nevertheless, the results obtained correspond to the results of classical rigid pancake tension test. Additionally, absolute values for the engineering stresses are shown in Fig. 4.15 a, which can be attributed to the pictures presented in Fig. 4.15 b, where whitening effects within the structural silicone can be observed qualitatively. The engineering stresses were calculated by dividing the force signal at a specific deformation by the pulled area of the adhesive. The images correspond to different load steps taken by filming through the opening of the PC-II test device. The pictures therefore show the PC-II specimen, in which a view is taken through the glass and transparent silicone onto the metal button. It is obvious that with increasing deformation, the initially transparent silicone undergoes a dense white

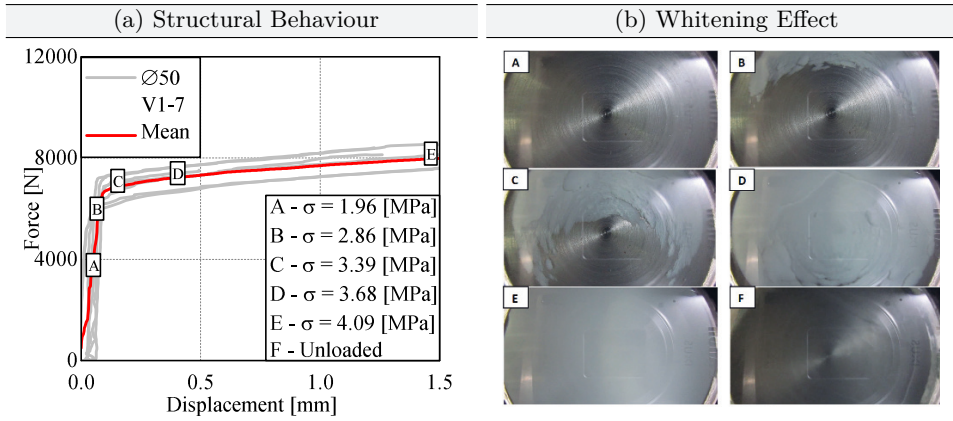


**Figure 4.15** Experimental pancake tension test PC-I results for TSSA (a) engineering stress-strain behaviour; (b) images of whitening effect during testing

colouring. In this context, stress whitening is interpreted as cavitation or nucleation of vacuoles at the nano-scale, whereby an infinite number of nano-cavities begin to grow over the entire thickness of the adhesive film. One test sample was unloaded shortly before failure occurred. The whitening has completely decreased, which is in line with the findings of Sitte et al. (2011). Based on this result, it can be postulated that the whitening effect or cavitation is a reversible effect for TSSA. This hypothesis is supported by the results of the following cyclic pancake tension tests according to Section 4.3.2. A detailed analysis and discussion of the whitening effect in silicones, not only for the pancake tension test but also for cyclic uniaxial tensile tests, is not part of this section but will be presented separately in Section 4.4.2.

A very important observation in the experimental investigation of TSSA in the pancake tension experiment is the type of cavities that arise in the material with increasing deformation. In contrast to the experimental results of Gent and Lindley (1959) and Lindsey (1967), where a finite number of macroscopic cavities were identified, the cavitation effect occurs much denser on a smaller scale in TSSA. This also leads to a new finding, namely that the initiation of cavitation does not only depend on the initial shear modulus as postulated by Gent and Lindley (1959); Ball (1982); Hou and Abeyaratne (1992); Lopez-Pamies et al. (2011b), but also on the porosity of the material. As will be shown later, TSSA exhibits a finite porosity measured at the nano-level. This means that the bifurcation load for the onset of cavitation is not at a critical load of  $p_{cr} = 2.5 \mu$ , which is the prevailing opinion, but significantly lower. Keeping in mind that the shear modulus of TSSA is approximately  $\mu = 2.66$  MPa (Drass et al., 2018b) and assuming a homogeneous

hydrostatic stress distribution, a simple manual calculation results in a failure load of  $p_{cr} \approx 1.5 \mu$ . This reference value is later verified by numerical simulations, but it should be noted at this point that the numerical failure load will be somewhat lower, since no homogeneous hydrostatic stress state prevails in the pancake tension test.

### 4.3.2 Cyclic Pancake Tension Test

According to the pancake tension tests described in Section 4.3.1, additional cyclic tests were performed to explain whether the cavitation effect is reversible and to study the Mullins effect in heavily constrained tensile tests. To characterize the material softening due to the Mullins effect, it is necessary to approach defined load levels with the testing machine and then unload it to a zero force level again. Since it was not possible to use the local displacement signal of the adhesive joint, which was measured optically, as a control signal for the testing machine, the cyclic pancake tension tests were performed force-controlled. This was necessary because although the global displacement of the traverse of the testing machine could be regulated to zero, compressive stresses could occur in the material due to slightly viscous effects or a permanent set of strains of the polymer. In order to make the axially displacement-controlled and cyclically force-controlled pancake tension tests comparable, the force-rate was set to  $v_{CPC} = 9.0 \text{ N/s}$ , which corresponds approximately to the displacement-rate of the classical pancake tension tests described in Section 4.3.1. Preliminary investigations showed no differences in the structural response of displacement- or force-controlled experimental tests. Accordingly, the proposed variant of the test procedure is legitimate. It should also be noted that all tests were carried out at room temperature to ensure comparability with the non-cyclical experimental studies described above.

Seven cyclic pancake tension tests were tested in a standard climate. As already mentioned for the tests described before, standard climate means a room temperature of 23°C and a relative humidity of 50 %. All test specimens were manufactured in an autoclave accordingly to the description in Section 4.1. The test set-up and the test samples are similar to the PC-I test series according to Section 4.3.1, in which two stainless steel buttons were bonded with TSSA and pulled axially. The first load cycle ended after reaching a force of 6,000 N and was then unloaded to a zero force level. With each load cycle, the load level was increased by 1,000 N until the material was completely damaged. For reasons of comparability, the cyclic heavily constrained pancake tension tests were also performed at room temperature.

The structural behaviour of the cyclic pancake tension tests is shown in Fig. 4.16. In addition, the load history is presented for reasons of clarity. The cyclic pancake tension tests performed show a very complex structural behaviour, which can be

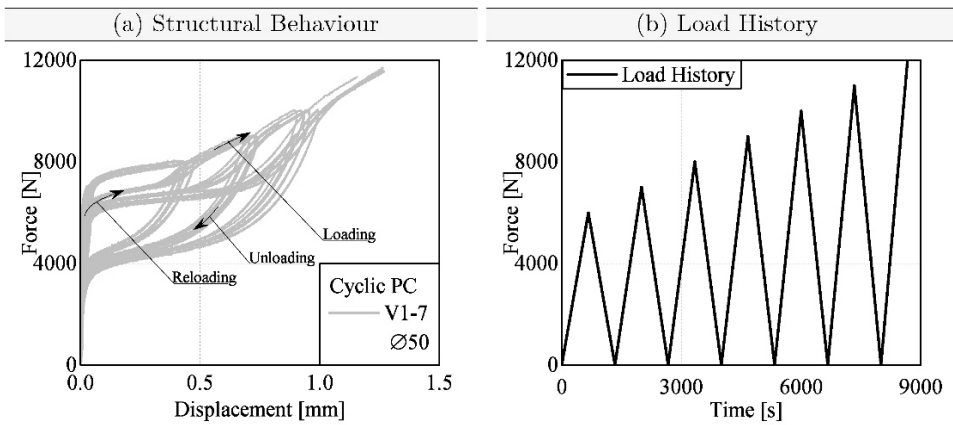


**Figure 4.16** Experimental results of cyclic pancake tension tests for TSSA (a) force vs. local displacement; (b) load history

divided into three essential parts. The first part of the structural response describes the loading path, also called the virgin path. It corresponds to the load path of the conventional pancake tension tests under uniaxial load and has the highest structural response to be achieved. The bifurcation load is approximately 7,000 N. The second part describes the unloading path, which exhibits a substantially reduced stiffness compared to the virgin loading path. This behaviour is characteristic for the Mullins effect, which is still subject of current research, since the processes of stress softening are not conclusively clarified. General theories describing the Mullins effect deal with the bond breakage of polymer chains, molecules slipping, filler rupture, disentanglement and double-layer models (Diani et al., 2009). The origin of the Mullins effect for TSSA is particularly related to filler rupture and bond breakage, which will be discussed later. To return to the test results, it is worth mentioning that all unloading paths converge to a force level of about 3,600 N at almost zero axial deformation. A very unusual behaviour occurs during reloading, which describes the third part of the classification of the structural response of cyclic pancake tension tests. In contrast to the Mullins effect, the unloading and reloading paths are not identical. It is clearly visible that a recovery or healing effect occurs during the reloading process, whereby the reloading curve is clearly above the unloading curve and below the virgin loading curve.

Experimental investigations on recovery or healing effects of polymers under cyclic loading hardly exist (M. A. Johnson and Beatty, 1993); especially in isochoric tests it is assumed that hysteresis form due to visco-elastic and / or visco-plastic material properties (Miehe and Keck, 2000; Machado et al., 2010). Their investigations show that the reloading curve is in general only slightly above the unloading

curve, so that only slight hysteresis are formed in isochoric experiments. Accordingly to D'Ambrosio et al. (2008), these hysteresis represents a supposed healing or recovery effect in the polymer with the result that the polymer network including cross-links gains stiffness during unloading. The healing effect is understood as the possibility of re-cross-linking of polymer chains and the associated strength recovery. Plagge and Klüppel (2017) assume that polymer filler structures gradually dissolve at a certain stress level and immediately bind again at zero loading. This creates an additional force component as the load increases, which slightly increases the stiffness. On the unloading path it reduces the stiffness and generates a more or less pronounced hysteresis (see Fig. 3.3 c). The author is only aware of one source that investigates the healing effect of cyclically loaded pancake tension tests. Solely Cantournet et al. (2014) investigates such experiments and postulates that the volume change is triaxiality dependent and can be reversible or non-reversible depending on the interaction between damage, stress softening and crystallization. Since the statements on the healing effect of elastomers under cyclic loading are generally very vague, it was necessary to examine TSSA also cyclically in the constrained tensile test. Looking at the structural behaviour, it can be assumed that the recovery or healing effect is due to elastic pore growth and shrinkage, which in combination with the Mullins effect and possible bond breakage and filler rupture leads to the present result. The cavitation effect must be reversible so that the reloading curve is above the unloading curve. However, since the reloading path remains below the virgin curves, an additional Mullins damage must occur. As it has already been shown in the cyclic uniaxial tensile tests, no remarkable hysteresis develops during testing. Hence, the phenomena mentioned must occur particularly in triaxially stressed areas, which are all but the peripheral areas in the pancake tension test sample. The hypothesis of elastic void growth in the loading paths (virgin loading and reloading) can be further consolidated, since the initial stiffness always corresponds to the virgin stiffness even after several load cycles. Furthermore, it should be noted that healing starts abruptly without the use of temperature storage or the use of relaxation by incorporating holding times in the test sequence. Interestingly, all reloading curves result in a uniform force level of 6,000 N, which, however, is below the virgin bifurcation load. However, following the reloading path and reaching the previously reached maximum elongation corresponding to the virgin curve, both curves are again identical.

## 4.4 Micro-Structure Analyses

### 4.4.1 Studies on Porosity

In order to describe the experimental behaviour of TSSA mechanically in a proper way, it is essential to investigate the microstructure of the material in order to physically explain the effects shown by Mullins (1948) but also the cavitation and whitening effect.

The micro-structure of TSSA consists of polydimethylsiloxanes (PDMS) and a high amount of nano-silica particles (ca. 20-30 %). The nano-silica particles form aggregates, where one nano-silica particle has a diameter of approximately 1 nm (Drass et al., 2018b). At the boundaries of these aggregates a multitude of nano-cavities can develop due to the manufacturing process (Ansarifar and Lim, 2006; Heyden et al., 2015), which may lead to an increased or finite porosity. In addition, the initially constant porosity can increase during deformation, when vacuoles arise during stretching at the boundaries of the nano-silica surfaces due to weak or non-existing filler-matrix interaction (Valentin et al., 2010).

To prove the assumption of finite void fraction and to get more insight into the micro-structure of TSSA, transmission electron microscope (TEM) images were taken. Therefore, a small piece of TSSA, after being processed according to Section 4.1, was placed in liquid nitrogen and then cut into pieces. To obtain very thin slices of TSSA with a thickness of about  $t \approx 70$  nm, a cryo-microtome was utilized. To improve the quality of the images or not to damage the material structure during cutting, the sample was tempered to a constant temperature of  $T = -100$  °C. After consolidation of the material, the specimens were cut into thin pieces and placed in the TEM. A selection of the TEM images are presented in Fig. 4.17 a at different positions. A multitude of nano-cavities with a diameter of  $d_v \approx 30$  nm up to  $d_v \approx 100$  nm could be determined. The contrast in the TEM images is referable to the high amount of nano-silica particles, the rubber matrix itself and inherent voids. These voids can be identified as dark spots in the TEM images.

Regarding Fig. 4.17, it is not clear whether the voids are free volume defects or nano-cavities at the boundaries of aggregates. However, based on the available images and an initial estimate, the finite void fraction for TSSA can be indicated due to the highly porous microstructure. This is qualitatively justified by the high amount of black spots in Fig. 4.17 a, but must be quantitatively substantiated in the following in the form of a statement regarding porosity or void fraction  $f_0$ .

To verify the assumption of finite porosity, the discrete digitized images can be divided into a finite number of pixels, each of which is assigned a certain grey value  $g \in [0, 1]$ . The grey values were post-processed to link them with material properties such as density or geometric properties such as pores. Since the pore content is of particular interest for the present thesis and single voids appear as

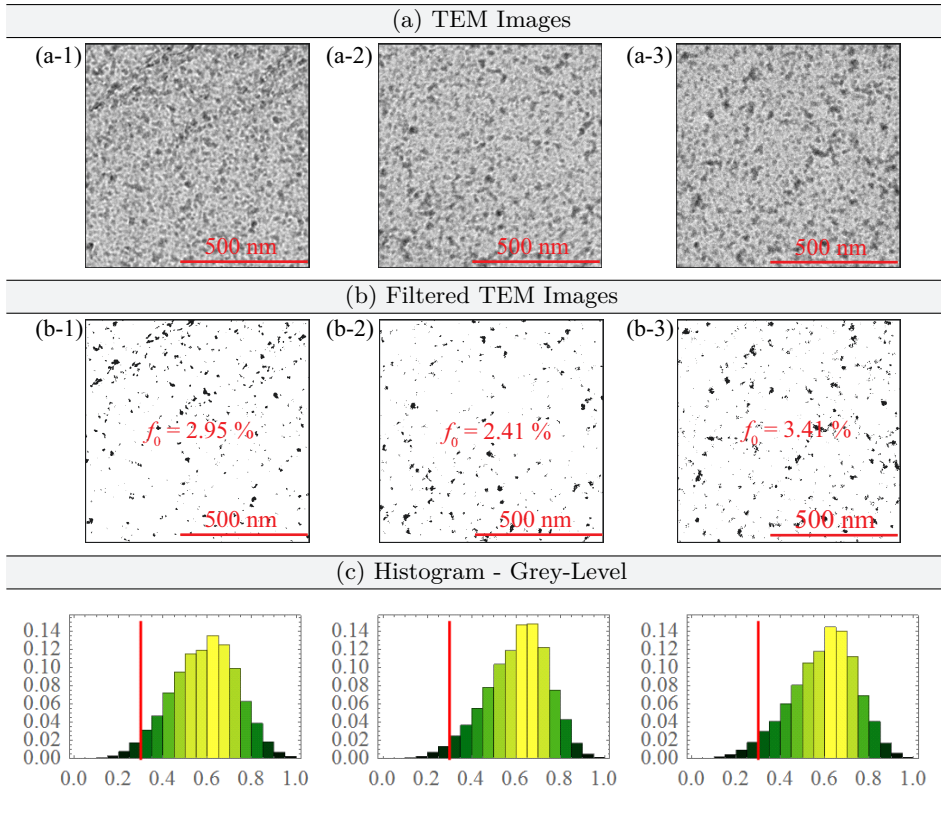


**Figure 4.17** (a) TEM images of TSSA at different positions; (b) filtered TEM images with specification of the void fraction; (c) grey-level histogram of the TEM images with indication of the critical grey-scale that still is part of a pore

black spots in the TEM images, a so-called level-cut or binary filtering was used to make individual pores visible. The binary filter converts all pixels below a critical grey-scale  $c$  into black pixels and above the border into white ones. Mathematically, the operation is described by

$$g'(\vec{\mathbf{X}}) = C(g) = \begin{cases} 0 & \text{if } g' \leq c \\ 1 & \text{if } g' > c \end{cases}, \quad (4.7)$$

where the binary filter  $C$  is applied on each pixel and its grey-scale. Therefore  $C$  operates on the raw grey-scale distribution  $g(\vec{\mathbf{X}})$ , so  $g'$  is also a function of the position vector  $\vec{\mathbf{X}}$ . In this context,  $\vec{\mathbf{X}}$  describes the positions vector of each pixel in the reference configuration according to the description in continuum mechanics.

The choice of the parameter  $c$  is decisive for the calculation of the porosity. Almost any pore content can be adjusted by arbitrary selection. An objective criterion for the selection of the parameter does not exist, but in this case it was tried to reconstruct the visible pores from the unprocessed TEM images also in the filtered images without adding or removing them virtually. The results of the binary filtered images of three TEM images are shown in Fig. 4.17 b. Furthermore, the porosity is indicated for each processed image. With the chosen method, individual pores at the nano-level could be isolated in good approximation, which is demonstrated by a direct comparison between unfiltered and filtered images. For reasons of completeness, Fig. 4.17 c also shows the grey-scale histogram corresponding to the TEM images. In addition, the selected critical grey level of  $c = 0.3$  is indicated.

By calculating the mean value of three processed TEM images, a porosity of  $f_0 = 2.92\%$  is obtained for the material TSSA. The described procedure was also applied to five additional TEM images at an even higher resolution. The results are presented in Appendix C. Here, too, a similar pore content is obtained.

#### 4.4.2 Stress Whitening Effect

Stress whitening is a frequent effect in polymeric materials where an increase in brightness or an increased opacity of the material can be observed under mechanical loading. The whitening effect is a phenomenon that occurs primarily in thermoplastics and not in elastomers (Bakshi et al., 1988). The strong elongation of thermoplastics leads to so-called crazes, i.e. micro-cracks in the polymer matrix, which result in a brightening of the material. Therefore it is also stated that crazing is the source of whitening in polymers (Kambour, 1973). An approach for the assessment of stress whitening effects is given by Gunel and Basaran (2010), who outlined that due to mechanical deformation transparent or translucent plastics exhibit an increase in opacity and a white appearance, whereas in opaque materials a milky-white colour can be detected.

Nevertheless, the effect of whitening can also become evident in rubber-like materials through so-called strain crystallization (Santarsiero, 2015). A definition of strain crystallization is given by Chenal et al. (2007) and Ozbas et al. (2012), in which polymer chains align in accordance to the direction of the applied load. Starting from an initially amorphous network of polymer chains, this effect occurs at high strains with the result that rubbers become self-reinforcing due to micro-crystallization at the molecular level (Toki et al., 2000). Another reason for the stress whitening can be insufficient strength and stiffness of the constituents and poor interfacial adhesion (matrix-filler interaction), as mentioned by Xiang et al. (2001) and Valentin et al. (2010). The detachment and failure of particles from particle-filled polymers can result in so-called vacuoles. With increasing deformation its volume increases, which leads to a dense white colouring (Drass et

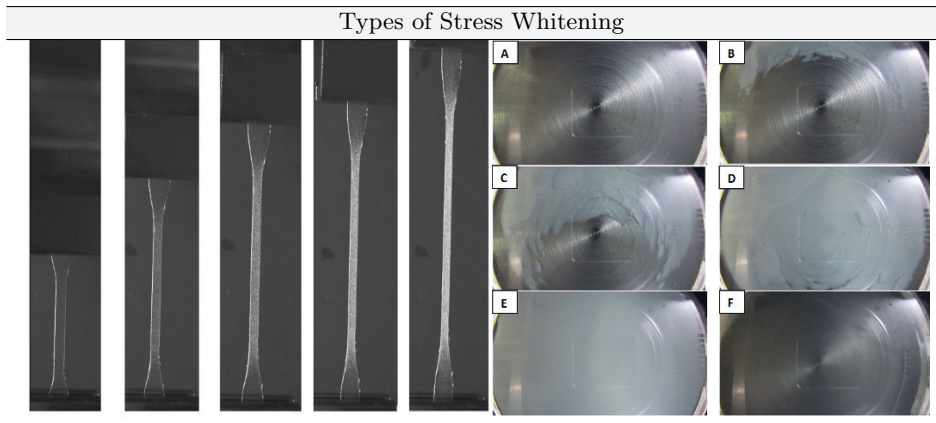


**Figure 4.18** Different forms of stress whitening under uniaxial tensile loading (Santarsiero et al., 2016) and constrained tensile loading (Drass et al., 2018b)

al., 2018b). Stress whitening is also documented in elastomer-modified (rubber-reinforced) plastics (Thomas et al., 2008), in which the reason for the whitening was given by micro-void formation (cavitation) within the elastomer additives. A reason for the visibility of these voids is presented by Misra et al. (2004), since they observed that voids that show a size range of  $\approx 1 \mu\text{m}$  reflect white light most efficiently. Another finding, reported by Dasari et al. (2003), implies that high crystalline polymers exhibit a large number of voids at a size of  $\approx 10 \mu\text{m}$ , which absorb visible light in a high extent, while low-crystalline polymers with significantly smaller cavities scatter visible light very strongly and do not absorb it. The hypothesis that stress whitening becomes visible through scattered visible light caused by growing cavities is confirmed by the studies of Bascom and Huston (1989). Gunel and Basaran (2010) concluded that a strong correlation between the degree of whitening and the micro-deformation properties can be observed.

Investigating the stress whitening for TSSA, this effect occurs in different forms depending on the applied deformation. The intensity and appearance of the whitening in TSSA depends decisively on the type of loading, i.e. under isochoric deformation a spot-wise whitening is formed, whereas under volumetric loading a very dense, cloud-like whitening becomes visible. Both types of whitening are shown as examples in Fig 4.18, where the spot-like whitening for the uniaxial tensile test and the dense, cloud-like whitening of the pancake tension test can be seen. Due to these very different properties of the whitening effect, it is necessary to describe why this phenomenon occurs in different forms and which mechanisms are responsible for it.

Considering the constrained tensile test (pancake tension test) first, in which an almost volumetric deformation predominates due to the disability of lateral contraction, the whitening is much more dense than in the uniaxial tensile test. In Section 4.3.1 it was already shown that the whitening completely disappears when the load is removed, which is confirmed by the studies of Sitte et al. (2011). Hence, the cloud-like whitening caused by elastic void growth is not an indicator of damage of the bulk material. The hypothesis of almost elastic pore growth and the fact that the cloud-like whitening effect is reversible was confirmed by the results of the cyclic pancake tension tests (see Section 4.3.2), in which a kind of healing effect for the reloading path could be observed. The healing in the cyclic pancake tension tension test manifests itself by the fact that the structural response during reloading does not correspond to the unloading path, which would be expected according to the classical theory of the Mullins effect. Rather, one almost achieves the virgin stiffness, so that the structural response lies above the unloading path. Thus, it can be concluded that the volumetric whitening effect is a reversible phenomenon caused by the cavitation effect. Following the considerations of Misra et al. (2004), the pore size during an applied deformation must reach the order of magnitude of the visible light ( $380 \leq l \leq 780$  nm), so that a strong refraction of light occurs, which becomes visible as whitening. Keeping in mind that the determined pore sizes of TSSA are in the range of 30 – 100 nm, the threshold value of visible light can be quickly exceeded in the pancake tension test in particular, so that a very dense white colouration can be observed.

Now the question has to be clarified why the uniaxial tensile test has a different form of whitening, which processes are responsible for this and whether this effect is reversible or not. To answer these questions, the cyclic miniature tensile tests are now evaluated, including the visualization of the whitening. The results of the cyclic uniaxial tensile tests presented in Section 4.2.2 are now assigned to the corresponding light microscope images to track the evolution of white colouration in terms of intensity and geometrical shape. Fig. 4.19 a shows a representative result of the cyclic tensile test including the locations where a light microscope image is taken. A distinction is made between the loading path, resulting in images for ever-increasing deformations. In addition, images were taken on the unloading path near the origin to determine whether the whitening is a reversible or an irreversible effect. Due to the image frequency rate of the light microscope of 1 image every 60 seconds, it was not possible to take an image at zero deformation. The corresponding images of the loading and unloading path are shown in Fig. 4.19 c,d, where a representative pore on the surface is tracked in order to gain new insights into the whitening effect. It is noticeable that with increasing deformation the spot-wise whitening increases in intensity and probability of occurrence. However, looking at the images of the unloading, it is evident that the white colouration does slightly decrease, but at

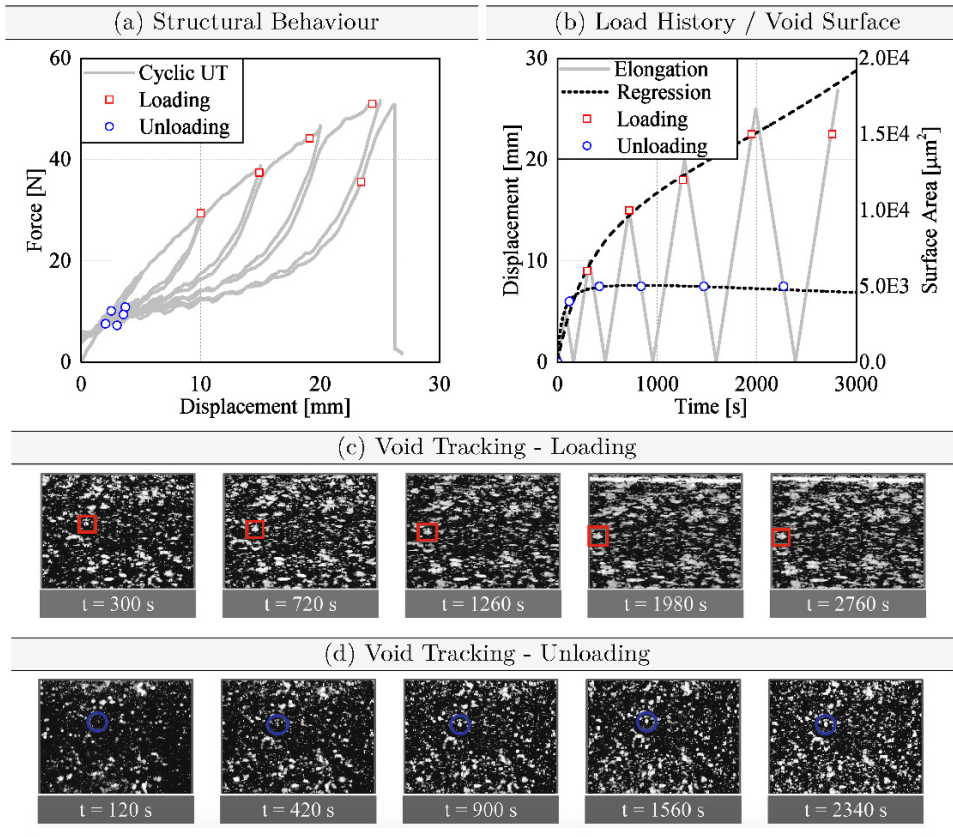


**Figure 4.19** (a) Structural behaviour of cyclic miniature tensile tests in which the set red markings are assigned to light-microscope images during loading and the blue markings are assigned to images with almost complete unloading; (b) analysis of the surface of a single white pore during loading and unloading as well as corresponding regression curves; light-microscope images of void tracking during (c) loading and (d) unloading

some point experiences a saturation. This means that the effect of white colouration is not reversible in isochoric tests in contrast to the findings of the pancake tension test.

This saturation spectrum can also be clearly seen by evaluating the surface area of the void for all captured images. Looking at Fig. 4.19 b , the evolution of the surface area of one arbitrary chosen white spot is shown as a function of time. Here it can be seen that for all unloading images the surface area of the pore experiences a saturation at  $A = 5.0 \text{ E}3 \mu\text{m}^2$ . As a result of the irreversible whitening, which consequently represents a real damage, the softening of the unloading path can now also be interpreted according to the Mullins effect. The Mullins effect is thought to

cause accumulated damage to the material under load, resulting in a significantly lower stiffness of the unloading path than the virgin loading path. For TSSA, this means that in the case of isochoric deformations, the accumulated damage is expressed as spot-wise whitening, which causes the material softening. In the present case, the damage is attributed to the classic Mullins damage mechanisms, such as bond breakage, filler rupture and detachment of matrix-filler interface (Diani et al., 2009).

In summary, the spot-wise whitening effect is an indicator of real Mullins damage observed in isochoric experiments, while dense, cloud-like whitening is an almost reversible effect in the form of elastic pore growth in volumetric experiments.

## 4.5 Conclusions

This chapter is dedicated to the experimental characterization of a transparent structural silicone which is used as an adhesive in modern façade systems. Uniaxial tensile and compression tests as well as biaxial tensile tests were performed as homogeneous experiments. Furthermore, shear tests and cyclic tensile tests were carried out to provide the experimental data basis for the later numerical material modelling. As a result of the homogeneous, experimental tests, individual stress-strain curves of the individual experiments were presented, which are used for material parameter identification. Furthermore, failure stretches of all experiments were presented in order to be able to calibrate failure criteria for the investigated structural silicone. As inhomogeneous tests pancake tension tests, i.e. flat bonded cylinder samples under axial tensile load, were used to characterize the material volumetrically. Here, too, cyclic tests were carried out to study the volumetric Mullins effect. Based on the experimental results of the inhomogeneous, volumetric tests, a new volumetric, hyperelastic material law is developed in Chap. 5, which is capable of representing the cavitation effect in silicone. In addition, a novel dilatational failure criterion will be developed by the volumetric experiments and calibrated using the experimental data (see Chap. 6).



# 5 Development of Constitutive Models for Poro-Hyperelastic Materials

This chapter is dedicated to the material modelling of polymers with a special focus on a transparent structural silicone adhesive. New material models are developed, which use the continuum mechanical basics presented in Chap. 2 and extend classical material models (see Chap. 3) to describe the structural behaviour of rubber-like materials especially under volumetric loading. Effects such as the cavitation effect, isochoric Mullins effect and effects under volumetric cyclic loading will be modelled with the developed material models. Furthermore, a new hyperelastic formulation is presented, which is particularly well suited to approximate any hyperelastic material behaviour under isochoric loading. The experimental data basis for the development of the novel hyperelastic material models for the transparent structural silicone TSSA was presented in Chap. 4.

## 5.1 Isochoric Helmholtz Free Energy Function

In this section, a novel isochoric, i.e. deviatoric, Helmholtz free energy function is developed phenomenologically, which is based on the inverse polynomial or rational function proposed by Nelder (1966) (Section 5.1.2). In contrast to classical polynomial formulations, the advantages of a rational formulation of a hyperelastic material model lie in the high adaptability and fitting quality of all experimental data, since literature has shown that structural silicones in particular cannot be adequately described with standard hyperelastic material models (Dias et al., 2014; Dispersyn et al., 2017).

To further increase the understanding about the novel hyperelastic material model, the parameter space of the material parameters to be fitted is limited by the proof of polyconvexity and convexity in order to guarantee a stable material behaviour (Section 5.1.3). These parameter limits are helpful for the approximation of new hyperelastic material data and their stable description on a material level. In order to motivate the phenomenologically derived material model physically, a reconciliation must be made between phenomenological and molecular-

statistical theory (Section 5.1.5). To do so, the novel isochoric Helmholtz free energy function is first transformed from the macro-scale to a micro-scale using an inverse homogenization approach in accordance to Khiêm and Itskov (2016). As a result of the micro-scale description, micro-kinematic variables, such as micro-stretch, micro-tube-contraction and micro-force, are derived with which classical molecular-statistical theories, such as Gaussian statistical, non-Gaussian statistical and the relaxed non-Gaussian statistical (relaxed Langevin) approach are approximated. This proofs that the initially purely phenomenologically motivated function can also be motivated by molecular statistics, which corresponds to the approach of Ehret (2015). The section is generally based on the work of Drass et al. (2017b); Drass et al. (2018f).

### 5.1.1 Classification of Isochoric Hyperelastic Material Model

The constitutive modelling of rubber-like materials under isochoric deformations is evidently dependent on the chosen hyperelastic Helmholtz free energy function. In literature, three ways of classifying Helmholtz free energy functions exist: (i) molecular-statistically motivated hyperelastic models accounting for the molecular structure and the motion of macromolecules (Wang and Guth, 1952; Treloar, 1975; Arruda and Boyce, 1993; Kaliske and Heinrich, 1999; Miehe et al., 2004a; Khiêm and Itskov, 2016) and (ii) phenomenological Helmholtz free energy functions, which are characterized by treating hyperelasticity only under a mathematical framework without reference to molecular concepts (Mooney, 1940; Rivlin, 1948; Ogden, 1972; Drass et al., 2017b; Drass et al., 2018f). Since material parameters must be determined for both approaches, within the last classification (iii) tabulated formulations for hyperelastic materials were developed, where the experimental data is used directly as input data characterizing the material behaviour (Marlow, 2003; Kolling et al., 2007). Hence, within the last classification no material parameters must be determined. Since there is a wide variety of hyperelastic material formulations, each with very specific advantages and properties (Marckmann and Verron, 2006), it was shown by Dias et al. (2014) and Dispersyn et al. (2017) that the structural behaviour of silicone adhesives and modified silane (MS) polymers can only be moderately represented over the entire strain range. Consequently, there is a need to develop improved models that approximate the initial stiffness well, as this is the practical area of construction.

### 5.1.2 New Isochoric Hyperelastic Material Model

A novel phenomenological Helmholtz free energy function is proposed and afterwards transferred into the context of molecular-statistical theory to reconcile both approaches of developing hyperelastic constitutive models. Developing phenomeno-

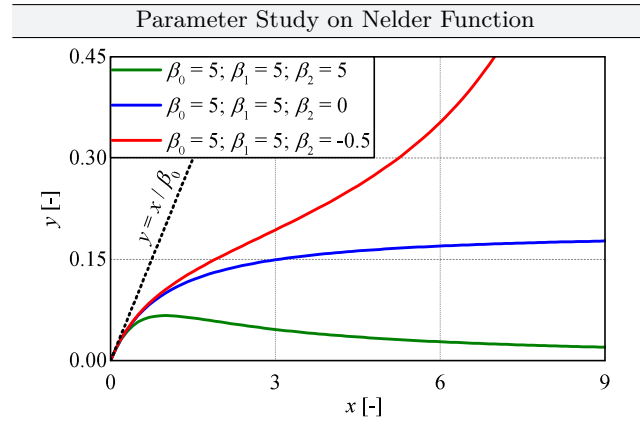


**Figure 5.1** Representation of behaviour of Nelder function utilizing different parameter sets for  $\beta_i$  with  $i \in [0, 1, 2]$

logical hyperelastic models, mathematical expressions must be found, which are able to account for strong non-linear shapes of the stress-strain behaviour of rubbers and rubber-like materials. The necessity of a high functional adaptability can be proven by the strongly non-linear structural behaviour of rubber-like materials under any deformations, which are to be approximated with one hyperelastic constitutive model. Hence, a further declared objective is the approximation of arbitrary deformation states with only one hyperelastic material model.

A promising mathematical function accounting for a strong non-linear behaviour is represented by an inverse polynomial or rational function, which was originally developed by Nelder (1966) to describe processes in agriculture. The Nelder function has the advantages over usual quadratic polynomials that it has no built-in symmetry and its two extremes are described by two separate parameters. The initial proposal by Nelder (1966) is formulated by

$$\frac{x}{y} = \beta_0 + \beta_1 x + \beta_2 x^2, \quad (5.1)$$

which provides three free parameters for the approximation of arbitrary correlations. Fig. 5.1 shows that the inverse polynomial of Nelder (1966) is able to approximate the initial stiffness of a material through the parameter  $\beta_0$ . In addition, stress softening, a plateau and even stiffening effects can be easily represented by the inverse formulation. Reformulating the original function of Nelder (1966) under the assumption of  $\beta_2 = 0$ , the simplified inverse polynomial reads

$$y = \frac{x}{\beta_0 + \beta_1 x}. \quad (5.2)$$

Bringing Eq. (5.2) into the context of hyperelasticity, the isochoric Helmholtz free energy may be represented by

$$\Psi(\bar{\mathbf{b}}) = \frac{(I_{1,\bar{\mathbf{b}}} - 3)}{\alpha_0 + \alpha_1(I_{1,\bar{\mathbf{b}}} - 3)}, \quad (5.3)$$

where  $I_{1,\bar{\mathbf{b}}} = \text{tr}(\bar{\mathbf{b}})$  characterizes the first isochoric, principal invariant of the left, isochoric Cauchy-Green tensor  $\bar{\mathbf{b}}$ . The free parameters of the original Nelder function have been renamed for reasons of clarity. Since it was shown by Horgan and Smayda (2012) that the second, isochoric invariant  $I_{2,\bar{\mathbf{b}}}$  of the left Cauchy-Green tensor has a major influence for the approximation of the structural behaviour of rubber-like materials under biaxial deformations, Eq. (5.3) is extended by the second invariant of the left Cauchy-Green tensor leading to

$$\boxed{\Psi_{\text{iso,ND}}(\bar{\mathbf{b}}) = \frac{(I_{1,\bar{\mathbf{b}}} - 3)}{\alpha_0 + \alpha_1(I_{1,\bar{\mathbf{b}}} - 3)} + \frac{(I_{2,\bar{\mathbf{b}}} - 3)}{\beta_0 + \beta_1(I_{2,\bar{\mathbf{b}}} - 3)}}, \quad (5.4)$$

where  $I_{2,\bar{\mathbf{b}}} = \frac{1}{2} [I_{1,\bar{\mathbf{b}}}^2 - \text{tr}(\bar{\mathbf{b}}^2)]$  is represented by the first isochoric, principal invariant and the trace of the isochoric left Cauchy-Green tensor. It is important to note that the denominator must always be positive to have stable material behaviour. The present Helmholtz free energy function of Eq. (5.4) is characterized by four material parameters, which must be identified based on independent experimental investigations.

Evaluating the present Helmholtz free energy function of Eq. (5.4) more in detail, the principal invariants  $I_{1,\bar{\mathbf{b}}}$  and  $I_{2,\bar{\mathbf{b}}}$  may reach a limit value in which stresses become singular thus infinitely large. This can be computed by setting the inverse of  $\Psi$  to zero for each invariant. Based on the four parameter model of Eq. (5.4), the maximum values for the invariants read therefore

$$\max I_{1,\bar{\mathbf{b}}} = I_m = 3 - \frac{\alpha_0}{\alpha_1} \quad \text{for } \alpha_0 > 0 \quad (5.5)$$

and

$$\max I_{2,\bar{\mathbf{b}}} = 3 - \frac{\beta_0}{\beta_1} \quad \text{for } \beta_0 > 0. \quad (5.6)$$

Based on the proposed inequality presented in Eq. (5.5), it is additionally possible to reconcile the phenomenologically developed rational hyperelastic material model with the theory of molecular statistics, which is the basis for physical material models of rubbers. In order to provide a link to the molecular statistics of polymers,

$\max I_1$  means that the finite extensibility  $I_m$  of a polymer chain is reached. Hence, if the rubber network is fully stretched,  $I_m$  is the limiting value for  $I_1$ , where  $I_m$  can be related to chain length  $l$  or inversely to the cross-link density  $n$  (Yeoh and Fleming, 1997). Considering natural rubbers, a reasonable value for  $I_m$  would be about 100, which corresponds to a maximum extension ratio  $\lambda_m \approx 10$  under the assumption of a uniaxial tensile loading with

$$I_m = \lambda_m^2 + 2\lambda_m^{-1} - 3 \approx \lambda_m^2 \quad \text{with } \lambda_m = \sqrt{n}. \quad (5.7)$$

A generally accepted relationship between the molecular-statistical theory and the maximal allowable value of the second invariant  $\max I_{2,\bar{\mathbf{b}}}$  does not yet exist.

Returning to the proposed macroscopic Helmholtz free energy function of Eq. (5.4) or Eq. (5.10) respectively, an advantage is that it can be easily reduced to classical material models, like the Neo-Hookean material model. Hence, setting  $m = 0$  and disregarding the second isochoric, principal invariant of the isochoric left Cauchy-Green tensor, the linearised form of Eq. (5.10) reads

$$\Psi_{\text{iso,ND}}(\bar{\mathbf{b}}) = \frac{(I_{1,\bar{\mathbf{b}}} - 3)}{\alpha_0} \Rightarrow \frac{1}{\alpha_0} \equiv \mu \equiv NkT, \quad (5.8)$$

which is identical to the Neo-Hookean formulation. Additionally, the novel isochoric Helmholtz free energy function can be transferred to the Mooney-Rivlin material model by setting  $m = n = 0$  in (5.10) leading to

$$\begin{aligned} \Psi_{\text{iso,ND}}(\bar{\mathbf{b}}) &= \frac{(I_{1,\bar{\mathbf{b}}} - 3)}{\alpha_0} + \frac{(I_{2,\bar{\mathbf{b}}} - 3)}{\beta_0} \Rightarrow \frac{1}{\alpha_0} \equiv c_{10} \\ &\quad \frac{1}{\beta_0} \equiv c_{01} \end{aligned} \quad (5.9)$$

For reasons of completeness,  $\Psi_{\text{iso,ND}}(\bar{\mathbf{b}})$  can be written in a more generalized form using a series expansion representation, which simply reads

$$\Psi_{\text{iso,ND}}(\bar{\mathbf{b}}) = \sum_{i=0}^m \alpha_i (I_{1,\bar{\mathbf{b}}} - 3)^i + \sum_{j=0}^n \beta_j (I_{2,\bar{\mathbf{b}}} - 3)^j \quad \text{with } i, j \in \mathbb{N}. \quad (5.10)$$

It has been shown by several authors that the Nelder function can be used in many areas of material modelling. Be it for the determination of true stress strain relations at a constant strain rate for acrylic adhesives (Silvestru et al., 2018a), for the representation of cavitation in rubber-like materials (Drass et al., 2018b) or for the calculation of an internal damage variable in structural silicones (Drass

et al., 2017a). Therefore, this function is a promising candidate to also characterize the isochoric material behaviour of hyperelastic materials.

### 5.1.3 Proof of Polyconvexity

Within the field of hyperelasticity, it is essential to guarantee a stable and therefore a convex material behaviour (Hartmann and Neff, 2003). A convex hyperelastic material means that no material softening or material instabilities can occur in the structural response under any deformations. Since hyperelastic materials are defined by stored energy functions dependent on the deformation mapping between the reference and current configuration of a material body (see Section 2.1.1), it is important that these functionals obey a stable material behaviour with respect to the applied deformation. To proof the material stability, different convexity conditions and inequalities were proposed in literature (Baker and Ericksen, 1954; Hill, 1970; Schröder and Neff, 2010). Since classical conditions guaranteeing a stable material behaviour may fail, e.g. the Baker-Ericksen inequality is not valid for anisotropic materials, the Legendre-Hadamard inequality is not sufficient to guarantee solutions for arbitrary BVP's, the proof of convexity excludes the principle of material frame-indifference as well as buckling and stability problems and the proof of quasi-convexity often results in a complicated mathematical formalism (Schröder and Neff, 2003), the proof of polyconvexity is promising and generally accepted to ensure material stability. A feature of a polyconvex material is that it implies ellipticity (Schröder and Neff, 2003), which is important in order to approximate the solution of elliptic PDE's via FEM. The loss of ellipticity is conterminous with the loss of material stability resulting in negative moduli and a change from an elliptic to an hyperbolic PDE (Belytschko et al., 2013:p.412).

To proof polyconvexity, an arbitrary Helmholtz free energy function must be expressed as convex function of the deformation gradient  $\mathbf{F}$ , the co-factor  $\mathbf{G} = \det \mathbf{F} \mathbf{F}^{-T}$  of the deformation gradient and the determinant  $J = \det \mathbf{F}$  of deformation gradient (Bonet et al., 2015). The co-factor or also called adjoint of a tensor is a notion of linear algebra. It refers to the transposition of the cofactor matrix, i.e. the transposition of the matrix whose entries are the signed minors.

In Fig. 5.2, a numerical example for a polyconvex and a non-polyconvex material formulation is illustrated for reasons of clarity, where a unit cell is uniaxially tensioned exploiting symmetry boundary conditions. As can be seen from Fig. 5.2 a, the loss of ellipticity respectively polyconvexity leads to hourglass modes within the finite element mesh in the deformed state, which is a typical observation. In contrast, utilising a polyconvex Helmholtz free energy function, the numerical calculation is stable without leading to hourglass modes of the finite elements and thus non-negative moduli without material instabilities (see Fig. 5.2 b).

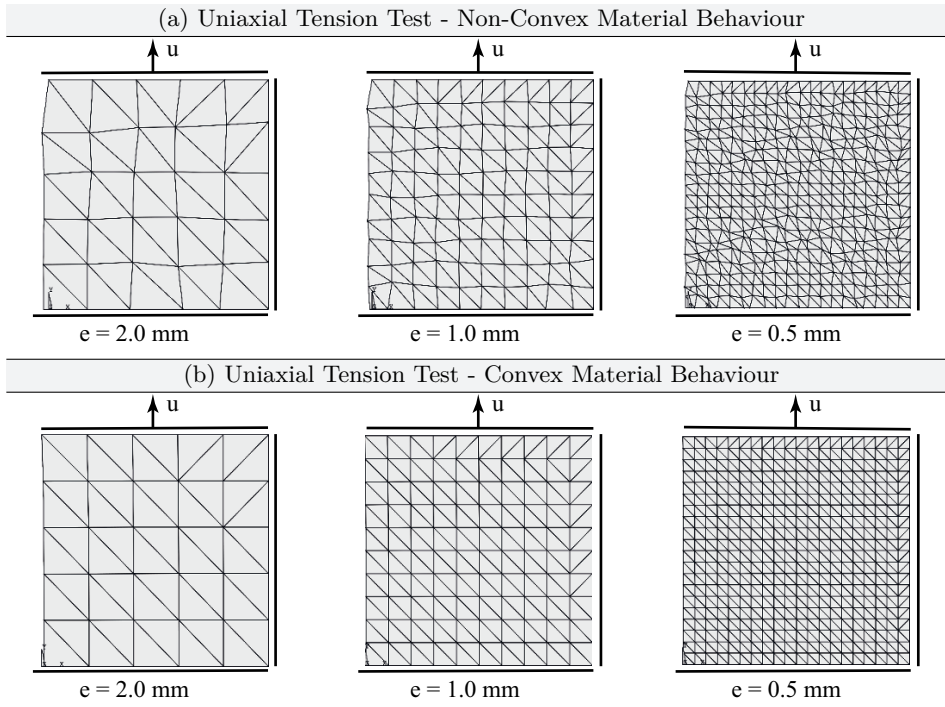


**Figure 5.2** Exemplary presentation of a finite element simulation of a tension problem for a (a) non-convex and (b) convex material formulation

It was shown by Bonet et al. (2015) and Bonet et al. (2016) that the classical proof of polyconvexity results in complex mathematical formulations by re-expressing the Helmholtz free energy function in terms of the deformation gradient  $\mathbf{F}$  only. To avoid this, an alternative concept will be applied in accordance to Bonet et al. (2015); Bonet et al. (2016) utilizing the concept of a so-called tensor cross-product, which was initially proposed by de Boer (1982):p.76. Based on the tensor cross product  $\times$  describing the outer tensor product of two tensors, simple expressions for the area and volume map are obtained, which are solely dependent on the deformation gradient  $\mathbf{F}$ . For a more precise definition of the tensor cross product, reference is made to the work of Bonet et al. (2015).

Following the new notation, the fibre, area and volume map can be summarized by:

$$d\vec{x} = \mathbf{F} d\vec{X} \quad \text{with} \quad \mathbf{F} = \nabla_0 \vec{x}, \quad (5.11)$$

$$d\vec{a} = \mathbf{G} d\vec{A} \quad \text{with} \quad \mathbf{G} = \frac{1}{2} (\mathbf{F} \times \mathbf{F}) = \det(\nabla_0 \vec{x}) (\nabla_0 \vec{x})^{-T}, \quad (5.12)$$

$$dv = JdV \quad \text{with} \quad J = \frac{1}{6} (\mathbf{F} \times \mathbf{F}) : \mathbf{F} = \det(\nabla_0 \vec{\mathbf{x}}), \quad (5.13)$$

where  $\nabla_0$  represents the gradient with respect to the material coordinates, i.e.  $\nabla_0 := \frac{\partial}{\partial \vec{\mathbf{X}}}$ . Following the remarks of Bonet et al. (2015); Bonet et al. (2016), an arbitrary strain energy functional  $\Psi(\mathbf{F})$  must be expressed as convex multi-variable function  $\hat{\Psi}(\mathbf{F}, \mathbf{G}, J)$ , which must be convex with respect to its 19 components. This number comes from the fact that  $\mathbf{F}$  and  $\mathbf{G}$  each consist of 9 components and  $J$  has only one entry. Due to the requirement that there is an invariance with respect to rotations in the material configuration,  $\hat{\Psi}$  must be defined independently of the rotational components of  $\mathbf{F}$  and  $\mathbf{G}$  in general. This is typically achieved by ensuring that  $\hat{\Psi}$  depends on  $\mathbf{F}$  and  $\mathbf{G}$  via the symmetrical tensors  $\mathbf{b} = \mathbf{F} \cdot \mathbf{F}^T$  and  $\mathbf{g} = \mathbf{G} \cdot \mathbf{G}^T$  respectively. By re-expressing the invariants  $I_{1,\bar{\mathbf{b}}}, I_{2,\bar{\mathbf{b}}}, I_{3,\bar{\mathbf{b}}}$  by the deformation gradient  $\mathbf{F}$  (Hartmann and Neff, 2003; Bonet et al., 2016), the co-factor  $\mathbf{G}$  of the deformation gradient and determinant of the deformation gradient  $J$ , which reads

$$I_{1,\bar{\mathbf{b}}} = \mathbf{F} : \mathbf{F}, \quad (5.14)$$

$$I_{2,\bar{\mathbf{b}}} = \mathbf{G} : \mathbf{G}, \quad (5.15)$$

$$I_{3,\bar{\mathbf{b}}} = J^2, \quad (5.16)$$

strain energy functionals can be easily expressed as  $\hat{\Psi}(\mathbf{F}, \mathbf{G}, J)$ . As above-mentioned, the multi-variable function  $\hat{\Psi}(\mathbf{F}, \mathbf{G}, J)$  must be convex with respect to its arguments. This can be proved by analysing the Hessian operator  $\mathbb{H}$ , which is applied on  $\hat{\Psi}$ . The application of the Hessian operator to  $\hat{\Psi}$  and the insertion of the individual entries into the so-called Hessian matrix or only Hessian via the operator  $[\bullet]$  leads to

$$[\mathbb{H}_{\hat{\Psi}}] = \begin{bmatrix} \hat{\Psi}_{\mathbf{FF}} & \hat{\Psi}_{\mathbf{FG}} & \hat{\Psi}_{\mathbf{FJ}} \\ \hat{\Psi}_{\mathbf{GF}} & \hat{\Psi}_{\mathbf{GG}} & \hat{\Psi}_{\mathbf{GJ}} \\ \hat{\Psi}_{\mathbf{JF}} & \hat{\Psi}_{\mathbf{JG}} & \hat{\Psi}_{\mathbf{JJ}} \end{bmatrix} = \begin{bmatrix} \frac{\partial^2 \hat{\Psi}}{\partial \mathbf{F} \partial \mathbf{F}} & \frac{\partial^2 \hat{\Psi}}{\partial \mathbf{F} \partial \mathbf{G}} & \frac{\partial^2 \hat{\Psi}}{\partial \mathbf{F} \partial J} \\ \frac{\partial^2 \hat{\Psi}}{\partial \mathbf{G} \partial \mathbf{F}} & \frac{\partial^2 \hat{\Psi}}{\partial \mathbf{G} \partial \mathbf{G}} & \frac{\partial^2 \hat{\Psi}}{\partial \mathbf{G} \partial J} \\ \frac{\partial^2 \hat{\Psi}}{\partial J \partial \mathbf{F}} & \frac{\partial^2 \hat{\Psi}}{\partial J \partial \mathbf{G}} & \frac{\partial^2 \hat{\Psi}}{\partial J \partial J} \end{bmatrix}. \quad (5.17)$$

The proof of polyconvexity is achieved, if the Hessian operator is positive semi-definite. Hence, the eigenvalues  $\mathcal{E}_i$  of  $[\mathbb{H}_{\hat{\Psi}}]$  must be  $\mathcal{E}_i \geq 0$  with  $i \in \mathbb{N}$ . Assuming an incompressible material behaviour, it is an easy task to proof polyconvexity for a two-term Mooney-Rivlin material model, which reads

$$\hat{\Psi} = c_{10} (\mathbf{F} : \mathbf{F} - 3) + c_{01} (\mathbf{G} : \mathbf{G} - 3). \quad (5.18)$$

Applying the Hessian operator to Eq. (5.18), the following Hessian results

$$[\mathbb{H}_{\hat{\Psi}}] = \begin{bmatrix} \hat{\Psi}_{\mathbf{FF}} & \hat{\Psi}_{\mathbf{FG}} & \hat{\Psi}_{\mathbf{FJ}} \\ \hat{\Psi}_{\mathbf{GF}} & \hat{\Psi}_{\mathbf{GG}} & \hat{\Psi}_{\mathbf{GJ}} \\ \hat{\Psi}_{\mathbf{JF}} & \hat{\Psi}_{\mathbf{JG}} & \hat{\Psi}_{\mathbf{JJ}} \end{bmatrix} = \begin{bmatrix} 2c_{10}\mathcal{I} & \mathbf{0} & \mathbf{0} \\ \mathbf{0} & 2c_{01}\mathcal{I} & \mathbf{0} \\ \mathbf{0} & \mathbf{0} & 0 \end{bmatrix}, \quad (5.19)$$

where  $\mathcal{I}$  denotes a fourth-order identity tensor. Hence, the incompressible material formulation of a two-term Mooney-Rivlin material model is polyconvex for  $c_{10} = c_{01} \geq 0$ . Setting  $c_{01} = 0$ , the proof of polyconvexity for the Neo-Hookean material model is also present. Consequently, the proof of polyconvexity for the classical material laws provides the trivial solution that the material parameters representing the shear modulus must be positive.

Applying the proposed mathematical formalism for proofing polyconvexity on the novel isochoric Helmholtz free energy function presented in Eq. (5.10),  $\Psi_{\text{iso,ND}}$  must be, first of all, reformulated in terms of a multi-variable function  $\hat{\Psi}_{\text{iso,ND}}(\mathbf{F}, \mathbf{G}, J)$ , i.e.

$$\hat{\Psi}_{\text{iso,ND}} = \frac{(\mathbf{F} : \mathbf{F} - 3)}{\sum_{i=0}^m \alpha_i (\mathbf{F} : \mathbf{F} - 3)^i} + \frac{(\mathbf{G} : \mathbf{G} - 3)}{\sum_{j=0}^n \beta_j (\mathbf{G} : \mathbf{G} - 3)^j} \quad \text{with } i, j \in \mathbb{N}. \quad (5.20)$$

Calculating the Hessian of Eq. (5.20) under the assumption of an incompressible material while setting  $m = n = 0$ ,  $[\mathbb{H}_{\hat{\Psi}}]$  reads

$$[\mathbb{H}_{\hat{\Psi}}] = \begin{bmatrix} \frac{2}{\alpha_0}\mathcal{I} & \mathbf{0} & \mathbf{0} \\ \mathbf{0} & \frac{2}{\beta_0}\mathcal{I} & \mathbf{0} \\ \mathbf{0} & \mathbf{0} & 0 \end{bmatrix}. \quad (5.21)$$

Hence,  $\hat{\Psi}_{\text{iso,ND}}(\mathbf{F}, \mathbf{G}, J)$  is polyconvex for  $\alpha_0, \beta_0 \geq 0$ , which is intuitively accessible since the parameters for the initial material stiffness must be positive. Setting  $m = n = 1$ , the components of the Hessian are more lengthy resulting in

$$[\mathbb{H}_{\hat{\Psi}}] = \begin{bmatrix} \mathcal{F} & \mathbf{0} & \mathbf{0} \\ \mathbf{0} & \mathcal{H} & \mathbf{0} \\ \mathbf{0} & \mathbf{0} & 0 \end{bmatrix}, \quad (5.22)$$

with

$$\mathcal{F} = \frac{2\alpha_0[\alpha_0 + \alpha_1(\mathbf{F} : \mathbf{F} - 3)]^2}{[\alpha_0 + \alpha_1(\mathbf{F} : \mathbf{F} - 3)]^4} \mathcal{I} - \frac{8\alpha_0\alpha_1[\alpha_0 + \alpha_1(\mathbf{F} : \mathbf{F} - 3)]}{[\alpha_0 + \alpha_1(\mathbf{F} : \mathbf{F} - 3)]^4} \mathbf{F} \otimes \mathbf{F} \quad (5.23)$$

and

$$\mathcal{H} = \frac{2\beta_0[\beta_0 + \beta_1(\mathbf{G} : \mathbf{G} - 3)]^2}{[\beta_0 + \beta_1(\mathbf{G} : \mathbf{G} - 3)]^4} \mathbf{I} - \frac{8\beta_0\beta_1[\beta_0 + \beta_1(\mathbf{G} : \mathbf{G} - 3)]}{[\beta_0 + \beta_1(\mathbf{G} : \mathbf{G} - 3)]^4} \mathbf{G} \otimes \mathbf{G}. \quad (5.24)$$

It is obvious from Eqs. (5.23, 5.24) that the proof of polyconvexity and therefore ellipticity is now dependent on the applied deformation.

### 5.1.4 Proof of Convexity vs. Drucker's Stability Postulate

Checking the convexity of a function that is dependent on two variables, here the principal invariant of the left, isochoric Cauchy-Green tensor  $I_{1,\bar{\mathbf{b}}}$  and  $I_{2,\bar{\mathbf{b}}}$ , it is sufficient to examine the following partial derivatives, which must be greater or equal to zero:

$$\frac{\partial^2 \Psi}{\partial I_{1,\bar{\mathbf{b}}}^2} \geq 0, \quad (5.25)$$

$$\frac{\partial^2 \Psi}{\partial I_{2,\bar{\mathbf{b}}}^2} \geq 0 \quad (5.26)$$

and

$$\frac{\partial^2 \Psi}{\partial I_{1,\bar{\mathbf{b}}}^2} \frac{\partial^2 \Psi}{\partial I_{2,\bar{\mathbf{b}}}^2} - \left( \frac{\partial^2 \Psi}{\partial I_{1,\bar{\mathbf{b}}} \partial I_{2,\bar{\mathbf{b}}}} \right)^2 \geq 0. \quad (5.27)$$

From these convexity conditions, the following limitation of the material parameters can be derived:

$$\left. \begin{array}{l} \alpha_0 > 0 \\ \alpha_1 < 0 \end{array} \right\} \text{for } 3 \leq \max I_{1,\bar{\mathbf{b}}} < 3 - \frac{\alpha_0}{\alpha_1} \quad (5.28)$$

and

$$\left. \begin{array}{l} \beta_0 > 0 \\ \beta_1 < 0 \end{array} \right\} \text{for } 3 \leq \max I_{2,\bar{\mathbf{b}}} < 3 - \frac{\beta_0}{\beta_1}. \quad (5.29)$$

This simple mathematical formalism leads to comprehensive equation in contrast to that obtained when proofing polyconvexity (Bonet et al., 2015). However, both approaches lead to the same results.

Returning to the described inequalities, all three conditions must be met for  $\Psi$  to represent a convex function in  $I_{1,\bar{\mathbf{b}}}$  and  $I_{2,\bar{\mathbf{b}}}$ . If one of the above-mentioned conditions is violated, there is a non-convex function, i.e. the material stability is not guaranteed. However, since this criterion only makes a binary distinction between convexity and non-convexity, it is desirable to be able to describe the beginning of non-convexity. Especially with regard to the approximation of experimental data, the experimentally observed deformation range should be represented by a convex potential function. If deformations fictitiously exceed the experimentally

**Table 5.1** Parameter studies of Eq. (5.4) to check the convexity and Drucker's stability criterion

Parameters	Convexity Criterion Eq. (5.25) - Eq. (5.27)	Drucker Stability (5.30)
$\alpha_0 = 1$	convex behaviour	
$\alpha_1 = -0.02$	for $I_{1,\bar{b}} < 3 - \frac{\alpha_0}{\alpha_1}$	Drucker
$\beta_0 = 1$	and $I_{2,\bar{b}} < 3 - \frac{\alpha_0}{\alpha_1}$	stable
$\beta_1 = -0.02$		
$\alpha_0 = 1$	convex behaviour	
$\alpha_1 = 0$	for $3 < I_{1,\bar{b}}$	Drucker
$\beta_0 = 1$	and $3 < I_{2,\bar{b}}$	stable
$\beta_1 = 0$		
$\alpha_0 = 1$		
$\alpha_1 = 0.1$	non-convex	Drucker
$\beta_0 = 1$	behaviour	unstable
$\beta_1 = 0.1$		

determined fracture strain of the analysed material in numerical calculations, the convexity condition may be violated, since the material has already failed. In order to find out when a non-polyconvex material model is unstable, i.e. shows a negative tangential material stiffness and related stress softening, the postulate of Drucker can be used Drucker (1957). The Drucker stability condition for an incompressible hyperelastic material requires that the change in stress  $d\sigma$  resulting from a slight change in logarithmic strain  $d\epsilon$  satisfies the inequality

$$d\sigma : d\epsilon > 0. \quad (5.30)$$

To show that even a non-convex or non-polyconvex material model shows stable material behaviour up to a certain deformation, three examples of (5.4) are presented in the following, in which different material parameter combinations leading to one convex and two non-convex Helmholtz free energy functions are analysed under uniaxial and biaxial tension loading. On the one hand, one non-convex function shows a singular behaviour where the stresses assume the limit value of infinity. On the other hand, a softening material behaviour is described where stresses in the material decrease with increasing deformation.

To summarize, all material parameters and the material behaviour of each model is described in Table 5.1. As can be seen from Fig. 5.3 a, where the uniaxial tensile behaviour is studied, all three material parameter combinations show a convex behaviour in terms of analysing Drucker's stability criterion. Only the material model with stress softening is no longer Drucker stable from the time of softening. The same behaviour can also be seen in the studies of the biaxial deformation (see Fig. 5.3 b). It is interesting to note that neither the model with stress softening

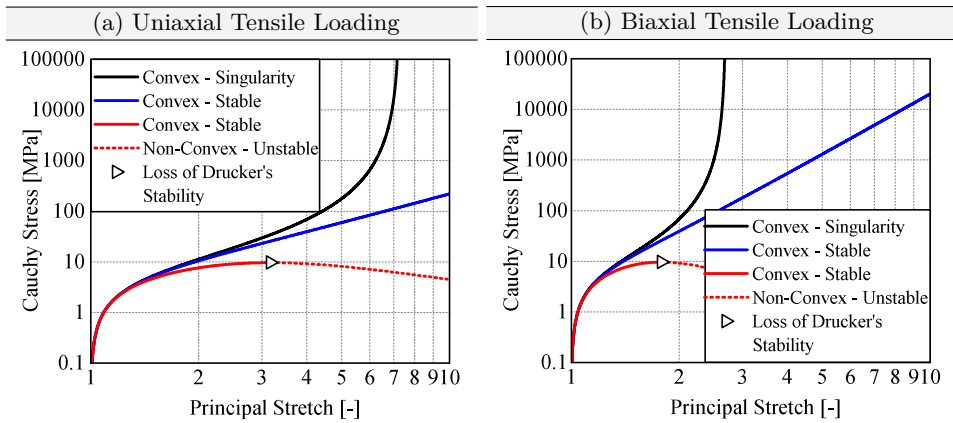


**Figure 5.3** Parameter study for checking convexity / polyconvexity and Drucker's postulate under uniaxial and biaxial tensile loading of a single-element test

nor the model with stress singularity satisfies the convexity condition of Eq. (5.25)-Eq. (5.27), but they are Drucker stable in the sense of Eq. (5.30) to a particular point of applied deformation. It should therefore be noted that even if the convexity condition is violated, a stable material behaviour may be present. Therefore it is essential to represent the experimentally determined deformation range with a stable material behaviour when determining material parameters. If the material is loaded beyond its material strength, the stability can be violated.

### 5.1.5 Reconciling Phenomenological and Molecular-Statistical Theory

Because the present isochoric Helmholtz function of free energy was determined exclusively phenomenologically, in this section the macroscopic strain energy density function  $\Psi_{\text{iso},\text{ND}}(\bar{\mathbf{b}})$  is transferred to the micro-scale (molecular-level) and compared with classical molecular-statistically models to show its physical nature.

In polymer mechanics, the elementary entropic molecular theory assumes that the sum of the elastic energy of individual polymer chains corresponds to the total entropic energy of the network (Miehe et al., 2004a). This results in a relationship between macroscopic quantities such as elongation, free energy and forces / stresses and micro-kinematic quantities (micro-stretches and micro-forces), which can be related to each other using analytical network-averaging approaches (Beatty, 2003; Khiêm and Itskov, 2016), for example. Theoretical models of polymer networks, such as the Gaussian and non-Gaussian approaches, use statistical mechanics to describe the motion / conformations and entropy of an unconstrained polymer

chain. The Gaussian statistical approach uses a Gaussian distribution of the end-to-end distance of a single polymer chain, neglects any kind of interaction with the surrounding environment and can be applied to approximate moderate deformations. In contrast, the non-Gaussian approach accounts for the finite extensibility of the chain and is therefore well-suited to account for large deformations (Yeoh and Fleming, 1997). So-called chain scission cannot be modelled with the previously described approaches due to the assumption of finite extensibility of a polymer chain leading to locking effects. This is due to the assumption of fully rigid chain segments each of same length (Mao et al., 2017). In order to solve this problem, extended, freely joint models were introduced which relax the rigidity assumptions, since it is assumed that the Kuhn segments are extensible due to deformation of the constituent atomic bonds (Mao et al., 2017). In addition, it is generally accepted in molecular-statistical theory that the motion of polymer chains is limited by surrounding chains and networks. Therefore, it is assumed that the movement of the polymer chain takes place in a tube from which the constrained junction and constrained segment theories have grown (Deam and Edwards, 1976; Edwards and Vilgis, 1988; Heinrich et al., 1988). From the latter theory, so-called tube-models were developed, which describe the cross-links and entanglement topology of a polymer network through a series of worm-like network chain paths (Miehe et al., 2004a). The corresponding micro-kinematic variable to describe the tube-like constraint is obtained by characterizing the changing tube diameter under axial loading of a polymer chain. This micro-kinematic variable is generally described as micro-tube-contraction  $\nu$ . Hence, the free energy of a single polymer chain in a cross-linked network is governed by two micro-kinetic variables, the micro-stretch  $\lambda$  and micro-tube-contraction  $\nu$ .

To reconcile the phenomenological and molecular-statistical theory of developing hyperelastic material models, the micro-kinematic variables and entropy of a single polymer chain enclosed by a tube using various statistical-mechanical theories are briefly summarized and compared with  $\Psi_{\text{iso},\text{ND}}(\bar{\mathbf{b}})$ . To be more specifically, the new isochoric Helmholtz free energy function working on a continuum level is transferred to the micro-scale based on an inverse homogenization approach in accordance to the approach of Khiêm and Itskov (2016). Afterwards its structural behaviour on a micro-scale is compared with the structural responses of different, classical molecular-statistical theories. However, since it is not sufficient to transfer the material model from the macro-scale to the micro-scale and to make a comparison, Ehret (2015) proposed the following postulates in order to reconcile a phenomenological Helmholtz free energy with the molecular-statistical theory:

- Physical micro-macro transition between the micro-stretch  $\lambda$  of a representative single polymer chain and the macro-stretch  $\Lambda$  of a full network model, which acts on a continuum scale.

- Physical micro-macro transition of the free energy  $\psi_s$  of a single polymer chain and the macroscopic free energy  $\Psi$  of a full network model.
- Consideration of additional contributions to the free energy from topological constraints, i.e.  $\psi_t$ , interrelating the contraction of the micro-tube with an average change of macroscopic area elements.
- Approximation of the inverse Langevin function  $\mathcal{L}^{-1}(\lambda_r)$  on a micro-scale representing the free energy of a single polymer chain in the context of non-Gaussian statistics.
- Approximation of average micro-force dependent on the micro-tube-contraction  $\nu$  and therefore the actual size of the diameter  $d$  of the tube (Miehe et al., 2004a).

In addition to the proposed postulates of Ehret (2015), which should be obeyed, new proposals of phenomenological Helmholtz functions should also include classical hyperelastic constitutive models, such as the Neo-Hookean or the Mooney-Rivlin material model as limit cases (Treloar, 1975).

### Micro-Kinematic Variables and Entropy of Single Polymer Chains

Considering rubbers and rubber-like materials, they are composed of long, flexible polymer chains with chemical cross-links at so-called junction points (see Fig. 5.4). The geometrical structure of a single, unconstrained polymer chain consists of  $N$  segments each of equivalent length  $l$ . This characteristic length is called Kuhn segment length. Although the Kuhn segments are connected to each other, they are free in their motion. Hence,  $N$  characterizes the number of statistical links per chain. The contour length  $L$  of a polymer chain is the product of the segment length  $l$  and the number of polymer chain segments with  $L = Nl$ . The end-to-end distance  $r$  of a polymer chain is governed by  $r = |\vec{r}|$ , where  $\vec{r}$  represents the end-to-end vector. Following Treloar (1975), the initial length  $r_0$  of an unstressed polymer chain assumes the random-walk-type root-mean-square value reading  $r_0 = \sqrt{Nl}$ . As  $r \rightarrow Nl$ , the deformed chain is fully stretched and straightened. Hence, no further deformations can be performed by the chains due to the assumption of fully rigid chains. An illustration of the proposed concept for a single polymer chain and the corresponding micro-kinematic variables is shown in Fig. 5.4. Based on the segment rigidity assumption according to Kuhn (1934); Kuhn (1936), which states that the segment length cannot change and therefore remains constant and rigid, the free energy  $\psi$  of freely joint models diverge at micro-stretches reaching  $r \rightarrow Nl$ . In this context, the finite extensibility  $\lambda_m$  of a polymer chain is characterized by  $\lambda_m = \sqrt{N}$ . The micro-stretch of a polymer chain reads then

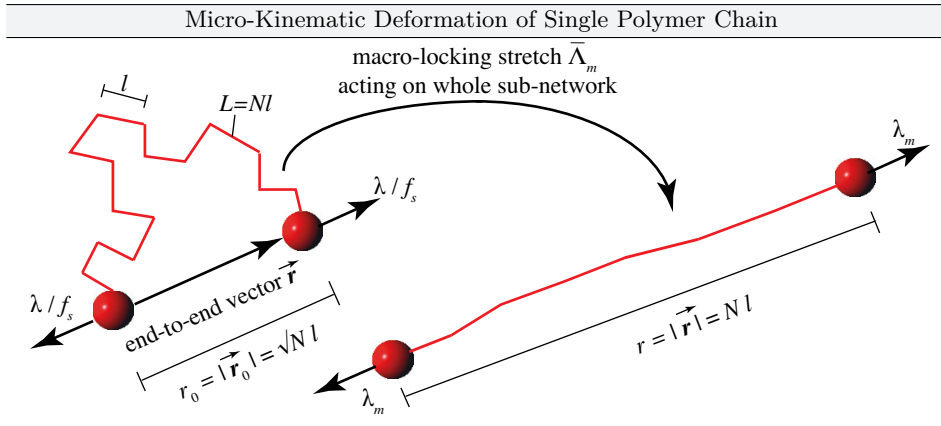


**Figure 5.4** Deformation of a single polymer chain from the reference to the current configuration:  $\bar{\Lambda}_m$  describes the average macro-locking-stretch acting on a polymer network and  $\lambda_m$  characterizes the micro-locking-stretch acting on a single polymer chain assuming an affine deformation

$$\lambda = \frac{r}{r_0} \text{ with } \lambda \in [0, \sqrt{N}], \quad (5.31)$$

whereas the relative micro-stretch can be expressed as

$$\lambda_r = \frac{r}{L} = \frac{\lambda}{\sqrt{N}} = \frac{\bar{\lambda}}{\lambda_m} \text{ with } \lambda_r \in [0, 1[. \quad (5.32)$$

It was shown by Deam and Edwards (1976); Edwards and Vilgis (1988); Heinrich et al. (1988) that the unconstrained deformation of polymer chains must be restricted to account for cross-links and the entanglement topology. Thus, so-called constrained junction and constrained segment theories were proposed. These tube models confine the motion of a polymer chain by a tube of constant diameter (Miehe et al., 2004a). Thus, the allowed conformations of a single chain are restricted to the free space within the tube, which is dependent on the interaction with the polymer network. The kinematic variable resulting from these model assumptions describes the micro-tube-contraction reading

$$\nu = \left( \frac{d_0}{d} \right)^2. \quad (5.33)$$

Here,  $d_0$  characterizes the initial tube diameter in the undeformed network, whereas  $d$  defines the current tube diameter (see Fig. 5.5).

Based on the proposed micro-kinematic variables of a single polymer chain confined by a tube, a key challenge in statistical mechanics is the calculation of

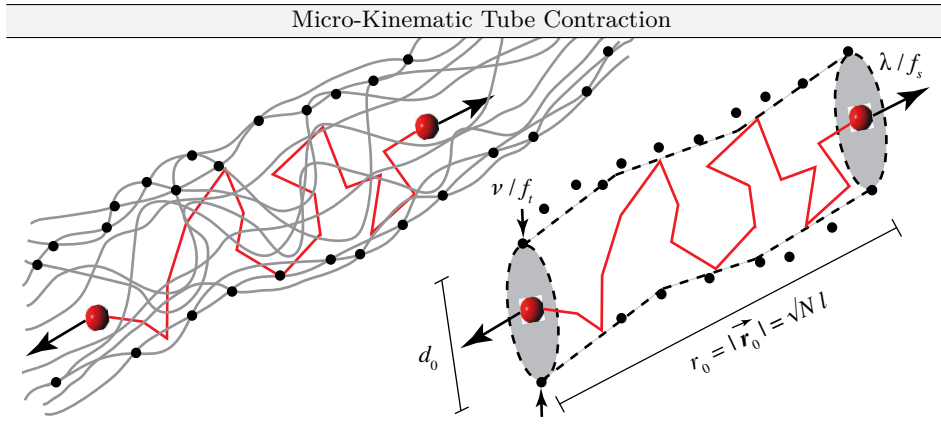


**Figure 5.5** Average tube contraction acting on a single polymer chain in the reference configuration

entropy. Entropy describes the allowed and available conformations of a single polymer chain within a micro-tube. The entropy  $s$  of a deforming single chain confined by a micro-tube can be calculated using Boltzmann's equation reading

$$s = k \ln p, \quad (5.34)$$

with  $k$  representing the Boltzmann constant and  $p$  describes the joint probability density. Regarding solely entropic and non-dissipative processes, the free energy  $\psi$  of a single polymer chain can be calculated by

$$\psi = -Ts, \quad (5.35)$$

where  $T > 0$  is the absolute temperature. The general joint probability density  $p$  can be split into an micro-stretch and micro-tube part

$$p(\lambda, \nu) = p_s(\lambda)p_t(\nu), \quad (5.36)$$

where  $p_s(\lambda)$  represents the probability density of the stretch part and  $p_t(\nu)$  the probability density of the tube part.

The free energy of single polymer chain within a micro-tube can be therefore obtained by inserting Eq. (5.36) into Eq. (5.35), which yields

$$\psi(\lambda, \nu) = \psi_s(\lambda) + \psi_t(\nu) = -kT[\ln(p_s(\lambda)) + \ln(p_t(\nu))]. \quad (5.37)$$

Based on the additive split of the free energy,  $\psi_s(\lambda)$  represents the free energy of an unconstrained polymer chain between the cross-links, whereas  $\psi_t(\nu)$  charac-

terizes the free energy due to topological constraints. The axial micro-force  $f_s$  or radial micro-forces  $f_t$  respectively acting on a single polymer chain are obtained by differentiating the free energies with respect to their kinematic variables, i.e.

$$f_s = \frac{d\psi_s(\lambda)}{d\lambda} \quad \text{and} \quad f_t = \frac{d\psi_t(\nu)}{d\nu}. \quad (5.38)$$

Depending on the selected probability densities, different molecular statistical approaches have been developed, which are summarised in Appendix E. In addition, these equations are used to determine micro-forces and micro-stretches for the Gaussian, non-Gaussian, relaxed Langevin and tube statistical approaches. These relations are later used to be approximated with a molecular-statistically motivated material model based on the macroscopic rational Nelder function (see Eq. 5.10).

### Generalized Network Averaging Concept

As the concept of molecular-statistical theory was briefly presented, an additional concept to describe the relation between microscopic and macroscopic variables must be found or presented respectively. An adequate concept to obtain a relationship of the micro-kinematic variables of a single polymer chain with the entire polymer network is the generalized network averaging concept accordingly to Khiêm and Itsikov (2016). It states that every directionally oriented polymer chain in a network is referred to as a mean polymer chain enclosed in a mean tube and is stretched by an average tube stretch  $\bar{\lambda}$  and / or an average tube contraction  $\bar{\nu}$ . The rubber network thus consists of several one-dimensional sub-networks that are distributed in different directions  $\vec{u}$  in a unit sphere.

To be more specific, the generalized network-averaging concept transfers the micro-stretch  $\vec{u}\lambda$  acting on a single polymer chain to an average micro-stretch  $\bar{\lambda}$  representing each directional chain in a polymer network by a mean chain confined in a mean tube undergoing an average tube stretch  $\bar{\lambda}$  and an average tube contraction  $\bar{\nu}$ . The notation for the micro-stretch  $\vec{u}\lambda$  as a function of the stretch-direction  $\vec{u}$  was deliberately chosen to make it clear that the micro-stretch can act in all directions of a unit sphere in a spherical coordinate system. The vector  $\vec{u}$  is characterized by

$$\vec{u} = \sin\theta \cos\varphi \vec{N}_1 + \sin\theta \sin\varphi \vec{N}_2 + \cos\theta \vec{N}_3, \quad (5.39)$$

where  $\vec{N}_i$  with  $i \in [1, 2, 3]$  describe the unit vectors in principal strain direction. The macro-stretch  $\vec{u}\Lambda$  acting on a polymer sub-network and the average macro-

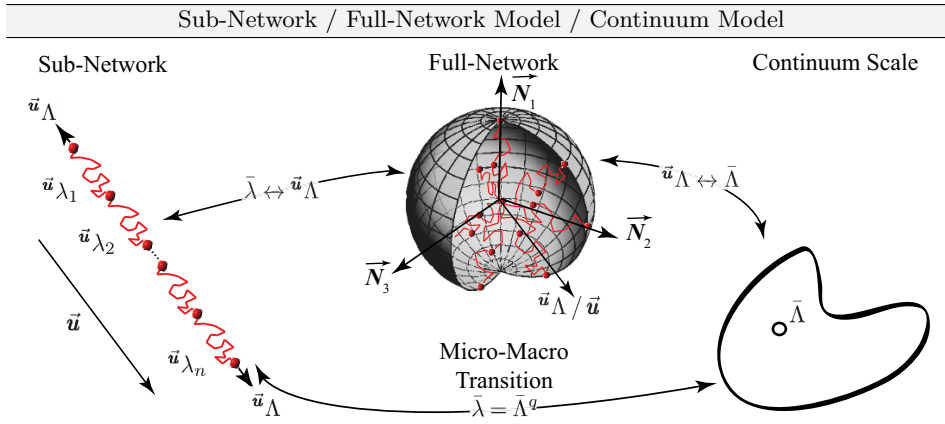


**Figure 5.6** Schematic illustration of a sub-network model consisting of  $N$  single polymer chains, a full network model consisting of polymer sub-networks in all spherical directions and a continuum model

stretch  $\bar{\Lambda}$  can be evaluated as the root-mean square of the macro-stretch over a unit sphere. Evaluating the surface integral by inserting

$$\vec{u}_{\Lambda}^2 = \Lambda_1^2 \sin^2 \theta \cos^2 \varphi + \Lambda_2^2 \sin^2 \theta \sin^2 \varphi + \Lambda_3^2 \cos^2 \theta \quad (5.40)$$

into

$$\bar{\Lambda} = \sqrt{\langle \vec{u}_{\Lambda}^2 \rangle} = \sqrt{\frac{1}{4\pi} \int_0^{2\pi} d\varphi \int_0^\pi \vec{u}_{\Lambda}^2 \sin \theta d\theta}, \quad (5.41)$$

gives a unique relationship between both macro-stretches. Following Heinrich et al. (1988), a physical micro-macro transition between the average micro-stretch  $\bar{\lambda}$  and the average macro-stretch  $\bar{\Lambda}$  was proposed by

$$\bar{\lambda} = \bar{\Lambda}^q, \quad (5.42)$$

where  $q$  represents a stretch amplification factor accounting for non-affine deformations. The concept of the mean polymer chain and generalized network averaging concept is schematically illustrated in Fig. 5.6.

### Reconciliation of $\Psi_{\text{iso},\text{ND}}$ with Molecular-Statistical Theory

In accordance to the proposal of Ehret (2015), a phenomenological Helmholtz free energy function can be transferred into the context of molecular-statistics based on five steps.

*In the first step*, a physical micro-macro transition between the average micro-stretch  $\bar{\lambda}$  of a representative single polymer chain and the average macro-stretch  $\bar{\Lambda}$  of a full-network model must be found. Heinrich et al. (1988) proposed the micro-macro transition  $\bar{\lambda} = \bar{\Lambda}^q$ , where  $q$  characterizes an amplification factor, which relates the stretch of a single polymer chain and the average macro-stretch of full-network model. From this it follows that the deformation on the micro and macro scales are affine to each other only for  $q = 1$ . In order to correlate the average macro-stretch  $\bar{\Lambda}$  of an polymer network with a macroscopic deformation on a continuum scale, an additional relationship must be found between the average macro-stretch  $\bar{\Lambda}$  and, for example, the first invariant  $I_{1,\bar{b}}$  of the left Cauchy-Green tensor, which is a common deformation measure on the continuum scale. Following the approach of Khiêm and Itsikov (2016), the average macro-stretch  $\bar{\Lambda}$  can be calculated as the root mean square of the directional macroscopic stretch  $\bar{u}\bar{\Lambda}$  over a unit sphere (see Eq. (5.41)), which results in a unique and simple relationship between the average macro-stretch and the first invariant of a general deformation measure. In accordance to the findings of Kearsley (1989), the relationship reads

$$\bar{\Lambda} = \sqrt{\frac{I_{1,\bar{b}}}{3}} \rightarrow I_{1,\bar{b}} = 3\bar{\Lambda}^2, \quad (5.43)$$

which was also obtained by Wang and Guth (1952); Arruda and Boyce (1993). Hence, the first invariant of a deformation measure is equal to three times the square of the macro-stretch ratio of an infinitesimal line element averaged over all possible orientations (Kearsley, 1989). Based on the proposed concept of Khiêm and Itsikov (2016), macroscopic deformations on a continuum scale represented by the first invariant  $I_{1,\bar{b}}$  of the isochoric, left Cauchy-Green tensor  $\bar{b}$  can be related to the average macro-stretch  $\bar{\Lambda}$  of a polymer full-network model. Summarizing all the results between the average micro-stretch and the deformation measure on a continuum scale, the following relationship results

$$\bar{\lambda} = \bar{\Lambda}^q = \left( \frac{I_{1,\bar{b}}}{3} \right)^{\frac{q}{2}}. \quad (5.44)$$

Hence, the axial deformation of a single polymer chain can be related to the first invariant of a deformation measure, which is generally acting on a continuum scale.

In contrast, regarding the second invariant of the left Cauchy-Green deformation tensor, it is equal to three times the square of the stretch ratio of an infinitesimal area element averaged over all possible orientations (Kearsley, 1989). Therefore,

the average macro-tube-contraction can be derived in accordance to Eq. (5.43), which leads to

$$\bar{\mathcal{V}} = \sqrt{\frac{I_{2,\bar{\mathbf{b}}}}{3}} \rightarrow I_{2,\bar{\mathbf{b}}} = 3\bar{\mathcal{V}}^2. \quad (5.45)$$

Under the assumption that the average micro-tube contraction  $\bar{\nu}$  and the average macro-tube-contraction  $\bar{\mathcal{V}}$  do not coincide, Miehe et al. (2004a) proposed the following micro-macro-transition

$$\bar{\nu} = \bar{\mathcal{V}}^p, \quad (5.46)$$

where  $p$  represents the non-affine tube parameter. Hence, the relation between the average micro-tube-contraction and a macroscopic deformation measure is given through

$$\bar{\nu} = \bar{\mathcal{V}}^p = \left( \frac{I_{2,\bar{\mathbf{b}}}}{3} \right)^{\frac{p}{2}}. \quad (5.47)$$

Based on shown relations, a physically motivated micro-macro transition of the kinematic variables was given.

The **second and third step** to bring a phenomenological constitutive model into the context of molecular-statistical theory can be achieved by proposing a physical micro-macro transition of the free energy  $\psi$  of a single polymer chain confined by a tube and the average macroscopic free energy  $\Psi$  of a full network model. Therefore, the novel, isochoric Helmholtz free energy function, which is dependent on the first and second isochoric invariant of the isochoric, left Cauchy-Green tensor  $\bar{\mathbf{b}}$ , must be transferred onto the micro-scale. Accordingly, the first and second isochoric invariant of the isochoric, left Cauchy-Green tensor must be replaced by the average micro-kinematic variables  $\bar{\lambda}$  and  $\bar{\nu}$ . Regarding the first isochoric invariant  $I_{1,\bar{\mathbf{b}}}$ , it can be expressed by the average micro-stretch  $\bar{\lambda}$ , whereas the second isochoric invariant  $I_{2,\bar{\mathbf{b}}}$  is replaced by the average micro-tube contraction  $\bar{\nu}$ . Therefore, inserting Eq. (5.44) and Eq. (5.44) into Eq. (5.10), the average macroscopic free energy is transferred to free energy of a single polymer chain acting on a micro-scale, which reads

$$\psi_{\text{iso,ND}} = \psi_s + \psi_t = \frac{3 \left( \bar{\lambda}^{\frac{2}{q}} - 1 \right)}{\sum_{i=0}^m \alpha_i \left( 3\bar{\lambda}^{\frac{2}{q}} - 3 \right)^i} + \frac{3 \left( \bar{\nu}^{\frac{2}{q}} - 1 \right)}{\sum_{j=0}^n \beta_j \left( 3\bar{\nu}^{\frac{2}{q}} - 3 \right)^j}. \quad (5.48)$$

Regarding Eq. (5.48), the macroscopic free energy function  $\Psi_{\text{iso,ND}}$  was successfully transferred into the context of molecular-statistical theory.

The **fourth and fifth step** to reconcile a phenomenological hyperelastic material model with the molecular-statistical theory is the approximation of the inverse Langevin function with the molecular-statistically motivated free energy of a sin-

gle polymer chain (see Eq. (5.48)). For this purpose, the free energy must be differentiated with respect to the micro-stretch  $\bar{\lambda}$  in order to obtain a relationship between the micro-force  $\bar{f}_s$  and micro-stretch  $\bar{\lambda}$  of a single polymer chain (see Eq. (5.38)). The better the approximation of behaviour of the non-Gaussian statistical approach, the better the new model is in line with molecular statistical Langevin theory.

To approximate the inverse Langevin function, an objective function  $\mathcal{S}$  must be formulated to minimise the root-mean squared error between the inverse Langevin function and the approximation of it. The material parameters of the derivative of Eq. (5.48) were optimized using MatLab curve fitting toolbox. Since Eq. (5.48) is defined as a stretch and tube part, which are additively combined, the average micro-force dependent on the tube diameter  $d$  must also be approximated for reasons of completeness. Additionally, the fitting results for the Gaussian statistical formulation and the relaxed Langevin approach are presented to show that Eq. (5.48) is well suited to approximate different molecular-statistical approaches and their structural responses (see Fig. 5.7). All relationships between the micro-forces dependent on the micro-stretches with regard to the analysed molecular-statistical approach are derived in Appendix E.

Regarding Fig. 5.7, it is obvious that the micro-mechanical motivated Nelder function of Eq. (5.48) for ( $m = 1, 2, 3$ ) is well suited to represent the structural response of a single polymer chain obeying Gaussian statistics. In Fig. 5.7 b, the fitting result of the inverse Langevin function is illustrated. As can be seen from Fig. 5.7b, the inverse Langevin function was approximated adequately by the third order Nelder function ( $m = 2$ ). Hence, the proposed phenomenological Nelder function was successfully transferred into a micro-mechanical context and is able to account for finite extensibility of a single polymer chain. In Fig. 5.7 c, the fitting results for the structural response of the average micro-force with respect to the average micro-tube contraction are illustrated. It is to note that the micro-mechanically motivated Nelder function ( $n = 0, 1, 2, 3$ ) is also well-suited to represent the average micro-force dependent on the tube diameter  $d$ . Regarding Fig. 5.7 d, the approximation of the relaxed Langevin approach by the micro-mechanically motivated Nelder function is illustrated. Again, the proposed function approximates the behaviour of the relaxed Langevin approach well, proving its micro-mechanical motivation.

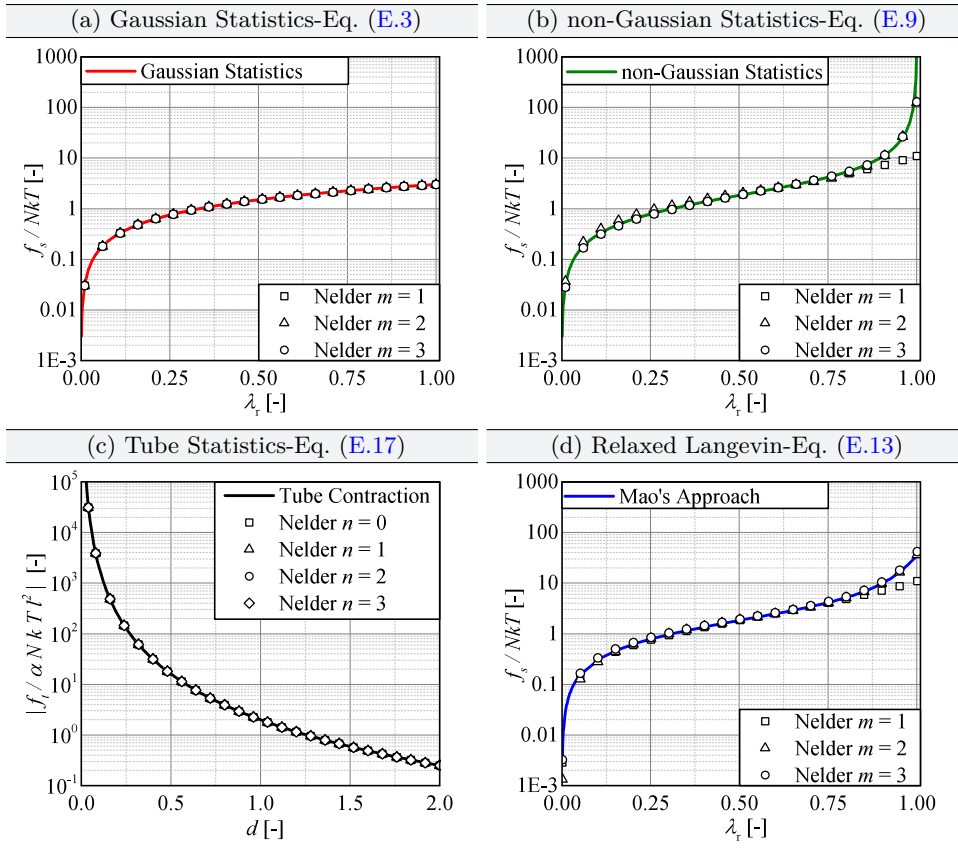


**Figure 5.7** Fitting results of the micro-force and micro-stretch response of different molecular-statistical theories, such as (a) Gaussian and (b) Langevin statistics, (c) the tube contraction and (d) the relaxed Langevin approach, with the micro-mechanically motivated Nelder function of Eq. 5.48 by varying the amount of fitting parameters, which are adjusted by the running indices  $m$  and  $n$

## 5.2 Novel Volumetric Helmholtz Free Energy Function

Regarding volumetric Helmholtz free energy functions, only a few proposals exist in literature to describe volumetric deformations under a physical viewpoint (Bischoff et al., 2001). Generally, the main focus in the development of volumetric Helmholtz free energy functions was set on a nearly incompressible material behaviour, which ensures the element stability even under small isochoric stiffness (Bonet and Wood, 2008:p.171). One approach is given by the penalty function method, which describes a procedure, where the strain energy potential is cal-

culated by the sum of an incompressible material plus a penalty term enforcing the incompressibility constraint reading  $J = 1$  (Simo and Taylor, 1982). In this approach, the penalty term is calculated using a so-called penalty parameter  $K$  multiplied by the relative volume change. Following Belytschko et al. (2013):p.253, the penalty parameter  $K$  should be chosen large enough enforcing the incompressibility constraint, however, yet not so large that numerical ill-conditioning occurs. For these classical approaches the consideration of the microstructure and its development under finite volumetric deformations is missing. The main goal is therefore the development of a volumetric Helmholtz free energy function, which represents the microstructure of the analysed structural silicone, in particular the porosity and its geometric shape and orientation and the void evolution at finite strains.

This chapter is therefore organised as follows. In order to develop a micro-mechanically motivated volumetric Helmholtz free energy function, numerical parameter studies on different types of RVEs were parametrically built up and numerically analysed. Therefore, cubic RVEs were loaded hydrostatically, because the focus lies on the volumetric behaviour only. Since TSSA exhibits a highly porous micro-structure on the nano-scale (see Section 4.4.1), the RVEs were simulated as matrix material containing discrete inherent voids, which were modelled geometrically as holes. Based on the structural responses of the RVEs, a novel volumetric Helmholtz free energy is developed based on the Nelder (1966) function, which was originally proposed to describe a Yield-fertilizer model in agriculture. This section is based on the work of Drass et al. (2018b).

### 5.2.1 Single and Multi-Voided Representative Volume Elements

This section presents modelling strategies for single and multi-voided RVEs of rubber-like materials, which are hydrostatically loaded. The overall goal is to approximate the structural responses of the RVEs with one homogenized volumetric Helmholtz free energy function.

#### Single-Voided Representative Volume Elements

To develop a volumetric Helmholtz free energy function accounting for isotropic void growth, a single-voided RVE containing a centred void was numerically analysed under hydrostatic loading conditions. The single-voided, cubic RVE was parametrically built up varying void fraction  $f_0$ . The void fraction  $f_0$  describes the ratio between void volume and the volume of the RVE in the undeformed condition (see Eq. (2.74)). In contrast to multi-voided RVEs, single-voided RVEs have the advantages that simple relationships of the effective properties of the RVE can be derived. Furthermore, the numerical calculation effort reduces immensely analysing single-voided RVEs. Finally, no constraint equations must be programmed to obtain pe-

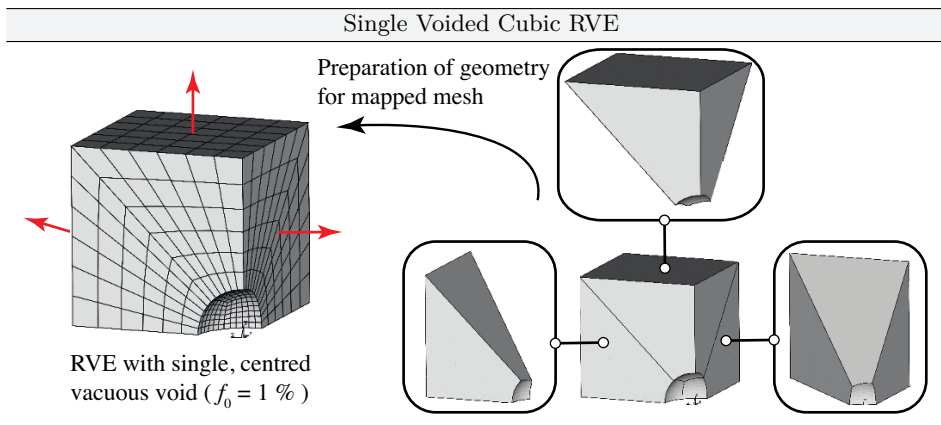


**Figure 5.8** One eighth of the single voided cubic RVE and its division in three equal volumes for mapped meshing

riodic boundary conditions, since periodic and displacement boundary conditions lead to the same structural responses for single-voided RVEs (Drass et al., 2018b).

Since the present approach accounts for void growth under solely elastic conditions, the analysed RVEs were modelled by an incompressible, normalized Neo-Hookean material with an initial shear modulus of  $\mu := 1.0$  MPa. The inherent void was modelled geometrically leaving a vacuous cavity in the geometrical structure with zero stiffness. It is to note that the single centred void represents all inherent voids in the material with respect to a representative aperture of the micro-structure of the material.

To reduce numerical calculation time, an eighth of the RVE was modelled in ANSYS FE Code exploiting symmetry boundary conditions (see Fig. 5.8). Three-dimensional, higher order solid elements were utilized, which exhibit a pure quadratic displacement behaviour. One solid element incorporates 20 nodes with three translational degrees of freedom. The single voided RVE was modelled by a cube with an edge length of  $l_{RVE} = 0.5$  mm, where a sphere was subtracted at one edge by boolean operation (see Fig. 5.8). Regarding the edge length of the RVE, it must be small enough to pertain as a single material point on a macro-scale level and large enough to account for a representative value of inhomogeneities. The length of a single segment of the inhomogeneity is described by  $l$ ,  $l_{RVE}$  represents the length of the RVE and  $L_{Macro}$  describes the macroscopic length of the medium (see Fig. 2.5), which yields

$$l \ll l_{RVE} \ll L_{Macro}. \quad (5.49)$$

To avoid volumetric locking effects due to large volumetric deformations and to reduce numerical calculation time, a mapped mesh was enforced for the numerical

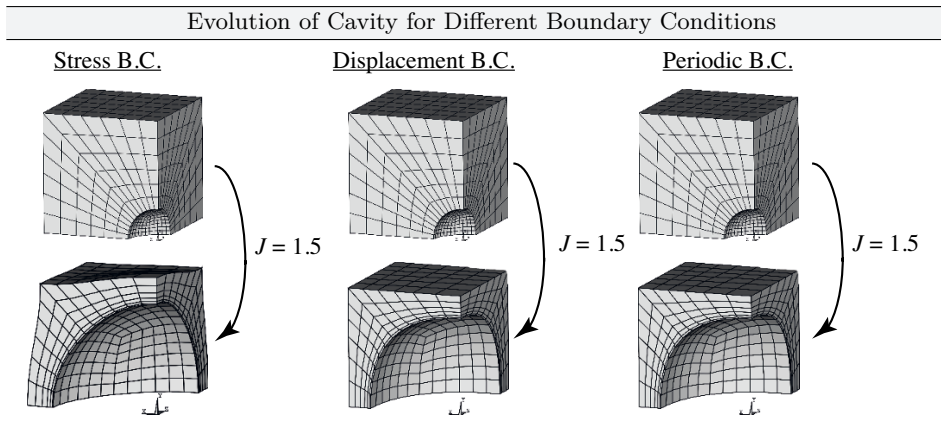


**Figure 5.9** Cavity evolution of single-voided RVE under hydrostatic loading for stress, displacement and periodic boundary conditions

calculation. A mapped mesh is usually more uniform, has less distorted elements, no triangles, and usually has less nodes. To obtain a mapped mesh in ANSYS FE Code, a general three-dimensional body must consist of six areas enclosing a volume. Since the body of the eighth of the RVE is enclosed by seven areas, it was divided into three equal volumes to satisfy the condition for a mapped mesh. Regarding Fig. 5.8, the mesh density was constrained in radial direction by six divisions of the total edge length. Thus, a total of 648 finite elements were analysed for a void fraction of  $f_0 = 1\%$ . It should be noted that as the void fraction decreases, the mesh density in the radial direction must be drastically increased in order to be able to represent the rapid cavity growth under hydrostatic stress.

For the sake of completeness, stress, displacement and periodic boundary conditions were analysed in the numerical models to study the influence on the structural behaviour. While stress boundary conditions lead to highly inhomogeneous displacements in surface normal direction of the analysed single-voided RVE, this boundary condition was not further investigated for the analyses of multi-voided RVEs. Regarding the results of displacement boundary conditions, the deforming surfaces were kept flat. Considering the special case of a single-voided RVE, the results for periodic boundary conditions are identical to them of the displacement boundary conditions. Exemplary, the undeformed and deformed configuration for each applied boundary condition are illustrated in Fig. 5.9, where a single-voided RVE with an initial void fraction of  $f_0 = 1\%$  was hydrostatically deformed until the relative volume equals  $J = 1.5$ .

Additionally to the geometrical analyses of stress, displacement and periodic boundary conditions, a comparative study on the structural response of single-

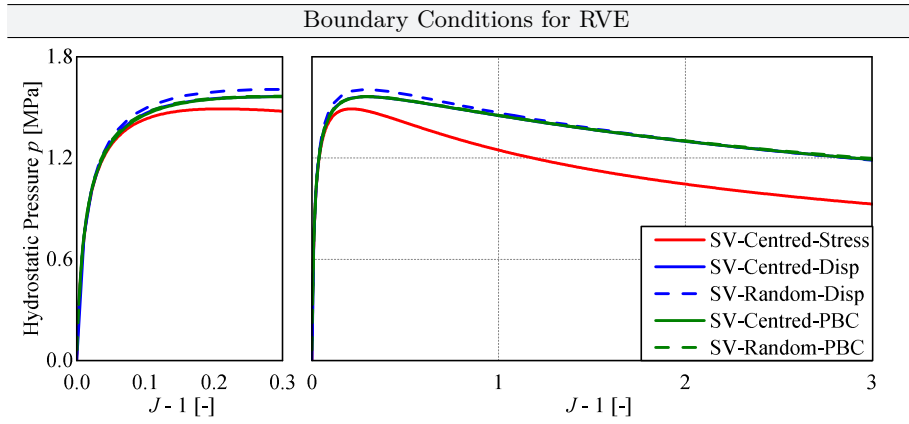


**Figure 5.10** Structural behaviour of single-voided RVEs under hydrostatic tension loading dependent on stress, displacement and periodic conditions respectively void position

voided RVEs with a given void fraction of  $f_0 = 1\%$  was investigated. Furthermore, the influence of the void position was analysed in terms of centred voided RVEs and a randomly positioned void within the RVE. Regarding the structural response of an RVE (hydrostatic pressure vs. relative volume change) under stress boundary conditions, it shows a similar behaviour in comparison to the results for the displacement and periodic boundary conditions (Drass et al., 2017a). Due to the compliance of the RVE, the deformation of opposite outer surfaces are evolving against each other. Based on this, stress boundary conditions represent a lower bound for the structural response in accordance to Miehe (1994). However, regarding the deformed RVE under stress boundary conditions, it does not represent a physically natural geometric shape. In contrast, considering displacement and periodic boundary conditions, more reliable results were obtained in the case of single-voided RVEs. Regarding the influence of the void position, the randomly distributed void under displacement boundary conditions lead to an upper bound for the structural response. However, the solution for a randomly distributed void under displacement boundary conditions approximates the solution of periodic boundary conditions at large volume strains asymptotically.

Regarding Fig. 5.10, it is interesting to note that the results for periodic boundary conditions with a centred or randomly distributed void are almost identical compared to the results of a centred void underlying displacement boundary conditions. Based on the proposed studies on different boundary conditions, only periodic boundary conditions lead to physical reasonable results for periodic microstructures, since an interaction of the single RVE with surrounding RVEs can be modelled with this special boundary condition. Hence, periodic boundary condi-

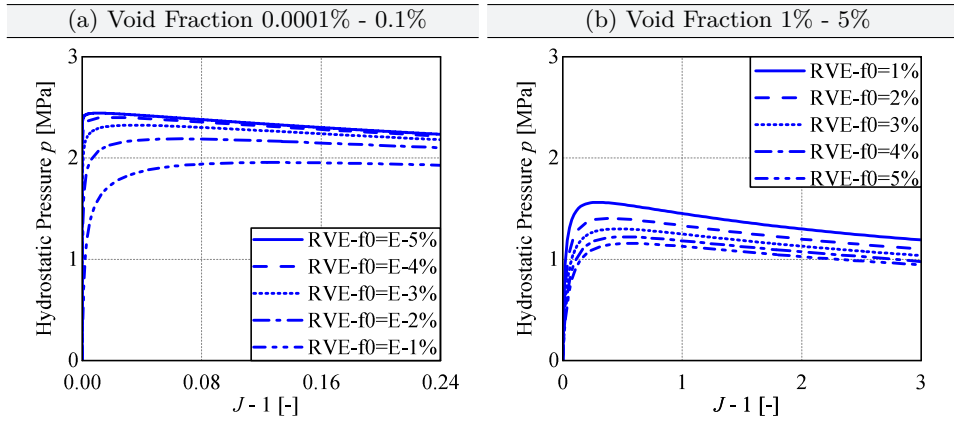


**Figure 5.11** Structural behaviour of single-voided RVEs with periodic and displacement boundary conditions respectively under hydrostatic tension loading dependent on void fraction  $f_0$

tions ensure a periodically repeating deformation of an RVE without overlapping cavities (Danielsson et al., 2007).

As final analyses of single-voided RVEs, the void fraction  $f_0$  was varied from almost infinite small to finite porosity. The results of the numerical analyses of single-voided RVEs containing a centred void are prepared in terms of illustrating the resulting hydrostatic pressure  $p$  with respect the dilatation  $D_V = J - 1$ . As boundary conditions, periodic boundary conditions were applied within the numerical model. The structural responses of the single-voided RVEs are represented in Fig. 5.11. For small volume changes, the hydrostatic stress increases immensely, which can be related to a high initial stiffness. Reaching critical volume changes, the initially stiff effective structural response is followed by a strong softening. It is interesting to note that the critical hydrostatic pressure  $p_{cr}$  depends obviously on the void fraction. Hence, a decrease of the initial void fraction leads to an increase of the critical hydrostatic pressure  $p_{cr}$ . Based on the performed numerical studies, the limit value for  $p_{cr}$  equals

$$\lim_{f_0 \rightarrow +0} p_{cr} = \frac{5}{2}\mu, \quad (5.50)$$

which corresponds to the well-known solution for the onset cavitation accordingly to Ball (1982), who analysed a class of non-smooth bifurcation problems, which account for cavity nucleation at the centre of a unit ball with an incompressible matrix.

## Multi-Voided Representative Volume Elements

Regarding more sophisticated RVEs, e.g. multi-voided RVEs containing a large amount of randomly distributed voids in the matrix, an enhancement towards a more complex modelling approach will be presented in accordance to Drass et al. (2017a). For numerical analyses of the micro-mechanical models, different types of RVEs are set up parametrically and analysed numerically. Generally, the RVEs differ in their distribution of voids and their boundary conditions.

In order to get a short overview of various strategies to set up RVE's with several inhomogeneities, a short literature overview is given below. Starting with the required size of an RVE, it can be approximated by the smallest unit cell considering global or local periodicity of the material structure (Suquet, 1987; Miehe and Koch, 2002; Nemat-Nasser and Hori, 2013). However, classical unit cell analyses can lead to an improper representation of the material behaviour when material or structural instabilities occur on the micro-scale (Ohno et al., 2002; Miehe et al., 2004b; Miehe et al., 2002). Evesque and Adjémian (2002) recommend that an RVE should contain at least ten inhomogeneities. Kanit et al. (2003) proposed a methodology, where different morphologies of the micro-structure were generated. The micro-structures were constructed by four to five different sample sizes of the unit cell. Afterwards the effective material properties were computed by averaging over all four structural models. It was found that only a small influence on the effective material properties could be determined. Gusev (1997) analysed statistically independent microstructures of a periodic elastic composite with a disordered unit cell of 8, 27, and 64 non-overlapping identical spheres, wherein the relative volume between matrix material and inhomogeneities was kept constant. Based on Monte Carlo realizations of the RVEs, in which the number and position of the pores were varied, the effective properties were calculated. It turned out that the scatter in the calculated elastic constants was remarkably small even for a small amount of inherent inclusions.

As shown in the short literature review, the number and position of inhomogeneities in the RVE has only a minor influence on the effective properties. However, to study the small influence of these parameters, the present approach analyses randomly distributed voids placed in a hexagonal cubic lattice (see Fig. 5.12). Therefore, the length  $l_{\text{RVE}}$  of the RVE is divided by the parameter  $n_{\text{div}}$ . The total amount of cells within the RVE is calculated by  $n_{\text{div}}^3$ . Based on the fragmentation of the RVE by  $n_{\text{div}}^3$  cells, it is possible to randomly place voided or solid cells respectively in the RVE satisfying a pre-defined initial void fraction  $f_0$ . To distribute the voids randomly, array fields and the random number generation in ANSYS FE code were utilized. The array fields were filled with zero and one entries representing voided or solid cells. The cell volumes were generated in a second step in accordance to this assignment. All analysed multi-voided RVEs were modelled uti-

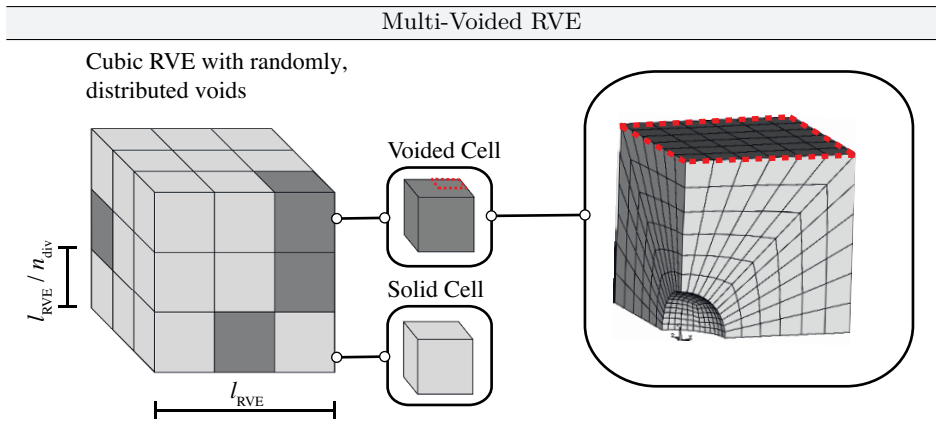


**Figure 5.12** Illustration of modelling approach for multi-Voided RVE

lizing mapped meshes to avoid volumetric locking effects. A free meshed variant is not recommended because here finite elements become highly distorted. To obtain a mapped mesh in a multi-voided RVE, the same meshing method was utilized as already mentioned in the previous section.

In accordance to the single-voided RVE, the bulk material of the multi-voided RVE was modelled as incompressible, normalized Neo-Hookean material. Due to the volume change of the RVE and the incompressibility constraint of the matrix, the vacuous voids grow excessively during calculation. Considering the boundary conditions for multi-voided RVEs, it was already shown that stress boundary conditions lead to unphysical results for single-voided RVEs. Hence, in the following only periodic and displacement boundary conditions are analysed. To model periodic boundary conditions in ANSYS FE Code, the nodes of opposing surfaces are coupled with constraint equations. By setting constraint equations for nodes on opposing surfaces of the RVE, their strains and thus their stresses are kept identical. Thus, the generated RVE can be repeated infinite times in all Cartesian directions, where equal deformation of opposing surfaces are guaranteed. More details on the numerical modelling of the RVE is given in Kiziltoprak (2016).

Similar to the numerical studies on single-voided RVEs, numerical calculations were performed, where multi-voided RVEs with an initial void fraction of  $f_0 = 1\%$  were loaded hydrostatically until a relative volume change of  $J = 1.5$  is reached. In Fig 5.13 the multi-voided RVE is illustrated in the undeformed and deformed configuration with respect to the applied boundary condition. Further, the cavity evolution is illustrated with respect to applied boundary conditions. As shown, the displacement boundary condition leads to an unnatural evolution of the cavities since the growth of cavities is constrained by the outer displacement boundaries.

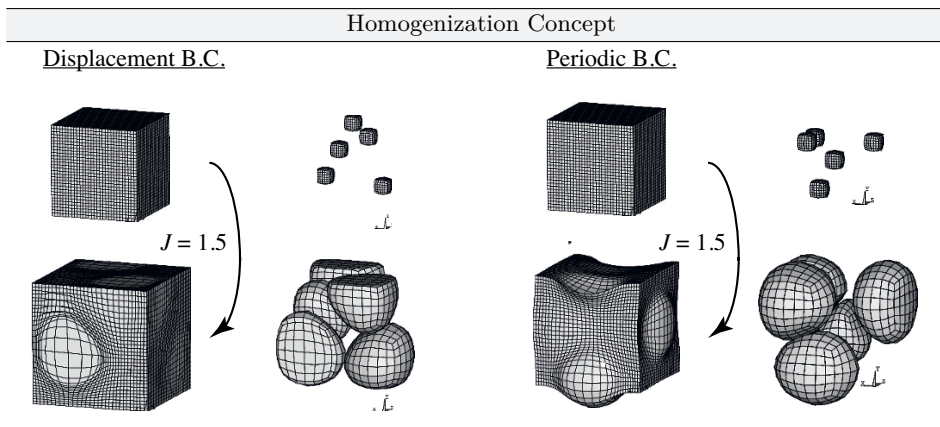


**Figure 5.13** Illustration of homogenization concept between RVE and EHM

To circumvent non-physical void growth due to displacement boundary conditions, the multi-voided RVE was equipped with periodic boundary conditions, where an interaction between the opposite outer surfaces of the RVE was modelled. From Fig 5.13, it is obvious that the initially spherical voids can grow unconstrained. Hence, in the deformed configuration the growing voids exhibit a geometrically natural shape. However, for large volume changes, an interaction between the growing voids cannot be precluded due to excessive void growth. This can be seen in Fig 5.13 on the right side, where the pores and their walls collide due to the increase in volume. Since stress and displacement boundary conditions led to unnatural, geometrical void growth due to the boundary constraint, for the following studies the focus was set on periodic boundary conditions.

For comparative studies, the influence of the amount of voids based on the parameter  $n_{\text{div}}$  was investigated. Additionally, the difference between single-voided and multi-voided RVEs was analysed. Therefore, hydrostatically loaded RVEs with different void fractions were analysed numerically. The single-voided and multi-voided RVEs are equipped with periodic boundary conditions with a constant amount of RVE cells reading  $n_{\text{div}}^3 = 3^3 = 27$ . An initial void fraction of  $f_0 = 1\%$  was assumed. As can be seen from Fig. 5.14 the structural behaviour between single-voided and multi-voided RVEs is almost identical independent on the void fraction. Regarding the influence of  $n_{\text{div}}$  it can be seen that with increasing  $n_{\text{div}}$  a slightly more stiff structural response can be observed. This can be explained by the fact that with increasing number of pores an interaction of the growing voids takes place, whereby a stiffening can be observed.

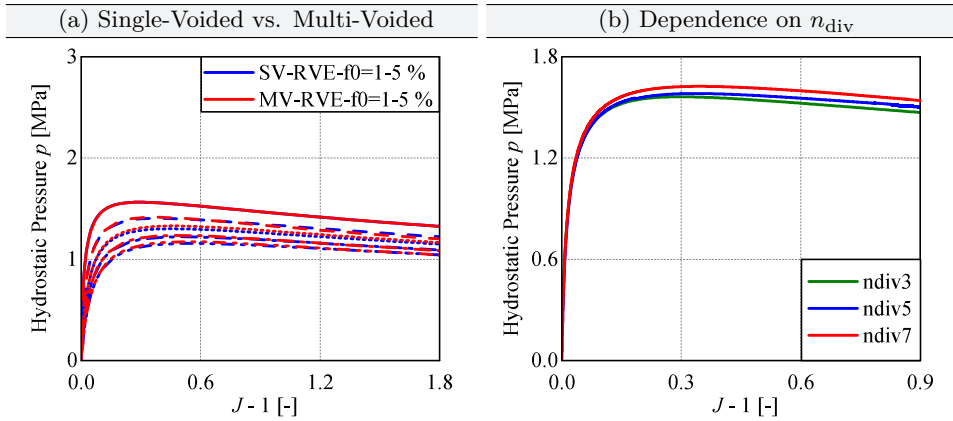


**Figure 5.14** Structural behaviour of single-voided and multi-voided RVEs with periodic respectively displacement boundary conditions under hydrostatic tension loading dependent on void fraction  $f_0$

### 5.2.2 Homogenization Concepts at Finite Strains

To homogenize the structural behaviour of single and multi-voided RVEs under hydrostatic loading, the strain-energy homogenization concept in accordance to Section 2.3.2 is applied. Following Hill (1952) and Ponte Castañeda and Suquet (1995), the strain energy equivalence between an RVE and EHM can be formulated in a non-incremental form reading

$$\langle \Psi^\circ \rangle = \langle \Psi^* \rangle. \quad (5.51)$$

Eq. (5.51) states that the volume-average strain energy density function  $\langle \Psi^\circ \rangle$  of an RVE must be equal to that of an EHM, which is defined as  $\langle \Psi^* \rangle$ . Thus, developing a Helmholtz free energy function, which can reproduce the strain energy of a voided RVE under homogeneous hydrostatic loading, the energetic homogenization of Eq. (5.51) is satisfied. It is to note that the equivalence of the strain energy function can only be achieved, if an equivalent deformation between RVE and EHM prevails in principle. Thus the deformation gradient of an RVE respectively EHM must satisfy

$$\langle F_{ij}^\circ \rangle = \langle F_{ij}^* \rangle. \quad (5.52)$$

Due to the volumetric-isochoric split proposed by Flory (1961), the presented energetic homogenization scheme is very effective in terms of developing a volumetric Helmholtz free energy function accounting for isotropic void growth under homogeneous hydrostatic loading. This is due to the fact that an averaged volumetric strain energy density function can be approximated from the macroscopic structural response of the RVE based of the dependence between the hydrostatic pressure and the relative volume.

Therefore, the approach to develop a volumetric Helmholtz free energy function based on the structural response of a multi-voided RVE under hydrostatic tensile loading is presented below. To do this, one uses the  $p - J$  behaviour of a RVE due to a hydrostatic tensile load and approximates it with any mathematical function capable of representing the initial stiffness followed by softening. Hence, building the integral of hydrostatic pressure  $p(J)$ , which depends on the relative volume  $J$ , the volumetric Helmholtz free energy of a voided RVE can be readily calculated. Following this, a novel volumetric Helmholtz free energy function can be derived by fitting the structural response of a voided RVE in terms of its pressure-volume change. Thus, if  $p(J)$  of a voided RVE is fitted by a function adequately, Eq. (5.51) is automatically satisfied because

$$\Psi_{\text{vol}}(J) = \int_J p(J) dJ, \quad (5.53)$$

$$\frac{d\Psi_{\text{vol}}(J)}{dJ} = p(J) = \int_J K dJ, \quad (5.54)$$

$$\frac{d^2\Psi_{\text{vol}}}{dJ^2} = K \quad (5.55)$$

readily shows how  $\Psi_{\text{vol}}(J)$ ,  $p(J)$  and the bulk modulus  $K$  are related to each other. The most qualified fitting results of the structural response  $p(J)$  of arbitrary voided RVEs were obtained using the already introduced inverse, polynomial function of Nelder (1966), who presented a Yield-fertilizer model in agriculture. Eq. (5.1) has some useful properties, when the function, which must be fitted, rises first and begins to fall with an increasing argument  $x$ . For small  $x$ , the function approximates  $y \approx \beta_0^{-1}x$ , while for large  $x$  the Nelder function can be approximated by  $y \approx (\beta_2 x)^{-1}$ . The peak of the function is present at  $x = \sqrt{\beta_0/\beta_2}$  with a value of  $y_{\text{max}} = 1/\left(2\sqrt{\beta_0/\beta_2} + \beta_1\right)$ . Thus  $\beta_1$  does not affect the position of the maximum. Only the value of  $y$  is influenced by it. Furthermore, the Nelder function has the advantages over usual quadratic polynomial functions that it has no built-in symmetry and its two extremes are described by two separate parameters. In the following, the originally proposed three parameters by Nelder, i.e.  $\beta_i$ , are replaced by  $\kappa_i$  to show that the original Nelder function is now transferred into a different context. Reformulating the original three-parameter Nelder function in the context of compressible hyperelasticity under applying the classical volumetric Helmholtz free energy as basis (see Eq. (3.28)), the hydrostatic pressure reads

$$p(J) = \frac{(J-1)}{\kappa_0 + \kappa_1(J-1) + \kappa_2(J-1)^2}. \quad (5.56)$$

Integrating Eq. (5.56) with respect to the relative volume, one obtains a novel volumetric Helmholtz free energy function with

$$\Psi_{\text{vol,ND}} = \frac{1}{2} \frac{\ln [\kappa_2(J-1)^2 + \kappa_1(J-1) + \kappa_0]}{\kappa_2} - \frac{\kappa_1 \arctan \left[ \frac{2\kappa_2(J-1)+\kappa_1}{\sqrt{4\kappa_0\kappa_2-\kappa_1^2}} \right]}{\kappa_2 \sqrt{4\kappa_0\kappa_2-\kappa_1^2}} \\ - \frac{1}{2} \frac{\ln [\kappa_0]}{\kappa_2} + \frac{\kappa_1 \arctan \left[ \frac{\kappa_1}{\sqrt{4\kappa_0\kappa_2-\kappa_1^2}} \right]}{\kappa_2 \sqrt{4\kappa_0\kappa_2-\kappa_1^2}}, \quad (5.57)$$

which is able to represent voided, incompressible materials under homogeneous hydrostatic loading conditions at finite volume strains. It should be noted that this formulation considers only isotropic processes, i.e. isotropic cavity growth. The novel volumetric Helmholtz free energy function is characterized by three independent parameters  $\kappa_0, \kappa_1, \kappa_2$ . The material parameters can be determined (i) based on the structural response of micro-mechanical models under hydrostatic loading or (ii) using a reverse engineering approach (Drass et al., 2018b). The parameter  $\kappa_0$  represents the inverse initial bulk modulus by  $\kappa_0 := 1/K$ , hence this parameter has a physical background. In contrast,  $\kappa_2$  gives the inverse slope of the secondary tangential bulk modulus representing the softening effect due to void growth. For small volume changes the function approximates  $p \approx \kappa_0^{-1}(J-1)$ , while for large  $J$  the Nelder function can be approximated by  $p \approx (\kappa_2(J-1))^{-1}$ . The bifurcation point, which can be understood as the critical hydrostatic load  $p_{\text{cr}}$ , where cavities start growing excessively, is characterized by all three parameters via

$$p_{\text{cr}} = \frac{\sqrt{\kappa_0\kappa_2}}{2\kappa_0\kappa_2 + \kappa_1\sqrt{\kappa_0\kappa_2}}, \quad (5.58)$$

and

$$J_{\text{cr}} = \frac{\kappa_2 + \sqrt{\kappa_0\kappa_2}}{\kappa_2}. \quad (5.59)$$

At this critical load, inherent cavities start growing excessively. The parameter  $\kappa_1$  controls the bifurcation point  $p_{\text{cr}}$  to great extent. This can be substantiated by calculating the limit of Eq. (5.58), which leads to

$$\lim_{\kappa_0 \rightarrow 0} p_{\text{cr}}(\kappa_0, \kappa_1, \kappa_2) = \frac{1}{\kappa_1}. \quad (5.60)$$

This parameter can also be physically motivated as it describes the critical load for the start of cavitation. Since it is generally known that the maximum critical load or the upper limit respectively is  $p_{cr} = 5/2 \mu$  in accordance to Gent and Lindley (1959) and Ball (1982), the lower limit for  $\kappa_1$  is then defined by

$$\kappa_{1,\text{lower}} = \frac{1}{5/2 \mu} \text{ [MPa].} \quad (5.61)$$

In the case of increasing porosity, it was shown in Fig. 5.11 that the critical hydrostatic load  $p_{cr}$  decreases. Hence,  $\kappa_1$  theoretically aims at infinity, since the critical hydrostatic load is in the denominator (see Eq. (5.62)). Nevertheless, the upper limit of this parameter is limited, since  $p_{cr}(f_0)$  is a function of the porosity. Based on numerical calculations corresponding to those in the chapter is, the critical hydrostatic load is  $p_{cr} \approx 1/4 \mu$  for a porosity of  $f_0 = 50\%$ , so that the upper limit value for a porosity of 50 % can be approximated to

$$\kappa_{1,\text{upper}} = \frac{1}{1/4 \mu} \text{ [MPa].} \quad (5.62)$$

To formulate a generalized form of the novel volumetric Helmholtz free energy function in order to obtain greater adaptability to experimental data, the hydrostatic pressure can be written as a function of the relative volume  $J$  as follows

$$p = \frac{(J-1)}{\sum_{i=0}^m \kappa_i (J-1)^i} \text{ with } i \in \mathbb{N}. \quad (5.63)$$

By integrating Eq. (5.63) with respect to the relative volume  $J$ , one obtains a general expression for the volumetric Helmholtz free energy function with

$$\Psi_{\text{vol,ND}} = \int_J \frac{(J-1)}{\sum_{i=0}^m \kappa_i (J-1)^i} dJ + A \text{ with } i \in \mathbb{N}.$$

(5.64)

To ensure a stress-free reference configuration determined from  $J = 1$ , the integration constant  $A$  must chosen accordingly.

Considering rubber-like materials,  $\kappa_0$  must be very small due to its relation to the inverse bulk modulus. Thus, it is straightforward to build the limit of the function  $p_{cr}$ . With an increase of compressibility, the amount of  $p_{cr}$  is indeed dominated by  $\kappa_1$ , however  $\kappa_0$  and  $\kappa_2$  also have an increasing influence on it. A generic plot of Eq. (5.63) in terms of illustrating the hydrostatic pressure  $p$  with respect to the relative volume  $J$  is represented in Fig. 5.15 a, where a similar structural behaviour

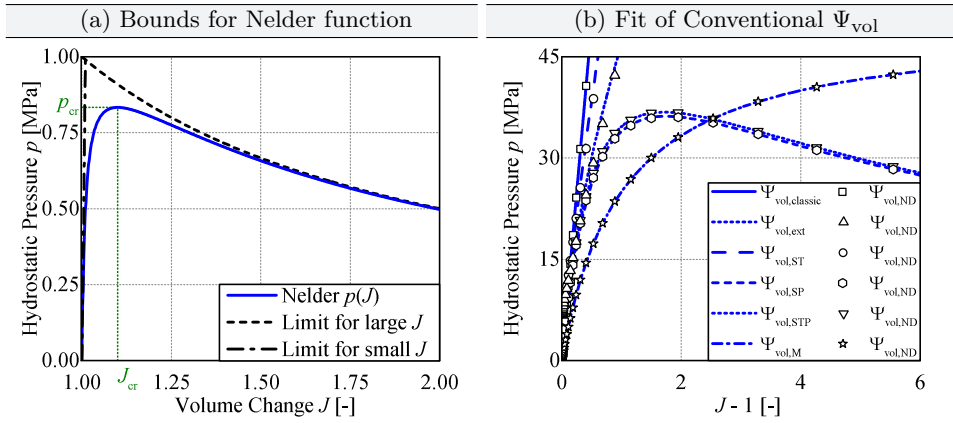


**Figure 5.15** (a) Generic structural behaviour for Nelder function including the limit function for small  $J$ :  $p \approx \kappa_0^{-1}(J - 1)$  and the limit function for large  $J$ :  $p \approx (\kappa_2(J - 1))^{-1}$ ; (b) Approximation of conventional volumetric Helmholtz free energy functions via  $\Psi_{vol,ND}$

to that of voided RVEs is obvious. Additionally, it is proved by Fig. 5.15 b that the novel volumetric Helmholtz free energy function can approximate the structural responses of classical volumetric Helmholtz free energy functions very well. All classical volumetric Helmholtz free energy functions have already been introduced in Section 3.2.5, so these are not described in detail here. However, with the chosen approach all volumetric functions are included by special choice of material parameters. Hence, conventional volumetric Helmholtz free energy functions as proposed in Eqs. (3.28)-(3.33) are incorporated by Eq (5.64).

To show the adaptability of the novel volumetric Helmholtz free energy function, parameter studies were conducted in terms of analysing homogeneous hydrostatic loading conditions. Regarding hyperelastic constitutive models in general, the volumetric-isochoric split of a strain energy density function is advantageous due to two separated strain energy density functions. For the isochoric part of the Helmholtz free energy function a classical, normalized Neo-Hookean material corresponding to Eq. (3.24) was utilized. In contrast to the volumetric Helmholtz free energy functions proposed in Section 3.2.3, all following studies were performed with the novel volumetric Helmholtz free energy function. Hence, the following parameter studies utilize Eq. (5.64) as material model, where the running index  $m$  was set constant to  $m = 3$ .

Starting with a pure homogeneous hydrostatic tension loading, Fig. 5.16 illustrates the structural behaviour of the novel volumetric Helmholtz free energy function in terms of analysing the  $p(J)$  behaviour. As obvious and already mentioned, each parameter of the Eq. (5.64) has a clear influence on the structural behaviour

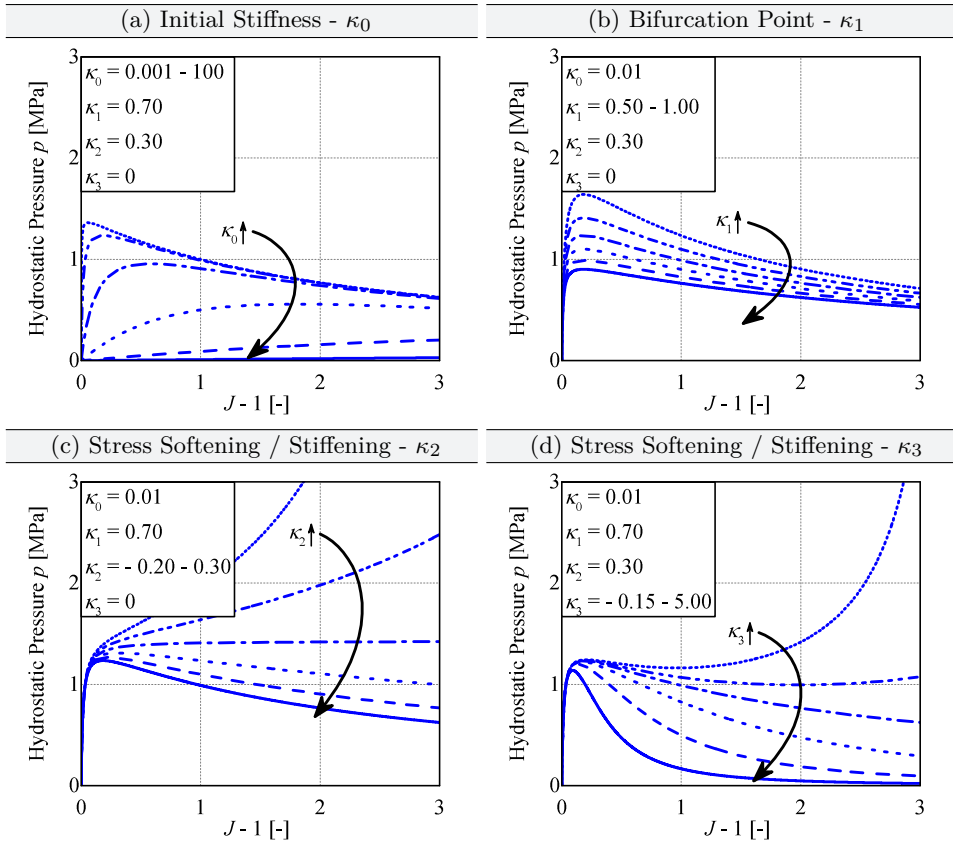


**Figure 5.16** Parameter studies on novel volumetric Helmholtz free energy function analysing a unit cell under homogeneous hydrostatic loading: (a) variation of  $\kappa_0$ , (b) variation of  $\kappa_1$ , (c) variation of  $\kappa_2$  and (d) variation of  $\kappa_3$

under homogeneous hydrostatic loading and a physical background. The initial stiffness is essentially influenced by the material parameter  $\kappa_0$ , whereas the bifurcation point is governed by  $\kappa_1$ . In this context, the bifurcation point denotes the critical hydrostatic load, at which stress softening effects ensue, which is conterminous with excessive void growth effects. It is worth mentioning again that softening caused by cavitation refers to the decrease of the effective hydrostatic pressure, but at the local material level in the matrix material an increase of the stresses occurs. Returning to the material parameters and its definitions,  $\kappa_2$  and  $\kappa_3$ , control the stress softening respectively stiffening after reaching the bifurcation point (see Fig. 5.16).

### 5.2.3 RVE vs. EHM - Numerical Homogenization

To analyse the accuracy of the numerical homogenization as well as the performance of the proposed volumetric Helmholtz free energy function  $\Psi_{\text{vol,ND}}$ , a comparison of the numerical results of a discrete RVE with those of an EHM is presented. Since the following chapter only refers to the development of a new volumetric strain energy density, which is able to reproduce the effective softening of the hydrostatic pressure with increasing hydrostatic deformation, only purely hydrostatic loading is analysed in this section. An extension of the present approach to arbitrary deformations is proposed in the next chapter.

The basis for structural response of the RVE is a single-voided cubic RVE under hydrostatic loading conditions. Referring to the results of Section 5.2.1, the single void was centred to reduce numerical calculation time. The analysed RVE was modelled by an incompressible, normalized Neo-Hookean material with an initial shear modulus of  $\mu := 1.0 \text{ MPa}$ . In contrast, the cubic, unvoided EHM was equipped with the new developed constitutive model. Referring to Eq. (5.64) respectively Eq. (5.63), the running index  $m$  was set constant to  $m = 3$ . Hence, four material parameters were fitted by non-linear regression analyses to obtain the material parameters for the EHM. In Fig. 5.17, the comparison of the structural response of RVE and EHM is presented by varying the void fraction from  $f_0 = 10^{-5} \%$  to 5 %. As can be seen from the comparison, the approximation of the structural behaviour of the RVE's with the homogenized structural behaviour of the EHM's provides good results. From these studies, it can be stated that firstly the numerical homogenization postulated in Eq. (5.51) is adequate, secondly the proposed volumetric Helmholtz free energy function in accordance to Eq. (5.57) was correctly implemented into the commercial FE package and thirdly the proposed approach represents the structural response of the RVE with a very good accuracy (cf. Fig. 5.17). Thus, the proposed constitutive model is adequate to represent excessive void growth at finite volume strains.

### 5.2.4 Bounds in Micro-Mechanics

Several analytical approaches exist in literature to identify initial and effective stiffness parameters (see Section 2.3.3), like the shear modulus, bulk modulus as well as the elastic stiffness tensor of inhomogeneous materials. Therefore, it is obvious to investigate whether the presented model is able to approximate the effective material parameters of a voided material and to correlate them with the approaches from the literature.

To be more specifically, a comparison between the numerical results for the initial bulk modulus  $K = 1/\kappa_0$  corresponding to the novel volumetric Helmholtz free energy function and values from literature is presented in the following. The com-

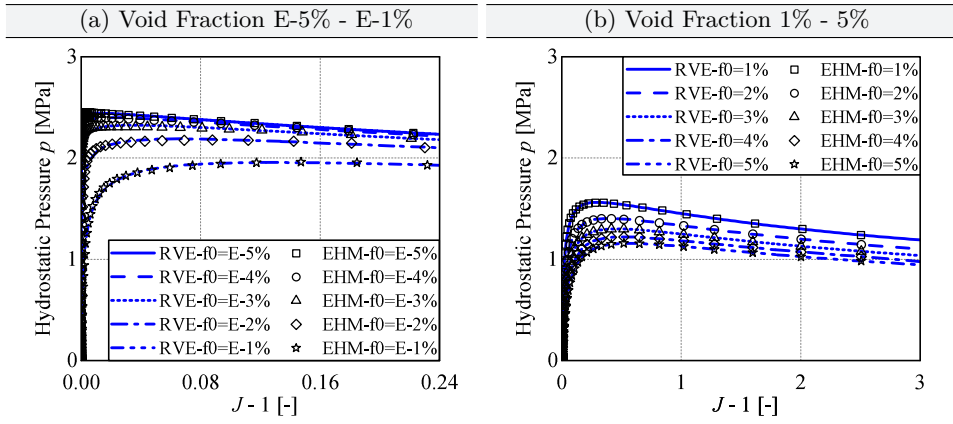


**Figure 5.17** Accuracy of numerical homogenization by comparison the results of the RVE and EHM based on an incompressible normalized Neo-Hookean material

parison of the initial bulk modulus  $K$  is instructive from an engineering standpoint, since the new proposed constitutive equation must include the analytical solutions for elastic constants of voided materials (Benveniste, 1987).

Considering a voided material, which is composed of an incompressible matrix containing a spherical void in the centre, Budiansky (1965) and Hill (1965) proposed an analytical, self-consistent estimate for the effective initial bulk modulus  $\bar{K}_0$ , which reads

$$\bar{K}_{BH} = \mu \frac{4(1-2f_0)(1-f_0)}{f_0(3-f_0)}. \quad (5.65)$$

This approach is limited to heterogeneous materials consisting of contiguous, more or less spherical grains of each phase, whereby Budiansky (1965) already writes in his contribution that the chosen approach provides only limited physical results for extreme conditions of phase stiffness.

A physically motivated solution for voided materials was proposed by Mori and Tanaka (1973), where the effective field approximation based on Eshelby's elasticity solution for inhomogeneity in infinite medium was proposed. The solution of Mori and Tanaka (1973) is given by

$$\bar{K}_{MT} = \mu \frac{4}{3} \left( \frac{1}{f_0} - 1 \right). \quad (5.66)$$

Fig. 5.18 shows the solutions for the effective bulk modulus of a voided material by varying the porosity, whereby the shear modulus of the matrix material was set constant to  $\mu = 1$  for reasons of comparability. Beginning with the results of the self-consistent estimates of Budiansky (1965) and Hill (1965), it can only be utilized

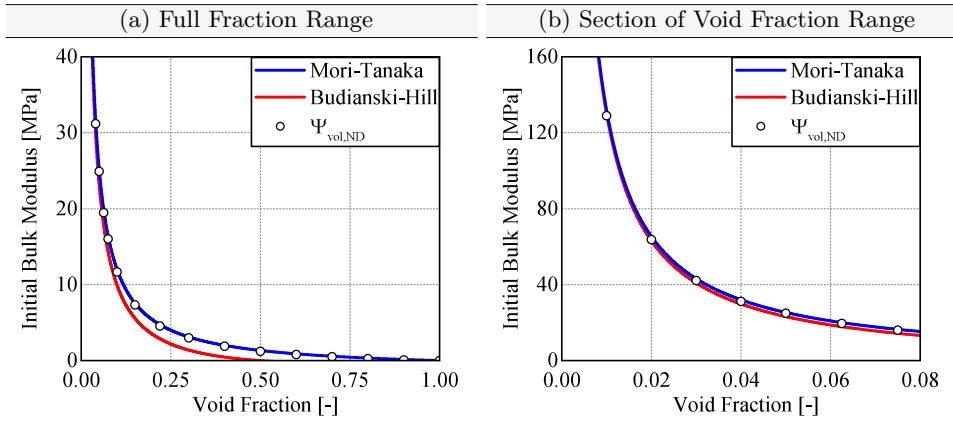


**Figure 5.18** Comparison of initial bulk modulus between analytical solutions and the present volumetric model at small strains: (a) full range of void fraction and (b) section of void fraction range

for small void fractions. Reaching a void fraction of  $f_0 = 50\%$ , the elastic moduli decrease to zero, which is not reasonable under a physical viewpoint. However, for small void fractions the strong decrease of the initial bulk modulus is adequately represented (see Fig. 5.18 b). From Fig. 5.18 it follows that the solution of Mori and Tanaka (1973) is also applicable for large void fractions on the one hand and agrees with the solution of Budiansky (1965); Hill (1965) under consideration of small voids on the other hand. Now, comparing the results for the effective initial bulk modulus of the present constitutive approach with the approximate solutions of Budiansky (1965), Hill (1965) and Mori and Tanaka (1973). Regarding Figure 5.18 both solutions are approximated by the approach of  $\Psi_{vol,ND}$  for small void fractions. Considering larger void fractions ( $f_0 > 10\%$ ) it is noticeable that the result of Mori and Tanaka (1973) is well approximated, which at the same time means that the new model reflects the physical behaviour of a voided material.

### 5.2.5 Remarks on Volumetric Helmholtz Free Energy Functions

In order to study the behaviour of the proposed volumetric strain energy density function not only in pure hydrostatic load cases, simple tension problems using a Flory-type hyperelastic material model are analysed in the following. The compressible Neo-Hookean material model combined with the novel non-linear volumetric Helmholtz free energy function reads

$$\Psi = \frac{\mu}{2} (I_{\bar{b}} - 3) + \int_J \frac{(J-1)}{\sum_{i=0}^m \kappa_i (J-1)^i} dJ. \quad (5.67)$$

Dealing with a compressible Flory-type hyperelastic material formulation, anomalies within the structural behaviour may occur due to the volumetric-isochoric split of an arbitrary Helmholtz free energy function (Ehlers and Eipper, 1998), which has already been shown in Section 3.2.3. Since the proposed non-linear volumetric Helmholtz free energy function accounts for stress softening due to the cavitation effect, it is logical that it may lead to an abnormal structural performance under isochoric deformation modes.

In accordance to Section 3.2.3, simple tension problems for a nearly incompressible behaviour ( $\kappa_0 \rightarrow 0$ ) and highly compressible material behaviour have been analysed, where classical formulations of the volumetric Helmholtz free energy function were applied. In contrast, in this study we analyse the novel, strongly non-linear volumetric strain energy density function, where the initial bulk modulus is varied between  $10 \leq K \leq 1000$  MPa. Since the present study does not investigate the influence of the bifurcation point for the onset of cavitation and softening behaviour, these parameters are set constant. Thus, the bifurcation point is governed by  $\kappa_1 = 0.7$  and the stress softening parameters read  $\kappa_2 = 0.3$  and  $\kappa_3 = 0$ .

In Fig. 5.19 the results for the simple tension problem are illustrated under different viewpoints. Fig. 5.19 a shows the first and second principal stretch of a unit cell under uniaxial tension are illustrated. Keeping in mind that the second principal stretch  $\lambda_2$  must be calculated by Eq. (3.16) as implicit function of the first principal stretch  $\lambda_1$ , an anomaly in the structural behaviour is obvious. With an increase of the first principal stretch  $\lambda_1$ , a decrease of the lateral stretch can be regarded. However, reaching a critical deformation level, the lateral stretch increases with an increasing longitudinal deformation. This means that the specimens becomes thicker under uniaxial tension deformation, which is not physical. This can be also observed regarding Fig. 5.19 b, where a strong increase of the relative volume can be regarded for large longitudinal stretches. The strong increase of relative volume leads to stress softening effects under a uniaxial deformation. Considering Fig. 5.19 c, where the axial Cauchy stress is plotted against the Hencky strain, the structural responses show a physical behaviour until a critical strain is reached. After reaching the critical point, a decrease of stress can be observed for all analysed case studies. This can be also confirmed with regard to Fig. 5.19 d, where a distinct stress softening can be observed for the Cauchy stress plotted against the dilatation  $J - 1$ . Since this behaviour shows evidently an anomaly in the structural performance in accordance to Ehlers and Eipper (1998), the proposed Helmholtz free energy function must be enhanced to exclude such softening effect under isochoric deformations. For pure volumetric deformations, however, the new volumetric Helmholtz free energy function is well suited to represent a stiff structural response followed by excessive stress softening. Even stress softening

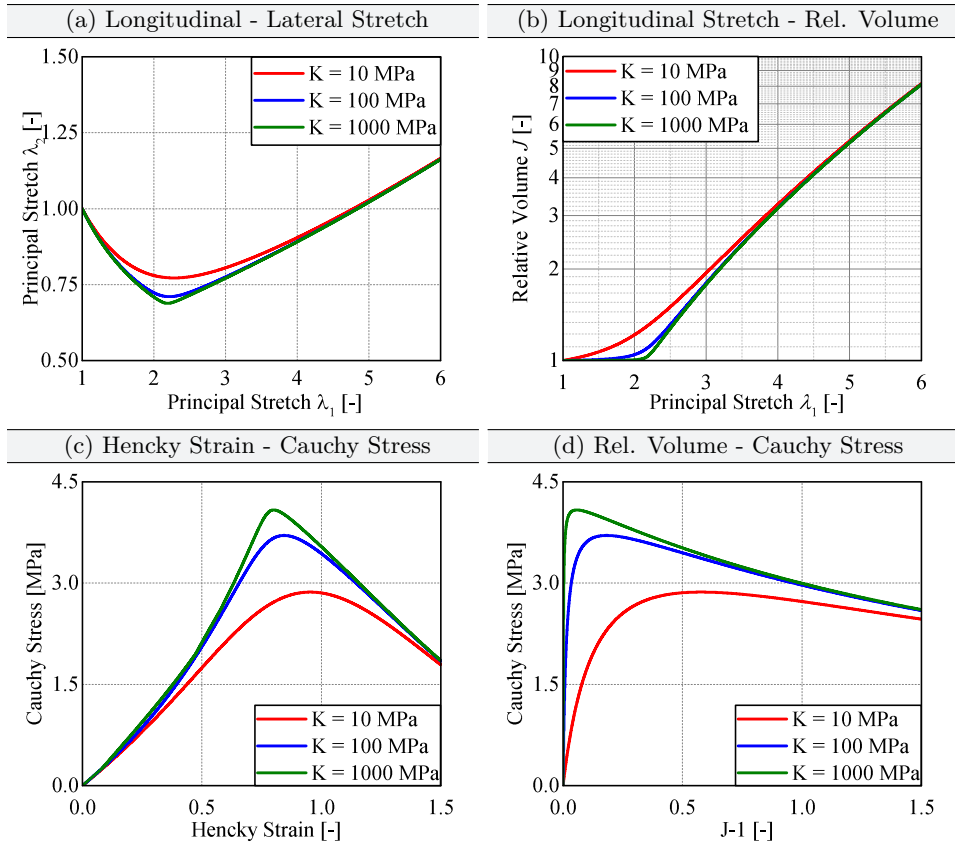


**Figure 5.19** Parameter studies on novel volumetric Helmholtz free energy function in accordance to Eq. (5.67) analysing a unit cell under uniaxial tension loading: (a)  $\lambda_1 - \lambda_2$ , (b)  $\lambda_1 - J$ , (c)  $\sigma - \varepsilon$  and (d)  $\sigma - (J-1)$

with subsequent stress stiffening can be easily adjusted with the newly proposed volumetric Helmholtz-free energy function (see Fig. 5.17).

To avoid this non-physical mechanical behaviour, Drass et al. (2018b) presented a so-called void growth criterion. The void growth criterion differentiates between isochoric and volumetric deformations based on case differentiation — an "if-request" during finite element calculations. Another possibility is to formulate a condition for the start of volumetric softening. This approach was followed by Drass et al. (2017a); Drass et al. (2018c) in terms of a continuum damage formulation. However, it is advantageous to avoid case differentiation in the algorithm in order to obtain an efficient and robust numerical calculation without obtaining mesh-dependent results (Waffenschmidt et al., 2014). This procedure is applied

and presented in detail in Section 5.3, where a continuous pseudo-elastic formulation of the non-linear volumetric Helmholtz free energy function is formulated without an if-request in the algorithmic setting.

## 5.3 Pseudo-Elastic Cavitation Model

A pseudo-elastic Helmholtz free energy function is derived in the following, which takes into account the effective stress softening caused by cavitation in rubber-like materials. In contrast to the approach of Ogden and Roxburgh (1999), in which the theory of pseudo-elasticity was used to calculate Mullins damage in filled rubbers, here the contribution of the strain energy due to the anisotropic geometrical evolution of inherent cavities in the bulk material for any deformation is determined. The pseudo-elasticity approach in accordance to Ogden and Roxburgh (1999) was deliberately chosen to avoid multi-scale modelling (Dal et al., 2018), homogenization methods (Lopez-Pamies and Castañeda, 2007a; Lopez-Pamies and Castañeda, 2007b) or even the FE<sup>2</sup> method (Feyel, 2003) for reasons of simplicity and time saving by the numerically complex calculation methods.

The advantages are that the hyperelastic Helmholtz free energy function can be explicitly described at the macro-scale, the Flory-type volumetric-isochoric split can be used, which is ideal for the separate determination of material parameters, damage and healing effects can be modelled without great effort and the renouncement of time-consuming multi-scale modelling methods.

### 5.3.1 General Concept

To define a macroscopic Helmholtz free energy function that calculates the volumetric Helmholtz free energy of a porous rubber-like material under any deformation phenomenologically, the pseudo-elasticity approach according to Lazopoulos and Ogden (1998) is used. In principle, we assume a Flory-type hyperelastic material law with the special feature that the volumetric part of the functional is able to describe isotropic void growth. Drass et al. (2018b) presented a non-linear volumetric Helmholtz free energy function, which is capable of representing the cavitation effect and thus effective stress softening due to growing voids caused by triaxial loading (see also Section 5.2). Hence, the strain energy density function reads

$$\Psi(\mathbf{b}) = \Psi_{\text{iso}}(\bar{\mathbf{b}}) + \Psi_{\text{vol,ND}}(J). \quad (5.68)$$

The advantages of this formulation lie in the application of the Flory-type volumetric-isochoric split, the possibility of representing stress softening due to cavitation and the adaptability of the volumetric formulation. The disadvantage was already described in Section 5.2.5, where under isochoric loads anomalies can be observed in

the structural response that only arise from the application of the Flory-type split of the Helmholtz free energy function. Therefore, the pseudo-elastic formulation is chosen in order to avoid the disadvantages mentioned above.

Nonetheless, to take advantage of the benefits of the Flory-type hyperelastic material and the non-linear volumetric Helmholtz free energy function  $\Psi_{\text{vol,ND}}$ , which is also capable of representing stress softening due to cavitation, an additional strain energy couple term  $\Psi_{\text{couple}}$  is added. This couple term expresses the amount of the strain energy due to anisotropic geometric evolution of a void in relation to the dissipated energy due to isotropic void growth. Keeping this in mind, the modified Helmholtz free energy function reads

$$\Psi(\mathbf{b}) = \Psi_{\text{iso}}(\bar{\mathbf{b}}) + \Psi_{\text{vol,ND}}(J) + \Psi_{\text{couple}}(J, \Omega). \quad (5.69)$$

To be more specific, the strain energy coupling term is defined by a shape function  $\Omega \in [0, 1]$  based on the geometrical evolution of a deforming void. The variable  $\Omega$  has therefore two main objectives. On the one hand, it governs the amount of how much dissipated strain energy  $\mathcal{D}_{\text{cav}}$  due to void growth goes into the functional additionally, and on the other hand, it basically decides whether there is a volumetric or isochoric deformation. In the case of a purely volumetric deformation,  $\Psi_{\text{vol,ND}}$  alone is able to calculate the strain energy as a result of void growth, so that the additional dissipated strain energy  $\mathcal{D}_{\text{cav}}$  due to cavitation must become zero. Consequently,  $\Omega$  must be zero for a volumetric load. Looking at isochoric deformations,  $\Omega$  must assume values of  $> 0$  to compensate for the loss strain energy caused by pore growth, as no significant pore growth is expected under isochoric deformations. The dissipated strain energy  $\mathcal{D}_{\text{cav}}$  is defined as the difference between an unvoided and voided hyperelastic material under hydrostatic loading. For reasons of simplicity it is assumed that the dissipated strain energy reads

$$\mathcal{D}_{\text{cav}} = \Psi_{\text{vol,classic}} - \Psi_{\text{vol,ND}}, \quad (5.70)$$

which serves as a working hypothesis. An exemplary illustration of the dissipated strain energy due to void growth is shown Fig. 5.20.

Since the coupling term depends on the global deformation gradient  $\mathbf{F}$ , i.e. on isochoric and volumetric deformations, it can be understood as an intermediate configuration between the volumetric and isochoric configurations. To illustrate this, Fig. 5.21 shows the volumetric, isochoric and intermediate configuration and the associated Helmholtz free energy functions. To clarify that the computation of the Helmholtz free energies for the respective configuration is concerned, the undeformed and deformed material bodies ( $\mathcal{B}_0$ ,  $\mathcal{B}_J$ ,  $\bar{\mathcal{B}}$  and  $\mathcal{B}$ ) including a deforming cavity for the respective configuration are shown.

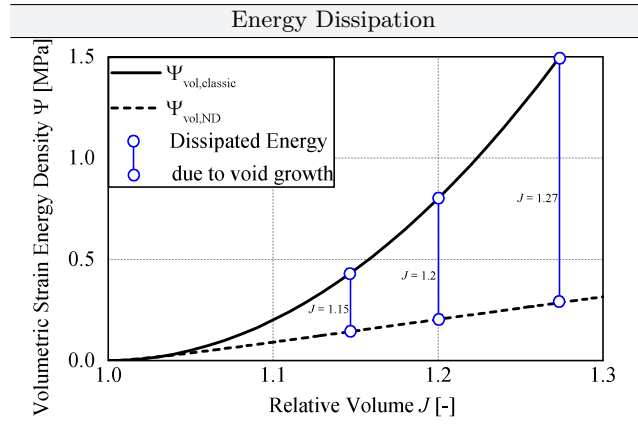


**Figure 5.20** Illustration of the total energy dissipation  $\mathcal{D}_{\text{cav}}$  due to void growth

To be in line with the theory of pseudo-elasticity, a function  $\phi$  depending on  $\Omega$  must also be added, which serves to implicitly calculate the shape function  $\Omega$  in terms of the state of deformation. In contrast to the approach of Ogden and Roxburgh (1999), in which  $\phi(\Omega)$  was understood as a kind of damage function to describe the Mullins effect under cyclic loading of filled rubbers,  $\phi(\Omega)$  represents the counterpart of a damage function in this case and thus serves only to determine the shape function  $\Omega$ .

This approach is consistent with the proposed ansatz of Lazopoulos and Ogden (1998); Ogden and Roxburgh (1999) and Dorfmann and Ogden (2003). Accordingly, the entire pseudo-elastic Helmholtz free energy function can now be written as

$$\Psi = \Psi_{\text{iso}}(\bar{\mathbf{b}}) + \Psi_{\text{vol,ND}}(J) + \underbrace{\Omega \mathcal{D}_{\text{cav}}(J) + \phi(\Omega)}_{\Psi_{\text{couple}}(J, \Omega)}, \quad (5.71)$$

where now the strain energy couple term  $\Psi_{\text{couple}}(J, \Omega)$  is defined as the sum of  $\Omega \mathcal{D}_{\text{cav}}$  and  $\phi(\Omega)$ .

The calculation of the Cauchy stress tensor for a Flory-type hyperelastic material is generally done by

$$\boldsymbol{\sigma} = \frac{2}{J} \left[ \frac{\partial \Psi_{\text{iso}}}{\partial \mathbf{b}}(\bar{\mathbf{b}}) + \frac{\partial \Psi_{\text{vol}}}{\partial \mathbf{b}}(J) \right] \cdot \mathbf{b}. \quad (5.72)$$

For the stress calculation of the couple term,  $\Omega$  must also be considered, since it depends on the macroscopic deformation gradient  $\mathbf{F}$  or on the left Cauchy Green

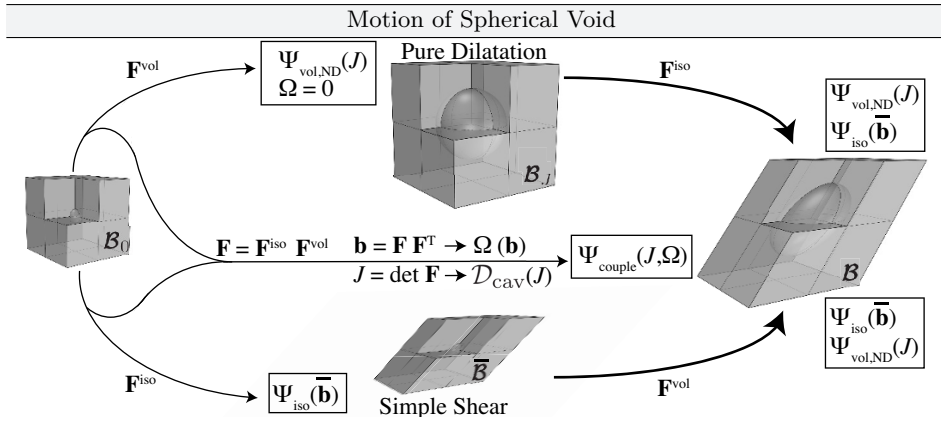


**Figure 5.21** Behaviour of initially spherical void under volumetric, isochoric and intermediate configurations

tensor  $\mathbf{b}$  respectively. Considering only  $\Psi_{\text{couple}}$  from Eq. (5.71), the Cauchy stress tensor is calculated as follows:

$$\boldsymbol{\sigma}_{\text{couple}} = \frac{2}{J} \left[ \frac{\partial \Psi_{\text{couple}}}{\partial \mathbf{b}} (J, \Omega) + \frac{\partial \Psi_{\text{couple}}}{\partial \Omega} (J, \Omega) \frac{\partial \Omega}{\partial \mathbf{b}} (\mathbf{b}) \right] \cdot \mathbf{b}. \quad (5.73)$$

Keeping in mind that Lazopoulos and Ogden (1998) determined an additional equilibrium equation based on equilibrium thermodynamics, which only results from the inclusion of an internal variable in the constitutive model, here  $\Omega$ , the calculation of the Cauchy stress tensor for the couple term simplifies considerably (Dorfmann and Ogden, 2003). Since the additional equilibrium equation

$$\frac{\partial \Psi_{\text{couple}}}{\partial \Omega} (J, \Omega) \stackrel{!}{=} 0 \quad (5.74)$$

must be ensured according to Lazopoulos and Ogden (1998), the Cauchy stress tensor is calculated after some mathematical manipulations with respect to the pseudo-elastic Helmholtz free energy function of Eq. (5.71) to

$$\boldsymbol{\sigma} = \left[ \frac{2}{J} \frac{\partial \Psi_{\text{iso}} (\bar{\mathbf{b}})}{\partial \bar{\mathbf{b}}} \cdot \bar{\mathbf{b}} \right]^{\text{dev}} + \underbrace{\left[ \frac{\partial \Psi_{\text{vol}}}{\partial J} (J, \Omega) + \frac{\partial \Psi_{\text{couple}}}{\partial J} (J, \Omega) \right]}_{=p} \mathbf{I}, \quad (5.75)$$

where  $p$  represents in general the hydrostatic pressure.

Since up to this point the shape function is still unknown but the constraint equation Eq. (5.74) implicitly defines the variable  $\Omega$ , the pseudo-elastic Helmholtz free energy function is now differentiated with respect to  $\Omega$  resulting in

$$\frac{\partial \Psi}{\partial \Omega} = \mathcal{D}_{\text{cav}} + \phi'(\Omega) = 0. \quad (5.76)$$

This equation is used in the following to derive the form function. However, additional constraint equations must be defined for  $\phi$ . An additional constraint equation accordingly to Ogden and Roxburgh (1999), which must be fulfilled to determine the shape function  $\Omega$ , reads

$$\phi(\Omega)|_{\Omega=0} = 0. \quad (5.77)$$

If  $\Omega$  is inactive, i.e.  $\Omega = 0$ , then the Helmholtz free energy describing isotropic void growth according to Eq. (5.68) must come out. A third condition is described by

$$\phi''(\Omega) \leq 0, \quad (5.78)$$

in particular, intended to provide a softer structural response on the unloading path due to the Mullins effect. Since the present material model initially ignores material softening due to cyclic loading, the condition of Eq. (5.78) is not further considered. A self-evident requirement, which must also be met, is that the shape function is within the limits of  $\Omega \in [0, 1]$ .

Fulfilling the constraint equations, the choice of  $\phi(\Omega)$  is arbitrary. In this case  $\phi(\Omega)$  was chosen in such a way that  $\phi'(\Omega)$  reads

$$\phi'(\Omega) = -\frac{\tanh^{-1}(\Omega - \Theta(1 - \Pi))}{\Theta\Pi}, \quad (5.79)$$

where  $\Theta \in [0, 1]$  and  $\Pi \in [0, 1]$  are additional variables that distinguish between volumetric and isochoric deformations or describe the aspect ratio between a deformed to an undeformed cavity. The exact derivation of both variables is described in the following sections.

Returning to the shape function, it can be explicitly described by inserting Eq. (5.79) into Eq. (5.76), which leads to

$$\Omega = \Theta(1 - \Pi) + \tanh(\mathcal{D}_{\text{cav}}\Theta\Pi). \quad (5.80)$$

Since  $\Theta$  and  $\Pi$  are limited in their functional values, but  $\mathcal{D}_{\text{cav}}$  can take any positive values depending on the applied deformation, the value range of the trigonometric function is additionally given with  $W = \{\tanh(\bullet) \in [0, 1] \mid \bullet \geq 0\}$ . Looking at the right side of Eq. (5.80), the first term aims for the value one and is monotonically increasing under the condition of increasing isochoric deformation, whereas the

second term becomes zero and monotonically decreases. This shows that  $\Omega$  lies in the range of  $\Omega \in [0, 1]$ .

As the shape function is now fully described, the energy function  $\phi(\Omega)$  can be determined by integrating Eq. (5.79) with respect to  $\Omega$ , which leads to

$$\phi(\Omega) = \frac{1}{2} \frac{-\ln(1 - (\Omega - \Theta(1 - \Pi))^2) + 2(\Theta(1 - \Pi) - \Omega) \tanh^{-1}(\Omega - \Theta(1 - \Pi))}{\Theta \Pi} \quad (5.81)$$

On the basis of this procedure, the first condition that  $\partial\Psi_{\text{couple}}/\partial\Omega$  must be zero is directly fulfilled, since this condition has just determined the shape function. Verifying the second constraint equation according to Eq. (5.77) by inserting  $\Omega = 0$  gives

$$\phi(\Omega = 0) = \frac{1}{2} \frac{-\ln(1 - (\Theta(1 - \Pi))^2) - 2\tanh^{-1}(\Theta(1 - \Pi))\Theta(1 - \Pi)}{\Theta \Pi} \quad (5.82)$$

To meet this condition, i.e. to obtain a constitutive model that represents isotropic void growth when  $\Omega$  is inactive, a new condition results for  $\Theta$ , which governs the shape function  $\Omega$ . The new condition to fulfil Eq. (5.77) is that the parameter  $\Theta$  must be zero at purely hydrostatic load. In contrast, it should take the value one for isochoric loads, so that this parameter can be described using a Heaviside step function, for example. Since the general concept of the Flory-type pseudo-elastic material model was presented, the parameters  $\Omega$  and  $\Theta$  of the shape function are defined more precisely in the following.

### 5.3.2 Isoperimetric Inequality

As described in the general concept of the pseudo-elastic cavitation model, there is a shape function that governs the strain energy due to the anisotropic geometric development of a deforming void in relation to the dissipated strain energy due to isotropic void growth. For this purpose, a scalar quantity must be found which defines the geometric evolution of a deforming cavity via a form parameter within the limits zero and one. To do so, one of the fundamental problems in the classical calculus of variations is employed, which is to find the geometric figure with maximum area at a given perimeter (Zwierzynski, 2016). The proposed problem can be described by formulating a so-called isoperimetric inequality

$$\vartheta = \frac{4\pi A_s}{L_s^2} \leq 1 \quad (5.83)$$

defined in the Euclidean space  $\mathbb{R}^2$ . The isoperimetric inequality holds if a simple closed curve  $s$  of length  $L_s$ , enclosing a region of the area  $A_s$ , is a circle. Thus,  $\vartheta$  describes the deviation between a deformed closed curve  $s$  and a circle. The classical formulation of the inequality  $\vartheta$  is defined in  $\mathbb{R}^2$  with  $\vartheta \in [0, 1]$ . To obtain a stricter criterion describing the deviation between a deformed closed curve  $s$  and a circle, the inequality can be provided with an exponent  $n$ , which reads then

$$\vartheta = \left( \frac{4\pi A_s}{L_s^2} \right)^n \leq 1 \text{ with } n \in \mathbb{N}. \quad (5.84)$$

$\mathbb{N}$  represents the set of natural numbers.

Since the present phenomenological pseudo-elastic approach is intended to model cavitation in rubbers and rubber-like materials, it is decisive to describe the geometrical evolution of an initially spherical cavity with one criterion. For this purpose, the isoperimetric inequality is converted into three-dimensional space in which  $\vartheta$  is evaluated in three unique geometrical planes. Since the shape of the spherical cavity changes only due to an external deformation, it is obvious to describe the isoperimetric inequality as a function of a macroscopic deformation measure. Therefore the eigenvalues  $\lambda_i$  with  $i \in [1, 2, 3]$  of the left stretch tensor

$$\mathbf{v} = \sqrt{\mathbf{b}} = \sum_{i=1}^3 \lambda_i \vec{n}_i \otimes \vec{n}_i, \quad (5.85)$$

are used to evaluate the isoperimetric inequality. The geometrical planes, in which  $\vartheta$  is evaluated, are uniquely defined by the cross product of the eigenvectors  $\vec{n}$  of the left stretch tensor  $\mathbf{v}$ , which reads  $\vec{P}_{i-j} = \vec{n}_i \times \vec{n}_j$  with  $i \neq j \in [1, 2, 3]$ . Duplicate planes are excluded in the following considerations. For reasons of simplicity, a geometric mean value is calculated to evaluate the isoperimetric inequality for the three geometric planes ( $\vartheta_{1-2}$ ,  $\vartheta_{2-3}$  and  $\vartheta_{3-1}$ ), i.e.

$$\Pi = \sqrt[3]{\vartheta_{1-2} \vartheta_{2-3} \vartheta_{3-1}}. \quad (5.86)$$

This simplification is permissible, since for the present pseudo-elastic Helmholtz free energy function, on the one hand, the strain energy contribution through anisotropic pore growth is considered purely phenomenologically and, on the other hand, a smeared isotropic material behaviour is assumed. Both assumptions are merely working hypotheses that can be improved by integrating structural tensors to describe anisotropic material behaviour

As an example, the isoperimetric inequality is determined for the 1-2 geometrical plane. Within this plane, the surface area of a cut void simply reads  $A_{s,1-2} = \pi \lambda_1 \lambda_2$ , whereas the perimeter can only be calculated using an approxi-

mation. Utilizing the approximate solution in accordance to Ramanujan (Villarino, 2005), the perimeter can be calculated with

$$L_{s,1-2} \approx \pi \left( (\lambda_1 + \lambda_2) + \frac{3(\lambda_1 - \lambda_2)^2}{10(\lambda_1 + \lambda_2) + \sqrt{\lambda_1^2 + 14\lambda_1\lambda_2 + \lambda_2^2}} \right). \quad (5.87)$$

To obtain the values for  $A_s$  and  $L_s$  for all other principal stretch planes (1-2, 2-3 and 3-1), the indices of the principal axis have to be interchanged cyclically without considering duplicates. Consequently, the isoperimetric inequality can easily be calculated in relation to Eq. (5.84) depending on the desired principal stretch plane (1-2, 2-3 and 3-1).

To better understand the behaviour of the isoperimetric inequality  $\Pi$ , a three-dimensional representation of it is shown in Fig. 5.22 depending on the exponent  $n$ . In addition, deformation paths according to uniaxial, biaxial and hydrostatic loading conditions are added in this plot to clearly show the dependency between  $\Pi$  and the applied deformation. It is obvious that the inequality assumes the value one for the reference configuration regardless of the deformation applied. Following the hydrostatic loading path, the inequality is always fulfilled and remains at the value one, even if the pore grows spherically. If the isochoric loading paths are followed, the value moves from one to zero for the inequality with increasing deformation. This behaviour can be enhanced rapidly by increasing the exponent  $n$ .

### 5.3.3 Equivalent Void Growth Measure

In this section, an equivalent void growth measure  $\Theta$  is introduced that distinguishes between isochoric and volumetric deformations in terms of a scalar value. To differentiate between these deformations, a so-called void growth criterion  $\varepsilon_{\text{eqn}}$  formulated in Hencky strain space according to Drass et al. (2018b) is used and mathematically modified, so that  $\Theta$  takes the value zero for volumetric deformations, whereas it becomes one under isochoric loading. The requirement that the criterion equals zero for volumetric deformations results from Eq. (5.77), which means that the pseudo-elastic Helmholtz free energy function degenerates to Eq. (5.68). That is, the Helmholtz free energy function is able to represent stress softening due to cavitation under pure hydrostatic loading.

Returning to the void growth criterion, it is defined by

$$\varepsilon_{\text{eqn}} = I_{1,\varepsilon} + I_{2,\varepsilon} + I_{3,\varepsilon}, \quad (5.88)$$

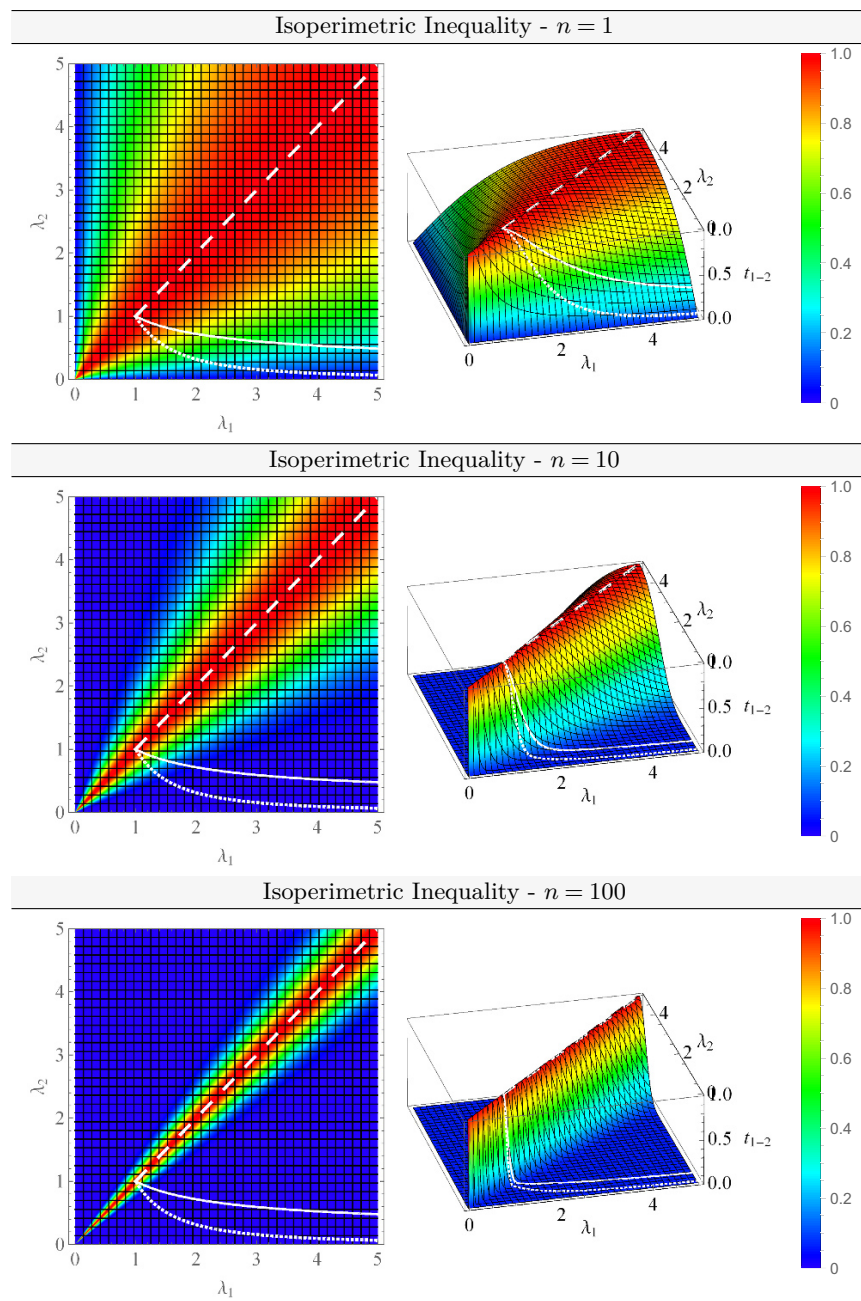


**Figure 5.22** Three dimensional illustration of isoperimetric inequality  $\vartheta_{1-2}$  in  $\lambda_1$ - $\lambda_2$  space

where  $I_{1,\epsilon}$ ,  $I_{2,\epsilon}$  and  $I_{3,\epsilon}$  describe the first, second and third invariants of the Hencky strain tensor  $\epsilon$  with

$$I_{1,\epsilon} = \epsilon_1 + \epsilon_2 + \epsilon_3, \quad (5.89)$$

$$I_{2,\epsilon} = \epsilon_1 \epsilon_2 + \epsilon_2 \epsilon_3 + \epsilon_1 \epsilon_3, \quad (5.90)$$

$$I_{3,\epsilon} = \epsilon_1 \epsilon_2 \epsilon_3. \quad (5.91)$$

As already mentioned, the equivalent void growth measure is a kind of Heaviside step function, which is generally defined by

$$\Theta_c : \mathbb{R} \rightarrow \mathbb{K} \text{ with } \epsilon_{\text{eqn}} \mapsto \begin{cases} 0: & \epsilon_{\text{eqn}} > 0 \\ c: & \epsilon_{\text{eqn}} = 0 \\ 1: & \epsilon_{\text{eqn}} < 0 \end{cases}, \quad (5.92)$$

where  $[0, 1, c = 0] \in \mathbb{K}$ . Keeping this in mind, the equivalent void growth measure can be fully described by

$$\Theta = \frac{1}{2} \frac{|\epsilon_{\text{eqn}}| - \epsilon_{\text{eqn}}}{|\epsilon_{\text{eqn}}|}. \quad (5.93)$$

This special formulation shows that  $\Theta = 1$  applies to isochoric deformations since  $\epsilon_{\text{eqn}} < 0$  or takes a value of  $\Theta = 0$  for the reference configuration and for purely volumetric deformations since  $\epsilon_{\text{eqn}} > 0$ .

### 5.3.4 Constitutive Modelling and Algorithmic Settings

The calculation of the Cauchy stress tensor for the pseudo-elastic material model has already been presented in Section 5.3.1 and is summarized in Eq. (5.75). Due to the additional equilibrium equation resulting from the inclusion of an internal variable in the constitutive model according to Lazopoulos and Ogden (1998), the calculation of the stress tensor could be significantly simplified.

For reasons of completeness the spatial tangent stiffness will be additionally derived in the following. As already shown in the derivation of the Cauchy stress tensor, the components of the additional strain energy coupling term depend on  $J$  and  $\mathbf{b}$ , but only the components of the derivative with respect to  $J$  are included in the final equation of the Cauchy stress tensor due to the additional equilibrium equation of  $\partial \Psi_{\text{couple}} / \partial \Omega = 0$ . Therefore, only the derivation terms according to  $J$  are described below. According to the proposal of Holzapfel (2000):p.265, the volumetric spatial tangent of the strain energy couple term  $\mathbf{c}_{\text{couple}}$  can be written directly in the Eulerian configuration by

$$\mathbf{c}_{\text{couple}} = (p_{\text{couple}} + J s_{\text{couple}}) \mathbf{I} \otimes \mathbf{I} - 2 p_{\text{couple}} \boldsymbol{\mathcal{I}}, \quad (5.94)$$

where  $\mathbf{I} \otimes \mathbf{I}$  represents the dyadic product of two second order identity tensors and  $\mathbf{I}$  describes a fourth-order identity tensor. Based on the simplifications due to the additional equilibrium equation of Eq. (5.74), the hydrostatic pressure of the strain energy couple term reads

$$p_{\text{couple}} = \Omega \frac{\partial \mathcal{D}_{\text{cav}}}{\partial J} (J). \quad (5.95)$$

Since  $p_{\text{couple}}$  is now by defined by Eq. (5.95), the parameter  $s_{\text{couple}}$  must be also computed. It describes the second order derivative of  $\Psi_{\text{couple}}$  with respect to  $J$ , which reads

$$s_{\text{couple}} = \frac{\partial p_{\text{couple}}}{\partial J} (J, \Omega) + \frac{\partial p_{\text{couple}}}{\partial \Omega} (J, \Omega) \frac{\partial \Omega}{\partial J} (\mathbf{b}). \quad (5.96)$$

Keeping in mind that  $\Omega$  was already defined in Eq. (5.80), the calculation of  $s_{\text{couple}}$  can be simplified to

$$s_{\text{couple}} = \Omega \frac{\partial^2 \mathcal{D}_{\text{cav}}}{\partial J^2} (J) + \frac{\Theta \Pi}{\cosh(\Theta \Pi \mathcal{D}_{\text{cav}})^2} \left[ \frac{\partial \mathcal{D}_{\text{cav}}}{\partial J} (J) \right]^2. \quad (5.97)$$

An algorithmic box for the numerical treatment is given in Tab. 5.2. The implementation in ANSYS FE code can generally be done via a UserHyper or UserMat (see Appendix F), whereby for reasons of numerical stability all following models were implemented in the UserHyper environment.

### 5.3.5 Parameter Studies of Isoperimetric Extension of Volumetric Helmholtz Free Energy Function

To get more insight into the function of  $\Omega$  or  $\Theta$  and  $\Pi$ , and to understand how the algorithm behaves with any deformations, reference Fig. 5.23. Here  $\Omega$ ,  $\Theta$  and  $\Pi$  are shown under different deformation modes with respect to the principal stretch  $\lambda_1$ . In this context,  $\lambda_1$  is displayed on a logarithmic scale to investigate the behaviour of  $\Omega$  or  $\Theta$  and  $\Pi$  at small deformations. For this purpose, a single element test under uniaxial, biaxial and hydrostatic load is numerically investigated. Since  $\Omega$ ,  $\Pi$  and  $\Theta$  depend only on the principal stretches  $\lambda_i$  and an acceleration parameter  $n$ , the results displayed depend on the deformation  $\lambda_1$  and  $n$ . As mentioned at the beginning, the parameter  $n$  controls how fast one moves from the initial value of  $\vartheta = 1$  of the isoperimetric inequality to the value zero due to an isochoric load. However, to obtain the classical isoperimetric inequality,  $n$  must be set to one.

To evaluate the described parameters  $\Omega$ ,  $\Pi$  and  $\Theta$  numerically, a normalized Neo-Hooke material model with  $\mu = 1$  MPa is used. The parameters of  $\Psi_{\text{vol,ND}}$  are selected as examples to perform the numerical calculations of the single-element benchmark tests ( $\kappa_0 = 0.02181$ ,  $\kappa_1 = 0.67900$  and  $\kappa_2 = 0.09791$ ). As shown in Fig. 5.23,  $\Theta$  starts at  $\Theta = 0$  and very quickly reaches  $\Theta = 1$  for isochoric deforma-

**Table 5.2** An algorithmic box of the FE procedure during numerical simulations for the pseudo-elastic cavitation model

- (1) given: deformation gradient  $\mathbf{F}$  at  $t_n = t^*$  and  $t_{n+1} = t^* + dt$
- (2) compute dissipated strain energy  $\mathcal{D}_{\text{cav}}$  due to isotropic void growth
$$\mathcal{D}_{\text{cav}} = \Psi_{\text{vol,classic}}(J) - \Psi_{\text{vol,ND}}(J)$$
- (3) compute principal stretches  $\lambda_i$  from left stretch tensor  $\mathbf{v} = \sqrt{\bar{\mathbf{b}}} = \sum_{i=1}^3 \lambda_i \vec{\mathbf{n}}_i \otimes \vec{\mathbf{n}}_i$  at  $t_{n+1} = t^* + dt$  and evaluate isoperimetric inequality  $\Pi$  and equivalent void growth measure  $\Theta$ 

$$\Pi = \sqrt[3]{\vartheta_{1-2} \vartheta_{2-3} \vartheta_{3-1}} \text{ with } \vartheta = \left( \frac{4\pi A_s}{L_s} \right)^n \leq 1 \text{ with } n \in \mathbb{N}$$

$$\Theta = \frac{1}{2} \frac{|\varepsilon_{\text{eqn}}| - \varepsilon_{\text{eqn}}}{|\varepsilon_{\text{eqn}}|} \text{ with } \varepsilon_{\text{eqn}} = I_{1,\varepsilon} + I_{2,\varepsilon} + I_{3,\varepsilon}$$
- (4) compute shape function  $\Omega$  based on (2) and (3)
$$\Omega = \Theta(1 - \Pi) + \tanh(\mathcal{D}_{\text{cav}} \Theta \Pi)$$
- (5) compute strain energy couple term  $\Psi_{\text{couple}}(J, \Omega)$  and the resulting pseudo-elastic Helmholtz free energy function
$$\Psi = \Psi_{\text{iso}}(\bar{\mathbf{b}}) + \Psi_{\text{vol,ND}}(J) + \underbrace{\Omega \mathcal{D}_{\text{cav}}(J) + \phi(\Omega)}_{\Psi_{\text{couple}}(J, \Omega)}$$
- (6) compute Cauchy stress tensor  $\boldsymbol{\sigma}$  at  $t_{n+1} = t^* + dt$ 

$$\boldsymbol{\sigma} = \left[ \frac{2}{J} \frac{\partial \Psi_{\text{iso}}(\bar{\mathbf{b}})}{\partial \bar{\mathbf{b}}} \cdot \bar{\mathbf{b}} \right]^{\text{dev}} + \underbrace{\left[ \frac{\partial \Psi_{\text{vol}}}{\partial J}(J, \Omega) + \frac{\partial \Psi_{\text{couple}}}{\partial J}(J, \Omega) \right]}_{=p} \mathbf{I}$$
- (7) compute tangent moduli  $\mathbf{c}_{\text{iso}}$  and  $\mathbf{c}_{\text{vol}}$  at  $t_{n+1} = t^* + dt$ 

$$\mathbf{c} = \mathbf{c}_{\text{iso}} + \mathbf{c}_{\text{vol}} \text{ with}$$

$$\mathbf{c}_{\text{iso}} = \frac{2}{3} \frac{\mu}{J} \left[ -\bar{\mathbf{b}} \otimes \mathbf{I} - \mathbf{I} \otimes \bar{\mathbf{b}} + I_{1,\bar{\mathbf{b}}} \mathbf{I} + \frac{I_{1,\bar{\mathbf{b}}}}{3} \mathbf{I} \otimes \mathbf{I} \right]$$

$$\mathbf{c}_{\text{vol}} = (p + J s) \mathbf{I} \otimes \mathbf{I} - 2p \mathbf{I} \otimes \mathbf{I}$$
- (8) compute tangent moduli  $\mathbf{c}_{\text{couple}} = (p_{\text{couple}} + J s_{\text{couple}}) \mathbf{I} \otimes \mathbf{I} - 2 p_{\text{couple}} \mathbf{I} \otimes \mathbf{I}$ , with
$$p_{\text{couple}} = \Omega \frac{\partial \mathcal{D}_{\text{cav}}}{\partial J}(J)$$

$$s_{\text{couple}} = \Omega \frac{\partial^2 \mathcal{D}_{\text{cav}}}{\partial J^2}(J) + \frac{\Theta \Pi}{\cosh(\Theta \Pi \mathcal{D}_{\text{cav}})^2} \left[ \frac{\partial \mathcal{D}_{\text{cav}}}{\partial J}(J) \right]^2$$

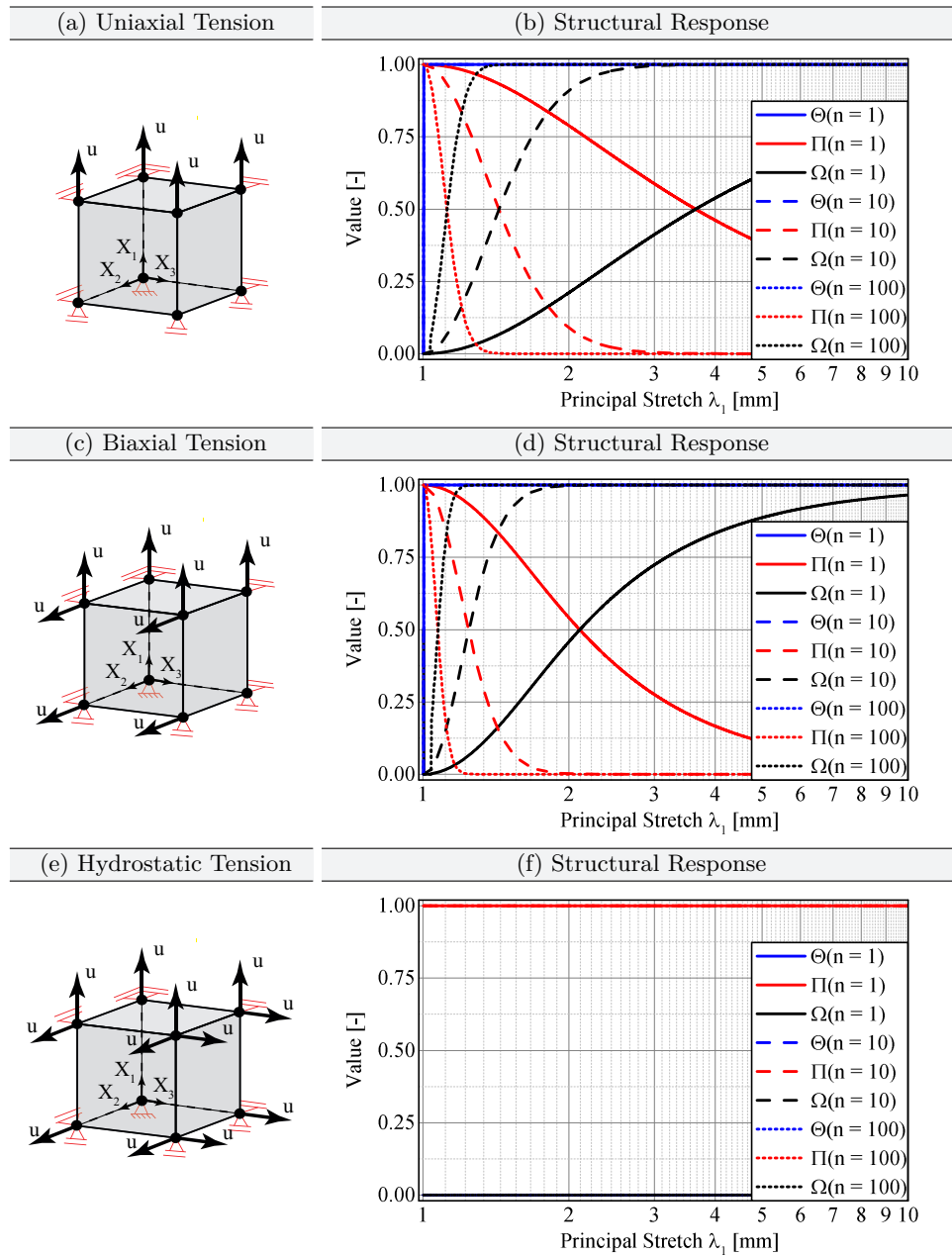


**Figure 5.23** Evaluation of  $\Omega$ ,  $\Pi$  and  $\Theta$  as function of  $n$  dependent on the applied deformation

tions (UT, BT). In contrast, for triaxial loading,  $\Theta = 0$  with the result that only  $\Psi_{\text{vol},\text{ND}}$  is active during numerical calculation. It should also be noted that the equivalent void growth measure  $\Theta$  starts at a value of  $\Theta = 0$  for zero deformations. The structural reaction of the isoperimetric inequality  $\Pi$  starts at zero deformations ( $\lambda_1 = \lambda_2 = \lambda_3 = 1$ ) with a value of  $\Pi = 0$ . For the homogeneous hydrostatic load state,  $\Pi = 1$  for the entire deformation regime, while for isochoric deformations the isoperimetric inequality decreases from one to zero depending on the parameter  $n$ . By increasing the parameter  $n$ , the proposed constitutive model converges to the classical formulation of  $\Psi_{\text{vol},\text{classic}}$  much faster, as the influence of  $\Psi_{\text{vol},\text{ND}}$  is reduced significantly.

In summary, in this section the new volumetric Helmholtz free energy function from Section 5.2 was successfully transferred into the context of pseudo-elasticity in order to prevent anomalies in structural behaviour, especially in isochoric deformation. Therefore, the volumetric component of the model was equipped with the non-linear Helmholtz free energy function that accounts for isotropic void growth under hydrostatic loading. An energy coupling term was then added that numerically explicates strain energy under isochoric deformation, while also guaranteeing physical material behaviour. The energy contribution is calculated internally by analysing the geometric evolution of inherent voids. On the basis of one-element tests at any deformation, parameter studies were carried out to confirm the physical behaviour and to analyse the influence of individual parameters.

## 5.4 Extension of Pseudo-Elastic Cavitation Model for Cyclic Loading

In this section an extension of the previously presented pseudo-elastic cavitation model is introduced in order to describe the structural behaviour of silicone adhesives under cyclic loading. The basic idea is to transfer the classical description of pseudo-elasticity for stress softening under cyclic loading according to Ogden and Roxburgh (1999) to the pseudo-elastic cavitation model presented in Section 5.3. Again, the advantages of the approach of pseudo-elasticity lie in the simple formulation, where the hyperelastic functional can be completely described at a macro-scale, the application of the volumetric-isochoric split, which brings advantages regarding the material parameter identification and the avoidance of computationally intensive and complex multi-scale modelling methods.

### 5.4.1 Motivation

Considering the experimental results for the investigated material TSSA according to Section 4.2.2 and Section 4.3.2, a very interesting structural behaviour was

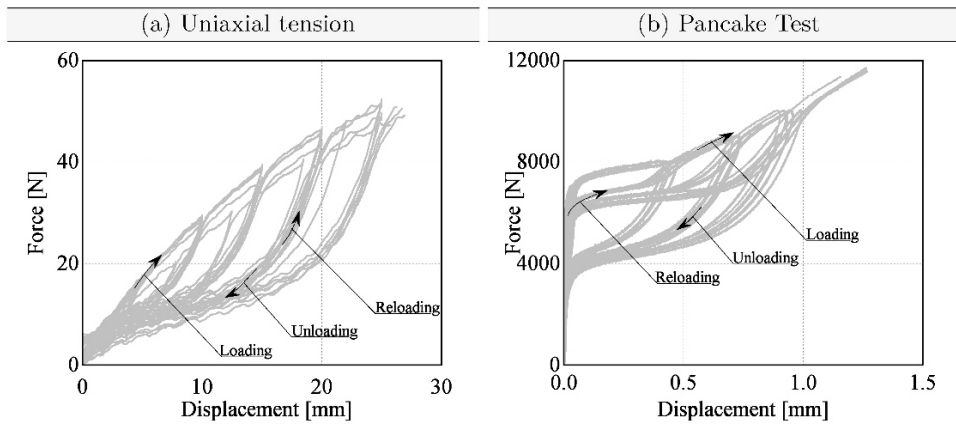


**Figure 5.24** Exemplary structural behaviour of TSSA under (a) uniaxial and (b) constrained cyclic loading (Pancake Test)

observed, which now has to be described numerically using a phenomenological approach.

Regarding the structural behaviour of TSSA under uniaxial cyclic loading, the material behaves according to the characteristics of the Mullins effect. A typical and pronounced stress softening due to real material damage can be clearly seen on the unloading path. Looking at the reloading path, the material shows the same structural response according to the unloading path until the previously reached maximum value of deformation is exceeded. Then the material response corresponds to the response of a virgin material (see Fig. 5.24 a). Further, it is important to note that no healing or recovery effects under cyclic uniaxial loading could be observed. According to Section 4.4.2 the effect of stress softening in isochoric deformations was attributed to a real damage in the material, which can be described phenomenologically e.g. by the approach of Ogden and Roxburgh (1999).

In contrast, in the cyclic constrained tensile test or cyclic pancake tension test according to Section 4.3.2 an atypical structural behaviour was observed in which the unloading path shows the classical stress softening due to the Mullins effect, however the reloading path does not follow the unloading path. Looking at the reloading path a kind of healing or recovery effect takes place, which is assumed to be due to elastic void growth and shrinkage. However, since no complete healing takes place, a combination of a healing effect through elastic pore growth and shrinkage and real Mullins damage through possible bond breakage and filler rupture must be present, especially in areas exposed to triaxial deformations and stresses respectively. Therefore, a modified pseudo-elastic approach must be cho-

sen for the volumetric part of a general Helmholtz free energy function based on Ogden and Roxburgh (1999), which can depict healing and damage effects phenomenologically according to the present loading condition.

### 5.4.2 General Concept

Since the pseudo-elastic approach of Lazopoulos and Ogden (1998) has already been presented, only the essential equations necessary for deriving the extended pseudo-elastic cavitation model for cyclic loading are summarized below.

Assuming a general Helmholtz free energy function  $\Psi(\mathbf{F})$  that depends solely on the deformation gradient  $\mathbf{F}$ , the pseudo-elastic approach to this problem reads

$$\Psi(\mathbf{F}, \eta) = \eta \hat{\Psi}(\mathbf{F}) + \phi(\eta), \quad (5.98)$$

which is capable of describing the classical Mullins effect in rubbers and rubber-like materials phenomenologically. In this context,  $\phi(\eta)$  describes a damage function, which serves to determine the damage parameter  $\eta \in [0, 1]$  implicitly in terms of the state of deformation through an additionally proposed equilibrium equation

$$\frac{\partial \Psi(\mathbf{F}, \eta)}{\partial \eta} = 0. \quad (5.99)$$

This general concept is now specifically applied to separately describe the effects proposed in Section 5.4.1 with respect to isochoric and volumetric deformations.

### 5.4.3 Isochoric Mullins Damage under Cyclic Loading

To describe the isochoric Mullins effect phenomenologically with the pseudo-elastic approach, exactly the model proposed by Ogden and Roxburgh (1999) is used, in which the isochoric part of any Helmholtz free energy function becomes

$$\Psi_{\text{iso}}(\bar{\mathbf{b}}, \eta) = \eta_{\text{iso}} \hat{\Psi}_{\text{iso}}(\bar{\mathbf{b}}) + \phi(\eta_{\text{iso}}). \quad (5.100)$$

By satisfying the additional equilibrium equation of Eq. (5.99) arising from the inclusion of an internal variable in the constitutive model, the damage variable  $\eta$  reads

$$\eta_{\text{iso}} = 1 - \frac{1}{r} \operatorname{erf} \left[ \frac{(\hat{\Psi}_{\text{iso}, \max}(\bar{\mathbf{b}}) - \hat{\Psi}_{\text{iso}}(\bar{\mathbf{b}}))}{m} \right]. \quad (5.101)$$

In this context  $r \in ]1, \infty]$  and  $m \in ]0, \infty]$  are material parameters, which must be determined through experiments. The operator  $\operatorname{erf}(\bullet)$  describes the error function, which is a sigmoid function. It is often used in statistics and in the theory of partial

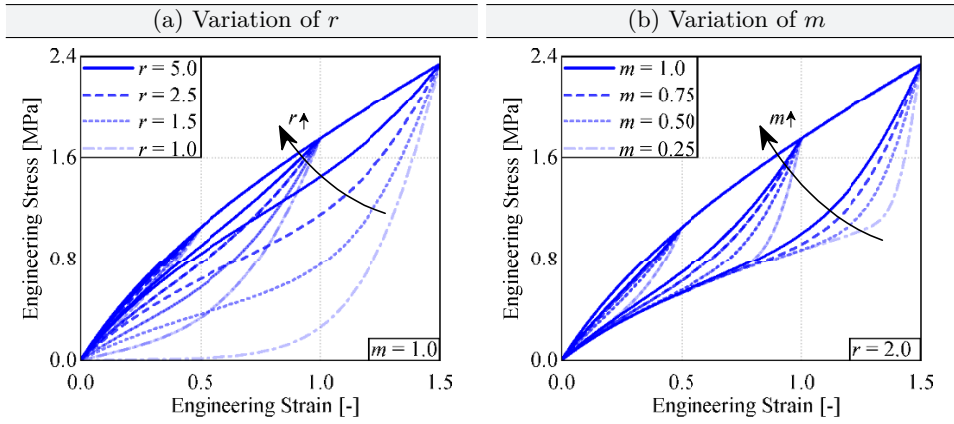


**Figure 5.25** Exemplary structural behaviour of one-element test under cyclic uniaxial tensile loading varying the parameter (a)  $r$  with  $m = 1.0$  and (b)  $m$  with  $r = 2.0$

differential equations and is closely related to the error integral. It is generally defined by

$$\text{erf}(x) = \frac{2}{\sqrt{\pi}} \int_0^x e^{-t^2} dt. \quad (5.102)$$

For a positive argument  $x$ , the error function has the value range of  $\text{erf}(x) \in [0, 1]$ . Returning to the governing parameters of  $\eta_{\text{iso}}$ , the larger  $r$  is chosen, the less the influence of Mullins damage on the structural response of the material under cyclic loading. In contrast, parameter  $m$  describes in particular how much damage occurs in the case of small deformations. The smaller  $m$  is chosen, the more Mullins damage occurs at small deformations. The strain energy  $\hat{\Psi}_{\text{iso},\max}$  is a history variable and stores the maximum reached isochoric strain energy density during loading history. To better illustrate the influence of parameters  $m$  and  $r$ , the structural responses are shown separately in Fig. 5.25 for each varying parameter for a uniaxial one-element test under cyclic loading. A normalized, incompressible Neo-Hooke material model with  $\mu = 1.0$  MPa was coupled with the pseudo-elastic approach according to Ogden and Roxburgh (1999).

Due to the choice of the pseudo-elasticity approach, the calculation of the isochoric stress tensor simplifies significantly, as all partial derivatives of the isochoric Helmholtz free energy function with respect to the damage variable disappear. Hence the isochoric stress tensor reads

$$\sigma_{\text{iso}} = \frac{2\eta_{\text{iso}}}{J} \left[ \mathbf{I} - \frac{1}{3} \mathbf{I} \otimes \mathbf{I} \right] : \frac{\partial \hat{\Psi}_{\text{iso}}(\bar{\mathbf{b}})}{\partial \bar{\mathbf{b}}} \cdot \bar{\mathbf{b}}, \quad (5.103)$$

where  $\mathbf{I} \otimes \mathbf{I}$  represents the dyadic product of two second order identity tensors and  $\mathbf{I}$  describes a fourth-order identity tensor. It can be clearly seen from Eq. (5.103), if  $\eta_{\text{iso}}$  is inactive ( $\eta_{\text{iso}} = 1$ ), then the classic undamaged material response is obtained, whereas stress softening only occurs when  $\eta_{\text{iso}}$  is active  $\eta_{\text{iso}} < 1$ . This means  $\eta_{\text{iso}}$  is only active if  $\hat{\Psi}_{\text{iso},\max}(\bar{\mathbf{b}}) \neq \hat{\Psi}_{\text{iso}}(\bar{\mathbf{b}})$ , which is generally the case for unloading and for reloading until the previously maximum reached strain energy is exceeded. Then  $\hat{\Psi}_{\text{iso}}(\bar{\mathbf{b}})$  and  $\hat{\Psi}_{\text{iso},\max}(\bar{\mathbf{b}})$  are identical again.

#### 5.4.4 Volumetric Damage and Healing under Cyclic Loading

In the following, an extension of the pseudo-elastic cavitation model is presented, which is intended to describe the structural behaviour of the pancake tension test under cyclic loading phenomenologically. As previously mentioned, individual sections of the structural response of TSSA under constrained cyclic tension could be assigned to different phenomena (see Section 4.3.2).

The primary or virgin loading path shows stress softening due to the cavitation effect and can be represented with the pseudo-elastic cavitation model presented in Section 5.3, which reads in a general form

$$\Psi = \Psi_{\text{iso}}(\bar{\mathbf{b}}) + \Psi_{\text{vol,ND}}(J) + \Omega \mathcal{D}_{\text{cav}}(J) + \phi(\Omega). \quad (5.104)$$

For reasons of clarity for the subsequent model extension, all operational terms of the pseudo-elastic cavitation model representing stress softening due to void growth are grouped together as

$$\Psi_{\text{cav}} = \Psi_{\text{vol,ND}}(J) + \Omega \mathcal{D}_{\text{cav}}(J) + \phi(\Omega), \quad (5.105)$$

so that the pseudo-elastic Helmholtz free energy function is now briefly described by

$$\Psi = \Psi_{\text{iso}} + \Psi_{\text{cav}}. \quad (5.106)$$

Further, looking at the cyclic pancake tension tests presented in Fig. 5.24 b, the unloading paths showed an additional material softening due to the Mullins effect, where all experimental curves meet at a force level of 3.600 kN and then decrease to zero again with full unloading. An appropriate approach to represent this phenomenon is the application of the classical pseudo-elastic approach according to Ogden and Roxburgh (1999) to  $\Psi_{\text{cav}}$  in order to characterize Mullins damage under cyclic loading. Since the classical approach of Ogden and Roxburgh (1999) to describe the Mullins effect is not able to represent healing or recovery effects, it needs to be extended with respect to a healing variable. This is necessary because from the cyclic pancake tension tests a kind of recovery effect could be observed for all reloading paths up to a force level of approximately 6.000 kN. Here it could be

shown experimentally that the unloading and reloading paths differ significantly, so that it is obvious to introduce an additional variable to describe the recovery effect.

To take into account the effects of volumetric Mullins softening on the unloading and healing on the reloading path phenomenologically, Eq. (5.106) is now extended through the already presented pseudo-elastic approach, which leads to

$$\Psi = \Psi_{\text{iso}} + \varsigma \Psi_{\text{cav}} + \phi(\varsigma). \quad (5.107)$$

In this context  $\phi(\varsigma)$  represents a damage or healing function depending on the current loading condition and  $\varsigma$  characterizes a history variable that determines the amount of volumetric Mullins softening for unloading and the amount of healing for the reloading conditions.

For the present approach, the Cauchy stress tensor with respect to  $\Psi_{\text{cav}}$  is calculated exactly in line with Section 5.3, which leads to

$$\begin{aligned} \boldsymbol{\sigma}_{\text{cav}} &= \frac{2}{J} \left[ \frac{\partial \Psi_{\text{cav}}}{\partial \mathbf{b}}(J, \varsigma) + \underbrace{\frac{\partial \Psi_{\text{cav}}}{\partial \varsigma}(J, \varsigma)}_{=0} \frac{\partial \varsigma}{\partial \mathbf{b}}(\mathbf{b}) \right] \cdot \mathbf{b} \\ &= \frac{\partial \Psi_{\text{cav}}}{\partial J}(J, \varsigma) \mathbf{I}. \end{aligned} \quad (5.108)$$

Here, too, the calculation of the stress tensor  $\boldsymbol{\sigma}_{\text{cav}}$  could be considerably simplified due to the additional equilibrium condition

$$\frac{\partial \Psi_{\text{cav}}}{\partial \varsigma}(J, \varsigma) = 0, \quad (5.109)$$

which results from the inclusion of the additional internal variable  $\varsigma$  in the pseudo-elastic constitutive model.

In order to describe the phenomenological constitutive model completely, the internal damage variable  $\varsigma$  must be defined more precisely. Starting with the description of the volumetric Mullins softening, a slightly modified approach according to Ogden and Roxburgh (1999) is used, which reads

$$\bar{\varsigma} = 1 - r_{\text{vol}} \text{erf} \left( \underbrace{\frac{\Psi_{\text{cav},\text{max}} - \Psi_{\text{cav}}}{m_{\text{vol}}}}_{=\eta_{\text{vol}}} \right). \quad (5.110)$$

Since Eq. (5.110) does not represent the final form for the volumetric softening and possible healing effects,  $\varsigma$  is provided with an bar. For the sake of clarity, the variable for volumetric Mullins softening is designated  $\eta_{\text{vol}}$ , which depends on two

material parameters,  $r_{\text{vol}} \in [0, 1]$  and  $m_{\text{vol}} \in ]0, 1]$ , and the difference between the maximum reached (volumetric) strain energy  $\Psi_{\text{cav},\max}$  and the current strain energy  $\Psi_{\text{cav}}$ . This is a standard approach that has been used to describe the isochoric Mullins effect in particular (Zhang et al., 2011), but has been transferred here in order to investigate volumetric Mullins softening due to volumetric deformations.

In order to transfer the standard approach of Eq. (5.110) to possible healing effects, Bartels (2018) proposed an ansatz in which  $\eta_{\text{mull}}$  is again multiplied by an additional healing variable  $\eta_{\text{heal}}$ , which is also defined in the same manner as  $\eta_{\text{mull}}$ . The healing variable reads

$$\eta_{\text{heal}} = r_{\text{heal}} \operatorname{erf} \left( \frac{\bar{\varsigma} - \bar{\varsigma}_{\min}}{m_{\text{heal}}} \right) \quad \text{with} \quad \bar{\varsigma}_{\min} = \min \left[ \bar{\varsigma}, \bar{\varsigma}_{\min}^{t=t^*} \right], \quad (5.111)$$

where  $r_{\text{heal}} \in [0, 1]$  and  $m_{\text{heal}} \in ]0, 1]$  are material parameters describing the course of healing. The minimum of the volumetric Mullins variable  $\bar{\varsigma}_{\min}$  for the current time step  $t = t^* + dt$  is calculated from the minimum of  $\bar{\varsigma}$  and the minimum of the previous time step  $\bar{\varsigma}_{\min}^{t=t^*}$ .

Since according to the results of the pancake tension tests the healing variable can only be active ( $\eta_{\text{heal}} > 0$ ) on the reloading path, its driving force is the difference between the current and the minimum volumetric Mullins softening. This uniquely characterizes the reloading path. Keeping this in mind, the internal variable is completely defined by

$$\varsigma = 1 - \eta_{\text{vol}} (1 - \eta_{\text{heal}}), \quad (5.112)$$

with  $\varsigma \in [0, 1]$ . Assuming no healing occurs in the material,  $\eta_{\text{heal}} = 0$ , the classic approach for volumetric Mullins damage is present, where the unloading and reloading path are identical. Upon complete healing of the material, the reloading path is equal to the virgin material response, but the structural response for the unloading path exhibits the typical stress softening due to the Mullins effect.

In order to gain a better understanding of the presented material model, which can represent cavitation, volumetric Mullins softening and even healing due to reversible pore growth, the load history of a one-element test under cyclic hydrostatic loading is examined below as an example. Looking at Fig. 5.26 a, the load history of a cyclic hydrostatic tensile test is shown separately for virgin loading, unloading and reloading. Additionally, the history variable  $\varsigma$  is shown, which is a combination of the Mullins damage variable  $\eta_{\text{mull}}$  according to the unloading pathway and the healing variable  $\eta_{\text{heal}}$  for the reloading path according to Eq. (5.112). Since the course of the history variable  $\varsigma$  is very complex, it can already be observed here that it lies within the limits of zero to one. Fig. 5.26 b and Fig. 5.26 c additionally show the development of the corresponding damage or healing variables. First, considering only the volumetric Mullins damage, Fig. 5.26 b shows that Mullins damage

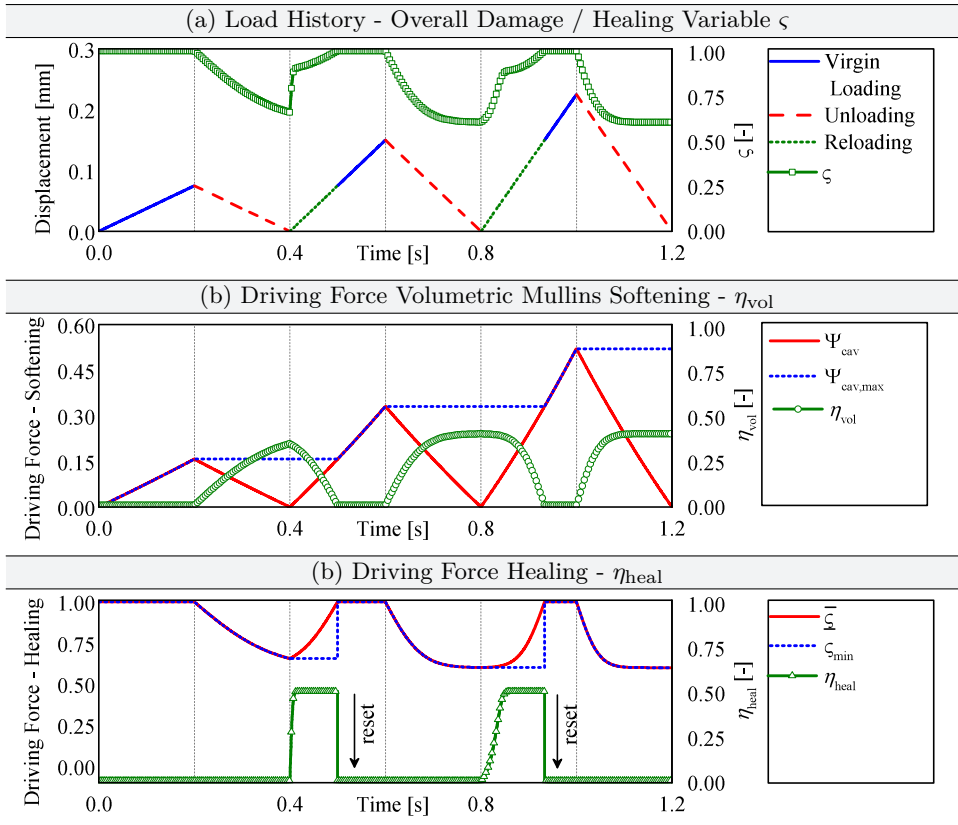


**Figure 5.26** Exemplary load history of cyclic hydrostatic tension loading

only occurs when  $\Psi_{\text{cav,max}}$  is not equal to  $\Psi_{\text{cav}}$ . This is generally the case whenever one is on the unloading or reloading path. Consequently, the Mullins damage variable  $\eta_{\text{mull}}$  must assume values greater than zero, as shown in Fig. 5.26 b. It should also be noted that the chosen driving force ( $\Psi_{\text{cav,max}} - \Psi_{\text{cav}}$ ) to describe the volumetric Mullins effect exactly reflects the ranges of unloading and reloading, which justifies the chosen phenomenological approach. In contrast, looking at the course of the healing variable  $\eta_{\text{heal}}$ , Fig. 5.26 c shows that, on the one hand, the selected driving force ( $\bar{\xi} - \xi_{\min}$ ) is a good measure to reproduce the recovery effect. On the other hand, the chosen formulation provides a clear distinction between virgin loading, unloading and reloading. Accordingly, healing occurs only on the reloading path until the maximum deformation reached before is exceeded. For the sake of completeness, the algorithmic box for the numerical treatment of the extended pseudo-elastic cavitation model for cyclic loading is given in Tab. 5.3.

**Table 5.3** An algorithmic box of the FE procedure during numerical simulations for the pseudo-elastic cavitation model

- (1) given: deformation gradient  $\mathbf{F}$  at  $t_n = t^*$  and  $t_{n+1} = t^* + dt$
- (2) compute pseudo-elastic Helmholtz free energy function of pseudo-elastic cavitation model according to Section 5.3  

$$\Psi = \Psi_{\text{iso}} + \Psi_{\text{cav}}$$
- (3) compute driving force and damage variable for isochoric Mullins effect  

$$\eta_{\text{iso}} = 1 - \frac{1}{r} \operatorname{erf} \left[ \frac{1}{m} (\Psi_{\text{iso,max}} - \Psi_{\text{iso}}) \right], \text{ where}$$

$\mathbb{D}_{\text{iso}} = \Psi_{\text{iso,max}} - \Psi_{\text{iso}}$  represents the driving force for the isochoric Mullins effect
- (4) compute driving force and damage variable for volumetric Mullins effect  

$$\eta_{\text{vol}} = r_{\text{vol}} \operatorname{erf} \left( \frac{\Psi_{\text{cav,max}} - \Psi_{\text{cav}}}{m_{\text{vol}}} \right), \text{ where}$$

$\mathbb{D}_{\text{vol}} = \Psi_{\text{cav,max}} - \Psi_{\text{cav}}$  represents the driving force for the volumetric Mullins effect
- (5) compute driving force and healing variable for recovery effect  

$$\eta_{\text{heal}} = r_{\text{heal}} \operatorname{erf} \left( \frac{\bar{\varsigma} - \bar{\varsigma}_{\min}}{m_{\text{heal}}} \right), \text{ where}$$

$\mathbb{D}_{\text{heal}} = \bar{\varsigma} - \bar{\varsigma}_{\min}$  represents the driving force for the volumetric recovery effect
- (6) compute internal history variable  $\varsigma$  accounting for volumetric Mullins softening and recovery effects  

$$\varsigma = 1 - \eta_{\text{vol}} (1 - \eta_{\text{heal}})$$
- (7) update (2) with internal history variable  $\eta_{\text{iso}}$  and  $\varsigma$  to calculate Helmholtz free energy function and Cauchy stress tensor  

$$\Psi = \underbrace{\eta_{\text{iso}} \Psi_{\text{iso}} + \phi(\eta_{\text{iso}})}_{\text{isochoric Mullins Effect}} + \underbrace{\varsigma \Psi_{\text{cav}} + \phi(\varsigma)}_{\text{volumetric Mullins and recovery Effect}}$$

$$\boldsymbol{\sigma} = \boldsymbol{\sigma}_{\text{iso}} + \boldsymbol{\sigma}_{\text{cav}} = \eta_{\text{iso}} \boldsymbol{\sigma}_{\text{iso},0} + \varsigma \boldsymbol{\sigma}_{\text{cav},0}$$

### 5.4.5 Parameter Studies on Cyclic Pseudo-Elastic Cavitation Model

Since the existing material model is now dependent on parameters describing a volumetric Mullins effect and / or a volumetric healing effect, a parameter study will be carried out in the following with regard to these parameters for reasons of comprehensibility. First, the influence of parameter  $r_{\text{mull}}$  on the structural response under cyclic hydrostatic loading is investigated. For reasons of clarity, all healing effects have been excluded, so that  $r_{\text{heal}} = 0$ . Fig. 5.27 a shows that this parameter determines the degree of Mullins damage compared to the virgin loading path. It

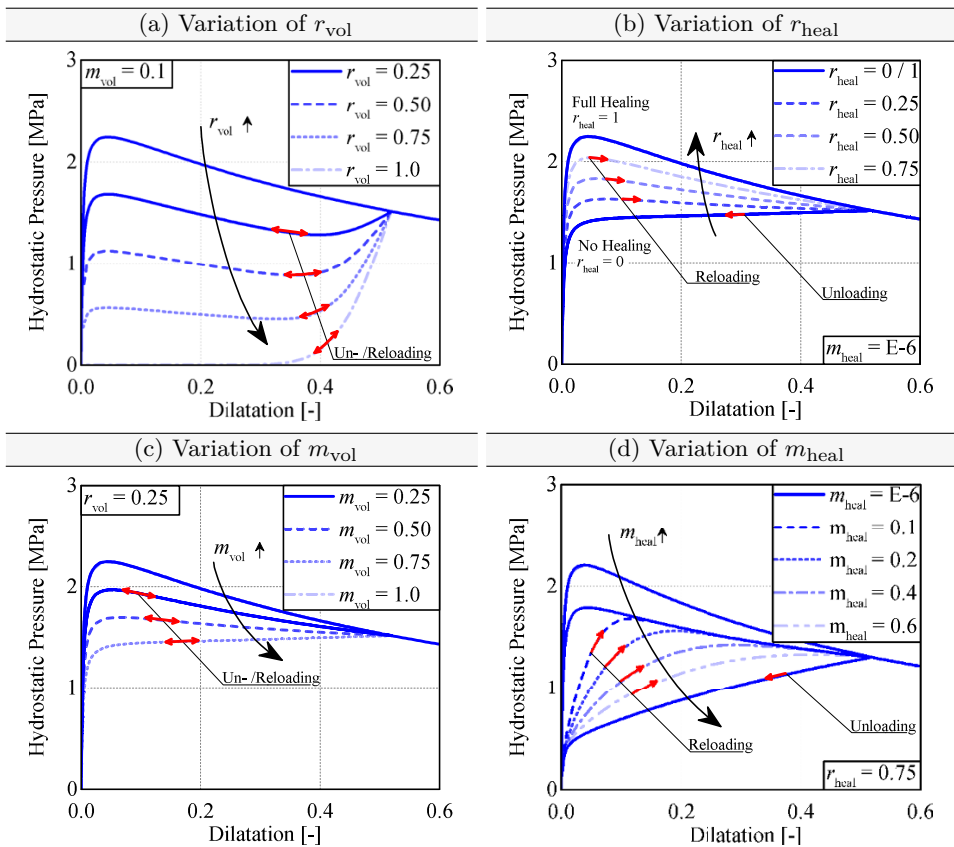


**Figure 5.27** Parameter studies on the extended pseudo-elastic cavitation model accounting for volumetric Mullins softening and healing effects respectively by variation of the parameters (a)  $r_{\text{vol}}$ , (b)  $r_{\text{heal}}$ , (c)  $m_{\text{vol}}$  and (d)  $m_{\text{heal}}$ , whereby all other parameters were set constant

is notable that with an increasing  $r_{\text{mull}}$  the amount of Mullins damage increases also for the unloading path. Since no healing effects have been considered in the

present study, the unloading and reloading paths are identical. Returning to the parameter  $r_{\text{vol}}$ , it gives the ratio between bifurcation load of the unloading paths and virgin loading path. Hence it can be stated that

$$r_{\text{vol}} \approx 1 - \frac{p_{\text{cr}}^{\text{vol}}}{p_{\text{cr}}} \quad (5.113)$$

applies. In this context  $p_{\text{cr}}$  describes the bifurcation point for the virgin load path, whereas  $p_{\text{cr}}^{\text{vol}}$  characterizes the critical stress, at which all unloading and reloading curves coincide disregarding healing effects. Therefore, using Eq. (5.113), the variable  $p_{\text{cr}}$  for the volumetric Mullins damage can be calculated approximately directly from the experimental data obtained, for example, from the pancake tension tests.

A similar statement applies considering the bifurcation load of the reloading path when healing effects are present (see Fig. 5.27 b). Here the parameter  $r_{\text{heal}}$  can be described as the ratio of

$$r_{\text{heal}} \approx \frac{p_{\text{cr}}^{\text{heal}} - p_{\text{cr}}^{\text{vol}}}{p_{\text{cr}} - p_{\text{cr}}^{\text{vol}}}. \quad (5.114)$$

Considering the experimental results of the cyclic pancake tension test, in which all unloading and reloading curves converged to a specific load level, the knowledge of these approximate solutions for the parameters  $r_{\text{vol}}$  and  $r_{\text{heal}}$  is very valuable, since both material parameters can be read directly from the experimental results. It should also be mentioned that these approximation formulas also apply to inhomogeneous stress and strain states, as is the case with the pancake tension test, since these have just been developed from the experimental results of the these tests.

If one also considers the parameter  $m_{\text{vol}}$  with neglect of healing, it is noticeable that it slightly influences  $p_{\text{cr}}^{\text{vol}}$  on the one hand, and in particular controls the course of the Mullins damage with small to moderate deformations on the other hand (see Fig. 5.27 c). In addition, the structural behaviour dependent on the parameter  $m_{\text{heal}}$  is investigated taking into account healing. Fig. 5.27 d shows that with increasing  $m_{\text{heal}}$  one approaches the course of the unloading curve. In contrast, a very small  $m_{\text{heal}}$  causes a bifurcation point that lies between the virgin loading and the unloading path, as could be observed in the cyclic pancake tension tests. It should be noted here that the approximate solution of Eq. (5.114) is particularly true for a very small  $m_{\text{heal}}$ , whereas for a large  $m_{\text{heal}}$  the bifurcation point  $p_{\text{cr}}^{\text{vol}}$  is approached.

Finally, the structural behaviour of the cyclic pancake tension test will now be qualitatively represented by the pseudo-elastic cavitation model extended for cyclic loading. Therefore a one-element test is analysed under cyclic hydrostatic tension,

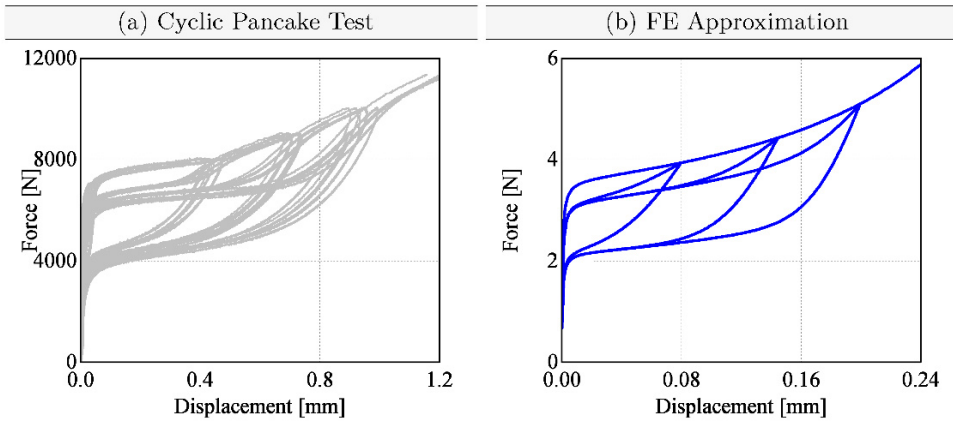


**Figure 5.28** Qualitative comparison between cyclic pancake tension test and numerical simulation of a one-element test under cyclic hydrostatic load using the extended pseudo-elastic cavitation model

knowing that no pure hydrostatic stress state prevails in the pancake tension test (cf. Appendix A). Nevertheless, the adaptability of the phenomenological model should be presented within this study. The material parameters of the pure pseudo-elastic cavitation model were chosen according to Drass et al. (2018b), whereas the parameters describing volumetric Mullins damage and healing due to elastic pore growth and shrinkage were adaptively adjusted to qualitatively approximate the experimental results of the cyclic pancake tension test. As the qualitative comparison in Fig. 5.28 shows, the extended pseudo-elastic cavitation model is well suited to reproduce material softening due to cavitation. Furthermore, the material softening caused by the Mullins effect can also be approximated when the material is unloaded. Qualitatively, all unloading paths meet in one point ( $p_{\text{cr}}^{\text{vol}}$ ) according to the experimental results. Finally, the healing effect due to elastic pore growth and shrinkage can also be simulated with the proposed model. It is further possible to reproduce the effect that all reloading curves coincide at one bifurcation point  $p_{\text{cr}}^{\text{heal}}$  and then continue along the reloading path until the maximum previous deformation state is exceeded.

## 5.5 Numerical Validation of Constitutive Models

This chapter aims at the validation of selected material models that were previously developed in this work and described in detail. First of all, the appropriateness and quality of the isochoric hyperelastic material model of Section 5.1 is analysed by fitting experimental data of different hyperelastic materials and simulating the so-called ETAG H-shaped test specimen (ETAG 002, 2012). Furthermore, the

quasi-static uniaxial tensile test and the bulge test are investigated with the pseudo-elastic cavitation model presented in Section 5.3. To show the general validity of this model, pancake tension tests with three different diameters are numerically calculated and compared with the experimental results. Finally, the cyclic uniaxial and constrained tension tests (pancake tension tests) are simulated using the extended pseudo-elastic cavitation model from Section 5.4.

### 5.5.1 Approximation of Different Hyperelastic Materials

In order to show the advantages of the hyperelastic material model based on the Nelder function (see Section 5.1.2), four different experimental data sets are approximated in the following. In addition to the experimental data for TSSA presented in Section 4, the data from Staudt et al. (2018) for the structural silicone DC 993, the data of an elastomer (Lahellec et al., 2004) and Treloar's data (Treloar, 1975) are utilized to show the quality of the present isochoric material model  $\Psi_{\text{iso},\text{ND}}$ . In addition, the extended tube model of Kaliske and Heinrich (1999) is also applied for reasons of comparison, since this model is stated to be one of the best and adaptable hyperelastic material models (Marckmann and Verron, 2006).

For the classical procedure of material parameter identification (MPI), test data of different homogeneous experimental test set-ups can be utilized to determine the desired parameters, which are on an average adequately suitable to describe different strain and stress states. Therefore, it is essential to conduct a simultaneous multi-experiment data fit to obtain optimized material parameters for a large number of deformation modes (Ogden et al., 2004). During the MPI it is important to ensure a polyconvex material. Therefore, the material parameters must be limited to a polyconvex area or, if this is not possible, the polyconvexity must be verified after determining the material parameters (see Section 5.1.3).

To determine the desired material parameters, an objective function must be calculated, which is able to account for more than only one experimental data set (Ogden et al., 2004; Drass et al., 2018f). A general objective function  $\mathcal{S}$  to determine the unknown material parameters  $p_j$  reads

$$\mathcal{S} = \|t_i^{\text{sim}}(\lambda_i, p_j) - t_i^{\text{exp}}\|_2^2, \quad (5.115)$$

where  $t_i$  describes the engineering stress, which in turn depends on the stretch  $\lambda_i$  at time  $i$ . In order to calculate optimized material parameters, the objective function must be minimized, which is described by

$$\min \mathcal{S} \equiv \min_{\vec{p}} \mathcal{S}(\vec{p}). \quad (5.116)$$

For the following determination of the material parameters for four different ma-

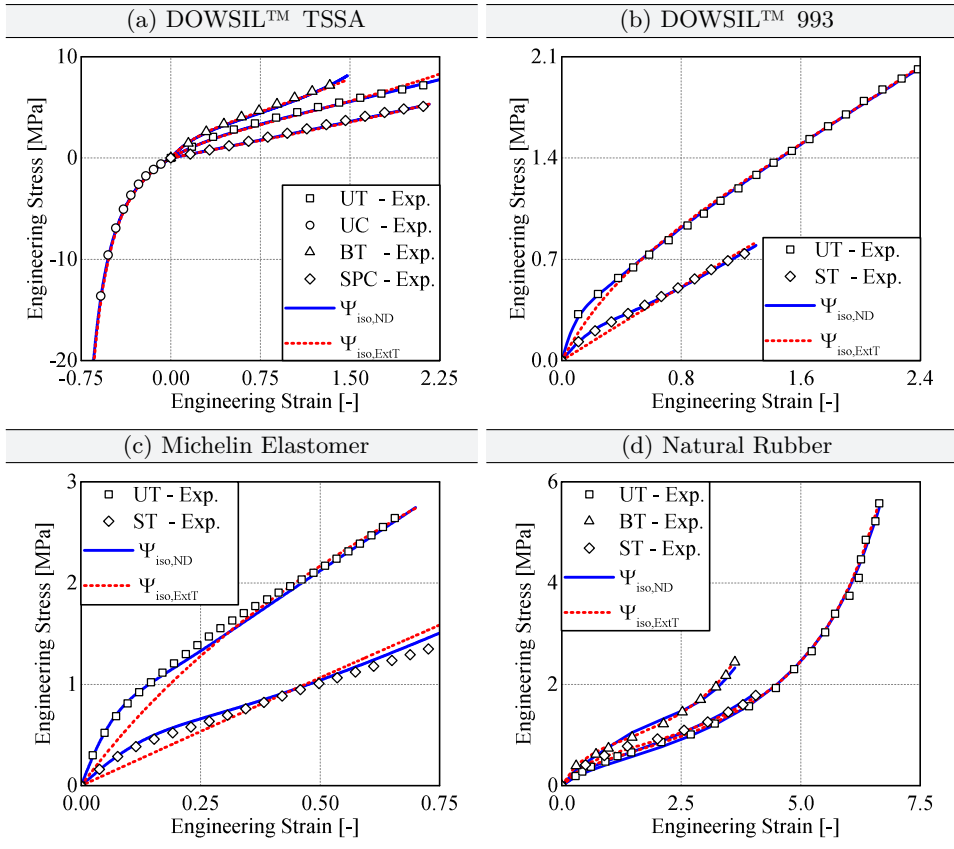


**Figure 5.29** Fitting results for different materials and experiments under arbitrary deformations: (a) DOWSIL™ TSSA, (b) DOWSIL™ 993 (Staudt et al., 2018), (c) Michelin elastomer (Lahellec et al., 2004) and (d) natural rubber (Treloar, 1975) with UT = uniaxial tension, UC = uniaxial compression, BT = biaxial tension, SPC = shear pancake and ST = shear tests

terials the random search algorithm of Mathematica was utilized. Based on a generated population of random starting points, the random search algorithm uses a local optimization method from each of the starting points to converge to a local minimum. The best local minimum is chosen as the solution. As can be seen from Fig. 5.29 a, both constitutive models are well suited to represent the experimental data of TSSA for four different types of experiments. The extended tube model of Kaliske and Heinrich (1999) only overestimates the structural response of TSSA under uniaxial tension at large deformations. However, in summary, both models are capable of representing TSSA under different type of loading. Considering the approximation of the experimental data of the filled silicone according to the

investigations of Staudt et al. (2018),  $\Psi_{\text{iso},\text{ND}}$  is well suited to represent the structural response over the entire deformation range (see Fig. 5.29 b). In contrast, the model of Kaliske and Heinrich (1999) can adequately approximate the structural behaviour only at large deformations. This behaviour can also be seen for the data of (Lahellec et al., 2004), where the new rational hyperelastic material model  $\Psi_{\text{iso},\text{ND}}$  leads to good results over the entire deformation path (see Fig. 5.29 c). Looking again at the data from Treloar (1975), which is illustrated in Fig. 5.29 d, both material models lead to similarly good results. Finally, it should be noted that the new model approximates the initial stiffness much better for structural silicones than the comparative model by Kaliske and Heinrich (1999). This is of great importance in the dimensioning of adhesive joints in civil engineering, since the range relevant for design only covers the beginning of the experimental curves.

### 5.5.2 Simulation of ETAG H-shaped Test Sample

The classical H-shaped test specimen is commonly used to investigate the structural behaviour and failure of silicone adhesives in façade joints (see Fig. 5.30). It is made up of steel or glass plates which are connected to each other with a so-called linear adhesive joint. In this context, linear means that the adhesive joint is applied linearly along the edges of two components to be joined. The adhesive joint has the dimensions 12 x 12 x 50 mm according to ETAG 002 (2012) and is stressed separately by tensile load or in simple shear. In contrast to conventional dumbbell-shaped tensile test specimens, the ETAG test sample exhibits an inhomogeneous stress and strain state, making it ideally suited for the validation of isochoric hyperelastic material models. Due to the height of 12 mm, this is not a constrained tensile test, as for the pancake tension tests, since the material is not hindered in its transverse deformation. This can be easily checked by evaluating the shape factor  $s$  postulated by Gent and Lindley (1959) for pancake tension test specimens with a radius of  $R$  and a height of  $h$ , which reads

$$s = \frac{\pi R^2}{2\pi Rh}. \quad (5.117)$$

This shape factor indicates the ratio of the axially pulled surface to the perimeter multiplied by the height. Evaluating  $s$  for the ETAG test specimen results in a value of  $s \approx 0.4 \ll 1.0$ , which is below the limit case for cavitation according to the investigations of Hamdi et al. (2014).

For validation, material parameters for four different hyperelastic material models are determined using experimental data based on uniaxial tensile tests on dumbbell-shaped test specimens and H-shaped specimens loaded in simple shear (Staudt et al., 2018). The ETAG tensile test is subsequently calculated numerically

**Table 5.4** Material parameters for four different constitutive laws

Material Model	Parameters		
NH	$\mu =$	0.6132	
MR2	$C_{10} =$	0.3009	$C_{01} =$ 0.0145
ExtTube	$G_c =$	0.5351	$G_e =$ 0.1227
	$\beta \approx$	0	$\delta =$ 0.0609
MD	$\alpha_0 =$	3.3032	$\alpha_1 =$ -0.0015
	$\beta_0 =$	3.2393	$\beta_1 =$ 19.1343

using the determined material parameters and compared with the macroscopically determined structural behaviour. The isochoric hyperelastic material laws used are the Neo-Hookean and Mooney-Rivlin material model on the one hand and the molecular-statistically motivated extended tube model by Kaliske and Heinrich (1999) on the other hand (see Section 3.2.4), which stands out as one of the most adaptable hyperelastic formulations (Marckmann and Verron, 2006). In addition, the new isochoric constitutive model based on an inverse polynomial proposed in Section 5.1.2 is also analysed to complete the comparison and demonstrate the qualities of the new hyperelastic formulation.

The experimental database was provided by Staudt et al. (2018), who extensively studied DOWSIL™ 993 material. Using standard routines for the determination of hyperelastic material parameters, the parameters for the material DOWSIL™ 993 were determined under the assumption of incompressibility according to Tab. 5.4. On this basis, the ETAG-H test specimen was simulated under tensile load in the subsequent step. A three-dimensional model with higher order element exhibiting quadratic shape functions was set up to avoid numerical locking effects. Four different hyperelastic material models were implemented, analysed and compared with the experimental results of the uniaxial tensile tests on the ETAG H-shaped test sample.

The numerical model and the results of the validation in the form of force-displacement diagrams are shown in Fig. 5.30. Comparing the results of the Neo-Hookean material model with the results of the Mooney-Rivlin model, one can conclude that none of the simple and commonly used models are capable of accurately reproducing the high initial stiffness. An approximation of the numerical simulation curves with respect to the experimentally determined structural response can only be seen at very large deformations. It should also be noted that even the incorporation of the second invariant of the left Cauchy-Green tensor in the Mooney-Rivlin model and the insertion of an additional material parameter does not show any improvements in the result of the validation. Looking at the very adaptable model of Kaliske and Heinrich (1999), the results are not significantly improved than those of the classic models. Even the two additional micro-mechanically motivated

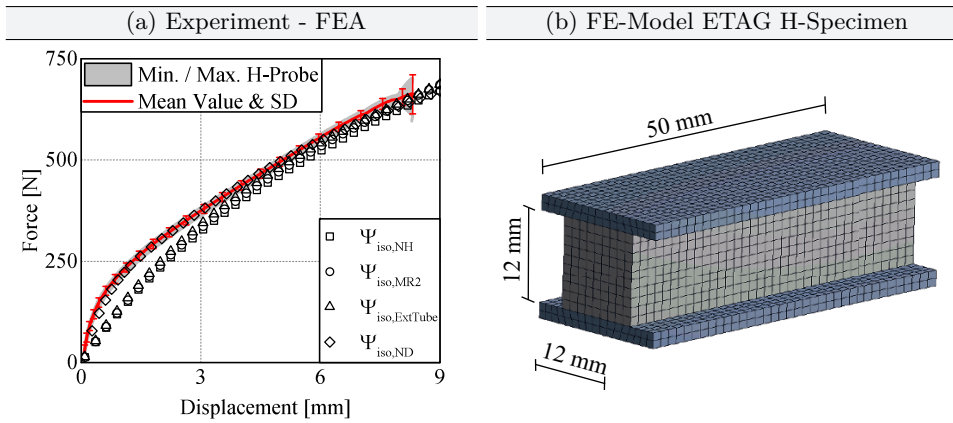


**Figure 5.30** (a) Validation of ETAG H-shaped test sample under uniaxial tensile loading analysing different isochoric hyperelastic material models; (b) FE-model of ETAG H-shaped specimen

material parameters cannot adequately represent the behaviour of the structural silicone. Considering that the design of façade constructions with structural silicones lies in deformation ranges of approximately 0.0 – 0.5 mm with respect to the ETAG H-shaped test specimen, it should be noted that the material models implemented in commercial FE programs are inadequate. Especially with regard to the representation of the correct initial stiffness, structural behaviour and failure, these models do not provide a realistic prediction, so it is not surprising that a global safety factor of 6-60 was introduced for the design of structural glazing façades in order to counter all shortcomings (ETAG 002, 2012). This was also confirmed by the work of Dias et al. (2014); Dispersyn et al. (2017); Staudt et al. (2018). In contrast to previous results, the new isochoric model  $\Psi_{iso,ND}$  allows a good approximation of the global structural behaviour of the H-shaped test sample under tensile loading. The high initial stiffness followed by moderate softening can be reproduced very well with the new model. As a result, the validation with the new proposed isochoric hyperelastic material model has been successful.

### 5.5.3 Simulation of Dumbbell-Shaped Tensile Test

Dumbbell-shaped tensile tests are the most common tests when analysing the structural behaviour of any materials. To proof that the pseudo-elastic cavitation model of Section 5.3 is able to approximate this behaviour correctly - not leading into a non-physical behaviour due to disproportional void growth - a full-scale simulation of the dumbbell-shaped tests presented in Section 4.2.1 is performed.

Since the present constitutive model only considers isothermal processes at a constant strain rate, this study investigates the stress-strain behaviour under a con-

**Table 5.5** Optimised Material parameters for TSSA for Pseudo-Elastic Cavitation Model

Material Model	Parameters			
Isochoric Neo-Hooke Material Model	$\mu =$	2.6652		
Pseudo-Elastic Cavitation Model	$\kappa_0 =$	0.0004	$\kappa_1 =$	0.2699
	$\kappa_2 =$	0.2501	$\kappa_3 =$	-0.195

stant temperature of  $T = 23^\circ\text{C}$  and a quasi-static displacement rate. Based on the results of Section 4.2.1, TSSA exhibits a non-linear elastic behaviour until fracture occurs — a characteristic property for rubber-like materials — however, TSSA does not exhibit strain stiffening due to locking stretches of the macro-molecules in the polymer matrix. Consequently, when considering isochoric deformations, simple isochoric constitutive models, like the Neo-Hookean model, can be used for TSSA (Drass et al., 2018f). The parameters of the pseudo-elastic cavitation model were obtained using inverse numerical optimization methods. Since the focus of this work is not on determining the parameters, reference is made to the work of Drass et al. (2017a) to determine them. The material parameters used to characterize TSSA are given separately in Tab. 5.5 for the isochoric and volumetric Helmholtz free energies. Based on the determined material parameters for the pseudo-elastic cavitation model, the critical hydrostatic pressure  $p_{\text{cr}}$  at which cavitation ensues is reached for a critical relative volume of  $J_{\text{cr}} = 1.041$ . This value can simply be approximated by evaluation Eq. (5.59).

During the uniaxial tension test the deformations are mainly volume-constant because the voids drastically change shape but not in volume. This means the numerical calculation of the test should not give-way to substantial void growth.

This can be confirmed regarding Fig. 5.31, where the results of the numerical calculation are visually compared with the experimental results. Fig. 5.31 a compares the structural response of both the experiment and the finite element calculations. The min. / max. values of the experiments are grey bars, the mean values are red circles and the standard deviation ( $1 \times \text{SD}$ ) is an error bar. All numerical calculations were performed with an increasing size of finite elements (328-23,142 Finite Elements) to analyse a potential mesh dependency. The results show no mesh-dependency for the simulations of the uniaxial tensile tests.

The numerical model in Fig. 5.31 b displays the boundary conditions at a constant mesh density. Since three-dimensional numerical calculations were performed, three-dimensional, higher-order volume elements with purely quadratic displacement behaviours were used. A solid element consists of 20 nodes with three degrees of translational freedom. In order to shorten the calculation time, three symmetry axes were used to analyse one eighth of a sample. A displacement of  $u = 75.00 \text{ mm}$  was applied incrementally to the top of the numerical model. This proves that the finite element calculation was carried out displacement-controlled.

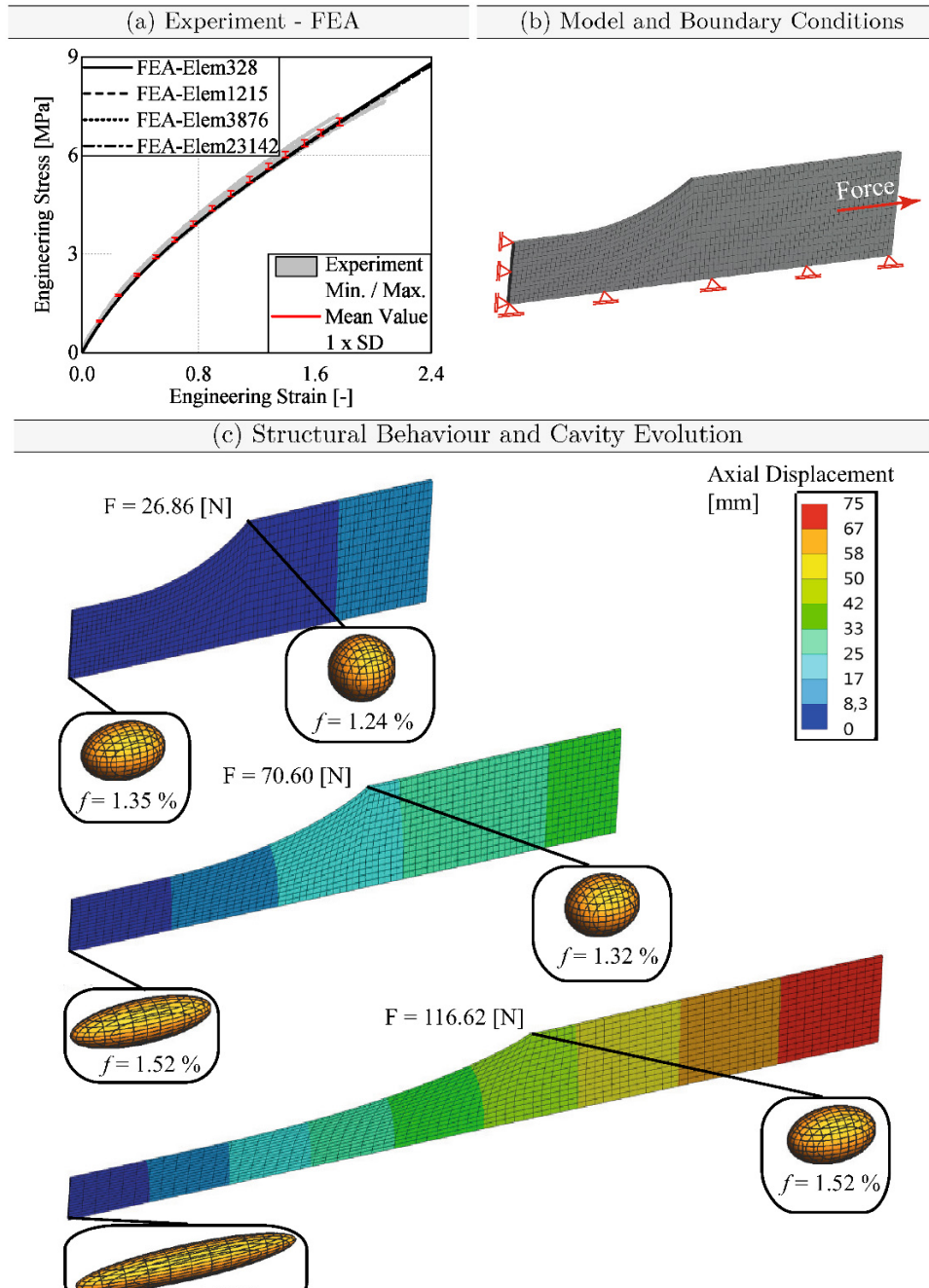


**Figure 5.31** Validation of uniaxial tensile tests proposed in Section 4.2.1 and schematic visualization of cavity evolution

The numerical results of the pseudo-elastic cavitation model and the experimental structural response calculations correspond well. Since the constitutive approach takes void growth and the geometric evolution of cavities into account, the cavity evolution at various positions and load-steps can be seen in Fig. 5.31 c. The geometrical evolution of the cavities is calculated by evaluating the isoperimetric, volumetric shape function  $\Omega(\Pi, \Theta)$ . Based on numerically calculated values of the equivalent void growth measure  $\Theta$  and the isoperimetric inequalities  $t_{1-2}$ ,  $t_{2-3}$  and  $t_{3-1}$ , the geometric evolution of an initially spherical cavity is calculated and visualized. Fig. 5.31 c illustrates how the initially spherical cavities deform with minimal change in volume: they actually morph into a "cigar-like" shape. This is confirmed by evaluating the actual void fraction  $f$  in the current configuration. The void fraction  $f$  can be calculated by

$$f = \frac{f_0}{J} \left( 1 + \frac{J - 1}{f_0} \right). \quad (5.118)$$

The relative volume  $J$  is calculated at each Gaussian point and at each load step. TSSA has an approximate initial pore content of approximately  $f_0 \approx 3.0\%$ , which was determined in Section 4.4.1 using TEM images.

Fig. 5.31 c demonstrates that when a compressible hyperelastic material is loaded isochoric, there is a slight increase of void fraction, especially at large strains. This is natural, since the bulk modulus is not infinite for the analysed material. Stress softening due to excessive void growth is not observed in the experiment or in the simulation. Consequently, the presented constitutive modelling approach, where an isochoric Neo-Hookean material model was coupled with the pseudo-elastic cavitation model from Section 5.3, is able to validate a simple tensile test without leading to non-physical results.

## 5.5.4 Simulation of Bulge-Test

In Section 4.2.4, so-called bulge tests on TSSA were presented. The foil-like TSSA was inflated in a balloon shape using a special test device. In order to measure local strains, a stochastic speckle pattern was applied to the material to be tested. The numerical model of the bulge tests was build up according to the test set-up. Rotational symmetries in the test set-up were employed to reduce the calculation time (see Fig. 5.32 b). In accordance with Section 4.2.1, higher order, three-dimensional solid elements were used to calculate the three-dimensional numerical model of the bulge test. The anchor plate and the edge of the TSSA were fixed supported. A pressure  $p$  was applied to the bottom of the TSSA film to inflate it like a balloon. The finite element calculation was accomplished force-controlled. As a result of the force-controlled simulation of the bulge test, an instability problem occurs with very large deformations, so that the arc length method must be applied in the

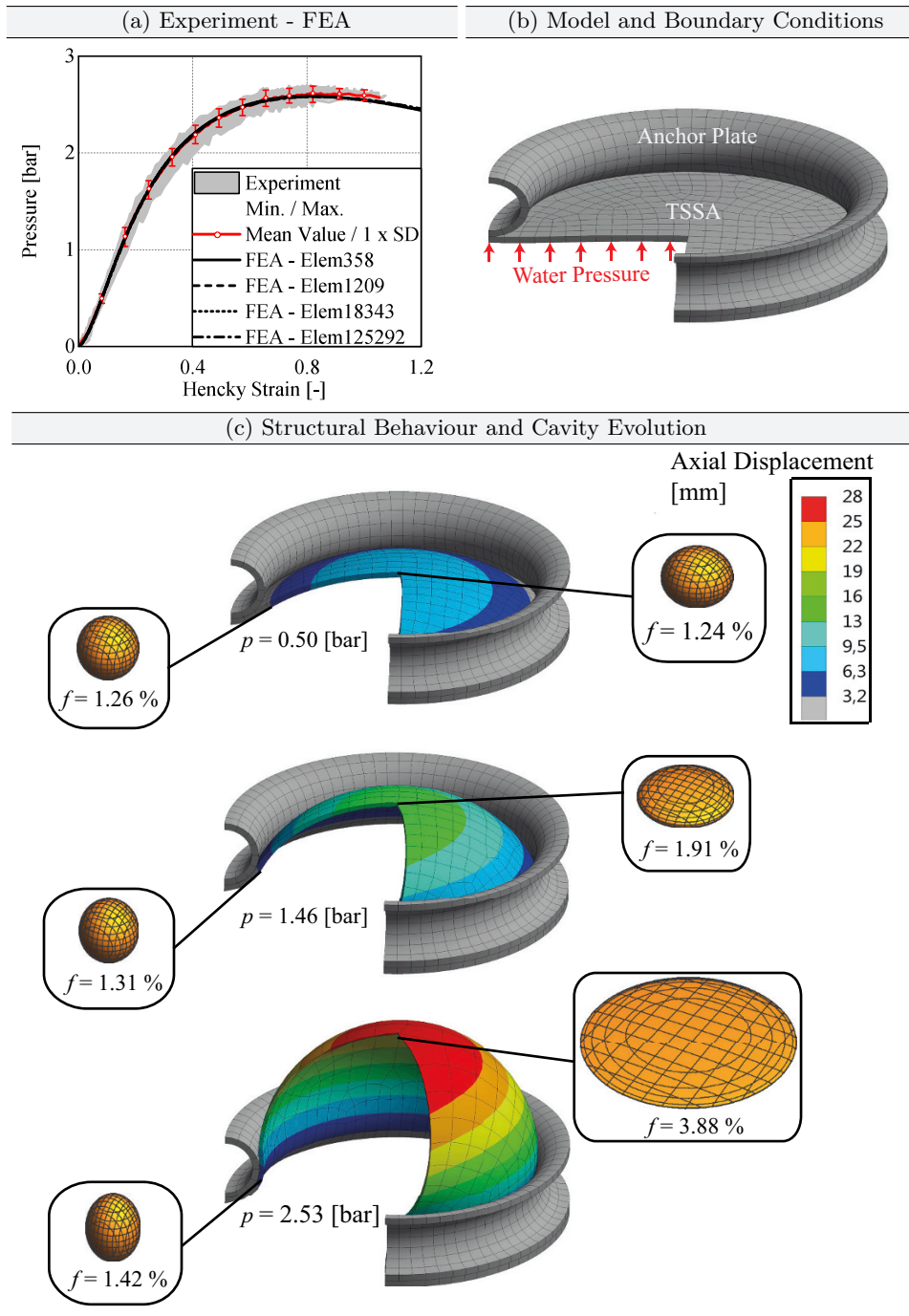


**Figure 5.32** Validation of biaxial tension tests presented in Section 4.2.4 and schematic visualization of cavity evolution

simulation. With increasing deformation, the TSSA film leans against the anchor plate so that a contact formulation must be used in the numerical model. The normal Lagrangian detection method was utilized for contact modelling. The contact formulation defines a surface contact that can only be open or closed, and the normal Lagrangian formulation closes all gaps and eliminates penetration between the contact and target surfaces. The investigation of the effects of friction determined that the coefficient of friction has no influence on the force-displacement behaviour. Therefore, the contact algorithm is formulated with a frictionless approach.

Fig. 5.32 a compares the structural response between the bulge test and the finite element analyses. Here it becomes clear that the structural responses of the numerical models lie within the standard deviation of the experiment. This proves that the novel constitutive model approach is ideally suited to take biaxial deformations into account. The increasing mesh density shows no significant deviation between the structural responses of the finite element calculations.

Fig. 5.32 c references the cavity evolution during biaxial deformation. According to the results of the uniaxial tensile tests (see Fig. 5.31 c), the initially spherical cavities deform under almost volume constant conditions. This is obvious, since the bulge test is supposed to represent a nearly isochoric deformation. Softening in the experimental and numerical structural responses is a typical phenomenon for the bulge test. However, the observed softening has nothing to do with stress-softening due to cavitation. This can be explained by the void volume's lack of change, even at large deformations. Due to the isochoric, biaxial deformation during the bulge test, the spherical cavities deform into a penny shape. As already mentioned, stress softening due to cavitation can be excluded when analysing the bulge test. Considering Fig. 5.32 c the actual void volume is shown at different positions and at different load steps. Here, a slight increase in void volume can be seen at very large deformations, but this is primarily due to the compressible material formulation and not to cavitation.

### 5.5.5 Simulation of Pancake Tension Tests

In this section numerical simulations of the pancake tests from Section 4.3.1 as well as pancake tension tests from literature (Hagl et al., 2012a; Hagl et al., 2012b) are carried out. Starting with the simulation of the pancake tension tests with a diameter of 20 mm based on the investigations by Hagl et al. (2012a); Hagl et al. (2012b), two flat-bonded steel cylinders were loaded in axial tension. Due to the lack of lateral contraction in the experimental set-up and the almost incompressible material behaviour, large volumetric deformations occur in the adhesive layer. These conditions lead to the cavitation effect, and consequently to severe stress softening in the structural behaviour.

The aim of this study is to numerically reproduce the structural response of the pancake tension test including the pronounced cavity growth that leads to a strong softening of the material. Symmetry boundary conditions were used to numerically model an angle ratio  $\varphi$  between a full cylindrical model and a specific section (see Fig. 5.33 b). The lower surface of the numerical model is only supported in the z-direction. Because of this,  $r$  and  $\varphi$  are free in their deformation. The radial and tangential degrees of freedom ( $r$  and  $\varphi$ ) were fixed for the upper side of the numerical model, while an axial displacement corresponding to the deformation of the pancake tension test was applied in the vertical z-direction. As a result, the finite element calculation was controlled by a continuous increase of the displacement. In accordance with the three-dimensional models for the uniaxial tensile test and the bulge test, the pancake tension test was also modelled three-dimensionally with three-dimensional volume elements.

Since the structural response of the numerical model and the experimental results agree, the novel constitutive modelling approach can adequately represent the strongly non-linear structural behaviour of the pancake tension test (see Fig. 5.33 a). Furthermore, no mesh-dependent results are observed in the numerical analyses.

Due to the initially almost incompressible material behaviour, void growth must be taken into account for the numerical analysis of the pancake tension test. Cavity evolution is easy to prove: The initially spherical cavities begin to grow in both axial and lateral directions, and a closer look at Fig. 5.32 c reveals that the void volume inside the adhesive increases significantly because of the constrained axial loading. At the edge of the adhesive, where the disability of lateral contraction is not very pronounced, the void volume increases only slightly. This demonstrates that there is a clear softening inside of the material due to excessive void growth, while the marginal areas are not influenced by the cavitation effect. Therefore, the deformation of the pancake tension test is not comparable with the almost volume-preserving deformation of uniaxial tensile tests and the biaxial tensile test.

Since it has already been shown that the pseudo-elastic cavitation model is well suited to approximate the pancake tension tests performed by Hagl et al. (2012a); Hagl et al. (2012b), the pancake tension tests proposed in Section 4.3.1 are simulated in the following. All simulation models are provided with the same set of material parameters, which are summarized in Table 5.5.

The simulation results for three different diameters are shown in Fig. 5.34 a. It is obvious that the pseudo-elastic cavitation model is very well suited to approximate the behaviour of TSSA in the pancake tension test for different diameters. The model is able to represent the increase in initial stiffness for larger diameters of the pancake tension test specimen. Furthermore, the occurrence of the cavitation effect and the associated strong material softening is well approximated. With

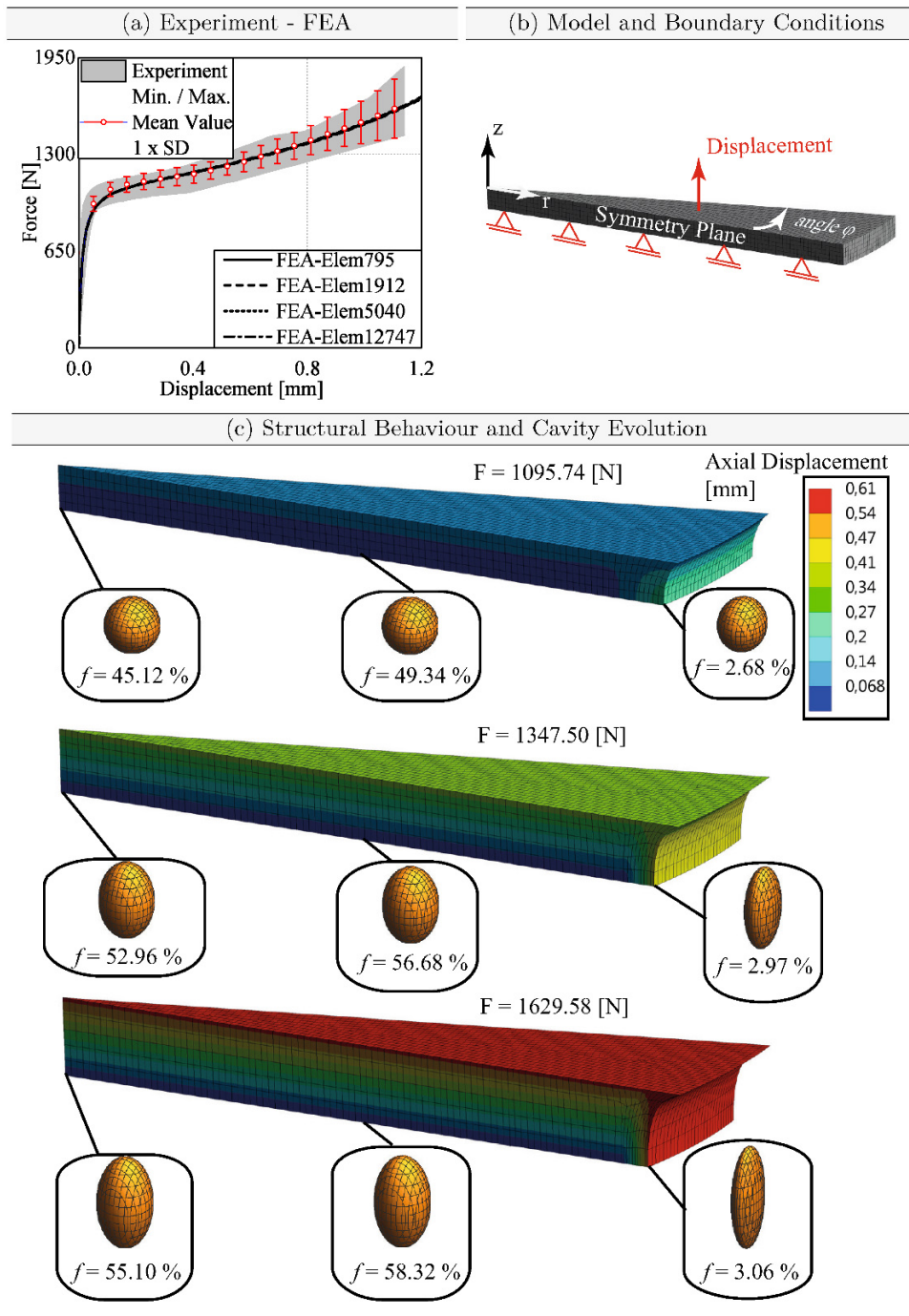
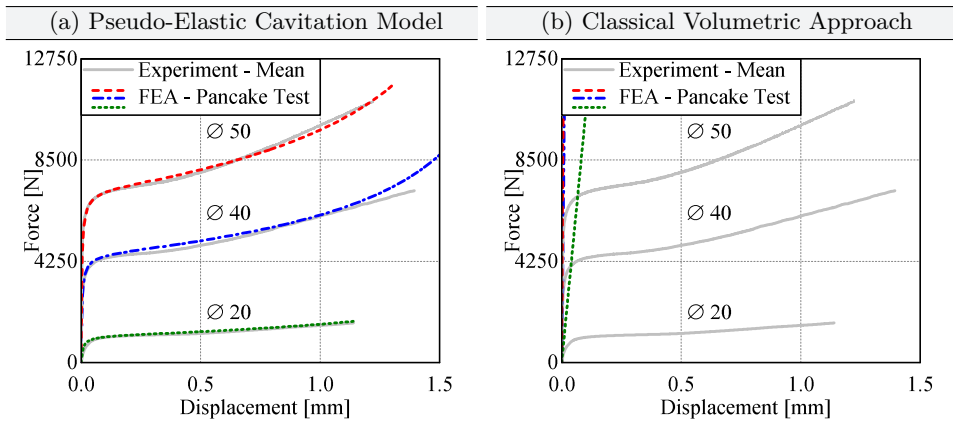


Figure 5.33 Validation of pancake tension tests performed by Hagl et al. (2012a); Hagl et al. (2012b) and schematic visualization of cavity evolution



**Figure 5.34** Validation of pancake tension tests performed by Hagl et al. (2012a); Hagl et al. (2012b) and pancake tension tests presented in Section 4.3.1 with (a) pseudo-elastic cavitation model and (b) classical volumetric Helmholtz free energy function  $\Psi_{\text{vol,classic}}$

increasing deformation, the load can be increased, which can also be modelled by the new model.

In order to further show that the classical formulation of the volumetric Helmholtz free energy function  $\Psi_{\text{vol,classic}}$ , which is generally implemented by default in commercial FE codes, is not sufficient to represent the material softening in the pancake tension test, these were simulated again (Fig. 5.34 b). Here only the initial stiffness can be approximated, which is not sufficient to represent the stress softening and accordingly the ductility of the bond.

The last comparison between FEM and pancake tension experiments involves the approach of Danielsson et al. (2004) (see Section 3.3), which can also represent cavitation in hyperelastic materials. The special feature of the model lies in the fact that only the initial shear modulus and the porosity of the material have to be known. Both material parameters were determined for TSSA in the context of this work. The shear modulus is  $\mu = 2.66 \text{ MPa}$ , whereas the initial porosity was determined to be  $f_0 \approx 2.92 \%$  (see Section 4.4.1). The approach of Danielsson et al. (2004) was implemented in ANSYS FE code and the pancake tension experiments were simulated according to the descriptions above. Looking at Fig. 5.35, it is noticeable that neither the initial stiffness nor the bifurcation point for the start of cavitation is hit. Furthermore, the post-cavitation behaviour cannot be simulated with this approach. This can be explained by the fact that Danielson's approach only approximately represents the complexity of pore growth. Furthermore, the actual micro-structural effects from the interaction between the growing voids and the matrix-filler interaction cannot be described. In conclusion, the new

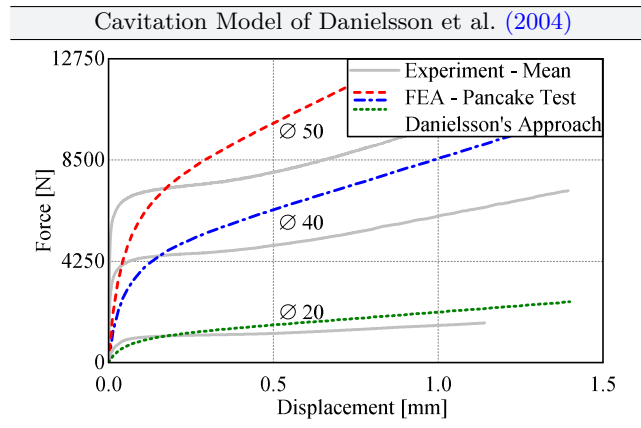


**Figure 5.35** Validation of pancake tension tests performed by Hagl et al. (2012a); Hagl et al. (2012b) and pancake tension tests presented in Section 4.3.1 with approach of Danielsson et al. (2004)

pseudo-elastic cavitation approach of Section 5.3 requires more parameters and thus increases the effort to determine them, but the experiments shown can be simulated very well, which was not possible so far.

In conclusion, the new pseudo-elastic cavitation approach of Section 5.3 requires more parameters and thus increases the effort to determine them, but the experiments shown can be simulated very well, which was not possible so far.

## 5.5.6 Simulation of Cyclic Uniaxial and Constrained Tensile Test

In this section the numerical simulations of the cyclic uniaxial tensile tests and the cyclically loaded pancake tension tests are performed. For this the extended pseudo-elastic cavitation model presented in Section 5.4 is used, which is able to simulate the softening of isochoric deformations due to the Mullins effect. Furthermore, it is able to characterize softening due to the Mullins effect in volumetric deformations and healing effects in case of reloading. The used material parameters of the pseudo-elastic cavitation model have already been summarized in Table 5.5. The material parameters for the description of the cyclic behaviour are shown in Table 5.6, which were determined by inverse numerical methods in accordance to the proposal of Drass et al. (2017a).

As already described in the presentation of the extended pseudo-elastic cavitation model in Section 5.4, the parameters  $r_{\text{mull}}$  and  $r_{\text{heal}}$  can be read directly from the experimental data of the cyclic pancake tension tests via Eq. (5.113) and Eq. (5.114) respectively. All other parameters to describe the isochoric / volumetric Mullins effect and possible healing effects had to be calculated.

The numerical simulations of the cyclic tests were carried out according to the models described above, in which three-dimensional volume elements were used. In order to save computing time, corresponding boundary conditions were applied in the model in order to have to calculate only a section of the cyclically loaded samples. The displacement boundary conditions were programmed according to the experimental test routine used.

The results of the simulation are shown in Fig. 5.36. Since the extended pseudo-elastic cavitation model can be enhanced by adding the effects of (i) isochoric Mullins / (ii) volumetric Mullins and (iii) volumetric healing, three graphs are plotted to study the effect of successively adding these phenomena. Starting with the numerical simulation of the cyclic tensile tests, an irreversible Mullins effect could be observed from the experiments, which can be reproduced with the isochoric pseudo-elastic approach of Ogden and Roxburgh (1999). As shown in Fig. 5.36 a, the pronounced material softening can be reproduced on the unloading path. Furthermore, the effect of virgin stiffness on reaching and exceeding the previously achieved maximum deformation can be approximated very well. Looking at the simulation of the cyclic pancake tension test (see Fig. 5.36 b), the isochoric Mullins effect has only a small impact on the simulation result. This is also obvious, since in the pancake tension test a predominantly volumetric deformation takes place, whereas isochoric stresses and strains only occur at the edges. By adding the volumetric Mullins effect to the material model, it can be seen that the strongly pronounced material softening can be approximated during unloading (see Fig. 5.36 c). However, it is not yet possible to numerically describe the healing effect. In the last simulation of the cyclic pancake tension test, the effects of isochoric and volumetric Mullins effect are coupled to the healing effect at reloading with the pseudo-elastic cavitation model. As can be seen in Fig. 5.36 d, it is possible to represent the healing effect on the reloading paths. However, it should be noted that the experimental curves are not quite met, which is due to numerical problems. For large deformations within the reloading path, it can be clearly seen that the simulation and experiment fit well together. However, the bifurcation point is not encountered during reloading. For this, the parameter  $m_{\text{heal}}$  would have to

**Table 5.6** Optimised Material parameters for TSSA for Extended Pseudo-Elastic Cavitation Model

Material Model	Parameters			
Isochoric Neo-Hooke Model	$\mu =$	2.6652		
Pseudo-Elastic Cavitation Model	$\kappa_0 =$	0.0004	$\kappa_1 =$	0.2699
	$\kappa_2 =$	0.2501	$\kappa_3 =$	-0.195
Isochoric Mullins Effect	$r =$	0.5882	$m =$	2.0
Volumetric Mullins Effect	$r_{\text{vol}} =$	0.45	$m_{\text{vol}} =$	0.2
Volumetric Healing Effect	$r_{\text{heal}} =$	0.67	$m_{\text{heal}} =$	0.07

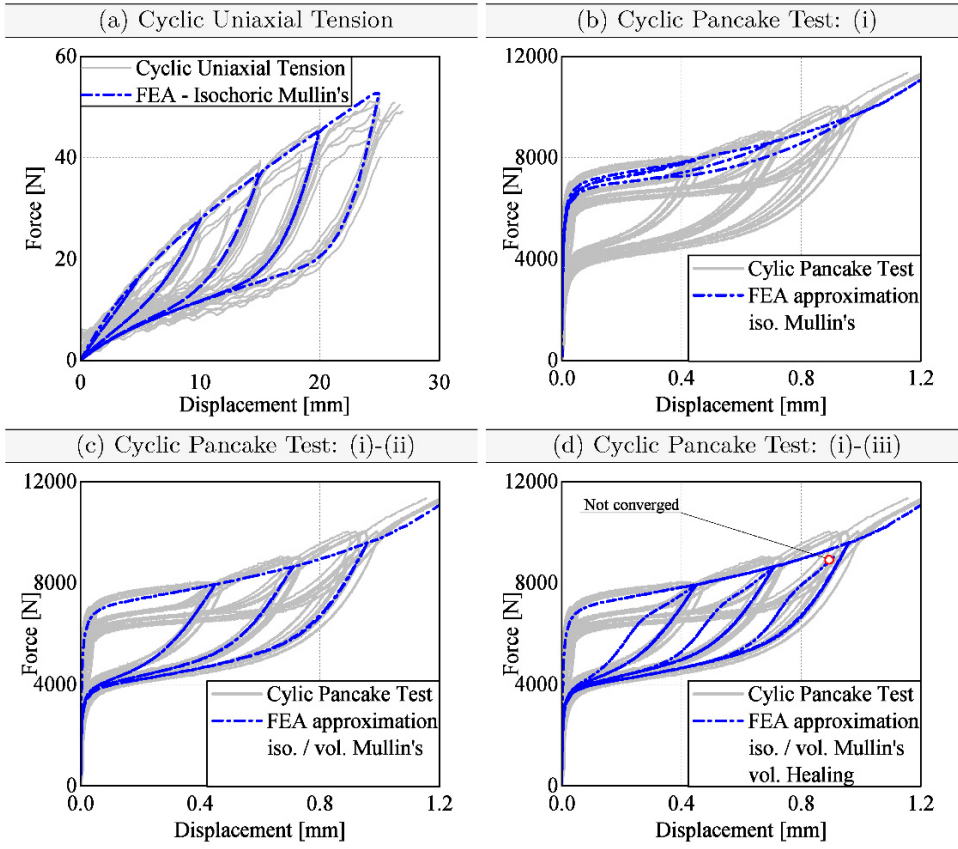


**Figure 5.36** Numerical validation of the cyclic tensile test under consideration of (a) isochoric Mullins effect. Numerical validation of cyclic pancake tension test under consideration of (b) isochoric Mullins effect, (c) isochoric and volumetric Mullins effect and (d) isochoric and volumetric Mullins effect coupled with volumetric healing effects

be selected much smaller in order to recalculate the cyclic pancake tension tests. If the parameter  $m_{\text{heal}} << 0.07$  is selected, there is no more convergence during the Newton-Raphson iterations. This could be corrected by an explicit numerical simulation, but this was not possible within the scope of this work. However, the validation presented here and the parameter study from Section 5.4.5 have shown that the extended pseudo-elastic cavitation model is very well suited to represent the cavitation effect, isochoric and volumetric Mullins effect as well as healing effects during reloading.

## 5.6 Conclusions

In this chapter, new hyperelastic material models have been developed based on the experimental data presented in Chap. 4, which can represent the structural behaviour seen in the experiments. First, based on the rational Nelder function, an isochoric, i.e. volume-constant hyperelastic material model was developed and transferred into the context of the molecular statistics of rubbers. It could be shown that the inverse formulation of the hyperelastic potential is particularly well suited to approximate various rubber-like materials under arbitrary deformations. Even a comparison with the very adaptive material model of Kaliske and Heinrich (1999), which is ranked number one in the ranking proposed by Marckmann and Verron (2006), showed that the structural behaviour of silicones can be modelled much better. In addition, a novel modelling of the volumetric material behaviour of rubber-like materials was presented, which makes it possible to map the cavitation effect via a pseudo-elastic potential. Although models exist in the literature to describe the cavitation effect in rubber, they are not suitable for mapping the material behaviour of the transparent structural silicone TSSA. It was shown that, for example, using the model of Danielsson et al. (2004), neither the initial stiffness, the bifurcation point, which describes the start of cavitation, nor the post-cavitation behaviour can be computed. With the new, phenomenological approach (Drass et al., 2019c), it is now possible to simulate the structural behaviour of silicones in particular, but also of other rubber-like materials, taking into account the cavitation effect. Furthermore, an extension of the pseudo-elastic cavitation model was presented (Drass et al., 2019a), which is additionally able to describe the volumetric cyclic behaviour.



# 6 Development of Failure Criteria for Poro-Hyperelastic Materials

This chapter deals with the description of failure of rubber-like materials under consideration of the porosity of the material, as this is decisive for the failure under triaxial loading conditions (Gent and Lindley, 1959; Hamdi et al., 2014; Drass et al., 2018c). Since failure of rubber-like materials depends strongly on the loading condition (isochoric or volumetric loading), failure criteria for the description of isochoric failure are first introduced and tested for their applicability to approximate the experimentally determined failure stretches of TSSA (see Section 4). Additionally, rubber-like materials exhibit cavitation failure under triaxial loading, which means that there is an effective stress softening of the hydrostatic pressure  $p$  with increasing volume. Thus, cavitation criteria are introduced from literature and their assumptions and limitations are briefly explained (Gent and Lindley, 1959; Hou and Abeyaratne, 1992; Lopez-Pamies et al., 2011b). Beforehand, since these classical criteria assume a material porosity of zero, a generalized cavitation criterion formulated in three-dimensional stress space is presented, which includes the classical criteria. In addition, the new stress-based cavitation criterion is extended to describe the cavitation failure in poro-hyperelastic materials exhibiting finite porosities. The individual failure stresses for arbitrary triaxial loading depending on the porosity of the material were calculated numerically with a special algorithm proposed by Lopez-Pamies et al. (2011b) and then approximated by the generalized cavitation criterion. Since the novel cavitation criterion is first described in the Cauchy stress space, an extension is proposed for the three-dimensional stretch space to make it possible to couple the stretch-based isochoric or distortional failure criterion with the stretch-based cavitation failure criterion, which can also be called dilatational failure criterion. Finally, a coupled distortional-dilatational failure criterion is presented and validated on the basis of the experimental tests carried out on TSSA, here the uniaxial tensile test, bulge test and pancake tests with three different diameters. The validation is performed by numerical calculations of the experimental tests and simultaneous evaluation of the coupled stretch-based failure criterion.

## 6.1 Isochoric Failure Criteria

The assumption of incompressibility and therefore an isochoric material behaviour for rubber-like materials is widespread (Baaser et al., 2013; Staudt et al., 2018), not only because of mathematical convenience and the description of simple constitutive relationships but also for the formulation of isochoric, disadvantageous stress-based failure criteria (Smith and Rinde, 1969; Kawabata, 1973; Tschoegl, 1971). To counter the disadvantages of stress-based failure criteria, such as dependence on the chosen material model, the material parameters used and the uniqueness of the solution to determine the failure load, recent work on polymer failure has used strain- or stretch-based failure criteria to obtain more satisfactory results for the prediction of the experimentally determined failure loads without having the above-mentioned disadvantages (Hamdi and Mahjoubi, 2015; Hamdi et al., 2006; Hamdi et al., 2007; Rosendahl et al., 2018; Staudt et al., 2018; Rosendahl et al., 2019)

Considering isochoric or distortional failure under assuming the material to behave incompressible, a very adaptable and comprehensible failure criterion was first presented by Podgórski (1984) and further developed by Bigoni and Piccolroaz (2004). The criterion is abbreviated below as the PBP criterion. Using the notation of Rosendahl et al. (2018), the distortional failure criterion formulated in three-dimensional stretch space is fully described by

$$\Phi(\mathbf{v}) = \rho \cos \left[ \beta \frac{\pi}{6} - \frac{1}{3} \arccos(\gamma \cos 3\theta) \right] - \lambda_{\text{eq}} = 0, \quad (6.1)$$

where  $\rho = \sqrt{2I_2'}$  represents the radius from the centre to the boundary failure surface in the  $\pi$ -plane and  $\mathbf{v}$  is the left stretch tensor. The parameters  $\beta$  and  $\gamma$  are fitting parameters to be determined,  $\lambda_{\text{eq}}$  describes an equivalent stretch and the stress angle  $\cos 3\theta$  has already been presented in Section 2.2.2. In order to guarantee a convex failure surface, the parameter  $\beta$  must be within the limits of  $\beta \in [0, 2]$  and the parameter  $\gamma$  within the limits of  $\gamma \in [0, 1]$ . To define the criterion in stretch space, principal stresses are directly replaced by principal stretches as proposed by Rosendahl et al. (2018).

Another promising failure criterion for rubber-elastic materials, such as unfilled and carbon black filled vulcanizates (NR, SBR and PU), and a thermoplastic elastomer (TPE) was presented by Hamdi and Mahjoubi (2015), which can be summarized via

$$\Phi(\mathbf{v}) = \rho \left[ 1 + \cosh \left( \beta \left( \theta - \frac{\pi}{3} \right) \right) \right]^{-1} - \lambda_{\text{eq}} = 0. \quad (6.2)$$

The fitting parameter  $\beta$  must be selected positively to ensure a convex failure surface without leading numerical instabilities, e.g. in a plastic material formulation.

The parameter  $\theta$  is an argument of the stress angle  $\cos 3\theta$  defined within the limits of  $\theta \in [0, \pi/3]$  and  $\lambda_{\text{eq}}$  describes an equivalent stretch, which is similar to the PBP criterion. This criterion has been specifically developed to approximate elastomers and their failure in asymmetric biaxial deformations.

The third isochoric failure criterion formulated in three-dimensional stretch space is based on the criterion developed by Altenbach and Zolochevsky (1995) and was modified by Kolupaev et al. (2018) to provide a better adaptivity concerning the fitting of experimental failure data. Therefore, it is called the modified Altenbach-Zolochesky (MAZ) criterion, which is defined by

$$\Phi(\mathbf{v}) = \sqrt{3I'_2} \left[ \left( \frac{1}{\beta} - 1 \right) \sin \varphi + \frac{1 + \beta - 2\beta\gamma}{\sqrt{3}\beta} \cos \varphi + \gamma \right] - \lambda_{\text{eq}} = 0. \quad (6.3)$$

The variables  $\beta$  and  $\gamma$  as well as  $\lambda_{\text{eq}}$  are fitting parameters to be determined based on experimental tests. In this context, the parameter  $\beta$  should be limited to  $\beta \in [0.5, 2]$ , whereas  $\gamma$  is in the range of

$$\gamma \leq \begin{cases} 2 - \frac{1}{\beta} & \text{for } \beta \in [0.5, 1] \\ \frac{2}{\beta} - 1 & \text{for } \beta \in [1, 2] \end{cases}. \quad (6.4)$$

The variable  $\varphi$ , which represents a variation of the stress angle, is defined accordingly to Kolupaev (2018):p.5 by

$$\varphi = -\frac{1}{3} \arcsin \left( \frac{3\sqrt{3}I'_3}{2I'^{3/2}_2} \right). \quad (6.5)$$

In the following, various failure criteria are used to approximate the failure stretches of TSSA according to Section 4. The failure stretches for uniaxial and biaxial tension, simple shear deformation and the maximum acceptable stretches of the pancake test are shown in Fig. 6.1. In order to obtain a comprehensible representation of the failure stretches, these are shown in the  $\pi$ -plane. The  $\pi$ -plane is characterized by the axes  $\xi_2$  and  $\xi_3$ , which span the plane perpendicular to the hydrostatic tensile axis (space diagonal). A concise description of the  $\pi$ -plane has already been presented in Section 2.2.2. Additionally to the experimental data, the approximation of the failure data by the PBP criterion as well as other failure criteria are shown in this figure. Hence, classical criteria such as von Mises's criterion, Tresca's and Ivlev's criteria are compared with modern criteria such as the PBP criterion, the MAZ criterion and the criterion of Hamdi and Mahjoubi (2015). In order to obtain more insight into classical criteria and their mathematical formulations, reference is made to Kolupaev (2018).

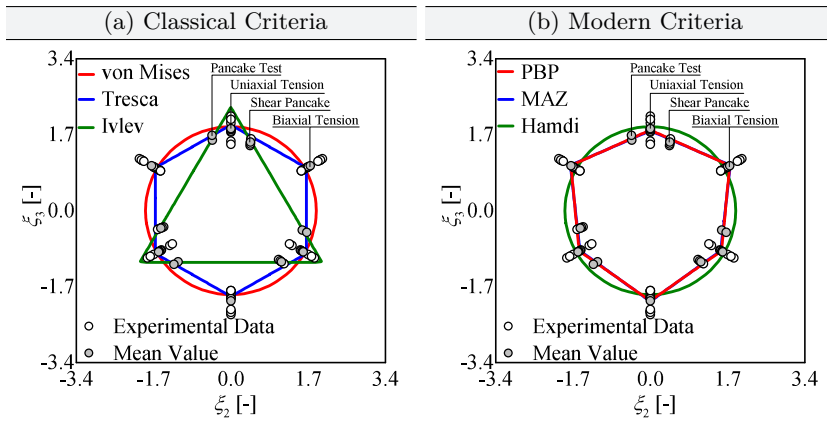


**Figure 6.1** Failure stretches of TSSA for uniaxial, biaxial, triaxial and simple shear loading and their approximations by classical and modern failure criteria: (a) classical criteria, such as von Mises, Tresca or Ivlev's criterion and (b) modern failure criteria, like the PBP, the MAZ and Hamdi's criterion, which are illustrated in the  $\pi$ -plane

**Table 6.1** Determined parameters for the isochoric failure criteria PBP, MAZ and the criterion of Hamdi applied to TSSA

failure criterion	$\lambda_{eq}$	$\beta$	$\gamma$
PBP Criterion - Eq. (6.1)	1.6432	0.8175	0.9999
MAZ Criterion - Eq. (6.3)	2.1916	1.1353	0
Hamdi Criterion - Eq. (6.2)	0.9391	$\approx 0$	/

As expected, the classical criteria do not approximate the measured experimental data well and / or show a  $C_0$  continuity, which may lead to numerical instabilities. Looking at the criterion of Hamdi and Mahjoubi (2015), the data set is not well approximated. It can even be seen that this criterion degenerates to the von Mises criterion for the present dataset. Therefore, it is not surprising that the parameter  $\beta$  takes the value zero, from which the direct connection to the von Mises criterion results. The best approximation of the failure stretches of TSSA could be achieved with the PBP and the MAZ criteria, which lead to nearly identical results. Comparing the functional adaptability, the PBP criterion shows more flexibility in the representation of the  $\pi$ -plane through the additional parameter  $\gamma$ . In the case of a more complex failure behaviour, the PBP criterion would therefore lead to better fitting results (Rosendahl et al., 2018). To summarize, the determined parameters for the PBP, MAZ and Hamdi criteria are shown in Tab. 6.1. The parameters were determined using the least squares method. For this purpose, an objective function was defined according to Eq. (5.115), which must be minimized in order to obtain optimized parameters.

## 6.2 Classical Cavitation Criteria

Relevant cavitation criteria from literature are discussed in this section, which represent the abrupt onset of cavitation in terms of excessive void growth due to high hydrostatic stresses. Since cavitation leads to a pronounced softening in the structural response of the analysed material, it is desirable to predict this effect and the exact strains and stresses, at which cavitation ensues. Therefore, first, classical cavitation criteria are summarized below, which were proposed by various researchers on the basis of different theoretical backgrounds. Subsequently, novel stress- and stretch-based cavitation criteria are developed and calibrated with experimental data on TSSA presented in Chap. 4.

### 6.2.1 Gent & Lindley Criterion

The first cavitation criterion was developed by Gent and Lindley (1959). Based on a large test series on natural rubbers under constrained tensile loading, i.e. pancake tension tests, a stress-based cavitation criterion was derived, which reads

$$\frac{1}{3}(\sigma_1 + \sigma_2 + \sigma_3) - \frac{5}{2}\mu = 0 \quad (6.6)$$

or

$$I_{1,\sigma} - \frac{15}{2}\mu = 0, \quad (6.7)$$

where  $\mu$  represents the initial shear modulus of the analysed material. The criterion was defined in the principal stress space in order to clearly illustrate it and to be able to read the critical stresses directly from the experimental tests. The idea for the criterion was developed based on the experimental investigation of pancake tension tests, from which the mathematical relationship Eq. (6.6) was derived.

Looking at Fig. 6.2, the criterion is represented by a simple planar surface in three-dimensional Cauchy stress space with a Gaussian curvature of  $\mathcal{K} = 0$ . The absolute values of the Gaussian curvature are indicated as colouration in the plot. Additionally, the critical hydrostatic pressure  $p_{\text{cr}}$  under homogeneous hydrostatic loading is given. Returning to the developed criterion of Gent and Lindley (1959), it gives a relationship between the initiation of cavitation dependent on the stress state. Regarding homogeneous hydrostatic loading ( $\sigma_1 = \sigma_2 = \sigma_3 = \sigma$ ), it is immediate that the critical homogeneous hydrostatic load corresponds to the well-known result of  $p_{\text{cr}} = 5/2\mu$  (Ball, 1982). Considering different stress states, like uniaxial tension with  $\sigma_1 = \sigma$  and  $\sigma_2 = \sigma_3 = 0$ , one obtains the solution that cavitation occurs while reaching  $p_{\text{cr,UT}} = 15/2\mu$ . At biaxial stress with  $\sigma_1 = \sigma_2 = \sigma$  and  $\sigma_3 = 0$ , the critical load is  $p_{\text{cr,BT}} = 15/4\mu$ , so that the relationship  $p_{\text{cr,UT}} = 1/2p_{\text{cr,BT}}$  can be derived from it. Since cavitation is a phenomenon under pure homogeneous

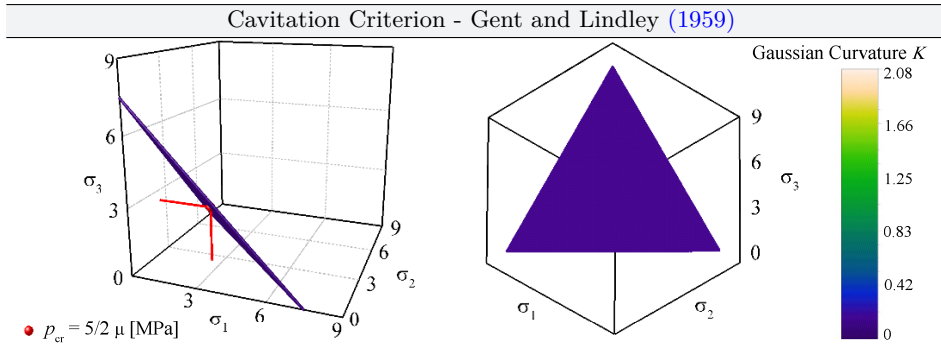


**Figure 6.2** Cavitation criterion by Gent and Lindley (1959) in three-dimensional principal Cauchy stress space

and inhomogeneous triaxial stresses, the above-mentioned criterion is not physical, since it permits cavitation even under isochoric (volume-preserving) deformations.

### 6.2.2 Hou & Abeyaratne Criterion

A second criterion, which determines the critical load for void growth under arbitrary triaxial loading ( $\sigma_1 \neq \sigma_2 \neq \sigma_3 \geq 0$ ), was presented by Hou and Abeyaratne (1992) with

$$(4\sigma_1 - \sigma_2 - \sigma_3)(4\sigma_2 - \sigma_3 - \sigma_1)(4\sigma_3 - \sigma_1 - \sigma_2) - 125\mu^3 = 0 \quad (6.8)$$

or

$$\frac{8}{27} I_{1,\sigma}^3 - \frac{50}{3} I_{1,\sigma} I'_{2,\sigma} + 125 I'_{3,\sigma} - 125\mu^3 = 0. \quad (6.9)$$

The expression to describe cavitation failure has been approximated according to Hou and Abeyaratne (1992) using a certain class of kinematically admissible deformation fields, taking into account the following limitations regarding Cauchy stresses:

$$\begin{aligned} 4\sigma_1 - \sigma_2 - \sigma_3 &> 0, \\ 4\sigma_2 - \sigma_3 - \sigma_1 &> 0, \\ 4\sigma_3 - \sigma_1 - \sigma_2 &> 0. \end{aligned} \quad (6.10)$$

The formulated restrictions are necessary from a physical point of view, since their neglect would lead to cavitation failure even under isochoric deformations. This

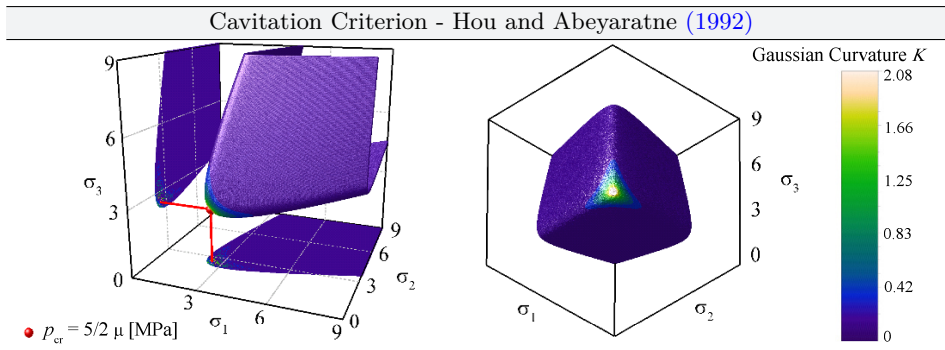


**Figure 6.3** Cavitation criterion by Hou and Abeyaratne (1992) in three-dimensional principal Cauchy stress space

non-physical behaviour could already be observed for the Gent and Lindley (1959) criterion.

An illustration of the proposed criterion is shown in Fig. 6.3 from different perspectives. As already mentioned, the critical hydrostatic stress  $p_{\text{cr}}$  and the Gaussian curvature are also shown. It is worth mentioning that the Gaussian curvature is always positive and therefore a convex criterion is present. Looking more closely at the absolute values of the Gaussian curvature, it is noticeable that they assume relatively small values. From this it can be deduced that the cavitation criterion converges sharply, which can also be seen in the three-dimensional representation of it in the Cauchy stress space. As it is obvious from Fig. 6.3, the proposed cavitation failure surface represents the onset of cavitation under arbitrary triaxial loading conditions. Penetrating the presented failure surface due to any deformation means that inherent voids suddenly begin to grow, which is equivalent to cavitation failure. From Eq. (6.8) it follows that cavitation occurs for homogeneous hydrostatic loading in accordance to the well-established solution of Gent and Lindley (1959) and Ball (1982), which reads  $p_{\text{cr}} = 5/2\mu$ .

### 6.2.3 Lopez-Pamies et al. Criterion

A third closed-form cavitation criterion was developed by Lopez-Pamies et al. (2011b). The proposed closed-form cavitation criterion represents an approximated solution of a more complex cavitation criterion proposed in an earlier publication of Lopez-Pamies et al. (2011a). However, for all practical purposes a simple expression was given by Lopez-Pamies et al. (2011b) to describe cavitation failure in arbitrary stress states. This solution reads

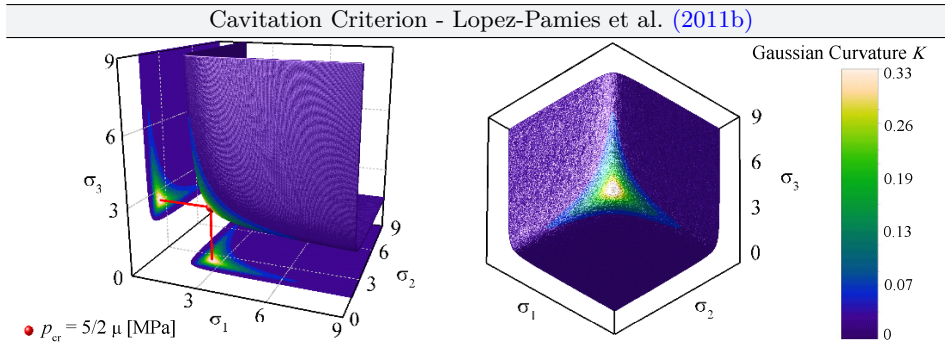


**Figure 6.4** Cavitation criterion by Lopez-Pamies et al. (2011b) in three-dimensional principal Cauchy stress space

$$8\sigma_1\sigma_2\sigma_3 - 12\mu(\sigma_1\sigma_2 + \sigma_2\sigma_3 + \sigma_3\sigma_1) + 18\mu^2(\sigma_1 + \sigma_2 + \sigma_3) - 35\mu^3 = 0 \quad (6.11)$$

or

$$8\left(\frac{I_{1,\sigma}^3}{3^3} - \frac{I_{1,\sigma} I'_{2,\sigma}}{3} + I'_{3,\sigma}\right) - 12\mu\left(\frac{I_{1,\sigma}^2}{3} - I'_{2,\sigma}\right) + 18\mu^2 I_{1,\sigma} - 35\mu^3 = 0. \quad (6.12)$$

In the case of homogeneous hydrostatic loading the solution of the critical load for the onset of cavitation is equal to the result of Eq. (6.6), which corresponds to the well-established solution for the onset of cavitation. Since the approximate solution of the criterion was restricted towards  $\sigma_k > \frac{3}{2}\mu$  with  $k \in \{1, 2, 3\}$  (Poulain et al., 2017), no cavitation occurs under isochoric deformations.

A three-dimensional representation in Cauchy stress space is shown in Fig. 6.4 from different perspectives. It can also be seen here that a convex criterion is also present, since the Gaussian curvature is always positive. In contrast to the cavitation criterion of Hou and Abeyaratne (1992), the failure surface of Lopez-Pamies et al. (2011b) is more bloated, so that cavitation failure can occur faster and more frequently. This fact can be verified by examining the Gaussian curvature. Looking at the Gaussian curvature of the criterion of Lopez-Pamies et al. (2011b), the absolute values are much larger than those of the criterion of Hou and Abeyaratne (1992). This shows that the criterion is much more bloated. Regarding a homogeneous hydrostatic loading, all three classical cavitation criteria lead to the same result of  $p_{cr} = 5/2\mu$ .

## 6.3 Generalized Cavitation Criterion

In contrast to classical cavitation criteria (Gent and Lindley, 1959; Hou and Abeyaratne, 1992; Lopez-Pamies et al., 2011b), which assume an infinitesimal void fraction, this section presents a new generalized stress-based cavitation criterion accounting for finite void fraction in poro-hyperelastic materials (Drass et al., 2018a). For this purpose, the established criterion of Podgórski (1984) and Bigoni and Piccolroaz (2004) is reformulated to describe cavitation failure in rubbers. Based on numerical investigations of voided RVEs under triaxial loading, virtual data points are determined describing cavitation failure for different porosities and triaxial loading conditions. The generalized criterion is then calibrated using the virtual stress-based data. In addition, it is shown that the generalized criterion includes the classical cavitation criteria of Section 6.2.

### 6.3.1 Extended Podgórski Criterion Accounting for Cavitation

A generalized cavitation criterion is presented, which is based on the work of Podgórski (1984) and Bigoni and Piccolroaz (2004); Piccolroaz and Bigoni (2009), who analysed yielding of quasi-brittle and frictional materials. This criterion is transferred into the context of rubber failure due to cavitation. The general form of the criterion reads

$$\Phi = f(p) + \Omega(\theta), \quad (6.13)$$

where  $f(p)$  defines the meridian function and  $\Omega(\theta) = q/g(\theta)$  represents the deviatoric function or in our context the distortional failure. As a meridian function one understands the course of the failure surface for a certain Lode angle along the hydrostatic axis.

The additive split of Eq. (6.13) readily show the decoupling between the pressure-dependent and deviatoric part of the classical criterion. Setting the focus on the deviatoric function, Bigoni and Piccolroaz (2004); Piccolroaz and Bigoni (2009) proposed the following deviatoric equation

$$g(\theta) = \frac{1}{\cos \left[ \beta \frac{\pi}{6} - \frac{1}{3} \arccos (\gamma \cos 3\theta) \right]}. \quad (6.14)$$

Manipulating Eq. (6.14) to obtain more flexibility of fitting pressure-sensitive cavitation failure surfaces and inserting the parameter  $\chi$ , which in turn is a function of the first invariant of the Cauchy stress tensor,  $g(\theta)$  reads

$$g(\theta) = \frac{1}{\cos \left[ \frac{1}{3} (\pi \beta - \arccos (\gamma \chi \cos 3\theta)) \right]}. \quad (6.15)$$

The parameter  $\beta \in [0, 1]$  and  $\gamma \in [-1, 1]$  describe the  $\pi$ -plane of the criterion. With the presented limitations for the parameters, the convexity condition of the  $\pi$ -plane is generally fulfilled (Kolupaev, 2017). Thus within the  $\pi$ -plane, the Gaussian curvature is always positive. This must also be proved for the meridian course of the generalised cavitation criterion. To ensure a smooth function course for  $\gamma$ , it is expressed as a sine function via

$$\gamma = \sin\left(\frac{k\pi}{2}\right) \text{ with } k \in [-1, 1]. \quad (6.16)$$

The parameter  $\xi$  is defined as

$$\chi = 1 - \left(\frac{\alpha}{I_{1,\sigma}}\right)^\eta, \quad (6.17)$$

which influences the course of the  $\pi$ -plane along the hydrostatic axis. The parameter  $\alpha$  indicates the hydrostatic pressure at which cavitation occurs for  $\sigma_1 = \sigma_2 = \sigma_3 \geq 0$ . The parameter  $\eta$  was introduced in order to approximate the classical cavitation criteria due to the strongly different geometric courses.

The deviatoric stress component  $q$ , which is related to the von Mises criterion for reasons of comparability, is determined as follows

$$q = \sqrt{\frac{3I'_{2,\sigma}}{\psi^2}}. \quad (6.18)$$

Inserting Eq. (6.18) into the deviatoric function  $\Omega(\theta) = q/g(\theta)$ , one obtains

$$\frac{q}{g(\theta)} = \sqrt{\frac{3I'_{2,\sigma}}{\psi^2}} \cos\left[\frac{1}{3}(\pi\beta - \arccos(\gamma\chi \cos 3\theta))\right]. \quad (6.19)$$

The unknown parameters  $\psi$ ,  $\beta$ ,  $\gamma(k)$  and  $\chi(\alpha, \eta)$  must be determined, for example, by the least squares method. Regarding the meridian function  $f(p)$ , it is represented by

$$f(p) = \frac{(I_{1,\sigma} + \mu\alpha)^m (I_{1,\sigma} - \mu\alpha)^m}{(\mu\alpha)^2}, \quad (6.20)$$

where  $\alpha$  represents the critical hydrostatic pressure at which cavitation ensues under homogeneous hydrostatic stress. The parameter  $\mu$  represents the initial shear modulus of the analysed material. For the following studies it is assumed that the proposed criterion is examined under normalized material behaviour, so

that  $\mu$  is equal to one. The total form of the generalized stress-based cavitation failure criterion can be summarized as follows

$$\frac{(I_{1,\sigma} + \mu\alpha)^m (I_{1,\sigma} - \mu\alpha)^m}{(\mu\alpha)^2} = \sqrt{\frac{3 I'_{2,\sigma}}{\psi^2}} \cos \left[ \frac{1}{3} (\pi\beta - \arccos(\gamma\chi \cos 3\theta)) \right]. \quad (6.21)$$

### 6.3.2 Parameter Studies on Extended Podgórski Criterion

In order to analyse the behaviour of the generalised cavitation criterion and study the impact on its geometrical evolution by changing specifically the fitting parameters separately, classical parameter studies are carried out in the following. The investigations are separated between parameters that have a strong influence on the meridian function course and parameters that strongly influence the  $\pi$ -plane.

Focussing on the parameters  $\alpha$ ,  $m$  and  $\psi$  it is obvious from Fig. 6.5 that they strongly influence the behaviour of the meridians. Hence, the results of the parameter study are plotted in the scaled Burzyński-plane. Varying the parameter  $\alpha$  clearly shows two effects. First,  $\alpha$  describes exactly the point of intersection with the abscissa, so that this parameter uniquely describes the point for cavitation under homogeneous hydrostatic tensile loading. On the other hand it is noticeable that with increasing  $\alpha$ , the inclination of the meridians decreases (see Fig. 6.5 a). From a physical viewpoint, this parameter must be within the limits of  $0 < \alpha \leq 7.5$ , since for a very small  $\alpha$  there would be an almost completely porous material, whereas  $\alpha = 7.5$  postulates a porosity of zero. By increasing the parameter  $m$ , the meridians change from a concave to a convex function course. This must be taken into account when a convex cavitation criterion with a positive Gaussian curvature is required (see Fig. 6.5 b). The analysis of the definiteness of the Hessian of the meridian function revealed that the parameter  $m$  must be within the limits of

$$0 < m < \omega \quad \text{with} \quad \omega \begin{cases} \lim_{I_{1,\sigma} \rightarrow +\alpha} \frac{I_{1,\sigma}^2 + \alpha^2}{I_{1,\sigma}^2} = 1.0 \\ \lim_{I_{1,\sigma} \rightarrow +\infty} \frac{I_{1,\sigma}^2 + \alpha^2}{I_{1,\sigma}^2} = 1/2 \end{cases}. \quad (6.22)$$

In order to have a convex criterion for large deformations and correspondingly high hydrostatic stresses  $p(I_{1,\sigma})$ ,  $m$  is defined within the limits  $0 < m < 1/2$ . The parameter  $\psi$  strongly influences the slope of the meridian function course. As  $\psi$  increases, the slope also increases, with no transition from a concave to a convex function course, as can be seen for the  $m$  parameter (see Fig. 6.5 c). For a very small  $\psi$ , the curve of the criterion is very flat, so that the parameter is defined within  $0 < m$ .

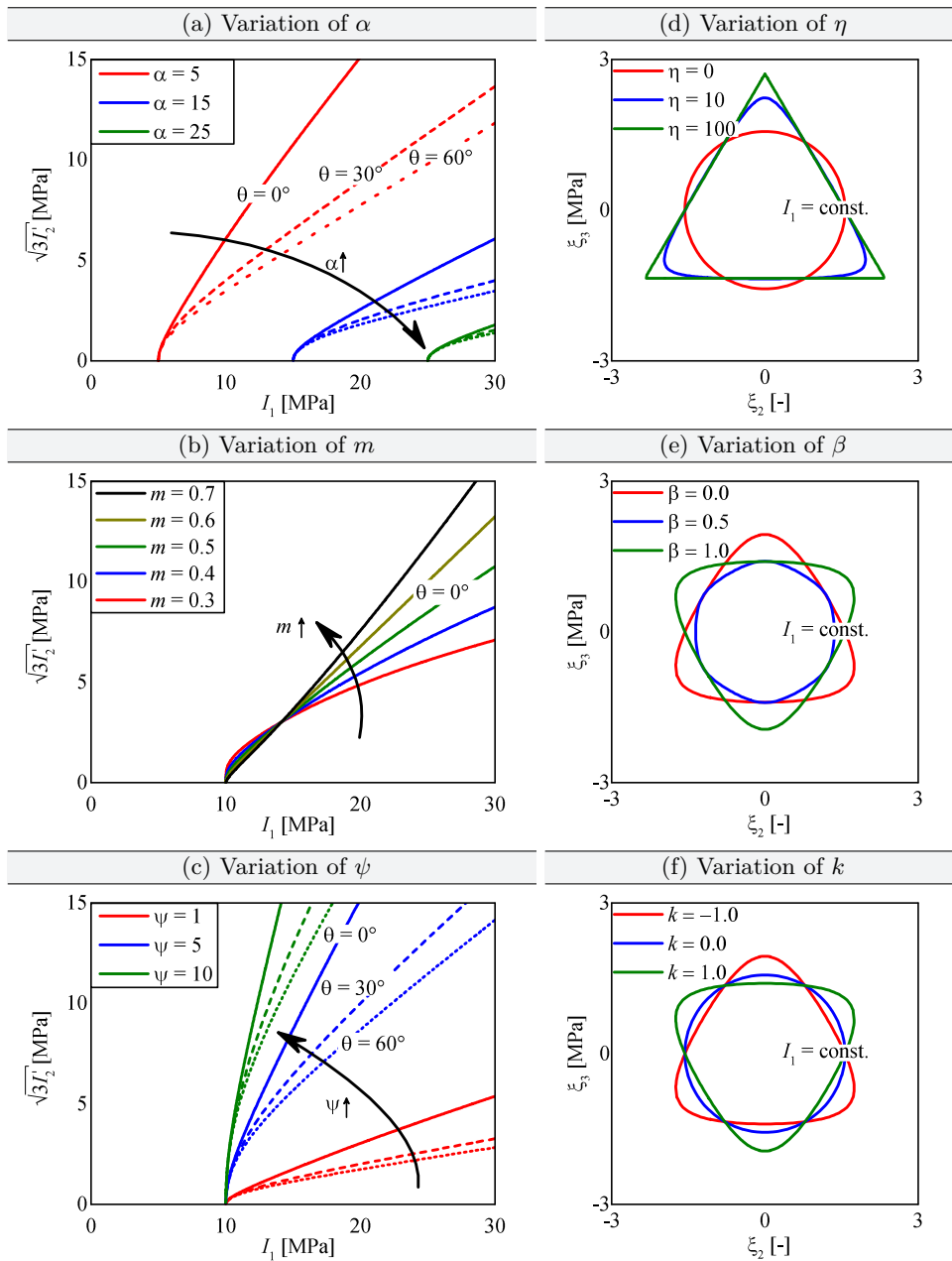


**Figure 6.5** Parameter study of the generalized stress-based cavitation criterion, separated according to effects influencing the course of the meridians or the shape in the  $\pi$ -plane

The results of the parameter study for  $\eta$ ,  $\beta$  and  $k$ , which particularly influence the  $\pi$ -plane, are shown in Fig. 6.5 d-f. Analysing the parameter  $\eta$ , it is noticeable that the angularity of the criterion expressed in the  $\pi$ -plane strongly increases with increasing  $\eta$ . Thus everything from circular shapes to sharp triangles can be reproduced (see Fig. 6.5 d). The parameter  $\eta$  is limited to  $0 < \eta < 100$ , since larger values for  $\eta$  only had a minor influence on the angularity within the  $\pi$ -plane. Looking at parameters  $\beta$  and  $k$ , both have a similar influence on the behaviour of the generalized criterion in the  $\pi$ -plane. The influence on the shape in the  $\pi$ -plane is not as strong as is the case for the parameter  $\eta$ . Nevertheless, it is possible to rotate the shape around the hydrostatic axis with both parameters, resulting in great flexibility for the approximation of test data (see Fig. 6.5 e,f). The bounds of both parameters have already been represented in Section 6.3.1.

### 6.3.3 Virtual Data For Cavitation Failure at Finite Porosity

To calculate virtually stress-based cavitation failure in poro-hyperelastic materials, numerical studies on single-voided RVEs under arbitrary triaxial loading are performed varying void fraction. For the numerical investigations, cavitation failure is assumed as soon as a critical relative volume  $J_{\text{cr}}$  is reached. When  $J_{\text{cr}}$  is exceeded, a pronounced, effective material softening in the form of excessive void growth commences, which can be regarded as an indicator of cavitation failure. The critical failure stresses for cavitation are numerically calculated applying two load steps. The first is a homogeneous hydrostatic loading until the critical relative volume  $J_{\text{cr}}$  is reached. The second load steps is defined by an arbitrary triaxial loading keeping the critical relative volume  $J_{\text{cr}}$  constant (Lopez-Pamies et al., 2011b). The microstructure of rubbery material and its evolution during triaxial loading is studied by parametrically constructing a centred, single-voided cubic RVE in which the void fraction is varied between  $1 \leq f_0 \leq 15\%$ . Here, void fraction  $f_0$  gives the ratio between void volume and the volume of the RVE in the undeformed configuration. For reasons of simplicity, a single-voided RVE is investigated instead of multi-voided RVEs, since the critical relative volume  $J_{\text{cr}}$  as an indicator of cavitation failure is almost identical for the same porosity (Drass et al., 2018b). The critical relative volume  $J_{\text{cr}}$  is calculated based on the maximum hydrostatic pressure  $p_{\text{cr}}$  of the RVE undergoing homogeneous, hydrostatic loading with  $\lambda_1 = \lambda_2 = \lambda_3 = \lambda$ . Due to this special case of loading, all calculated  $p - J$  responses exhibit a maximum turning point, hence  $J_{\text{cr}}$  can be easily determined (see Fig. 6.6). The critical relative volume  $J_{\text{cr}}$  and critical homogeneous, hydrostatic stresses  $p_{\text{cr}}$  depending on the assumed fixed porosities are listed in Tab. 6.2.

Fig. 6.7 shows the analysed RVE with the undeformed and two deformed configurations. The deformed configurations correspond to load steps 1 and 2, in which the cavity evolution can be vividly tracked.

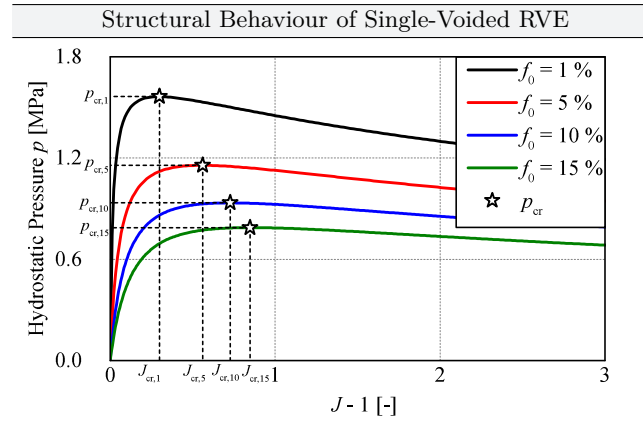


**Figure 6.6** Representation of structural behaviour and critical hydrostatic stresses  $p_{\text{cr}}$  with corresponding  $J_{\text{cr}}$  of different RVEs under homogeneous hydrostatic loading

**Table 6.2** Critical relative volume and critical hydrostatic stress dependent on different fixed porosities

porosity	$f_0 = 1\%$	$f_0 = 5\%$	$f_0 = 10\%$	$f_0 = 15\%$
critical relative volume $J_{\text{cr}}$ [-]	1.2983	1.5609	1.7281	1.8489
critical hydrostatic load $p_{\text{cr}}$ [MPa]	1.5639	1.1569	0.9343	0.7878

The analysed RVE is modelled by an incompressible, normalized Neo-Hookean material with an initial shear modulus of  $\mu := 1.0$  MPa. The centred void has no stiffness and represents all inherent voids in the material with respect to a representative aperture of the material. To reduce calculation time, symmetry boundary conditions are applied with the result that 1/8 th of the full model is analysed only. The RVE is three dimensionally modelled, where three-dimensional higher order solid elements are utilized as finite elements, which exhibit a pure quadratic displacement behaviour. One single solid element incorporates 20 nodes with three translational degrees of freedom. Furthermore, to prevent volumetric mesh locking in incompressible and nearly incompressible cases, the element technology utilizes a uniform reduced integration scheme.

In the first load step, the principal stretches applied to the RVE are defined as follows

$$\lambda_1 = \lambda_2 = \lambda_3 = \lambda \quad \text{for } 1 \leq \lambda \leq J_{\text{cr}}^{1/3}. \quad (6.23)$$

In the second load-step, a non-homogeneous triaxial deformation is consecutively applied, which read

$$\lambda_1 = \lambda, \quad \lambda_2 = \lambda^m \quad \text{and} \quad \lambda_3 = J_{\text{cr}} \lambda^{-(1+m)} \quad (6.24)$$

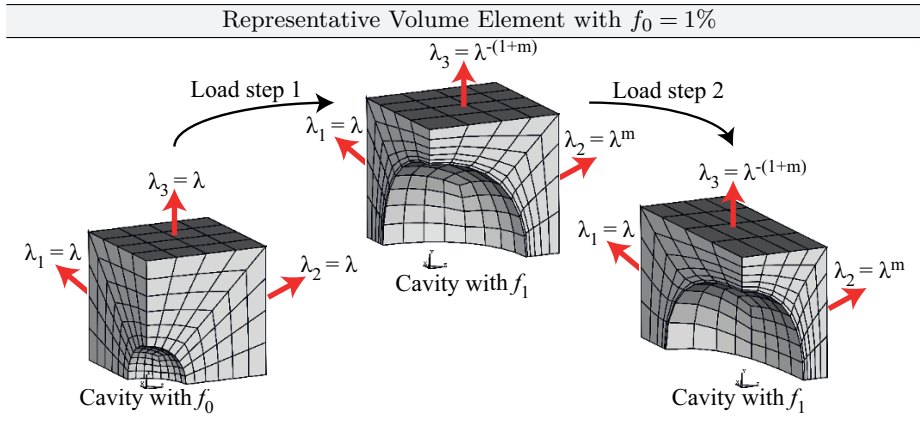


**Figure 6.7** Schematic illustration of an RVE under hydrostatic loading conditions: (a) Load step 1 - homogeneous, hydrostatic loading condition; (b) Load step 2 - inhomogeneous, triaxial loading condition under constant relative volume  $J = J_{\text{cr}}$

Within the second load step, each additional incrementally applied load fulfills the condition of  $\lambda_1 \lambda_2 \lambda_3 \equiv J_{\text{cr}}$  for  $\lambda > J_{\text{cr}}^{1/3}$ . By varying the parameter  $m$ , different failure stresses result for different degrees of triaxiality. It is sufficient to choose the parameter  $m \in \mathbb{R}$  within the limits of  $-0.5 \leq m \leq 1.0$  due to planes of symmetry of the resulting failure surface.

### 6.3.4 Approximation of Cavitation Failure in Stress Space

In this section the unknown parameters of the proposed generalized cavitation criterion of Eq. (6.21) are determined based on the least squares method using the data sets from Section 6.3.3. Least squares means that the sum of the squares of the residuals described by an objective function must be minimized. In addition, it is shown that the generalized cavitation criterion includes the classical cavitation criteria of Hou and Abeyaratne (1992) and Lopez-Pamies et al. (2011b).

To perform an efficient parameter identification, only data of the  $0^\circ$ ,  $30^\circ$  and  $60^\circ$  meridians are utilized to determine the unknown parameters (Fahlbusch et al., 2016). In order to determine the unknown parameters, an objective function  $S$  must be formulated, which reads

$$S = \sum_{i=1}^n [\Phi(p_j, \sigma_1^i, \sigma_2^i, \sigma_3^i)]^2, \quad (6.25)$$

where  $\sigma_1^i, \sigma_2^i$  and  $\sigma_3^i$  represent the calculated stresses from the virtual experiment. In this context, the control variable  $i$  describes the total amount of measured

data. In order to approximate the virtual data representing cavitation failure in stress space, the unknown parameters  $\vec{p} \Rightarrow p_j = [p_1, p_2, \dots, p_o]^T$  must be optimized in such a way that  $\mathcal{S}$  becomes minimal. The unknown material parameters  $\vec{p}$  can be determined by formulating the minimization problem with

$$\min_{\vec{p}} \mathcal{S} \equiv \min_{\vec{p}} \mathcal{S}(\vec{p}). \quad (6.26)$$

To find the global minimum for this non-convex optimization problem, a constrained optimization coupled with the random search method is used. The random search algorithm generates a population of random start points and uses a local optimization method from each of the start points to converge to a local minimum. The best local minimum is chosen as the solution.

First, the approximations of the classical cavitation criteria of Hou and Abeyaratne (1992) and Lopez-Pamies et al. (2011b) are presented. For this purpose, both criteria are first reformulated so that they represent the  $0^\circ$ ,  $30^\circ$  and  $60^\circ$  meridians in the scaled Burzyński-plane. Replacing the second deviatoric invariant with  $I'_{2,\sigma} \rightarrow T^2/3$  and using

$$I'_{3,\sigma} \rightarrow \frac{2}{27}T^3 \quad \text{for the } 0^\circ \text{ meridian} \quad (6.27)$$

$$I'_{3,\sigma} \rightarrow 0 \quad \text{for the } 30^\circ \text{ meridian} \quad (6.28)$$

and

$$I'_{3,\sigma} \rightarrow -\frac{2}{27}T^3 \quad \text{for the } 60^\circ \text{ meridian} \quad (6.29)$$

for the third deviatoric invariant depending on the desired meridians, the three-dimensional formulations of Eq. (6.9) and Eq. (6.12) can easily be transformed into the scaled Burzyński-plane. The fitting results for both criteria are shown separately for the scaled Burzyński-plane and  $\pi$ -plane in Fig. 6.8. The approximations of the classical criteria show very good results so that it can be stated that the generalized criterion includes the solution of Hou and Abeyaratne (1992) and Lopez-Pamies et al. (2011b).

In the second step, the determined virtual cavitation failure stresses of Section 6.3.3 has to be approximated for different porosities with the proposed criterion of Eq. (6.21). Based on the large amounts of data points obtained, it is important to process the data in such a way that the identification of the parameters of a failure criterion is efficient and fast. The  $0^\circ$ ,  $30^\circ$  and  $60^\circ$  meridians can be filtered out or analytically determined and subsequently numerically calculated in order to reduce the calculation time.

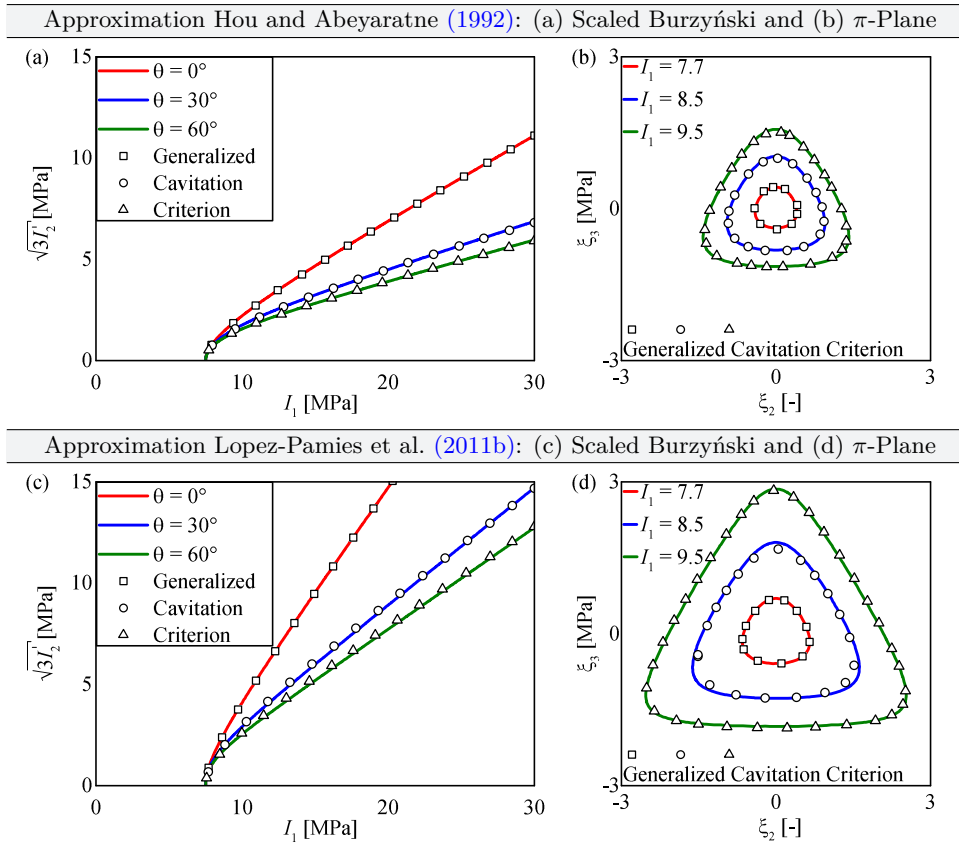


**Figure 6.8** Approximation of the cavitation criteria of Hou and Abeyaratne (1992) and Lopez-Pamies et al. (2011b) by generalized cavitation criterion proposed in Eq. (6.21)

In order to be able to determine the data points of the  $0^\circ$  meridian directly with one numerical simulation, the applied principal stretches for load step 2 read  $\lambda_1 = \lambda$ ,  $\lambda_2 = \lambda^m$  and  $\lambda_3 = J_{cr}\lambda^{-(1+m)}$  with  $m = 1/2$ . Hence, one obtains the classical deformation gradient for a uniaxial tension loading (load step 2) superposed with a hydrostatic tensile load (load step 1), which reads

$$\mathbf{F} = \begin{bmatrix} \lambda & 0 & 0 \\ 0 & \frac{1}{\sqrt{\lambda}} & 0 \\ 0 & 0 & \frac{J_{cr}}{\sqrt{\lambda}} \end{bmatrix}. \quad (6.30)$$

From this it is obvious that the determinant of the deformation gradient  $\mathbf{F}$  reads  $\det \mathbf{F} = J_{\text{cr}}$ . To obtain the critical stresses corresponding to the  $60^\circ$  meridian, the parameter  $m$  is set to one, hence the deformation gradient is described by

$$\mathbf{F} = \begin{bmatrix} \lambda & 0 & 0 \\ 0 & \lambda & 0 \\ 0 & 0 & \frac{J_{\text{cr}}}{\lambda^2} \end{bmatrix}, \quad (6.31)$$

which represents a biaxial deformation superposed with a hydrostatic tensile load within second load step. The loading for the  $60^\circ$  meridian also yields  $\det \mathbf{F} = J_{\text{cr}}$ , so that the volume is kept constant during the second loading. Since no direct analytical relationship can be determined for the  $30^\circ$  meridian, these data were filtered out.

The results of single failure stresses for fixed porosities of  $f_0 = 1, 5, 10, 15\%$  and the approximation based on Eq. (6.21) are shown in Fig. 6.9. The virtual failure stresses are plotted as scatter plot, where due to the large amount of data generated for each porosity, only every 75th data point is plotted. Additionally, all data points are plotted coloured, where the colour scale from blue to red indicates the amount of the hydrostatic pressure. The approximated failure surfaces are shown as a transparent mesh. Regarding Fig. 6.9, it is obvious that the generated critical stresses and therefore the limit surfaces resemble one another in appearance, however, the critical stress under homogeneous, hydrostatic loading decreases with increasing porosity (see Tab. 6.2). Furthermore, it can be seen that the generalized cavitation criterion approximates all failure points very well. Therefore, it should be noted that the presented criterion is not only able to approximate the classical criteria, but can also describe cavitation failure for finite porosities.

Fig. 6.10 shows a clearer representation of the cavitation failure surfaces at different porosities without virtually calculated failure points. In addition to the failure surfaces, the Gaussian curvature is illustrated in colour. On this basis it becomes obvious that there is always a positive Gaussian curvature for all approximated failure surfaces. Consequently, the proof of convex failure surfaces in the sense of a positive Gaussian curvature has taken place. Furthermore, each plot shows the critical failure load  $p_{\text{cr}}$  for a homogeneous hydrostatic tensile load. This shows that with increasing porosity the failure load decreases. Compared to the classical cavitation criteria of Gent and Lindley (1959), Hou and Abeyaratne (1992) and Lopez-Pamies et al. (2011b), which represent physical failure criteria only through the formulation of constraints, the generalized cavitation criterion always shows a physical behaviour. This can be proven by the fact that the failure surfaces do not intersect with the stress planes  $\sigma_1 - \sigma_2$ ,  $\sigma_2 - \sigma_3$  and  $\sigma_3 - \sigma_1$ .

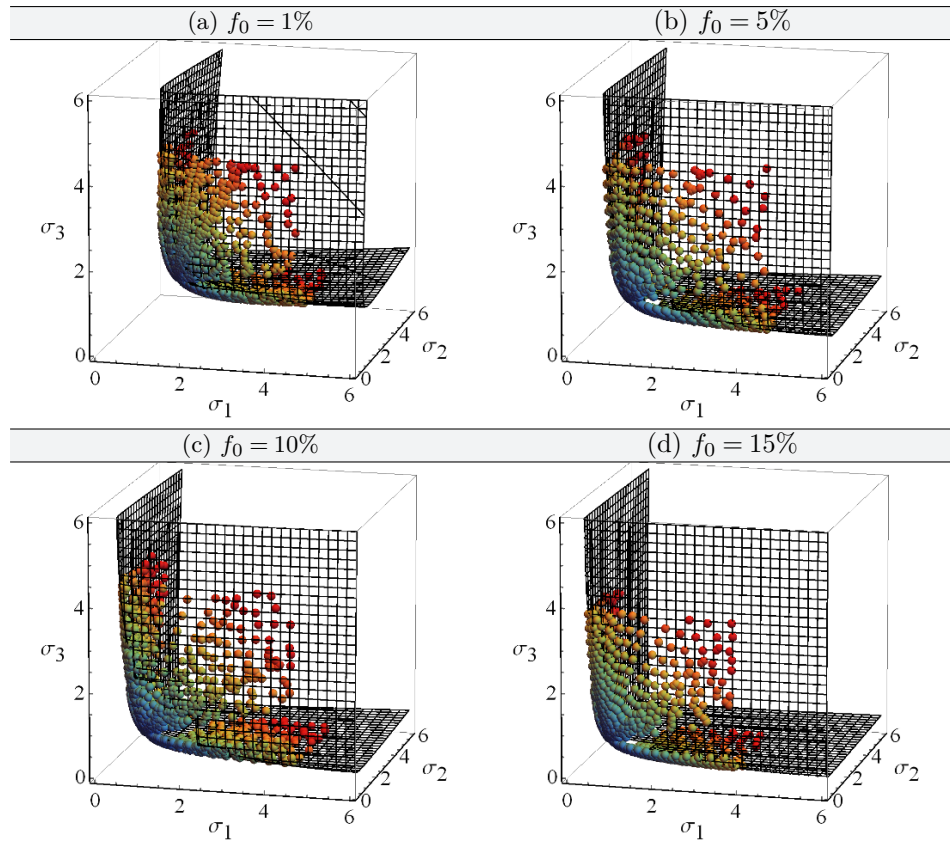


**Figure 6.9** Data points for critical stresses under arbitrary, triaxial deformations in three-dimensional Cauchy stress space and approximated failure surfaces based on generalized cavitation criterion

### 6.3.5 Approximation of Cavitation Failure in Stretch Space

In general and as already mentioned, failure criteria can be formulated in the stress or strain space. A big disadvantage of stress-based cavitation failure criteria based on virtually calculated failure data lies in the strong dependence on the selected material model, especially when non-polyconvex material models are utilized to determine the failure surface. This may lead to non-convex failure surfaces, which additionally show a non-physical course (Nakamura and Lopez-Pamies, 2012). In case of a stress-based failure criterion, the limit state analysis or reaching the maximum failure load is directly dependent on the selected material model. If material parameters were determined incorrectly, the statement whether failure is present or not cannot be proven. Another disadvantage is the ambiguous de-

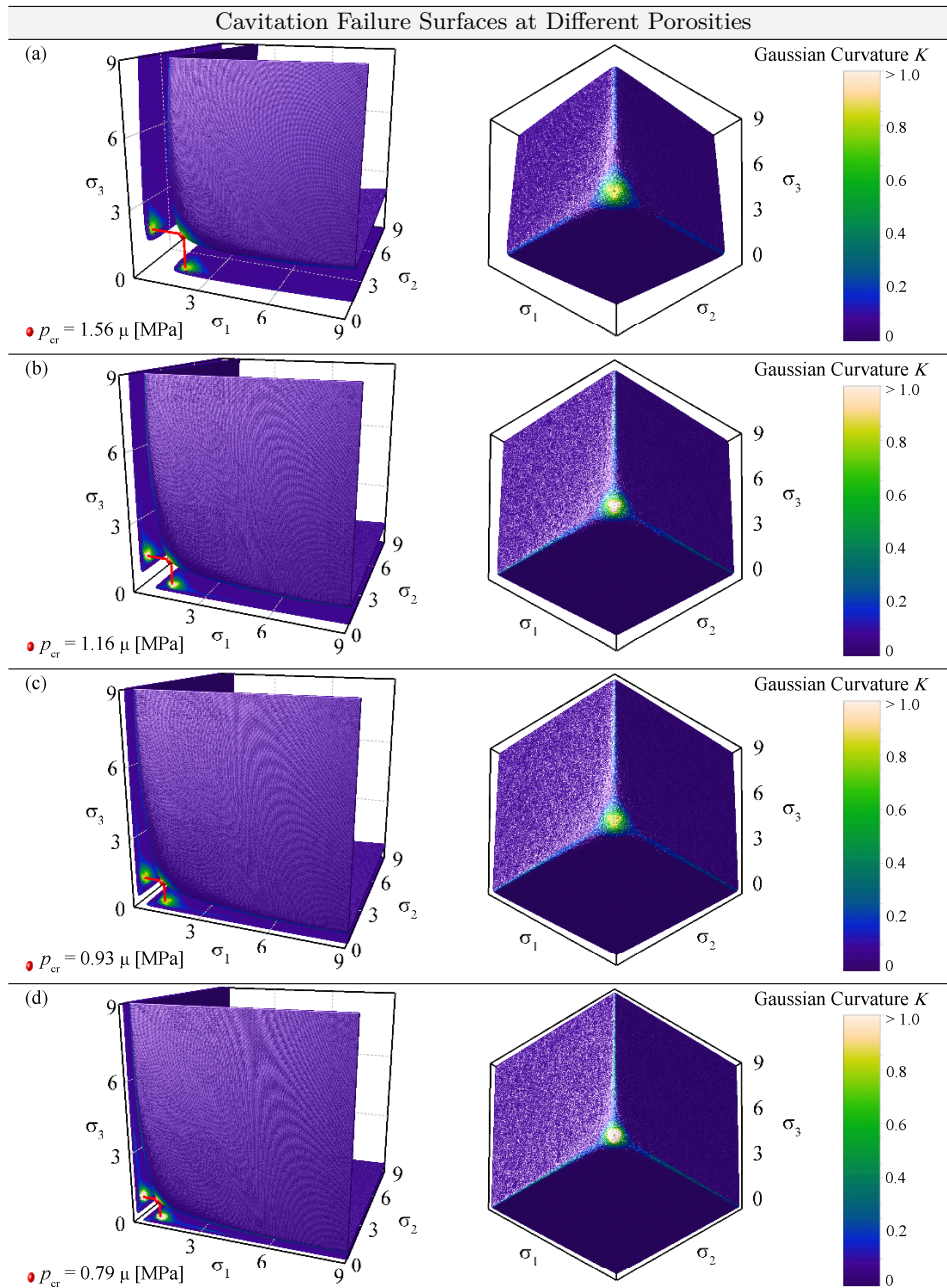


**Figure 6.10** Representation of cavitation failure surfaces in three-dimensional principal Cauchy stress space and Gaussian curvatures under different perspectives for porosities of (a)  $f_0 = 1\%$ , (b)  $f_0 = 5\%$ , (c)  $f_0 = 10\%$  and (d)  $f_0 = 15\%$

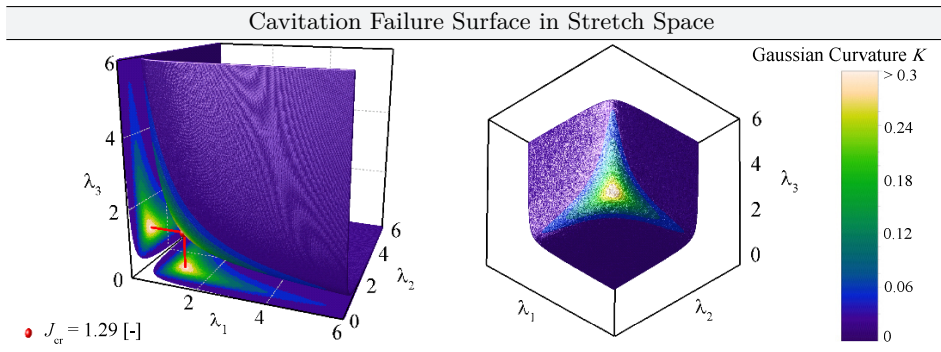


**Figure 6.11** Exemplary cavitation failure area and representation of local Gaussian curvature in three-dimensional stretch space for a critical relative volume of  $J_{cr} = 1.29$

scription of failure in very complex material behaviour (stress softening followed by stress-stiffening), which makes a failure evaluation impossible. Therefore, it is absolutely logical to formulate a stretch-based failure criterion, which does not show the above-mentioned disadvantages in such a form as with stress-based failure criteria.

Considering the structural behaviour of rubbers and rubber-like materials and their mechanical description through hyperelastic material models, the stretch measure is often used to characterize these materials (Ogden, 1972; Arruda and Boyce, 1993). Accordingly, it is obvious to formulate cavitation failure or failure criteria also in the stretch space (Ayatollahi et al., 2016; Heydari-Meybodi et al., 2017). To mathematically describe cavitation failure in the stretch space, a failure surface must be generated, which on the one hand represents any deformation on this surface and on the other hand is defined for a constant relative volume. The description of any deformations on a defined surface can be achieved via the determinant of the deformation gradient, which reads  $\det \mathbf{F} = J > 0$ .

Additionally and in accordance to Section 6.3.3, a critical relative volume  $J_{cr}$  ( $f_0$ ) must be defined as a function of the initial porosity, at which a drop in force occurs under further hydrostatic loading. According to the above-mentioned limitations, a general stretch-based cavitation criterion can be easily defined by

$$J - J_{cr} = 0 \quad \text{or} \quad \lambda_1 \lambda_2 \lambda_3 - J_{cr} = 0, \quad (6.32)$$

where the critical relative volume  $J_{cr}$  is set constant. The great advantage of the stretch-based cavitation criterion is that no parameters have to be identified as is the case for the stress-based criterion. Only the value for the critical relative volume must be identified or derived from numerical calculations in accordance to Section 6.3.3.

Two perspectives of the stretch-based cavitation criterion for an exemplary critical relative volume change of  $J_{\text{cr}} = 1.29$  are shown in Fig. 6.11. In addition, the positive Gaussian curvature shows that there is a convex failure criterion formulated in three-dimensional stretch space.

## 6.4 Coupled Distortional-Dilatational Failure Criterion

Incompressible and almost incompressible rubbers and rubber-like materials exhibit distortional and dilatational failure modes, which are explicitly determined by the deformation applied (Hamdi and Mahjoubi, 2015; Rosendahl et al., 2018; Drass et al., 2018e; Drass et al., 2018b). Since purely distortional or purely dilatational deformations can never occur independently for any structural components and loading situations, where e.g. structural silicones are used as bonding material, it would be reasonable to define an overall failure criterion that evaluates both failure mechanism at the same time. Therefore, a coupled distortional-dilatational failure criterion defined in three-dimensional stretch space will be presented in the following. Both the distortional and the dilatational failure criteria have already been presented separately in Section 6.1 and Section 6.3.5. Hence in this section both theories are reconciled.

Coupled stress-based failure criteria or pressure-sensitive failure criteria for materials such as steel, concrete and plastics already exist in large quantities (Kolupaev, 2018:p.195 ff.), but they exhibit the already presented general disadvantages of stress-related formulation of failure. In addition, the measurement of failure under hydrostatic load is hardly possible, so that the definition of triaxial failure usually remains vague (Santarsiero et al., 2018b). Considering rubber-like materials, Knauss (1967) postulated the idea of a coupled distortional-dilatational failure criterion. However, he lacked an adequate experimental data basis and a reasonable connection of distortional failure, which is generally formulated in stress space and dilatation failure formulated in strain space. A modern failure criterion for structural silicones was presented by Santarsiero et al. (2018b), which is formulated very generally as a function of temperature and strain rate. The disadvantage of this criterion lies again in the formulation of the criterion in stress space and the rotationally symmetric behaviour in the  $\pi$ -plane. Since there is so far no adequate combined failure description of distortional and dilatational failure for rubber-like materials, it is logical to define a coupled failure criterion based on the concepts of Section 6.1 and Section 6.3.5.

### 6.4.1 Concept of Coupled Distortional-Dilatational Failure Criterion

Let us denote the set of all stress or deformation states a material can sustain safe region  $\mathcal{R}$  and the corresponding surface comprising all limit states of a material failure surface  $\Phi$ . The failure surface constitutes the boundary of the safe region  $\Phi = \partial\mathcal{R}$ . A general phenomenological failure criterion may be formulated in terms of stresses, strains or stretches

$$\Phi(\boldsymbol{\sigma}) = 0, \quad \Phi(\boldsymbol{\varepsilon}) = 0, \quad \text{or} \quad \Phi(\mathbf{b}) = 0, \quad (6.33)$$

where the Cauchy stress tensor  $\boldsymbol{\sigma}$ , the Hencky strain tensor  $\boldsymbol{\varepsilon}$  and the left Cauchy-Green tensor  $\mathbf{b}$  are chosen exemplary. A material will sustain given loads for  $\Phi < 0$  and fail when  $\Phi \geq 0$ . Let us distinguish surfaces associated with isochoric (distortional)  $\Phi^{\text{iso}}$  and volumetric (dilatational)  $\Phi^{\text{vol}}$  failure. Both describe surfaces in the respective stress, strain or stretch space and are boundaries of corresponding safe regions  $\Phi^{\text{iso}} = \partial\mathcal{R}^{\text{iso}}$  and  $\Phi^{\text{vol}} = \partial\mathcal{R}^{\text{vol}}$ , respectively. The failure surface of a coupled distortional-dilatational criterion is obtained from the boundary of the union of both safe regions

$$\Phi = \partial\mathcal{R} \quad \text{where} \quad \mathcal{R} = \mathcal{R}^{\text{iso}} \cap \mathcal{R}^{\text{vol}}. \quad (6.34)$$

To illustrate this idea of a unified failure criterion, a classical pressure-insensitive distortional criterion as well as a typical cavitation criterion are presented in Figs. 6.12 a and b in principal stretch space. Fig. 6.12 a shows a von Mises type cylinder in its stretch-based formulation (Rosendahl et al., 2019). The cavitation failure surface shown in Fig. 6.12 b is based on the idea of Nakamura and Lopez-Pamies (2012) who calculate Cauchy stresses corresponding to a critical volume change numerically. Of course, the computation of critical stresses can be omitted in principal stretch space because the critical volume change describing the onset of cavitation is expressed directly by the third invariant of the deformation gradient  $J_c = \text{const.}$  (Drass et al., 2018a). Details on the cavitation failure criterion are given in Section 6.3.5. For the sake of simplicity let us assume that only isochoric deformations at a critical relative volume of  $J_c = \lambda_1 \lambda_2 \lambda_3 = 1$  are permissible, where  $\lambda_i$  are principal stretches. That is, any volume change  $J > 1$  would cause cavitation. Hence, Fig. 6.12b shows the so-called incompressibility surface  $J = 1$ . Isochoric deformations are found within this surface. Volumetric deformation paths point out of the surface and along the hydrostatic axis. Fig. 6.12c shows the coupled distortional-dilatational failure criterion, i.e. the intersection of the von Mises type cylinder of Fig. 6.12 a and the incompressibility surface of Fig. 6.12 b. For the sake of clarity, the cylinder is displayed only for  $J > 1$ . The safe region according to

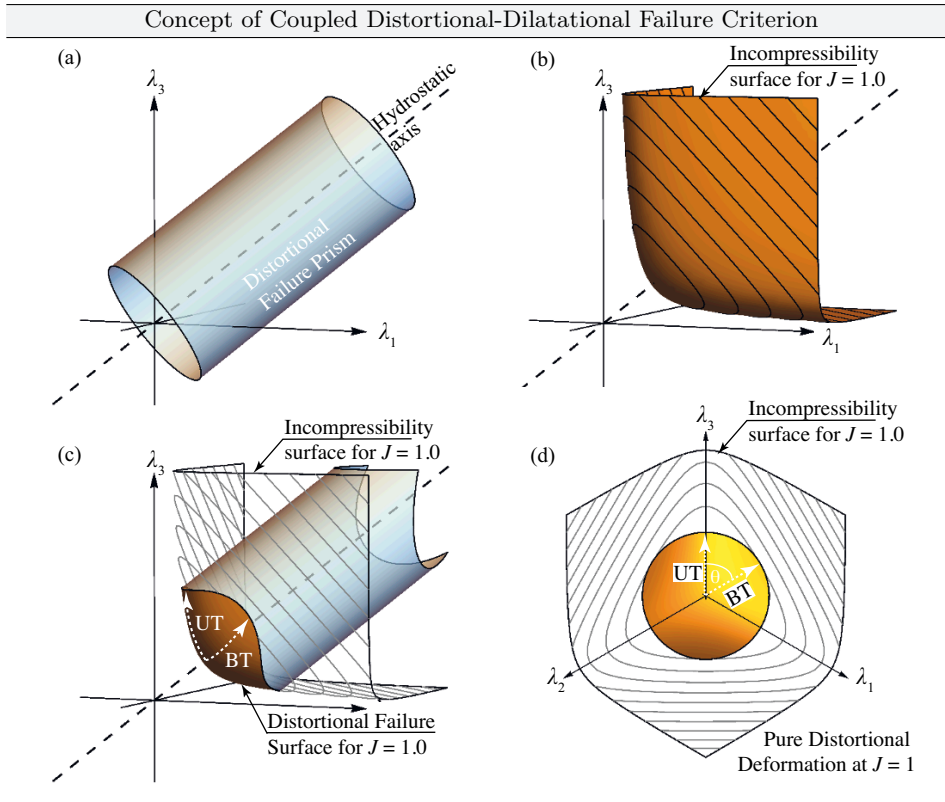


**Figure 6.12** Concept of a coupled distortional-dilatational failure criterion in principal stretch space: (a) distortional failure prism resembling the von Mises cylinder, (b) incompressibility surface representing cavitation failure, (c) intersection of distortional and dilatational failure criteria and (d) its representation in the deviatoric plane. Deformation paths for isochoric uniaxial (UT) and biaxial tension (BT) are shown as dashed white lines.

Eq. (6.34) is displayed in orange. Truncated parts of the cavitation criterion which do not belong to the unified criterion are illustrated by a grey mesh. Fig. 6.12 d shows the deviatoric plane projection of the criterion. Deviatoric planes are cross sections perpendicular to the hydrostatic axis Kolupaev (2018). Permissible deformations without failure are found within the orange safe region, illustrated in Figs. 6.12 c and d by the deformation paths of isochoric uniaxial (UT) or biaxial tension (BT). Moving outside the circular contour within the incompressibility surface or leaving the incompressibility surface in the direction of the hydrostatic axis both causes failure.

Our initial assumption of incompressibility in the description of dilatational failure is unphysical because small changes in rubber volume occur even under

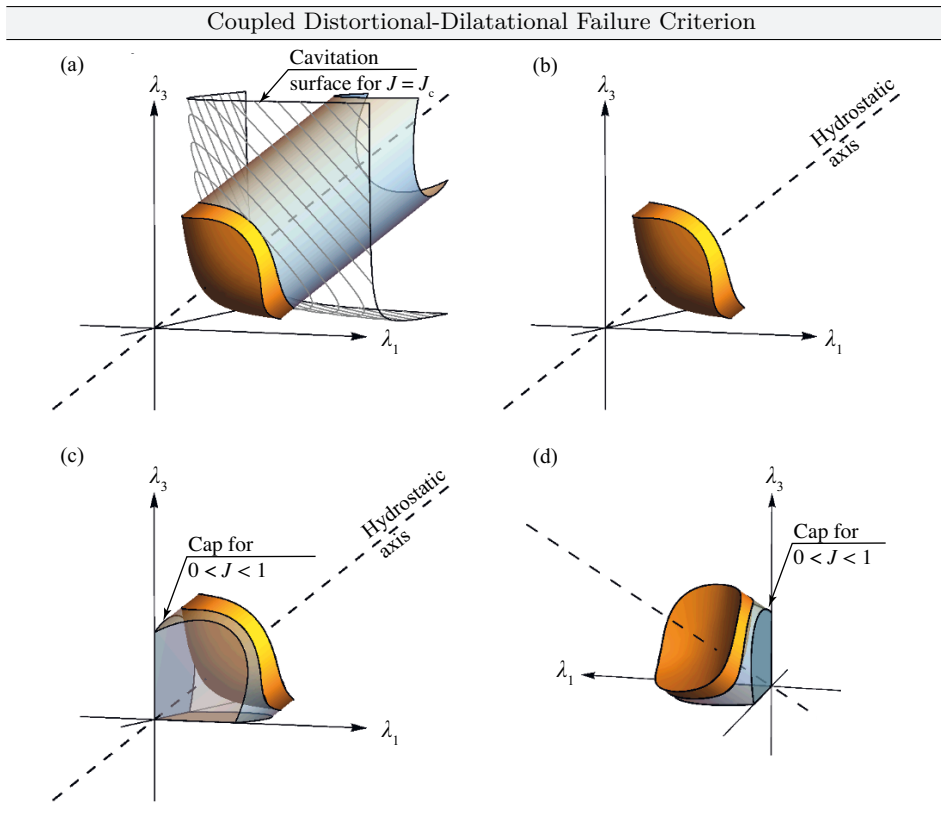


**Figure 6.13** Illustration of a coupled distortional-dilatational failure criterion bounded the incompressibility surface  $J = 1$ , the cavitation failure surface  $J = J_{\text{cr}}$  and a cylindrical distortional failure surface. (a) Cavitation failure surface for a critical relative volume of  $J_{\text{cr}} = 1.29$ , (b) Body representing safe deformation states in principal stretch space and (c-d) possible simplest assumed cap for volumetric compression deformations for  $0 \leq J \leq 1$ .

dominantly distortional deformations such as uniaxial and biaxial tension (Le Cam, 2010). Following the basic idea illustrated in Fig. 6.12 we may also consider a finite critical volume change  $J_{\text{cr}} = \text{const.}$  defined according to the studies of Nakamura and Lopez-Pamies (2012) and Drass et al. (2018a). A cavitation failure surface corresponding to a constant critical relative volume  $J_{\text{cr}}$  is obtained from a shift of the incompressibility surface along the hydrostatic axis as shown in Fig. 6.13 a.

Both  $J = 1$  and  $J = J_{\text{cr}}$  now cap the distortional failure prism forming a three-dimensional volume, the safe region marked in orange. The orange body thus describes the set of rubber deformations which may occur without distortional or dilatational failure. That is, volumetric deformation paths leaving  $J = 1$  along

the hydrostatic axis up to  $J = J_{\text{cr}}$  and isochoric deformation paths away from the hydrostatic axis within the boundaries of the distortional failure prism are permitted. Note that we do not consider compressive volumetric failure and no assessment of volume ratios  $0 < J < 1$  can be given at this point. Since there is no data on volumetric compression failure of rubber in literature, the shape of the compressive shape region can only be assumed. Its simplest, yet likely inaccurate, form (cap) is shown in Figs. 6.13 c and d. For the sake of clarity and because no information about this region is available, we will omit the cap in the following.

### 6.4.2 Coupled Failure Surface in Section Planes

Failure surfaces enclose three-dimensional bodies in, e.g., principal stretch space. The characteristics of such bodies can be visualized using two distinctive planes: i) The meridian plane spanned by the first invariant  $I_1$  of the left stretch tensor and the second invariant of the deviator  $I'_2$  of the left stretch tensor and ii) the deviatoric plane, a cut perpendicular to the hydrostatic axis. Both planes allow for the visualization of permissible deformations and different isochoric and volumetric loads together with boundaries of the permissible deformation space. In principal stress space, the meridian plane is often referred to as Burzyński-plane and the deviatoric plane as  $\pi$ -plane.

Fig. 6.14 illustrates the structural behaviour of compressible hyperelastic solids in the scaled meridian plane (Kolupaev, 2018). Here,  $I_1 = I_{1,\text{v}}$  corresponds to the first invariant of the left stretch tensor and  $I'_2 = I'_{2,\text{v}}$  to the second invariant of the deviator of the left stretch tensor. Figs. 6.14 a and b show different meridians, i.e., different discrete deformation paths corresponding to different slices along the hydrostatic axis. We consider uniaxial and equi-biaxial loading, respectively. The area between the incompressibility surface  $J = 1$  and the cavitation failure surface  $J = J_{\text{cr}}$  comprises permissible deformations with volume increase of a compressible hyperelastic material. It is a two-dimensional representation of the three-dimensional safe region shown in Fig. 6.13 b. In contrast, considering cavitation failure of an incompressible material, a triaxial deformation would immediately cause penetration of the surface  $\Phi$  for  $J = 1$  and hence cavitation failure. Note that the volumetric deformation threshold  $J_{\text{cr}}$  increases considerably with increasing compressibility. Significantly more volumetric deformation must take place for cavitation to occur Drass et al. (2018b); Drass et al. (2019b).

The coupled failure criterion covers not only dilatational but also distortional failure. The prismatic distortional failure surface is represented by a line parallel to the  $I_1$ -axis (hydrostatic axis) in the scaled meridian plane. Hence, the region of permissible deformations is truncated by this line in Fig. 6.14. Rotationally symmetric criteria such as the von Mises criterion have the same radius in all meridian

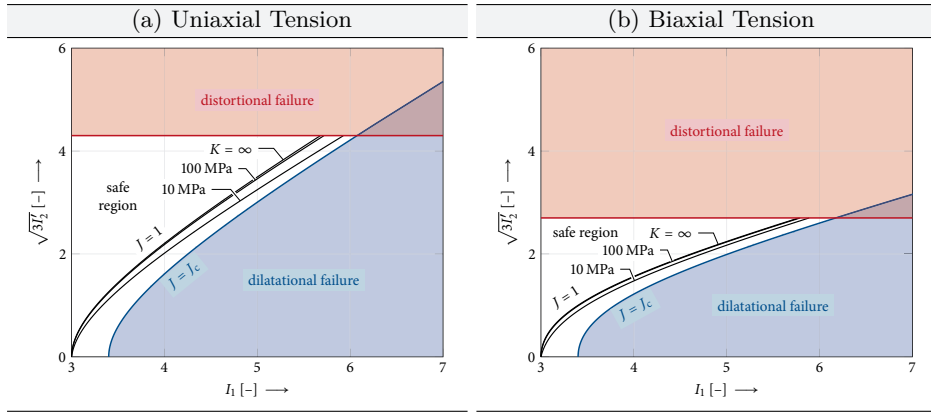


**Figure 6.14** Scaled meridian plane. Two-dimensional representation of the coupled distortional-dilatational failure surface and load paths for (a) uniaxial tension and (b) biaxial tension with variation of the bulk modulus.

planes. However, the present example material behaves differently under uniaxial and biaxial loading which is reflected by different radii of its distortion failure surface in different meridian planes. This results in different sizes of the safe region in Figs. 6.14a and b. The present material can sustain larger uniaxial than biaxial deformations before distortion failure occurs. The dependence of the radius of distortion failure surfaces on loading conditions can be illustrated in the deviatoric plane (see Fig. 6.1). To show how uniaxial or biaxial deformations of a compressible hyperelastic material develop in the meridian plane, these deformations are illustrated in Figs. 6.14a and b, respectively. Different bulk moduli  $K$ , i.e., materials of different compressibility are considered. All deformation paths emerge from the undeformed state at  $\lambda_1 = \lambda_2 = \lambda_3 = 1$  but move away from the incompressibility surface ( $J = 1$ ) with increasing deformation and decreasing bulk modulus. Theoretically, cavitation failure can occur even under uniaxial and biaxial loading if the chosen bulk modulus is very small and thus the volume change large. However, rubber-like materials are typically almost incompressible due to their thermodynamical state of entropy-elasticity at room temperature and hence dilatational failure only observed under triaxial loading. Instead, the shown deformation paths penetrate the distortion failure surface indicating distortion failure of the material, as expected.

### 6.4.3 Novel Failure Criterion for DOWSIL™ TSSA

Combining the distortion failure criterion introduced in Section 6.1 with the dilatational failure criterion proposed in Section 6.3.5 yields a description of the

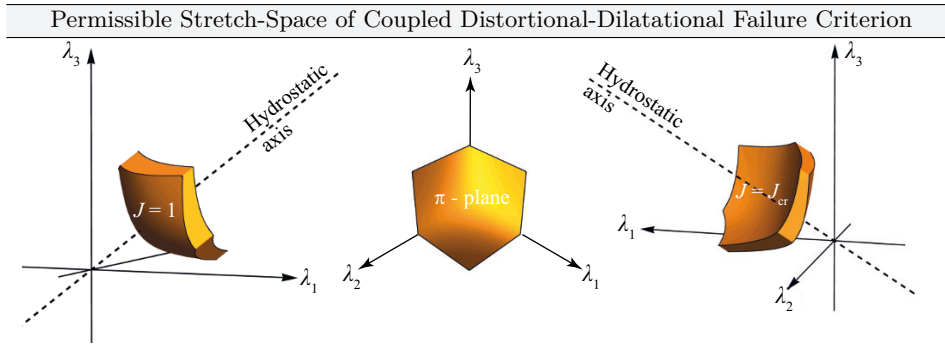


**Figure 6.15** Safe region of permissible deformation states without failure in principal stretch space for the transparent structural silicone adhesive DOWSIL™ TSSA. Although the distortion failure surface seems to feature corners, it is in fact slightly rounded and  $C^1$ -continuous.

complete failure surface of DOWSIL™ TSSA. The main ideas of the present coupled dilatational-distortional failure criterion are the high functional adaptivity of the distortion failure function and the simplicity of the dilatational failure formulation in terms of stretches.

The permissible stretch space comprising deformation states without distortion or dilatation failure of DOWSIL™ TSSA is illustrated in Fig. 6.15. This figure shows the failure-free stretch space based on the distortional PBP criterion, Eq. (6.1), which describes the failure surface of DOWSIL™ TSSA in accordance with Section 6.1. The acceptable critical volume ratio resulting in cavitation failure has been determined in Section 6.3.5 and amounts to  $J_{cr} = 1.041$ . Restricting the analysis to volume increase, the coupled distortional-dilatational failure criterion is also capped by the incompressibility surface  $J = 1$ .

## 6.5 Numerical Validation of Failure Criteria

In this section, the presented coupled distortional-dilatational failure criterion is evaluated in different numerical FE calculations (uniaxial tensile, bulge and pancake tension test) and validated by experimental failure data. For this purpose, the numerical simulation models from Section 5.5 are used, which initially only served to validate the pseudo-elastic material model proposed in Section 5.3. As already shown, the new material model is well suited to re-calculate the tensile, bulge and pancake tension tests with different diameters. However, since the material model lacks knowledge about the occurrence and onset of failure, the coupled failure criterion from Section 6.4.3 is added. Validation is performed by calculating the ultimate breaking load, which must be in the range of the scatter of the

experimental failure, and by making a qualitative statement about the location of the predicted failure from the numerical model, which must correspond to that of the experiments.

However, a delimitation is made in advance. Effects from the FE mesh and mesh density in relation to the occurrence of failure and the discrete value for the failure load are not further investigated. Helpful methods for this are, for example, the approach of finite fracture mechanics (FFM), which assumes failure as soon as a failure criterion and a critical fracture energy are reached at the same time. The interested reader is referred to the investigations of Staudt et al. (2018) and Rosendahl et al. (2018), who calculated the failure of a structural silicone with the FFM approach, and Rosendahl et al. (2017), who investigated crack patterns around open holes. Further research was performed by Felger et al. (2017) to describe mixed-mode fracture in composite laminates, crack nucleation in adhesive butt joints (Felger et al., 2019) and crack nucleation in adhesive joints (Stein et al., 2015). An overview on finite fracture mechanics is given by Weißgraebner et al. (2016).

### 6.5.1 Limit State Analysis - Uniaxial Tensile Test

In this section the uniaxial tensile test on TSSA is again simulated. However, now the simulation model is combined with the coupled distortional-dilatational failure criterion to predict the location of failure and the failure load. The predicted values of the failure load from FE calculation are then compared with the experimental data to validate the proposed failure criterion. Since for all following investigations the same failure criterion with one set of parameters are applied, which have been previously determined, it will be briefly summarized in the following.

The distortional failure criterion is based on the PBP criterion (see Eq. (6.1)), which is defined in three-dimensional stretch space. The determined parameters for the PBP criterion based on the experimental results for TSSA are summarized in Tab. 6.1. Since this criterion is developed to describe failure at isochoric deformations, such as uniaxial or biaxial stress or strain state, a dilatational criterion was additionally added to describe the onset of cavitation. In our case the onset of cavitation means an elastic void growth, which leads to an effective stress softening of the hydrostatic pressure with increasing volumetric deformation. The dilatational or cavitation criterion is also defined in three-dimensional stretch space in order to be able to couple both criteria. The cavitation criterion simply reads  $J - J_{\text{cr}} = 0$ . The critical relative volume  $J_{\text{cr}}$  describing the onset of cavitation was determined experimentally to a value of  $J_{\text{cr}} = 1.041$  accordingly to the results of Section 5.5.3.

To come back to the validation and the limit state analysis, a three-dimensional FE model according to the model proposed in Section 5.5.3 was set up. The symmetry boundary conditions as well as the load are applied accordingly. The

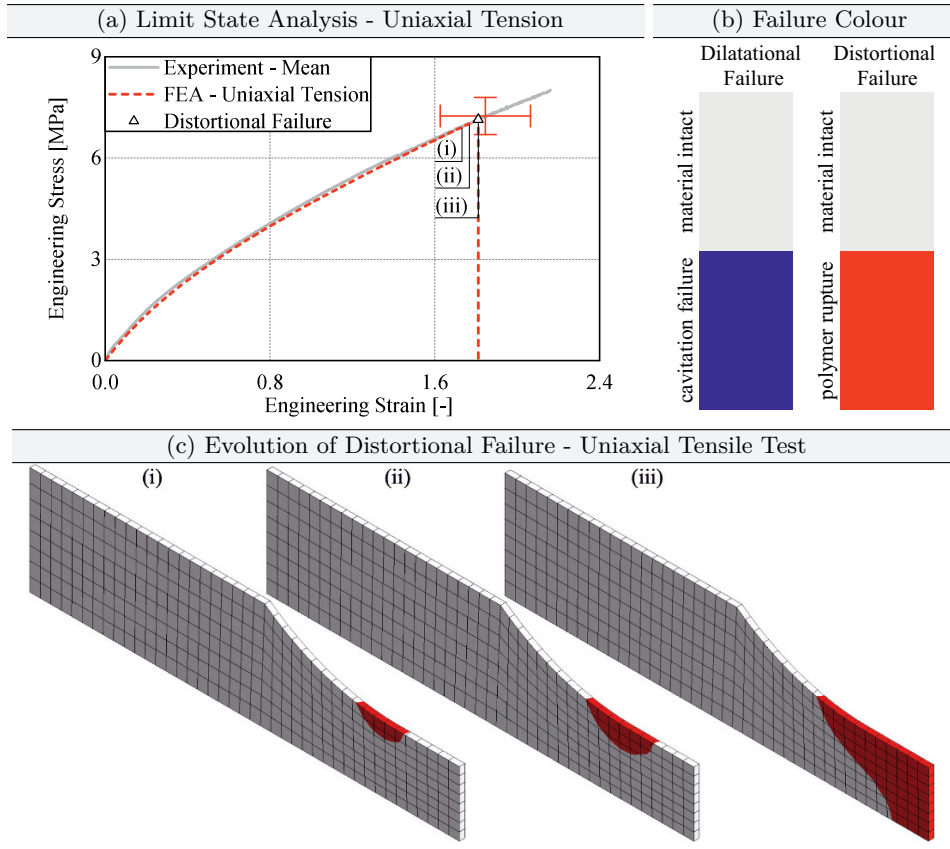


**Figure 6.16** Limit state analysis of the uniaxial tensile test for TSSA using the coupled distortion-dilatational failure criterion: (a) comparison of the FEA with experimental results and prediction of failure, (b) colouring of an intact material and cavitation or distorted failure, and (c) development of the failure under evaluation of the failure criterion in the FE model

comparison between uniaxial tensile experiments and numeric calculation is illustrated in Fig 6.16 a, in which the experimental mean value curve and the scatter of the failure engineering stress / strain are represented as error bars.

As can be seen from Fig 6.16 a the structural behaviour can be represented well, which has been already proven in Section 5.5.3. Regarding the predicted engineering failure stress for the isochoric uniaxial tensile load, it also can be well predicted because it lies in the scatter of the experimentally determined failure load. Hence, the proposed distortion failure criterion is well-suited to calculate the failure stress under isochoric deformations. By evaluating the dilatational failure criterion it is not satisfied during the numerical calculation of the uniaxial tensile

test. Hence, no cavitation failure ensues during this deformation, which is physical due to the fact that an isochoric deformation is present.

With regard to the defect location (see Fig 6.16 c), it is located at the rounded corner between the edge-parallel area and the area for clamping the specimen into the testing machine. This corresponds well to the experimentally determined defect location, since many specimens do not break at the desired edge-parallel location, but exactly where the specimen is rounded, since stress singularities occur here.

### 6.5.2 Limit State Analysis - Bulge Test

Accordingly to the failure analysis for the uniaxial tensile test, this section examine the failure under a biaxial deformation. As already mentioned, a study on the mesh density with regard to the predicted failure load was not performed. Nonetheless, the FE model was built up with 608 finite elements accordingly to Section 5.5.4, which was also equipped with the same boundary conditions. Also here, the coupled distortional-dilatational failure criterion proposed in Section 6.4.3 is evaluated to predict the biaxial failure load.

The experimental mean value curve and the scatter of the failure load (pressure) / Hencky strain are represented as error bars. For the limit state analysis, the numerical results should firstly approximate the structural behaviour and secondly the numerically determined failure load should lie in the range of the experimental scatter. As can be seen from Fig. 6.17 a the structural behaviour as well as the failure load for a biaxial loading is well predicted. The location of failure corresponds the experimentally observed failure location, which is the centre of the specimen. Since an almost isochoric deformation is also present in the bulge test, only the distortional failure is relevant here, as for the uniaxial tensile test. The evaluation of the cavitation or dilatational failure confirmed this, since no exceeding of the criterion could be determined. Therefore only the distortional failure is shown in Fig. 6.17 c.

### 6.5.3 Limit State Analysis - Pancake Tension Test

In this section, the limit state analysis of the pancake tension tests is performed under evaluating three different diameters. Here, too, the simulation models correspond to those from Section 5.5.5, in which the newly developed pseudo-elastic cavitation model was used in order to be able to numerically reproduce the structural response at all. Since the experimental investigations of the pancake tension tests have already shown that softening occurs in the structural response due to the onset of cavitation and that the complete failure of the pancake tension test samples occurs subsequently, the following two questions need to be answered. Is the coupled distortional-dilatational failure criterion capable of predicting cavitation

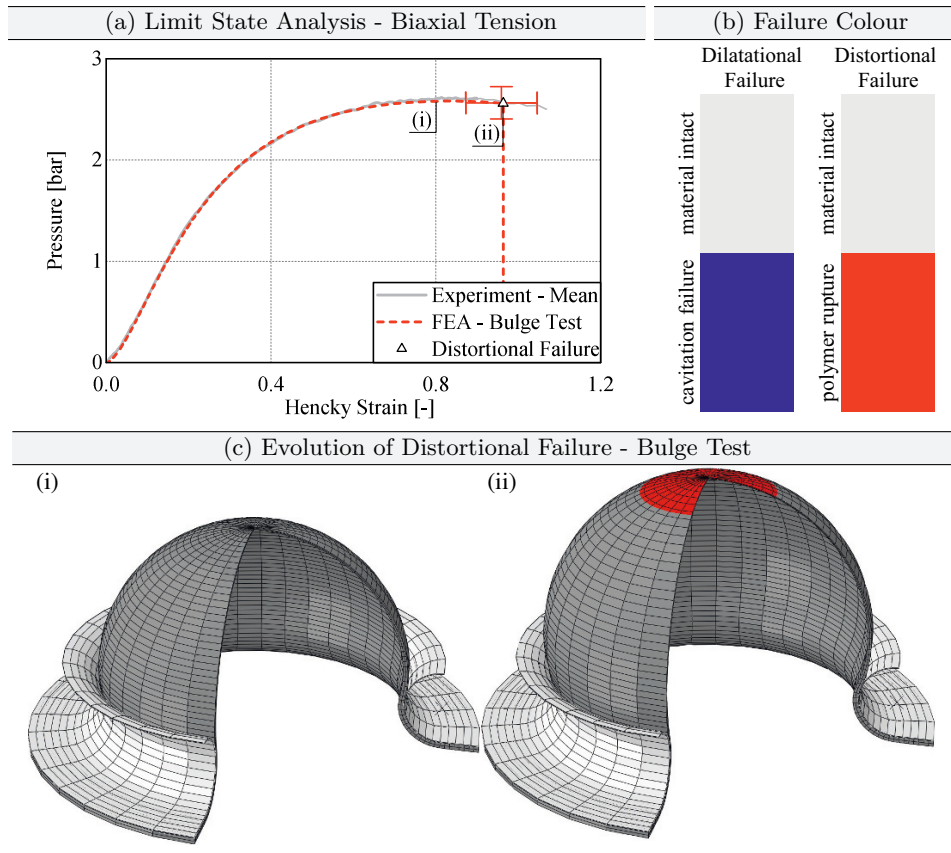


**Figure 6.17** Limit state analysis of the bulge test for TSSA using the coupled distortion-dilatational failure criterion: (a) comparison of the FEA with experimental results and prediction of failure, (b) colouring of an intact material and cavitation or distorted failure, and (c) development of the failure under evaluation of the failure criterion in the FE model

failure, i.e. stress softening, and the final failure of TSSA within pancake tension tests at different diameters?

To answer the proposed questions, the pancake tension tests with the diameters of  $d = 20/40/50$  mm were numerically simulated and the model coupled with the proposed distortional-dilatational failure criterion. Here it is important to note that the material parameters and parameters used to describe the failure criterion are the same as in the previous studies. As a result, all calculations were performed with one set of parameters. The results of the limit state analysis for the pancake tension tests are illustrated in Fig. 6.18.

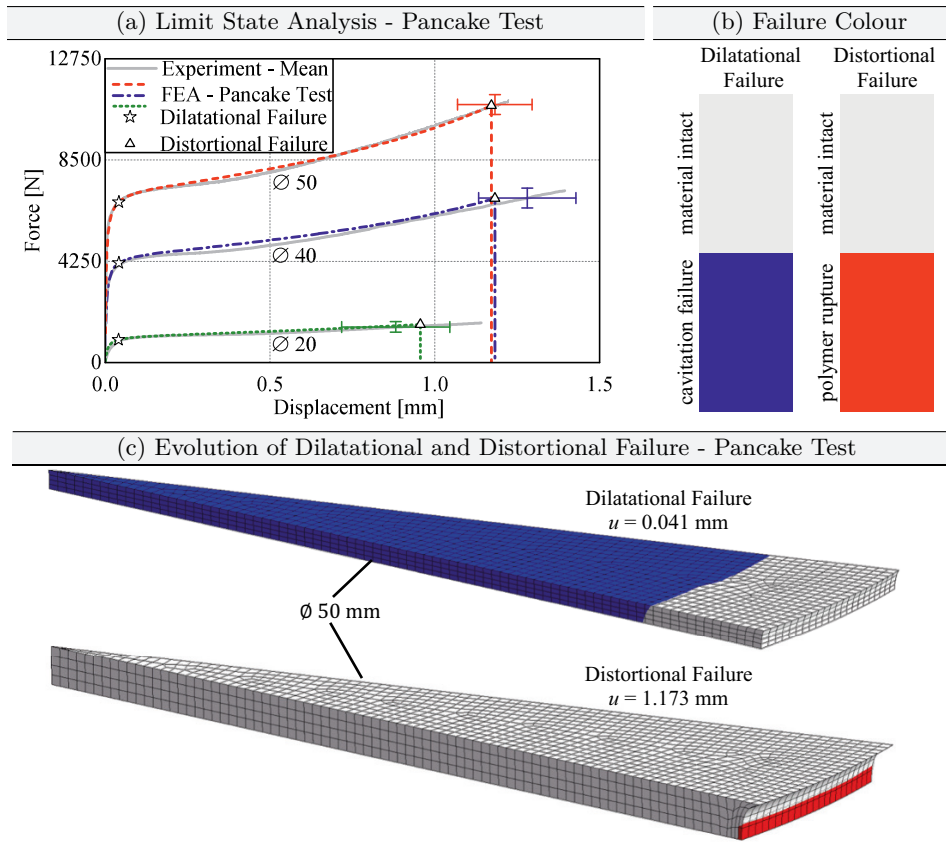


**Figure 6.18** Limit state analysis of the pancake tension test for TSSA at three different diameters using the coupled distortion-dilatational failure criterion: (a) comparison of the FEA with experimental results and prediction of failure, (b) colouring of an intact material and cavitation or distorted failure, and (c) development of the failure under evaluation of the failure criterion in the FE model

As can be seen from Fig. 6.18 a, cavitation failure can be well predicted in terms of determining the onset of a pronounced stress softening for all investigated diameters. However, since the load can be further increased, this criterion only indicates the beginning of an effective volumetric softening. As a result, both the experiments and the numerical studies showed that the final failure occurs later. Due to the softening of the material in the centre of the sample, a stress redistributions to the edge of the material takes place (see Fig. 6.18 c), causing the material to finally fail. This can be confirmed by the fact that although the cavitation criterion is first exceeded in the centre of the sample, the final failure is initiated from the edge of the sample, which corresponds to the experimental observations. Looking

at the prognosis of the calculated failure loads with the experimental failure loads, the distortional failure criterion is also decisive, which corresponds to the results of the uniaxial and biaxial tensile tests. Consequently, the final failure in the pancake tension test is due to distortional failure in the marginal area of the sample, which was also confirmed by the experimental observations. It should be noted that not only the beginning of cavitation but also the final failure can be predicted very well with the coupled distortion-dilatational failure criterion. It is even possible with the proposed criterion to represent the not symmetrically distributed failure loads. As symmetrically distributed, we understand that with increasing diameter not only the failure load but also the deformation increases before the failure is reached. This was confirmed neither by the experiments nor by the numerical simulation.

Looking at location of the onset of cavitation, the prediction of the numerical model indicates that cavitation starts from centre of the specimen and quickly expands to the edges of it (see Fig. 6.18 c). This corresponds to the experimental results of the pancake tension tests presented in Section 4.3.1, where a similar behaviour in terms of the whitening effect could be observed

## 6.6 Conclusions

Summarizing the results of this chapter, a novel stretch-based distortional failure criterion was developed for the transparent structural silicone adhesive TSSA, which is well-suited to approximate the measured failure stretches of different experiments proposed in Chap. 4. In addition to the volume constant, i.e. distortional failure, a new stretch-based dilatational failure criterion was developed, which can predict cavitation failure of rubber-like materials via only one parameter. By coupling the distortional with the dilatational failure criterion it is possible to predict the failure of the investigated structural silicone. Additionally, the location of the beginning of the failure could also be approximated very well with the help of the criterion, which is confirmed by the experimental results of a uniaxial and biaxial tensile test as well as pancake tension tests analysing different diameters.



# 7 Design Methods for Structural Silicone Adhesives

This chapter is dedicated to the design of silicone-bonded constructions in glass and façade systems. The main findings of the present work and the preceding chapters will be summarized and essential remarks and limits will be given for the experimental characterization, the material parameter identification, the material modelling as well as the limit state analyses for structural sealant glazing systems. In particular, structural engineers should be provided with guidance as a result of the categorisation of adhesive joint systems, enabling them to make decisions on, for example, the type and extent of experimental investigations to be carried out, the choice of material model and the design and dimensioning of adhesive joints. Since not all scenarios occurring in the building industry could be considered in the present work, such as thermal-hygroscopic influences, cyclic fatigue and artificial ageing, these effects are excluded in this chapter.

## 7.1 Normative Concepts on Structural Sealant Glazing Systems

In order to better understand the current normative background on structural sealant glazing systems for the area of application of façade construction and also to understand the background of the design concepts, this section briefly summarises the concept according to ETAG 002 (2012) and the DIBt Concept (2012) and examines their limitations.

### 7.1.1 ETAG 002 Concept

ETAG 002 describes the calculation, testing and application of structural sealants in façades and roofs with a maximal inclination of 7° above horizontal. It covers the adhesion between glass, either uncoated or with an inorganic coating, and anodised aluminium or stainless steel. Specific requirements from ETAG 002 (2012) for supported (types I and II) and unsupported (types III and IV) systems can be summarized by:

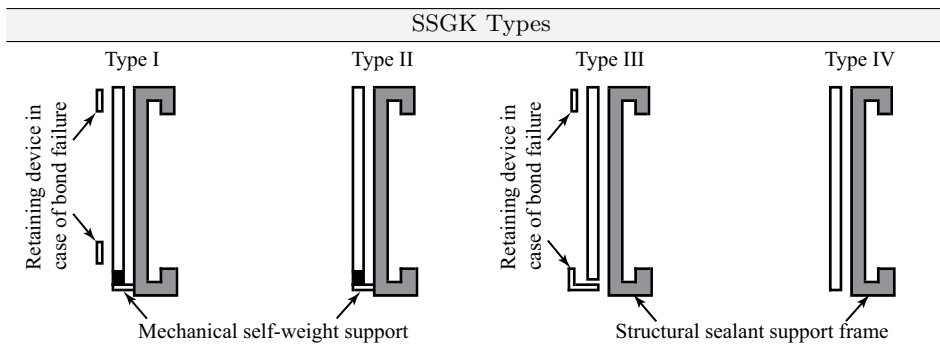


Figure 7.1 Presentation of the four ssgk types in accordance to ETAG 002 (2012)

- Adhesive joint must be silicone in a linear bead
- Discontinuities in the structural bond are allowed, however no edge may be entirely free, except if it is mechanically fastened
- Adhesive joint must be applied in the factory
- More than two adhesion surfaces are not allowed
- Linear adhesive bead must have a minimal thickness of  $e = 6 \text{ mm}$ , whereas the lateral dimensions must lie within  $6 \leq h_c \leq 20 \text{ mm}$ .

To better understand the four types of structural sealant glazing kits (SSGK), Fig. 7.1 shows the differences in a schematic representation.

To design with structural sealants in façade application, ETAG 002 (2012) proposes two methods. The first method uses design formulas, from which the dimensions of the adhesive joint are backwards calculated depending of the design stress (engineering stress) in the adhesive joint. The second method foresees the dimensioning of adhesive joints based on simulations and research results, which at first sight sounds very vague, but also offers possibilities to deviate from the strict restrictions of ETAG 002 (2012). Considering supported system, the width  $h_c$  of the adhesive joint, also called bite in accordance to ETAG 002 (2012), can be calculated by

$$\sigma = \frac{aW}{2h_c} \leq \sigma_{\text{des}} \Rightarrow h_c \geq \left| \frac{aW}{2\sigma_{\text{des}}} \right| \text{ with } 6 \leq h_c \leq 20 \text{ mm} \quad (7.1)$$

where  $a$  is short side dimension of a glass pane,  $W$  means the relevant combined actions of wind, snow and self-weight acting on the adhesive joint and  $\sigma_{\text{des}}$  describes the tension design stress. According to ETAG 002 (2012), a homogeneous stress

distributions is assumed, so that the calculated stress  $\sigma$  represents the engineering stress. In contrast to the dimensioning of the bite, the design shear stress  $\Gamma_{\text{des}}$  of the silicone is used to calculate the width  $e$  of the adhesive joint via

$$\tau = \frac{G\Delta}{e} \leq \Gamma_{\text{des}} \Rightarrow e \geq \left| \frac{G\Delta}{\Gamma_{\text{des}}} \right| \text{ with } e \geq 6 \text{ mm} \quad (7.2)$$

where  $G$  represents the shear modulus of the silicone adhesive and  $\Delta$  means the maximum thermal movement, as a combination of elongation in directions  $a$  and  $b$  of a window for example. On this basis, it is also proposed that the relation

$$e \leq h_c \leq 3e \quad (7.3)$$

should be met when designing silicone adhesive joints in façade applications. If unsupported structures are considered, the shear stress is calculated slightly differently. Since the load-bearing capacity must now be calculated under permanent shear loading, the entire dead weight  $P$  of the glazing is supported by two vertical adhesive joints, each of length  $h_v$ . Hence, the bite  $h_c$  can be calculated by

$$h_c \geq \frac{P}{2\Gamma_\infty h_v} \quad (7.4)$$

where  $\Gamma_\infty$  means the shear design stress under permanent load. It is interesting to note that the dimensioning formulas directly include information from the geometry of the bonded joint system, which makes it necessary to bond exactly according to ETAG's specifications. This means that the formulas given cannot be applied if more than two bites are used. Finally the tension design stress  $\sigma_{\text{des}}$ , shear design stress under dynamic load  $\Gamma_{\text{des}}$  and shear design stress under permanent load  $\Gamma_\infty$  will be discussed. The design stresses are determined by evaluating the 5 % quantile failure stress measured on the ETAG H-samples for tension and shear and dividing it by a global safety factor of  $\gamma_{\text{tot}} = 6$  if the adhesive is not permanently exposed to load. Thus, the design resistances are calculated by

$$\sigma_{\text{des}} = \frac{R_{u,5}}{\gamma_{\text{tot}}} \text{ for tension and } \Gamma_{\text{des}} = \frac{R_{u,5}}{\gamma_{\text{tot}}} \text{ for shear.} \quad (7.5)$$

In this case, all data refer to the reference temperature of 23°C at which the ETAG H-samples are tested. Although the global safety factor can be regulated nationally, the value of six is proposed to take account of influences from temperature, stress duration and inaccurate calculation methods. In Germany, therefore, this value is often reduced to the value of  $\gamma_{\text{tot}} = 4$  as a result of more precise numerical calculations of the adhesive joints, but it would in principle be appropriate to use a semi-probabilistic safety concept instead of a global safety factor in order to obtain

a proper material safety factor (EN 1900, 2002). However, this is not further pursued in the present work and is the subject of future research. Returning to the calculation of the design resistance for structures under constant load as a result of the dead weight of a glass pane, it is determined as follows

$$\Gamma_{\infty} = \frac{\Gamma_{\text{des}}}{\gamma_c} \quad \text{with } \gamma_c = 10. \quad (7.6)$$

From this it becomes clear that the 5 % quantile value of the experimentally determined shear strength is reduced to approximately 1.67 %, since the long-term behaviour under constant load has not yet been substantially researched.

### 7.1.2 DIBt Concept

In Germany, for example, it is necessary to verify the load-bearing capacity by means of an increased experimental and / or numerical effort in accordance to the DIBt Concept (2012) if there is a slight deviation from the required geometric conditions according to ETAG. The expression of a slight geometric deviation is not clearly defined and is therefore always in need of discussion. However, there is a consensus that three-flank bonding or flat bonded joints cannot be proven with the mentioned concepts. This concept provides for a five-point program to prove adhesive joints with slightly modified geometry. These points are briefly presented and summarized in the following:

#### **Step 1 Description of the subject matter of the authorisation**

Data to be provided by the applicant concerning design, choice of materials and intended field of application. This includes in particular the description of application area, climatic zones, installation situations including assembly system, measures for installation monitoring, component drawings with material specification, material data and material laws, for FE calculation, action-dependent of the adhesive for the relevant stress states (compression, tension, shear, combination tension-shear-compression) and the definition of the service life to be verified and the required safety level (usually 25 years).

#### **Step 2 Quantification of external influences on the adhesive joint**

In particular, this involves the quantification of controlled impacts on a component with regard to its dead weight, snow and wind loads, additional damaging impacts such as physical-chemical impacts (UV, moisture, cleaning agents, aerosols and trace gases as well as migration from materials in contact), determination of the mechanical loads and time-related

classification of the impacts according to quasi-static and periodically recurring stresses.

**Step 3 Determination of the local extreme stresses in the adhesive joint**

In this step, the aim is to simulate component tests carried out using validated mechanical-numerical models with the result of identifying so-called hot spots, which form the basis for experimental long-term and/or fatigue proof with laboratory samples.

**Step 4 Realization of the long-term and fatigue tests**

Based on the local stresses in the adhesive determined in step 3, load values for adhesion and stress loss as well as creep and fatigue tests, for example, are determined, on the basis of which a large test program with small part specimens must be carried out, in which the geometry of the adhesive joint corresponds to the dimensions of its actual application.

**Step 5 Assessment of the safety level of the bonded joint**

The last step is to describe and fulfil a verification concept regarding the static long-term strength, the proof under creep load and the proof for dynamic tensile-threshold loading. On the basis of the experiments carried out, an equivalent stress for a service life of 25 years is to be defined. Furthermore, partial safety factors must be calculated for the bonded joint.

## 7.2 Logical Experimental Testing Program

This section proposes a logical test program for silicone adhesives that extends the test program to ETAG 002 (2012) in order to fully describe the structural behaviour as well as the material failure. Again, thermal-hygric, cyclic fatigue and artificial ageing are excluded for the following studies. A main objective of engineering science is the experimental characterization of materials for two main reasons: (i) description of the structural behaviour to determine effective material properties, such as Young's modulus, shear modulus and bulk modulus for rubber-like materials and (ii) determination of the failure of the investigated material at any deformation state.

Looking at the experimental characterization of rubber-elastic materials, this material class generally exhibits a strongly non-linear stress-strain relationship including large deformations (Treloar, 1943). Furthermore, the failure of the material under the condition of large deformations is strongly dependent on the multi-axiality of loading. The multi-axiality or triaxiality represents the magnitude of the ratio of hydrostatic pressure  $p$  to von Mises equivalent stress  $\sigma_{vM}$ . A detailed

description of triaxiality can be found in Section 7.4.1. Due to the described complexity of the material behaviour and also the failure, it is decisive to be able to describe the multi-axial structural behaviour and failure by only a limited number of experimental tests.

To present as clearly as possible which experiments are necessary for the characterization of the material and its failure, typical experiments on hyperelastic materials are briefly presented in the following. The experimental characterization of elastomers can be summarized into uniaxial, biaxial, shear and volumetric tests (Crocker and Duncan, 2001; Sasso et al., 2008; Dias et al., 2014; Drass et al., 2018e). Since experiments are generally expensive, the industry usually demands a minimum, but just enough experiments for a proper material characterization to take place. In order to decide which experiments are necessary, we will look at the so-called invariant plane as proposed by Treloar (1975) and Baaser et al. (2013). This plot gives a range of permissible deformations of rubbers and rubber-like materials exhibiting an incompressible material behaviour. Since no material is incompressible, the assumption of incompressibility is only chosen for mathematical convenience. Since this chapter deals with design methods for structural silicones, working hypotheses are necessary to simplify complex models, for example. Returning to the invariant plane for  $J = 1$ , it is generally defined by the first and second isochoric invariant of the left Cauchy-Green tensor. The lower bound for permissible deformations is defined by the uniaxial tension curve, whereas the upper bound defines a biaxial tensile loading. Between both curves there is a pure shear deformation, which for reasons of comprehensibility is also shown in Fig. 7.2a. As shown in Fig. 7.2a, all conceivable deformation paths for an incompressible material occur between the lower and upper bounds, which are characterized by a uniaxial or biaxial loading. To show this random deformations paths of an incompressible hyperelastic material are added as black spots in the plot. Coming back to the question which experiments are necessary for a robust material characterization, it is obvious from the invariant plane to carry out those experiments which are located as far away from each other as possible. These would be the uniaxial and biaxial tensile tests, since these deformation paths span the invariant plane. For reasons of determination of the shear modulus, the performance of additional shear tests is desirable but not necessary, since the shear modulus can also be determined using uniaxial and biaxial test data.

Since the mentioned two experiments serve in particular to characterize the isochoric, i.e. volume-preserving, material behaviour, the volumetric material behaviour must also still be determined. Volumetric tests can be performed via confined compression tests or pancake tests. The confined compression test is characterized by compressing a cylindrical specimen inside a metallic cylinder. The outer metallic cylinder prevents the sample from expanding, causing volumetric stress in

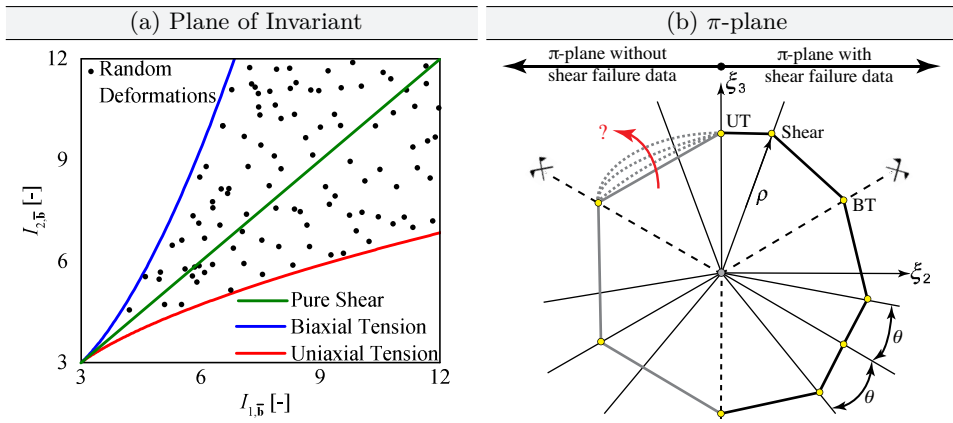


**Figure 7.2** (a) Representation of the plane of the invariants with the deformation paths for uniaxial and biaxial stress, pure shear and the representation of random deformations, which must lie between the upper and lower limit, under the assumption that an incompressible material is present and (b) split  $\pi$ -plane to describe the failure surface with data for uniaxial, biaxial tension and shear failure and  $\pi$ -plane without shear data

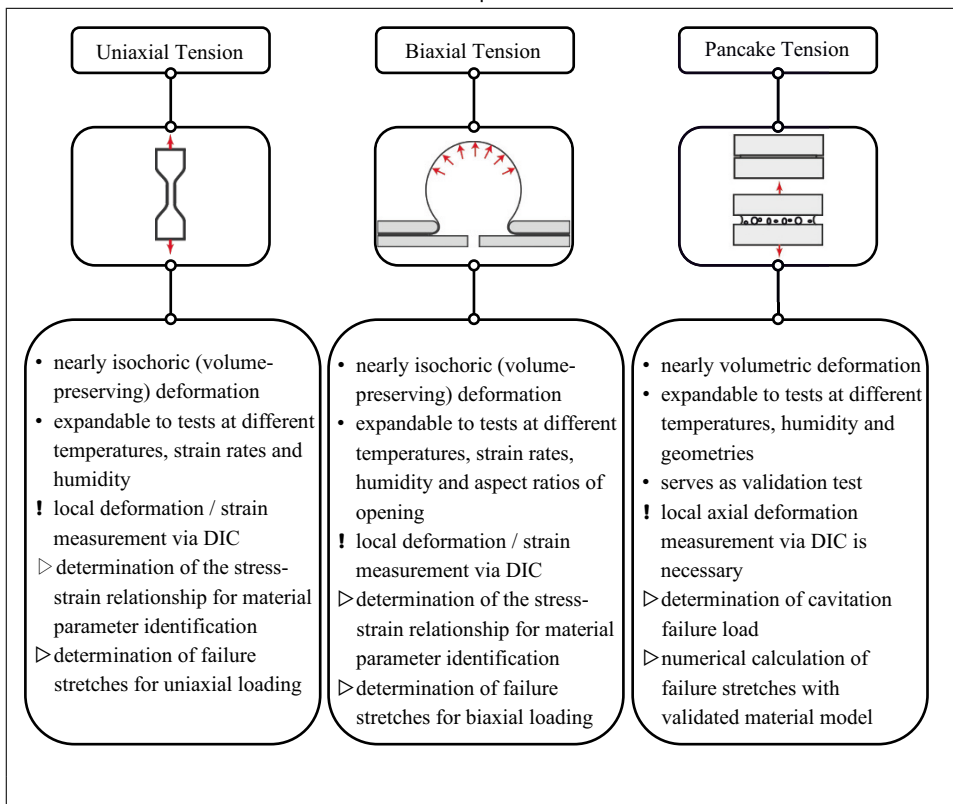
the material. With this test, the bulk modulus can be determined, but it is relatively difficult to determine the initial bulk modulus, since the test set-up must first form full-surface contact everywhere (Crocker and Duncan, 2001; Dias et al., 2014). In contrast to the confined compression test, the pancake test in tension can also generate an almost homogeneous hydrostatic stress state in the material by axially pulling a flat bonded sample. The pancake tension test not only provides sound information on the initial bulk modulus (Crocker and Duncan, 2001), but also on cavitation failure of rubber-like materials that are hydrostatically pulled (Gent and Lindley, 1959; Hocine et al., 2011). Furthermore, the pancake test can also be used as a validation test to confirm the suitability of a selected hyperelastic material model (Drass et al., 2018b). Therefore, in addition to the uniaxial and biaxial experimental tests representing isochoric deformation, pancake tension tests are recommended to calibrate a hyperelastic material model for as many deformation scenarios as possible.

In contrast to the pure characterization of the material behaviour, the description of a strength hypothesis requires not only data from uniaxial and biaxial tensile tests but also data from shear tests. This fact is illustrated in Fig. 7.2 b, where the  $\pi$ -plane is displayed for an arbitrary material. The special feature of the  $\pi$ -plane is that it is divided in the middle. On the right-hand side, the failure data (yellow dots) for uniaxial and biaxial tension as well as shear failure and their approximation are represented by an arbitrary criterion. It can be clearly seen that shear failure has a great influence on the form of a failure criterion in the  $\pi$ -plane. This

can be further substantiated by looking at the left-hand side of the  $\pi$ -plane. Here the approximation of the failure points is shown only for the uniaxial and biaxial tension. As can be seen, various cross-sectional shapes of the failure criterion can be used for the approximation of the uniaxial and biaxial tensile failure. Therefore, from the perspective of the unambiguous description of a failure criterion, failure due to shear stress is an important parameter. However, in order to avoid shear tests and the evaluation of the failure stresses / stretches due to a shear deformation, additional failure data can be numerically calculated based on the obligatory pancake tests, given that the material model is able to properly approximate the structural response from the pancake test. This approach is reasonable because the numerically calculated failure data from the pancake tests are similar to those from the shear tests with respect to the location in the  $\pi$ -plane. This has already been successfully demonstrated in this thesis, where additional failure points were obtained from the simulation of the pancake test (see Section 5.5.5) and used to describe the failure criterion (see Section 6.1).

To give structural engineers a concise overview of the necessary experimental investigations for a robust description of the material behaviour and failure, the above-mentioned recommendations are briefly summarised in a so-called engineering toolbox. Accordingly, in Tab. 7.1 necessary experimental tests are shown briefly, useful hints are presented and the expected output from these tests are given. The general information on the recommended experiments is indicated by the symbol (●), necessary boundary conditions, such as the local deformation measurement via DIC, are marked by a (!) and the output by (>). Looking at the necessary boundary conditions, a local deformation measurement using DIC is required for all recommended experiments, since not only the stress strain behaviour can be adequately determined experimentally but also failure stretches can be derived, which are of utmost importance for the later formulation of a failure criterion. Since the local deformation measurement is rarely used for the experimental evaluation, but only the traverse displacement of the testing machine in order to save costs, an adequate description of the material behaviour and the failure is in principle not possible. In particular, the initial stiffness of the experiment and the FEA differ considerably with respect to the numerical simulation of the experiments, which were only evaluated with global information such as the traverse deformation.

**Table 7.1** Engineering toolbox for the concise presentation of the necessary experimental investigations on rubber-like materials for the robust description of material behaviour and failure



## 7.3 Material Parameter Identification

Based on the recommended experiments on structural silicones and rubber-like materials in general, material parameters have to be determined to approximate the non-linear structural behaviour of the material under investigation. As already mentioned, an analytical determination of material parameters via regression analyses can only be accomplished when a homogeneous stress and strain state is present during testing (see Section 4.2). Considering the three proposed experimental tests on rubber-like materials for a robust material characterization from Section 7.2, only uniaxial and biaxial tensile tests show such a homogeneous deformation. Consequently, these tests can be used to determine analytically isochoric stiffness and thus provide material parameters for a selected hyperelastic constitutive model. In contrast, the experimental results of the pancake tension tests must

be used to determine the material parameters for volumetric deformations, since a triaxial state of stress and strain is present here. As the pancake tension test does not provide a homogeneous state of stress and strain, inverse numerical methods must be used to determine the volumetric material parameters (Drass et al., 2017a; Drass et al., 2018b). For this reason, the following briefly describes a two-stage determination of material parameters using the experimental database based on the experiments proposed in Section 7.2.

The two-step material parameter identification first uses the isochoric experimental database to determine the isochoric material parameters for the novel incompressible hyperelastic material model proposed in Eq. (5.4). The assumption of incompressibility is chosen due to mathematical convenience. Since the isochoric material parameters change only marginally when a small compressibility is added or the influence disappears, the material parameter identification can initially be carried out separately but consecutively. Thus, these isochoric material parameters are then used as initial or start values in the second step of material parameter identification and subsequently the volumetric material parameters are optimized by inverse numerical calculations of the pancake tension test. This means that the material parameters in the numerical model are continuously updated until the global force-displacement behaviour matches that of the experiment.

To do so, first the experimental data from the uniaxial and biaxial experiments must be prepared in such a way that engineering stress and strain relationships are present. Then a hyperelastic constitutive model must be chosen, which is capable to represent the non-linear behaviour of both experiments. Since there are more than forty material models to describe hyperelastic behaviour (Steinmann et al., 2012), it is up to the engineer to make a choice regarding a suitable material law. As already shown by Marckmann and Verron (2006), one material model exists which is excellently suited to represent arbitrary isochoric deformation states. As shown in his studies, the model of Kaliske and Heinrich (1999) offers a high functional adaptivity, even for large deformations under simultaneous molecular-statistical motivation of the material parameters. However, it has already been shown in this work that this model provides poor results in the approximation of the structural behaviour of structural silicones, especially with regard to the approximation of the initial stiffness (see Section 5.5.1). A more suited model for the approximation of the structural behaviour of structural silicones, especially with respect to the approximation of the initial stiffness, is provided by the novel model based on an inverse polynomial (see Eq. (5.4)). As proposed in the present work, the very adaptable hyperelastic model, which is based on the Nelder (1966) function, can be used to approximate the experimental data. To do so, the constitutive model must first be prepared in such a way that it describes the uniaxial and biaxial stress-strain behaviour. Since it is difficult to determine the true or Cauchy stress

experimentally by measuring the true cross-sectional dimensions, it is useful to express the measurement data as well as the analytical relationships as engineering stress-strain measures. To be more precisely, these relations will be presented for the novel isochoric Helmholtz free energy in the following. Having the hyperelastic material model at hand, a way to do this is to first express the invariants via principal stretches and then differentiate the results with respect to the corresponding principal stretches to obtain the engineering stresses in the principal directions. To do so, the principal invariants of the isochoric left Cauchy-Green tensor of the novel Helmholtz free energy function

$$\Psi_{\text{iso,ND}}(\bar{\mathbf{b}}) = \frac{(I_{1,\bar{\mathbf{b}}} - 3)}{\alpha_0 + \alpha_1(I_{1,\bar{\mathbf{b}}} - 3)} + \frac{(I_{2,\bar{\mathbf{b}}} - 3)}{\beta_0 + \beta_1(I_{2,\bar{\mathbf{b}}} - 3)} \quad (7.7)$$

must be replaced by

$$I_{1,\bar{\mathbf{b}}} = \lambda_1^2 + \lambda_2^2 + \lambda_3^2 \quad (7.8)$$

and

$$I_{2,\bar{\mathbf{b}}} = \lambda_1^2 \lambda_2^2 + \lambda_2^2 \lambda_3^2 + \lambda_3^2 \lambda_1^2. \quad (7.9)$$

Then, the principal Cauchy stresses can be calculated by differentiating  $\Psi_{\text{iso,ND}}$  with respect to  $\lambda_1$ ,  $\lambda_2$ ,  $\lambda_3$ . Hence in a general form the Cauchy stress reads

$$\sigma_i = \frac{\partial \Psi_{\text{iso,ND}}}{\partial \lambda_i} - p \quad \text{with } i \in [1, 2, 3], \quad (7.10)$$

where the variable  $p$  describes an indeterminate Lagrange multiplier in accordance to (Holzapfel, 2000:p.225), which must be calculated due to boundary conditions. Keeping in mind that for a uniaxial deformation the Cauchy stresses  $\sigma_2$  and  $\sigma_3$  are zero and the principal stretches read  $\lambda_1 = \lambda$  and  $\lambda_2 = \lambda_3 = 1/\sqrt{\lambda}$ , the Cauchy stress in stretch-direction reads

$$\sigma_1 - \underbrace{\sigma_3}_{=0} = \frac{\partial \Psi_{\text{iso,ND}}}{\partial \lambda_1} - \frac{\partial \Psi_{\text{iso,ND}}}{\partial \lambda_3}, \quad (7.11)$$

whereby the skilful choice of  $\sigma_1 - \sigma_3$  makes the determination of the Lagrange multiplier superfluous, since it vanishes. The same formula can be utilized to calculate the Cauchy stress in a biaxial deformation, however the principal stretches read  $\lambda_1 = \lambda_2 = \lambda$  and  $\lambda_3 = 1/\lambda^2$ . Based on Eq. (7.11) the engineering stress can easily be calculated using  $T_i = \sigma_i/\lambda$ . Since the analytical stress-strain relationship is now present, an objective function must be defined which, for example, minimizes the error between the experimental data and the analytical description using the least squares method for example while simultaneously optimizing the

material parameters. Since this procedure was already described in Eq. (5.115), it is only pointed out. It should also be mentioned that the material parameters are not freely selectable in order to achieve the best possible fitting result. Since, for example, negative material parameters can lead to material instabilities, the proof of polyconvexity must also be fulfilled (see Section 5.1.3). In this context, material instability is defined as negative stiffness, which can lead to numerical problems. Another example is that in a uniaxial tensile test at a certain deformation, compressive stresses can also occur in the material, which is not physical. As a result, the material consistency must also be checked when selecting the material parameters. Please refer to Section 5.1.3 for more information. Returning to the optimization of the isochoric material parameters, a defined tolerance must be reached during the optimization to finish the optimization algorithm, so that these parameters have been analytically determined and the second step of material parameter identification can be initialized.

The second step in determining the desired material parameters, here the volumetric material parameters of the novel volumetric Helmholtz free energy function of Eq. (5.64) accounting for the cavitation effect in rubber-like materials, is based on inverse numerical calculations based on Finite Elements. It is defined by the FEA of an experiment in which the material parameters are initially unknown, but are varied until the structural response between the simulation model and the experiment is almost identical. Hence, the structural response of the pancake test is approximated under varying solely the volumetric material parameters  $\kappa_0, \kappa_1, \kappa_2, \kappa_3$  of Eq. (5.64), whereas the isochoric material parameters from step 1 are kept constant. To be more specific, the inverse material parameter identification is conducted via Finite Element Model Updating (FEMU) approach (Avril et al., 2008), which is a numerical method based on the Finite Element Method solving inverse problems. The FEMU approach describes a technique, where numerical calculations with randomly chosen initial parameters are conducted iteratively and compared with experimental data as long as a pre-defined residuum is smaller than the fixed tolerance. To evaluate the results of the FEMU approach, an additional objective function must be formulated. The objective function compares the numerical response, here the global force / displacement behaviour of the numerical simulation, with the experimental response under minimizing the L2-norm by adjusting the volumetric parameters of the chosen constitutive material model. Thus, the force-displacement behaviour of the pancake tests are compared with the results of the numerical simulation of the pancake tests under optimizing the initially assumed material parameters. Good start values can be determined by so-called sensitivity studies, in which the material parameters are randomly distributed within defined limits. In the sensitivity analysis all material parameter combinations must be calculated numerically once completely, in order to be able

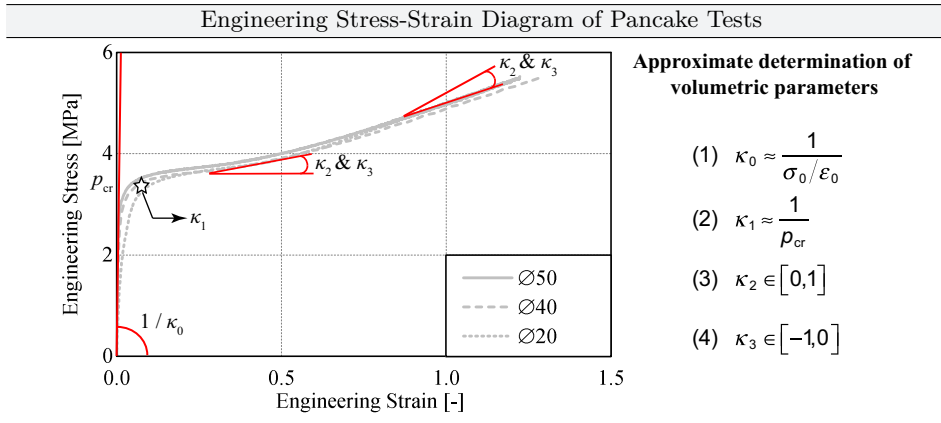


**Figure 7.3** Presentation of the experimental results of the pancake tests in the engineering stress-strain diagram, annotation of the meaning of the material parameters in the diagram and approximate equations for the volumetric parameters of the new volumetric Helmholtz free energy function

to evaluate the quality of the result, here a value for the deviation between experiment and numerics. Since all designs have to be calculated once, this process is time-consuming because many calculations have to be made. However, the effort can be significantly reduced by skilfully selecting the volumetric parameters and limiting them to parameter limits. In order to obtain good initial values for the volumetric parameters, initial estimates can be read directly from the pancake tests. Converting the force-displacement curves of the pancake tension tests into engineering stress strain curves results in the following diagram. As can be seen from Fig. 7.3, the initial stiffness or the volumetric material parameter  $\kappa_0$  respectively can be approximately calculated by the reciprocal of the initial engineering stress  $\sigma_0$  divided by the initial strain  $\varepsilon_0$ . This is indicated in the diagram by the gradient at the origin. The second parameter describes the bifurcation point or bifurcation stress  $p_{cr}$  in the stress-strain diagram. From this the second volumetric material parameter  $\kappa_1$  can be read approximately by forming the reciprocal of the bifurcation stress  $p_{cr}$ . Since the last two volumetric material parameters are related to each other, they cannot be read directly from the engineering stress-strain diagram of the pancake tests. However, for such pancake diagrams the material parameter  $\kappa_2$  must be within the limits  $\kappa_2 \in [0, 1]$  and the parameter  $\kappa_3$  within the limits  $\kappa_3 \in [-1, 0]$ . At this point it should be noted that the material parameter  $\kappa_2$  describing the inclination after the occurrence of cavitation failure reflects the effective stress softening due to excessive void growth, from which it is positive according to the definition of Nelder (1966). In contrast, the material parameter

$\kappa_3$  describes the effective stress stiffening behaviour after cavitation has occurred, so that this is given a negative sign.

Going back to the question of the initial values for the material parameter optimization, which takes place after the sensitivity analysis, one selects the determined parameters based on the sensitivity analysis, which delivered the best possible result with regard to minimizing the error between experiment and numerics. With these initial values and narrowly defined parameter spaces, a direct optimization of the material parameters can be connected. To do so, an objective function  $\mathcal{S}$  must be formulated for an initial set of volumetric parameters  $p_j^{\text{init}}$ , whereas the isochoric material parameters were obtained within the first step of material parameter identification based on analytical relationships. A qualified objective functions can be defined by

$$\mathcal{S} = \sqrt{\frac{1}{n} \sum_{i=1}^n \left[ \frac{F_i^{\text{sim}}(u_i, p_j^{\text{init}}) - F_i^{\text{exp}}}{F_i^{\text{exp}}} \right]^2}, \quad (7.12)$$

where the function  $\vec{F}^{\text{sim}} \Rightarrow F_i^{\text{sim}}(u_i, p_j)$  represents the engineering results of the numerical simulation. The principal stretch vector is defined by  $\vec{u} \Rightarrow u_i = [u_1, u_2, \dots, u_n]^T$  corresponding to the length of data points of the experiment. The unknown material parameters  $\vec{p} \Rightarrow p_j = [p_1, p_2, \dots, p_o]^T$  can be determined by solving the minimization problem with

$$\min \mathcal{S} \equiv \min_{\vec{p}} \mathcal{S}(\vec{p}). \quad (7.13)$$

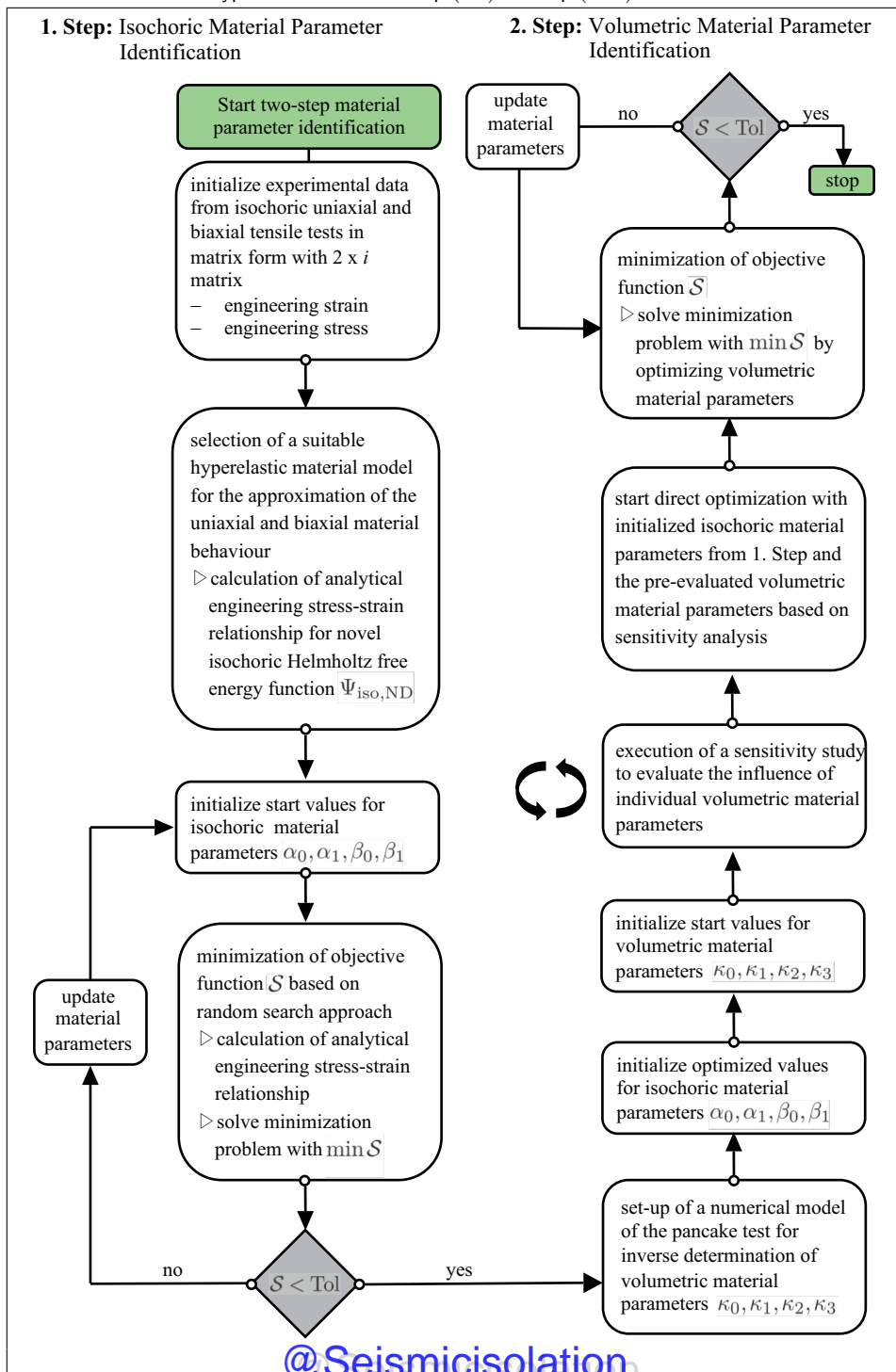
If  $\text{Tol} < \mathcal{S}$ , the optimization procedure proceeds with a perturbation of the initially chosen material parameter  $p_j^{\text{init}}$  by  $p_j^{\text{init}} + \Delta p_j$  resulting in

$$\mathcal{S} = \sqrt{\frac{1}{n} \sum_{i=1}^n \left[ \frac{F_i^{\text{sim}}(u_i, p_j^{\text{init}} + \Delta p_j) - F_i^{\text{exp}}}{F_i^{\text{exp}}} \right]^2}, \quad (7.14)$$

until a defined tolerance is with  $\mathcal{S} \leq \text{Tol}$ . The perturbation of the initially chosen damage parameters can be achieved by evolutionary or by direct optimization strategies (Drass et al., 2017a).

On the basis of the proposed two-step approach for the material parameter identification, isochoric and volumetric material parameters can be determined separately, on the one hand, and on the other hand, it is possible to control the effort of determining material parameters, since it is not necessary to determine the full set of volumetric parameters for all building situations. To introduce the two-step algorithm for determining the material parameters, reference is made to engineering toolbox presented in Tab. 7.2, which displays a flowchart. It summarizes the analytical determination of the isochoric material parameters and describes all nec-

**Table 7.2** Engineering toolbox for the concise presentation of the two-step material parameter identification for the novel hyperelastic models of Eq. (5.4) and Eq. (5.64)



essary intermediate steps. After successful analytical determination of the isochoric material parameters, the numerical determination of the volumetric material parameters follows, in which all necessary intermediate steps are also listed.

## 7.4 Modelling of Silicone Adhesive Joints

This section is dedicated to the general modelling of silicone adhesive joints in façades and other applications to assist structural engineers in choosing an adhesive joint geometry that directly affects the applicability of constitutive models and the description of failure. First, adhesive joint systems and adhesive geometries from special applications are summarized and special features are discussed. For reasons of clarity, the term "adhesive joint system" will also be used in the following for the applied geometric design of an adhesive joint. In order to objectively categorize the different adhesive joint systems, two criteria from the literature are briefly presented and applied to the different systems. On this basis, assistance is given for the constitutive description of the different systems in order to create a kind of catalogue with regard to adhesive joint systems and the application of material models. Since the choice of material models is also directly related to the type of adhesive system or adhesive used, a constitutive model is assigned to each of the various but frequently used adhesives in façade applications.

### 7.4.1 Classification of Adhesive Joints

In this section, different adhesive systems that have already been used in practice are briefly introduced and divided into cavitation-sensitive and cavitation-insensitive systems using objective criteria. The criteria for distinguishing between the two cases are briefly presented below and evaluated for their applicability on typical adhesive bonding systems in the façade sector. This classification makes sense insofar as, for example, the ETAG 002 ([2012](#)) concept can be used for cavitation-insensitive adhesive bonding systems as long as the adhesive is linear in its geometry and has only two flanks for bonding. Deviations from the ETAG 002 ([2012](#)) concept can only be proven with considerable experimental effort, expert opinions and decision-making boards. In Germany for example, if one deviates from the geometric specifications of adhesive joints according to ETAG 002 ([2012](#)), it is possible to proof the ultimate limit state of the adhesive joint using a concept developed at the German Institute for Building Technology. This concept is called the DIBt Concept ([2012](#)) and requires a wide range of experimental investigations which even exceed the requirements of ETAG 002 ([2012](#)). However, if one deviates from the ETAG concept or the DIBt concept in such a way as is the case, for example, with flat-bonded point holders, there is still no concept for carrying out

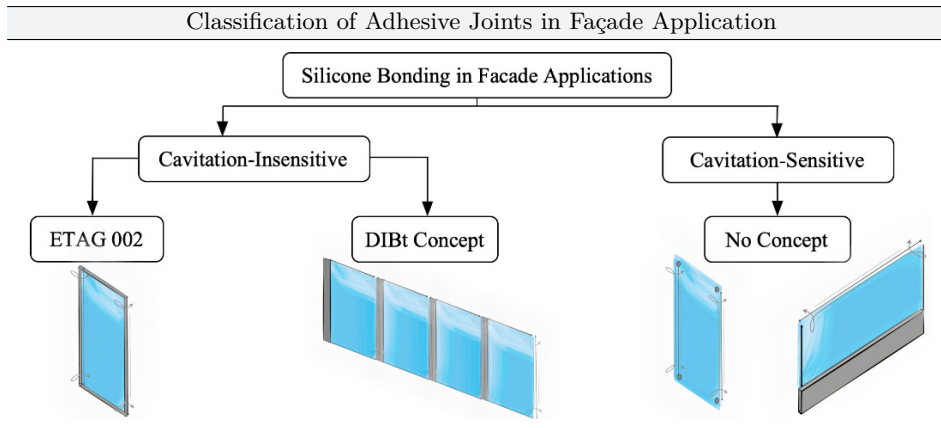


**Figure 7.4** Schematic classification of adhesive joints for façade applications into cavitation-sensitive and cavitation-insensitive adhesive joints, where the last are subdivided again into adhesive joints according to ETAG 002 (2012) and joints with slight deviations

a sensible dimensioning. A schematic representation of the classification of typical adhesive bonding systems in façade design is shown in Fig. 7.4. First of all, a distinction is made between cavitation-sensitive and cavitation-insensitive adhesive joints, while in the last case an additional distinction is made between adhesive joints, which correspond to ETAG 002 (2012), and adhesive joints, which show slight geometric deviations concerning the geometry and requirements according to ETAG 002 (2012).

### Criteria for Classification

As already presented in Section 7.1.2, slight geometric deviations of adhesive joints in comparison to the geometry defined in ETAG 002 (2012) require considerable effort in order to provide the proof of structural integrity and safety according to the DIBt Concept (2012). To create a clear differentiation between adhesive joints according to ETAG 002 (2012), adhesive joints with slight geometric adjustments or adhesive joints which cannot be proven with any of the concepts mentioned, objective criteria are required to categorise adhesive joints according to their application, external loads and mechanical stresses within the adhesive. This is intended to create a better understanding of structural engineers in order to be able to better design and calculate adhesive joints in façade construction.

Accordingly, a criterion must first be found which is capable of clearly distinguishing between cavitation-insensitive and cavitation-sensitive adhesive joints. Hamdi et al. (2014) have made a suggestion, which forms the ratio between the diameter  $d$  divided by four times the height  $h$  of a cylindrical pancake test sample,

which is axially loaded. Based on a large test series on pancake tension tests under variation of the shape factor

$$S = \frac{d}{4h}, \quad (7.15)$$

cavitation failure was investigated and a critical limit for a cavitation-insensitive geometry of  $S \leq 1.0$  (no cavitation) was determined. Since the criterion can only be applied on cylindrical adhesive joint geometries, it will be extended to any geometries in the following. The basic idea of the criterion is to determine the ratio of the pulled surface to the free surface. Accordingly, it can simply be transferred to the following general form

$$S = \frac{A}{U h}, \quad (7.16)$$

where  $A$  is the pulled surface area,  $U$  represents the perimeter of the adhesive joint and  $h$  was already introduced as bondline thickness. Since this geometry factor is a good first approximation to distinguish between cavitation-insensitive and cavitation-sensitive adhesive joints, it is essential to clearly define its limits here as well.

Assuming that this criterion was developed from the experimental results of axially loaded pancake tests, it can only be applied to axially loaded adhesive joints. If, for example, one has a very flat adhesive joint that can only be subjected to shear stress due to structural boundary conditions, it is questionable that this stress can lead to cavitation failure. In order to have a criterion that can show whether cavitation is relevant for any structure and stress situation, the criterion of so-called triaxiality is introduced. It is a measure to describe the multi-axiality of stresses in any component under any load scenario. Based on the work of Sikora (2014) the triaxiality is defined as the magnitude of the ratio of hydrostatic pressure  $p = \text{tr}(\boldsymbol{\sigma})$  to von Mises equivalent stress  $\sigma_{vM} = \sqrt{3I'_{2,\sigma}}$ . For reasons of comprehensibility, this criterion is scaled with the result that under uniaxial tensile loading the discrete value of  $\eta_{\text{mod}} = 1$  is obtained. Thus, the modified triaxiality reads

$$\eta_{\text{mod}} = \left| -3 \frac{p}{\sigma_{vM}} \right|. \quad (7.17)$$

Sikora (2014) recommends to extend the discrete, theoretical values of triaxiality to a bandwidth, since single scalar values without upper and lower limits are not realistic boundaries with regard to prevailing stresses and strains in any structural components. Therefore, Sikora (2014) analysed arbitrary combinations of principal stresses,  $\boldsymbol{\sigma}'' = \boldsymbol{\sigma}'' \pm 1/10 \boldsymbol{\sigma}''$ , where the variation of the Cauchy stress was applied in one or more principal stress directions. With the help of this parameter study, threshold values for uniaxial, biaxial, triaxial and shear deformations could be evaluated (Tab. 7.3). At this point it should be noted that these ranges can be

**Table 7.3** Theoretical and threshold values for modified triaxiality

Stress State	Theoretical Value	Modified Triaxiality $\pm 10\%$
Triaxial	$\eta_{\text{mod}} = \infty$	$\infty \geq \eta_{\text{mod}} \geq 20$
Biaxial	$\eta_{\text{mod}} = 2$	$2.3 \geq \eta_{\text{mod}} \geq 1.7$
Uniaxial	$\eta_{\text{mod}} = 1$	$1.3 \geq \eta_{\text{mod}} \geq 0.72$
Shear	$\eta_{\text{mod}} = 0$	$0.17 \geq \eta_{\text{mod}} \geq 0$

individually adapted in case one is interested in stronger or weaker delimitations of deformation processes. In order to decide whether any adhesive joint system is independent of cavitation failure, it is necessary that the triaxiality evaluation does not exceed the critical value of  $\eta_{\text{mod}} \leq 20$ . This means that there is no pronounced volumetric deformation in the material, which excludes excessive pore growth and stress softening.

Since this criterion is able to describe the predominant stress state in the sense of multi-axiality for arbitrary adhesive situations and loadings, it is obvious to evaluate and visualize it in the FE model. Since ANSYS FE code was used in the course of this work, the procedure for evaluating and visualizing the triaxiality is briefly explained in the following. For this purpose, a user-defined result must be created in the post-processing after a successful three-dimensional calculation of a bonded joint has been carried out. The evaluation takes place via principal stresses to which the variables S1, S2 and S3 are assigned in ANSYS FE code. The input file for the user-defined result to evaluate the triaxiality is given by

```
SUBROUTINE Triaxiality(S1,S2,S3)
eta_mod = abs(2*((S1+S2+S3)
& /(6*((S1)**2-S1*S2-S1*S3
& +(S2)**2-S2*S3+S3**2)**0.5))*3
END SUBROUTINE
```

Furthermore, a user-defined colour scheme has to be added, where the threshold values are equal to those defined in Tab. 7.3.

### Examples for Classification

In the previous section, two criteria were presented for classification into cavitation-insensitive and cavitation-sensitive adhesive joint systems. The first criterion is only suitable for axially loaded adhesive joint systems and can be analytically evaluated (Hamdi et al., 2014). The second criterion evaluates the multi-axiality of the three-dimensional stress state in an FE model and thus analyses which deformation states occur in the adhesive as a result of an external loads (Drass et al., 2018e). Now that two criteria are available for categorization, typical adhesive

bonding systems used in façades are evaluated below to verify the quality of both criteria.

First of all, the ETAG H-shaped test sample is evaluated because it corresponds to the geometrical boundary conditions according to ETAG 002 (2012) and secondly because it is used to experimentally determine the structural behaviour and strength for tensile and shear loading. Calculating the shape factor according to Hamdi et al. (2014) results in a value of  $S = 0.4 < 1.0$ , which means that this joint geometry is cavitation-independent. The numerical evaluation of the triaxiality of the ETAG H-shaped sample under pure shear loading shows that large areas of the specimen are actually subjected to pure shear loading since  $\eta_{\text{mod}} < 0.17$ . Furthermore, it can be seen from Fig. 7.5 a that no defined deformation state prevails in the marginal areas, since stress superposition occurs here. Finally, it should be noted that according to the criterion of triaxiality, no triaxial stress results, which can also be confirmed by the evaluation of the shape factor according to Hamdi et al. (2014), since it is significantly smaller than one. Therefore, the strict geometrical requirements for adhesive joints according to ETAG 002 (2012) could be made comprehensible on the basis of the presented criteria for distinguishing between cavitation-insensitive and cavitation-sensitive by evaluating the ETAG H-probe. In the second example, a cantilevered, flat-bonded glass railing system from Glas Trösch Group is examined with the aforementioned criteria with regard to its susceptibility to cavitation or triaxial stresses. As can be seen in Fig. 7.5 b, it is a cantilevered glass pane, which is flat-bonded in the lower area and functions as a cantilever beam with regard to the fall protection of people. The adhesive joint has a thickness of 8 mm and in this example has a length of 800 mm with a height of 80 mm. Although the adhesive dimensions are based on the Swissrailing system of Glas Trösch (Kassnel-Henneberg, 2018), they do not necessarily have to correspond to structures actually installed. The evaluation of the shape factor  $S$  of Hamdi et al. (2014) results in a value of approx. 4.5, so that this system can be classified as cavitation-sensitive. This can be further proven by the numerical evaluation of the triaxiality, where a triaxial deformation in the centre of the adhesive is clearly visible. Consequently, the standardized design approach according to ETAG 002 (2012) is not applicable for such a system. A prime example of cavitation-sensitive adhesive joints are so-called point holders, in which large glass panes are connected to the secondary building structure at certain points via thin adhesive joints. As shown as an example in Fig. 7.5 c, the shape factor is  $S = 12.5$ , which indicates a high risk for cavitation. Furthermore, if triaxiality is evaluated for different stress scenarios, the visual representation quickly shows that large areas in the flat adhesive joint undergo triaxial deformations, so that the cavitation effect is likely to occur. In the last example a complicated adhesive joint detail is presented, where a U-shaped adhesive joint was formed in a U-steel profile in order

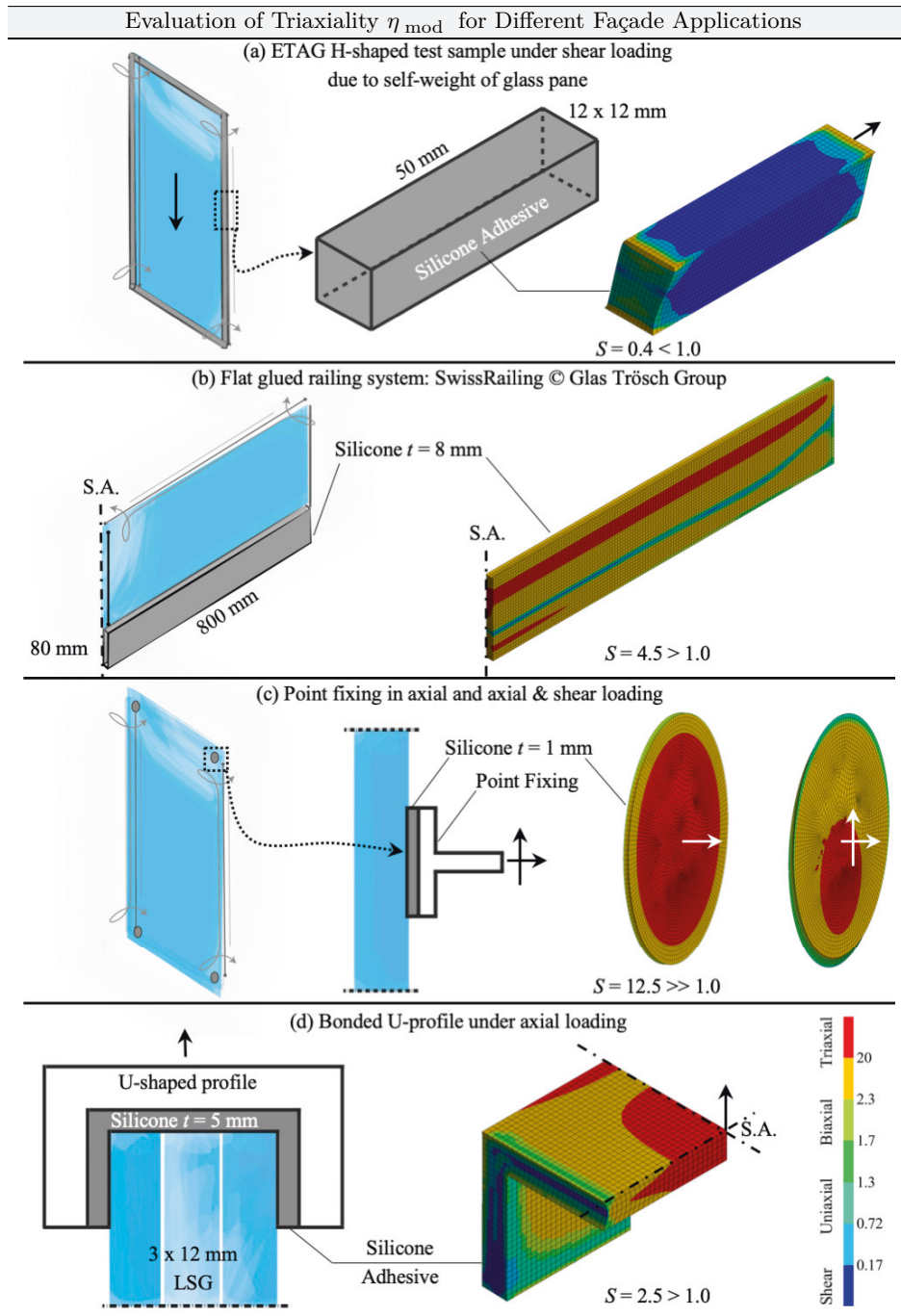


**Figure 7.5** Numerical evaluation of triaxiality  $\eta_{\text{mod}}$  for (a) ETAG H-shaped test sample under shear loading, (b) cantilevered flat-bonded glass railing system under handrail load, (c) point fixing under axial and mixed mode loading and (d) U-shaped bondline for glass beams under axial loading (Hagl, 2016)

to connect so-called glass beams (Hagl, 2016). The evaluation of the shape factor results in a value of 2.5 under axial load, so that cavitation failure is probable. If one continues to evaluate the visual criterion of triaxiality, it becomes clear that large areas also experience triaxial deformations here. As a result, the effect of cavitation is also present in this adhesive joint geometry (see Fig. 7.5 d).

This descriptive analysis should clearly explain structural engineers that the topic of cavitation is an important parameter in most cases when designing adhesive joints in façade applications. Not only in the field of material modelling but also in dimensioning and proof of failure and structural integrity. Considering above all the stress-based dimensioning of cavitation-sensitive silicone adhesive joints using FE calculations, which are frequently used in façade applications, however, this happens unknowingly, the calculations lead to large stresses as a result of the triaxial deformation in the core of the material. However, in order to dimension the adhesive joint in accordance with the established technical rules, either the load level is greatly reduced or the global safety factor is adapted to meet the design requirements (Hagl, 2016). Although this procedure leads to the desired result, i.e. the static proof is met, this procedure is not appropriate since, according to ETAG 002 (2012), a purely isochoric failure is assumed. However, since cavitation-sensitive adhesive joints undergo a triaxial deformation, which is caused in particular by the bulk modulus and not the shear modulus for stress calculation, it is not surprising that high stresses occur in the material even at small external loads and deformations. This can be explained by the fact that in rubber-like materials the bulk modulus is several orders of magnitude larger than the shear modulus. Attempting to calculate the structural behaviour cavitation-sensitive adhesive joints and to evaluate the isochoric failure criterion according to ETAG 002 (2012) for volumetric deformations, it is logical that the statical proof makes no sense on the one hand and is quickly exceeded on the other. Therefore, it seems reasonable to categorize the material models for cavitation-insensitive and cavitation-sensitive adhesive joints and to define a separate failure criterion for isochoric and volumetric failure.

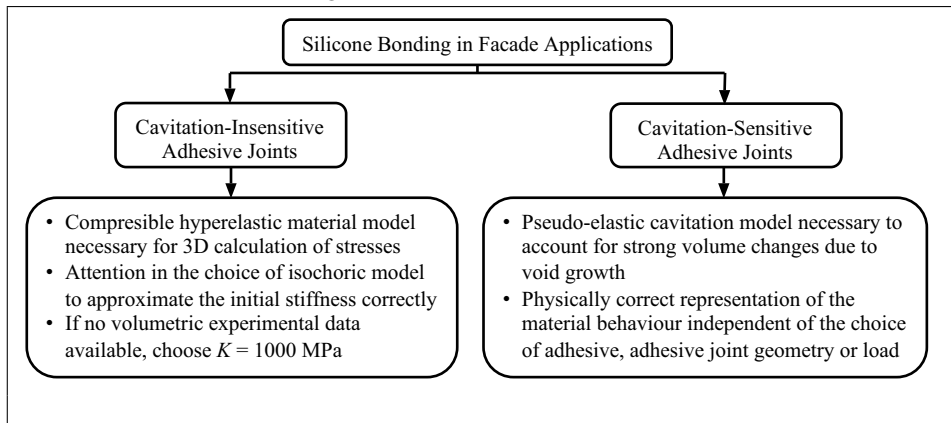
#### 7.4.2 Classification of Material Models

As from the categorization of different, in practice established adhesive joint systems into cavitation-insensitive and cavitation-sensitive adhesive joints, the influence of the lateral contraction constraint, which may lead to cavitation, has a direct influence on the calculation of stresses. Working with wrong assumptions regarding the material model with respect to three-dimensional FE analysis leads to wrong results and incorrect designs of bonded components. Therefore, a recommendation regarding the material models to be used is made in the following in accordance with the categorisation shown in Fig. 7.4.

Considering first cavitation insensitive adhesive joint systems, only isochoric, i.e. volume-constant deformations occur in the material, so that material models implemented in commercially available FE codes can be used for stress calculation. Since for typical structural silicones with respect to the façade application, the initial stiffness has to be approximated well in order to perform a robust and physically correct calculation of the occurring stresses (Dispersyn et al., 2017), it is recommended to use hyperelastic material models such as the models proposed by Marlow (2003), Dias et al. (2014) and Drass et al. (2018f). With these material models it has already been shown that the structural response of silicone adhesives can be very well approximated over the entire deformation range. Furthermore, it is recommended to avoid an incompressible material formulation, since on the one hand silicones also allow a slight increase in volume even under isochoric deformations and on the other hand the assumption of incompressibility in numerical calculations can lead to disturbances in the stress calculation. If, for example, the process of a FE calculation is considered, the condition of  $J = 1$  must be enforced via the element technology used. However, this cannot necessarily be guaranteed in all structural situations and calculations. Thus, if the solver allows a supposedly very small increase in volume, the so-called penalty term takes effect, by which the small increase in volume is multiplied by the infinitely large bulk modulus. This punishes the user or structural engineer, in which in addition to the stresses from the isochoric deformations, stresses are also arising as a result of the penalty term, which can lead to the static proof being exceeded when dimensioning an adhesive joint at stress level. If the structural engineer has no experimental data available regarding the bulk modulus, a bulk modulus of approximately  $K \approx 1000$  MPa can be assumed as a first approximation. This results in a deviation between incompressible to compressible material formulations of less than 1 % for nearly isochoric deformations, but one avoids the problem of the penalty method.

In contrast, cavitation-sensitive adhesive joint systems must take into account the compressibility due to void growth. As already described in this thesis, void growth caused by a triaxial deformation of the material leads to effective stress softening and to large volume changes in the material. Since especially in cavitation-sensitive adhesive joints a triaxial loading of the material occurs, it is proposed to use the pseudo-elastic cavitation model presented in Section 5.3. This model is characterized by a high quality of adaptation to volumetric experimental data and comprehensible and physically motivated material parameters (see Fig. 7.3). The volumetric material parameters for the pseudo-elastic cavitation model to describe the cavitation effect in rubber-like material, here in silicone adhesives, can be determined on the basis of pancake tension tests and their inverse calculation. A concise flow chart for this is shown in Tab. 7.2. In order to obtain a clear representation for the choice of the material model depending on the adhesive joint

**Table 7.4** Engineering toolbox for the schematic classification of adhesive joints for facade applications into cavitation-sensitive and cavitation-insensitive adhesive joints and the recommendation of material models for their modelling or calculation



geometries to be investigated, reference is made to Tab. 7.4, in which material models are proposed according to the classification of cavitation insensitive and cavitation sensitive adhesive joints.

## 7.5 Safety Concept and Limit State Analyses

This section deals with the limit state analysis of structural silicones, here TSSA, and the question on safety concepts and how they can be applied to cavitation-sensitive adhesive joint systems. As already postulated by Hagl (2016), the ETAG safety concept refers to a global safety concept with high safety factors in order to compensate for simplifications from the linear elastic calculation of adhesive joints based on engineering stresses and to neglect external influences such as temperature and ageing effects of polymers (see Section 7.1.1). The exact determination of the global safety factor of  $\gamma_{\text{tot}} = 6$  cannot be reconstructed on the basis of ETAG 002 (2012). However, when dimensioning elastomer components, it is common practice to reduce the characteristic strength values from short-term isothermal and long-term isochronous experiments multiplicatively via reduction factors that take into account strength-reducing influences such as static / dynamic loading conditions, temperature, humidity, cyclic fatigue, etc. (Stommel et al., 2011). The

calculation of a global safety factor  $\gamma_{\text{tot}}$  as a function of individual influencing factors can be carried out via

$$\gamma_M = \gamma_1 \cdot \gamma_2 \cdot \gamma_3 \cdot \gamma_4 \cdot \gamma_5 \cdot \gamma_6 \cdot \gamma_{\text{Ed}} \quad \text{with} \quad \begin{aligned}\gamma_1 &= \text{static / dynamic loading condition} \\ \gamma_2 &= \text{model assumptions} \\ \gamma_3 &= \text{temperature influence} \\ \gamma_4 &= \text{humidity influence} \\ \gamma_5 &= \text{cyclic fatigue} \\ \gamma_6 &= \text{short or longterm loading} \\ \gamma_{\text{Ed}} &= \text{dead vs. live load.}\end{aligned} \quad (7.18)$$

In addition, a safety factor for actions on structures needs to be introduced to take account of the variation of impacts on structures. Presumably, these considerations were also made in determining the global safety factor of  $\gamma_{\text{tot}} = 6$  in accordance to ETAG 002 (2012), but this was never documented, so that one can only make assumptions about this. Nevertheless, in the following the global safety factor of six is used for calculation, as this complies with the requirements of ETAG 002 (2012). In general, a global safety concept is a deterministic approach in which the mean values of actions and resistances of structures and materials are compared independently of their stochastic distribution. The classical verification is carried out under consideration of e.g. permissible engineering stresses. Nevertheless, in order to take the ETAG concept into account, but also to make it possible to increase the load bearing capacity of adhesive joints as a result of advanced material models and failure descriptions, a general procedure is described below using the example of flat-bonded adhesive joints. Therefore, the ETAG concept and a more generalized safety concept are applied and summarized in the following using the example of TSSA or flat-bonded, cavitation-sensitive silicone adhesive joints respectively.

According to ETAG 002 (2012), engineering stresses related to the original cross-sectional area of the stressed joint geometry are used to calculate design failure strengths for tension and shear loading, for example. The dimensioning of silicone adhesive joints on the basis of engineering stresses does not take into account the nonlinear material behaviour and the strong dependence of the structural response as a result of the geometry of the adhesive joint. Here it has already been shown in this thesis that a distinction between thick and thin or cavitation-insensitive and cavitation-sensitive adhesive joints can be made (see Section 7.4.1), which is crucial for material modelling and limit state analysis. Besides the use of a linear elastic material model and the prediction of failure based on engineering stresses, a further disadvantage of the ETAG concept lies in the fact that the limit state analysis is carried out using a stress-based failure criterion. Again and as already discussed in Section 6.1, it is questionable to calculate hyperelastic adhesive joints by stresses and not by strains or stretches, since stress-based failure criteria are

strongly dependent on the chosen hyperelastic material model and the material parameter determined, which may lead to incorrect results up to an overestimation of the load bearing capacity (see Section 6.3.5). It should be mentioned, however, that this disadvantage is particularly noticeable when silicone adhesive joints are dimensioned using finite element calculations.

Nevertheless, to be in line with the concept of ETAG 002 (2012), design stresses are presented for TSSA under tensile and shear loading, which are based on engineering stresses. These design stresses are presented only for the reason to be used later for comparison with the failure stresses based on the stretch-based failure criterion (see Section 6.4.3) and thus to make the new approach directly assessable. Hence, the global ETAG safety concept and a more generalized one are subsequently applied on the previously presented stretch-based distortional-dilatational failure criterion of Section 6.4.3, which was calibrated on the experimental data of TSSA for tension, shear and biaxial loading. Thus, the aim of this study is to show that the concept and safety philosophy of ETAG 002 (2012) can also be applied and transferred to physically more advanced material models and novel stretch-based failure descriptions. In addition, it will be shown that it is also possible to significantly increase the load bearing capacity without reducing the safety level according to the ETAG regulations.

In the following, the design stresses for TSSA are first derived according to the ETAG concept, which are determined based on the 5 % quantile values of the individual failure stresses of the pancake tension tests. Thus, for the calculation of the quantile values related to the tensile and shear failure of the experimentally investigated TSSA, the report of Lieb and Mutter (2011) can be used, in which the single values of the engineering failure stresses are listed. All failure stresses have been determined on pancake tension tests in a standard climate. Hence, the results of the ten pancake tension tests with a diameter of  $d = 50$  mm under axial and shear loading are used to calculate the quantiles. This calculation includes the mean value  $X_{\text{mean},23^\circ\text{C}}$  of all failure stresses determined at  $23^\circ\text{C}$ , the standard deviation  $S$ , the number of tests performed and the eccentricity  $\tau_{\alpha\beta}$  of 5 % with a 75 % confidence. According to ETAG 002 (2012), the 5 % quantile is defined by

$$R_{u,5} = X_{\text{mean},23^\circ\text{C}} - \tau_{\alpha\beta} S. \quad (7.19)$$

From this, the quantile value for the engineering stress in axial direction is calculated by  $R_{u,5,\text{PC}} = 3.71$  MPa, whereas the quantile value for shear reads  $R_{u,5,\text{SPC}} = 5.88$  MPa. The quantiles and their subsequent conversion into design values can be obtained by dividing them by a global safety factor  $\gamma_{\text{tot}}$ . As already mentioned, ETAG 002 (2012) proposes a  $\gamma_{\text{tot}}$  of six to compensate for the model assumptions made.

**Table 7.5** Failure quantile values for TSSA determined on axially and shear loaded pancake tests with  $d = 50 \text{ mm}$  ( $A \approx 1924 \text{ mm}^2$ ) and their subsequent conversion into design values

Experiment	$R_{u,5}$	$\sigma_{\text{des,ETAG}} = R_{u,5}/6$	$\sigma_{\text{des,DOW}}$
Pancake Tension Test	7285 N	1217 N	2611 N
$\sigma = F/A$	3.71 MPa	0.62 MPa	1.33 MPa
Shear Pancake Test	11545 N	1924 N	2611 N
$\tau = F/A$	5.88 MPa	0.98 MPa	1.33 MPa

In contrast to the design strengths of TSSA accordingly to the ETAG concept, the manufacturer specifies a different design value for short-time dynamic loads, for example a wind load. A typical design strength for TSSA for dynamic loads reads  $\sigma_{\text{des}} = \tau_{\text{des}} = 1.33 \text{ MPa}$  (Kłosowski and Wolf, 2016:p.346). This design strength for TSSA was determined by defining the stress whitening effect occurring at approximately 2.0 MPa as failure. As a result, the design strength under short-term load was determined by dividing the engineering stress of 2.0 MPa by a global safety factor of 1.5, which corresponds to a global safety factor of approximately three with regard to the ultimate failure stress. An exact derivation of the global safety factor of  $\gamma_{\text{tot}} = 1.5$  is not given by Kłosowski and Wolf (2016). Nevertheless, this design strength, which also refers to engineering stresses and a linear elastic material behaviour, is used as a comparative value for the following studies. In Tab. 7.5 the corresponding design strengths are summarized. With the help of the mentioned design values, it is now possible to dimension flat, cylindrical silicone adhesive joints in accordance to ETAG 002 (2012). However, it should be noted that these design strengths lead to conservative solutions, which will be described and discussed in more detail later.

Since the presented design values lead to conservative results with regard to the dimensioning of a flat-bonded adhesive joint and its load bearing capacity due to outdated approaches and assumptions, in the following the ETAG safety concept with a global safety factor of  $\gamma_{\text{tot}} = 6$  is applied to the new developed stretch-based distortional-dilatational failure criterion, which was specifically developed for TSSA in Section 6.4.3. Furthermore, an additional global safety factor based on the experimental investigations carried out on TSSA will be presented to show that ETAG safety factor  $\gamma_{\text{tot}} = 6$  is to be estimated rather conservatively. This methodology provides some transparency for determining a new global safety factor based on experimental observations. Starting with the ETAG safety concept, it is applied or transferred to the distortional PBP failure criterion presented in Section 6.1 without being modified. Since the isochoric or distortional failure criterion is defined in three-dimensional stretch space and the necessary parameters have already been calculated based on experimentally determined failure stretches of TSSA (see Tab. 6.1), it is easy to transfer the criterion into the safety concept

according to ETAG 002 (2012) or in a more general safety concept. In order to transform the proposed stretch-based distortional failure criterion  $\Phi$  to a safety level using a global safety factor  $\gamma_{\text{tot}}$ , only the parameter  $\lambda_{\text{eq}}$  of the PBP criterion must be divided by the desired reduction factor. Keeping in mind that the global safety factor according to ETAG 002 (2012) is  $\gamma_{\text{tot}} = 6$ , for a general safety concept this factor has to be calculated based on experimental observations, expected loads and external influences. For this purpose, Eq. (7.18) can be used, in which a general global safety factor  $\gamma_M$  is calculated by multiplying individual safety factors. To do this, these parameters are first determined for pure distortional failure or assumed using meaningful working hypotheses.

The uncertainty between the stresses caused by static or dynamic loading of the material is given by the first reduction parameter  $\gamma_1$ . Since TSSA exhibits only a minor influence in the structural response due to dynamic loading, this parameter is assumed to be  $\gamma_1 = 1$ . The second reduction factor  $\gamma_2$  gives uncertainties between model (numerical or calculation model) and reality. In other words, it describes how well a model is capable of approximating the physical behaviour of a material under arbitrary loading. Since the proposed pseudo-elastic material model as well as the proposed stretch-based distortional-dilatational failure criterion are well suited to approximate the behaviour of TSSA, the reduction factor must be quite small. As the structural behaviour was well approximated, in the following  $\gamma_2$  is only referred to the quality of the failure formulation or failure prediction respectively. For this purpose, the predicted displacement to failure in the pancake tests is related to the 5 % quantile of the measured values, resulting in a reduction factor of  $\gamma_2 = 1.27$ . The third factor to reduce the design strength describes influences from temperature. Appendix B shows the experimental results of the pancake tension tests for 80°C according to ETAG 002 (2012). If the 5 % quantile values of the failure at 23°C are related to the values of 80°C, a reduction factor of  $\gamma_3 = 1.39$  is obtained. From this it becomes clear that the influence of temperature has a larger influence on the failure of TSSA than in comparison to  $\gamma_2$  describing model uncertainties. With regard to the parameters considering the influence of moisture, cyclic fatigue and long-term behaviour, no data are currently available, so that the parameters  $\gamma_4, \gamma_5, \gamma_6$  are given the value one, which initially serves only as a working hypothesis. This has to be confirmed by experiments or more realistic values have to be assumed based on theoretical conceptions. Finally, a safety factor must also be taken into account which records the statistical distribution of the action side globally. Since the so-called semi-probabilistic safety concept is applied in civil engineering (EN 1900, 2002), in which a distinction is made on the action side between permanent and live loads, in the following the value  $\gamma_{\text{ED}} = 1.5$  for the load increase factor is selected as it represents a limit case. This load increase factor is normally only used to increase the live loads, but it is also the upper limit value, so that in the

following this value is used from conservative considerations regarding the influence of the loads. As a result, the new global safety factor can now be calculated by

$$\begin{aligned}\gamma_{M,\text{dist}} &= \gamma_1 \cdot \gamma_2 \cdot \gamma_3 \cdot \gamma_4 \cdot \gamma_5 \cdot \gamma_6 \cdot \gamma_{\text{Ed}} \\ &= 1.0 \cdot 1.27 \cdot 1.39 \cdot 1.0 \cdot 1.0 \cdot 1.0 \cdot 1.5 \\ &= \underline{\underline{2.65}}.\end{aligned}\quad (7.20)$$

With the following investigations a new safety factor for the distortional failure of TSSA was calculated. However, since the stretch-based failure criterion proposed in Section 6.4.3 also examines cavitation failure, the same procedure has to be performed again to reduce to ultimate load or strength concerning cavitation failure. Similar to the above,  $\gamma_1 = 1$  is set, since the investigated material shows only minor viscous effects. The model reduction factor  $\gamma_2$  is set to one as the proposed model predicts cavitation failure very well. Influences from an external temperature on the start of cavitation could not be determined so far, so that the factor  $\gamma_3$  is also set to one. Furthermore, it should be noted that moisture has no influence on cavitation failure, since cavitation takes place especially in the centre of the sample and accordingly the outer edge of the sample prevents the influence of moisture on cavitation. Hence,  $\gamma_4$  is set to one. Looking at the cyclic fatigue behaviour in the pancake tension test, Ioannidou-Kati et al. (2018) confirmed that there is no influence on the occurrence of cavitation if one remains below an engineering stress of  $\sigma \leq 3.57$  MPa. Since the proposed dilatational criterion predicts a failure at an intrinsic engineering stress of  $\sigma = 3.41$  MPa, the reduction parameter  $\gamma_5$  is also set to one. Since no data on the long-term behaviour is available so far, the factor  $\gamma_6$  is also set to one, which is only a working hypothesis. The load increasing factor is also set to 1.5 according to the previous considerations, so that the global safety factor for cavitation failure results in

$$\begin{aligned}\gamma_{M,\text{dila}} &= \gamma_1 \cdot \gamma_2 \cdot \gamma_3 \cdot \gamma_4 \cdot \gamma_5 \cdot \gamma_6 \cdot \gamma_{\text{Ed}} \\ &= 1.0 \cdot 1.0 \cdot 1.0 \cdot 1.0 \cdot 1.0 \cdot 1.0 \cdot 1.5 \\ &= \underline{\underline{1.5}}.\end{aligned}\quad (7.21)$$

To summarize, the following design criteria result for distortional-dilatational failure according to different global safety factors:

$$\begin{aligned}\Phi_{\text{des,I}} &= \frac{\Phi}{\gamma_{M,\text{disto}}} = \frac{\Phi}{2.65} \\ \Phi_{\text{des,II}} &= \frac{\Phi}{\gamma_{\text{tot}}} = \frac{\Phi}{6} \\ \Phi_{\text{des,I,J}} &= J - 1 + \frac{J_{\text{cr}} - 1}{\gamma_{M,\text{dila}}} = J - 1 + \frac{J_{\text{cr}} - 1}{1.5}.\end{aligned}\quad (7.22)$$

**Table 7.6** Parameters for the isochoric stretch-based failure criteria for different safety levels

distortional PBP failure criterion	$\lambda_{\text{eq}}$	$\beta$	$\gamma$
$\Phi$	1.64	0.82	0.99
$\Phi_{u,5}$	1.31	0.82	0.99
$\Phi_{\text{des},I} = \Phi / \gamma_{M,\text{dist}}$	0.62	0.82	0.99
$\Phi_{\text{des},II} = \Phi / 6$	0.27	0.82	0.99

However, the equations shown are to be understood only schematically, since one does not divide the entire criterion but only the measure of equivalence of the criterion by the safety factor. A summary of the stretch-based distortional PBP failure criterion and the parameters depending on defined safety levels is summarized in Tab. 7.6.

In order to show what influence the integration of safety concepts has with regard to the distortional failure criterion, the original criterion  $\Phi$ , the criterion  $\Phi_{u,5}$  approximated to the 5 % quantile values, as well as the criterion transferred to the safety level according to the newly defined safety level ( $\Phi_{\text{des},I}$ ) and the safety level in accordance to ETAG 002 (2012) ( $\Phi_{\text{des},II}$ ) are shown in Fig. 7.6 a in the  $\pi$ -plane. Comparing the original criterion with the criterion based on the 5 % quantile values, the geometric shape has changed and the criterion is less inflated. This is explained by the fact that the calculation of the quantile values also includes the statistical distribution of the measurement data, whereby the resulting quantile values are not shifted proportionally, but are shifted quasi weighted along the radius in the  $\pi$ -plane. Regarding at the geometrical shapes when the newly defined safety concept and the concept in accordance to ETAG is applied, this conversion only shortens the radius  $\theta$  in the  $\pi$ -plane, whereas the geometric form remains untouched with respect to the original failure surface of  $\Phi$ . Summarizing, it could simply be shown that any failure criterion can easily be combined with a global safety concept by dividing the equivalent measure, be it stress, strain or stretch based, by a global safety factor.

To make a direct comparison of the classical ETAG concept with the novel stretch-based failure criterion for the same safety level, Fig. 7.6 b shows the force-displacement behaviour of the pancake tension test with  $d = 50$  mm as well as the corresponding failure loads, which are calculated by evaluating the quantiles and the design measures for both approaches. As can be seen clearly, the failure loads according to the ETAG concept are at an absolutely low level. The design strength under consideration of the manufacturer's specifications is approximately 200 % above ETAG's level, so that it can already be stated here that according to the manufacturer's specifications more trust is placed in the silicone adhesive. This quickly shows that the ETAG concept is a very conservative approach, which means that the potential of the silicone adhesive cannot be fully exploited. In contrast,

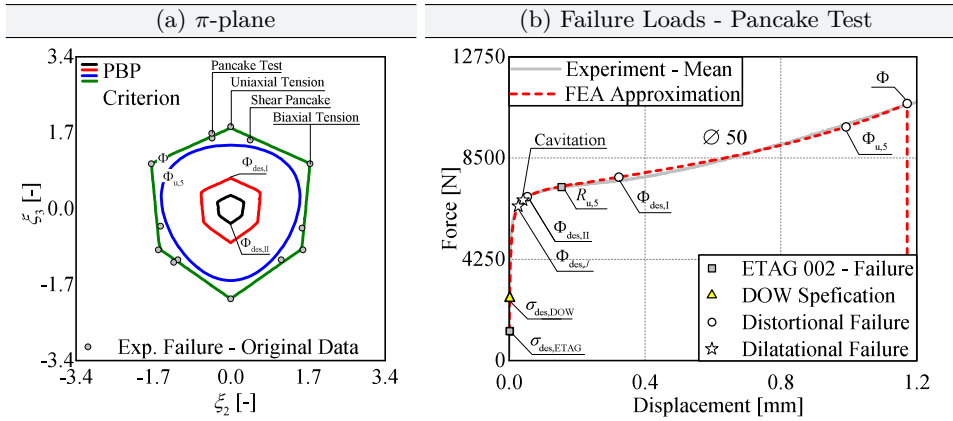


**Figure 7.6** (a) Representation of the  $\pi$ -plane of the PBP criterion with approximation of the experimental raw data, the 5 % quantile and the design values and (b) illustration of the calculated failure points based on the ETAG concept as well as the new stretch-based distortional failure criterion applied to the pancake tension test with a diameter of  $d = 50$  mm

the failure loads for the new approach are significantly higher for the same safety level, which is justified by the fact that, on the one hand, the structural behaviour of the bond is reproduced very well through the use of the pseudo-elastic cavitation model and, on the other hand, that the stretch-based failure criterion presented reproduces the failure of TSSA very well in any deformation scenario. If the global safety factor of  $\gamma_{tot}$  is applied to the pure distortional failure criterion, this results in a load increase of more than 550 % compared to the ETAG approach. This can be further increased if the safety factor of  $\gamma_{M,disto} = 2.65$  is applied, whereby the load can even be increased by more than 600 % by purely evaluating the distortional failure. Nevertheless, it is not enough to evaluate distortional failure alone, since cavitation failure can also occur. If one evaluates  $\Phi_{des,J}$ , there is an increase in load compared to the ETAG concept of approximately 520 %, so that it becomes clear that the cavitation proof becomes decisive for the flat adhesive joint of a point fixing.

In order to clearly demonstrate that it is possible to significantly increase the load bearing capacity with the new approach without reducing the safety level in accordance with the specifications of ETAG 002 (2012), a bar chart with the failure stresses determined for both concepts is shown in Fig 7.7. The classical design failure stresses were determined using engineering stresses in accordance with the ETAG concept, so that the failure loads were related to the initial cross-section. Hence, these design stresses were determined based on simple hand calculations. On the other hand, the ETAG concept was also applied to the stretch-based distortional failure criterion proposed in Section 6.1 to show its potential as a result

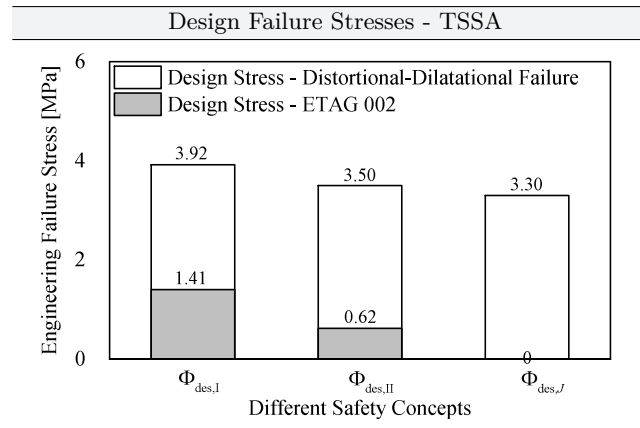


**Figure 7.7** Presentation of the engineering design failure stresses for TSSA using the ETAG concept and the calculation of the failure stresses over engineering stresses as well as applications of the novel stretch-based approach to prediction of failure.

of a more precise and physically motivated description of the failure of TSSA. Thus, the design stress values for the second approach are determined based on three-dimensional FE calculations.

Looking at the absolute values of the design stresses, the calculated design strength according to ETAG 002 (2012) is significantly lower than the calculated values on the basis of the coupled distortional-dilatational failure criterion under the condition of the same safety level. It is interesting to note that for flat-bonded adhesive joints the proof of cavitation after the evaluation of the distortional-dilatation failure criterion is decisive. ETAG 002 (2012) generally does not offer such a proof, as these adhesive joints are not part of the guideline. As a result of the use of more advanced material models and failure descriptions, considerable load reserves can be gained at the same safety level as with the classic ETAG concept. In summary, an increase in load capacity of more than 520 % could be determined, which offers structural engineers significantly more possibilities for the safe dimensioning and design of flat-bonded silicone adhesive joints. However, this load increase can only be used if three-dimensional FE calculations of the bonded joint are carried out, whereas with the ETAG approach the bonded joint can be calculated manually.

## 7.6 Conclusions

Recapitulating, the classical ETAG concept for the determination of design strengths for the dimensioning of flat bonded silicone adhesive joints in the façade area was presented in this section. In addition, the global safety concept according to ETAG

002 (2012) was applied to the new stretch-based distortional-dilatational failure criterion in order to determine the load bearing capacity of the adhesive joint for the pancake test, whereby the safety level remained the same for both concepts for reasons of comparability. In addition, two further global safety factors for distortional and dilatational failure were derived based on experimental observations, which are significantly below the value according to ETAG 002 (2012). As a result, the application of the novel failure description over stretches and the use of improved material models (here the pseudo-elastic cavitation model) has dramatically increased the load bearing capacity compared to result accordingly to ETAG 002 (2012) without changing the global safety level. This has clearly shown that it is worthwhile to use such models and failure descriptions to design adhesive joints, as on the one hand the load bearing capacity of the silicone is precisely assessed and exploited and on the other hand new possibilities in construction and design are made possible for structural engineers. An alleged disadvantage in the concept and the utilisation of the significantly increased load bearing capacity is that silicone adhesive joints have to be designed using complex three-dimensional FE calculations, which may not always be possible. Nevertheless, this concept can also be applied to other silicone adhesives in order to increase the ultimate load here as well. Finally, however, it should be noted that the load bearing capacity decreases with increasing adhesive thickness, since the influence of triaxiality is no longer so dominant as in the case of cavitation-sensitive adhesive joint systems.



# 8 Conclusion and Outlook

The present work has been dedicated to the experimental and numerical characterization of silicone adhesives in façade construction (see Chap. 4–5). On the basis of fundamental experimental investigations in which effects such as whitening, cavitation and even healing occurred, mechanical models have been presented and validated for their constitutive description. Furthermore, models for the description of failure in three-dimensional stretch-space have been presented (Chap. 6), which have been transformed into a global safety concept in Chap. 7 dedicated to structural engineers.

## 8.1 Conclusions

In the following a conclusion of the work is described separately according to main chapters. The introduction and the fundamental chapters on mechanics and hyperelasticity are not addressed here, so that **Chap. 4** is the starting point.

### **Chap. 4 Experiments on Transparent Structural Silicone Adhesive**

In the experimental chapter, essential experiments have been presented separately for homogeneous and inhomogeneous stress states, which are necessary for the material characterization of TSSA. The description was presented in the same way for all experiments in which the experiment, the test set-up, the structural response and the failure loads and strains were summarized. This type of representation is necessary because it is the basis for the mechanical description of basic effects, such as the cavitation effect. In order to investigate the cavitation effect experimentally, a special experimental set-up was developed in which the whitening in the pancake tension test could be assigned to the void growth at the nano-level. Furthermore, miniature tensile tests were carried out in which a near-surface whitening occurred which could not be related to the cavitation effect. However, it could be shown experimentally by cyclic uniaxial tensile tests that the near-surface whitening is irreversible damage due to the Mullins effect. In contrast, it has been shown that the dense, cloud-like whitening in the bulk material of the pancake tension test samples represents reversible void growth, which has never been correlated before in literature. The reversible process of cavitation was investigated

by cyclic pancake tension tension tests, which showed an effective stress softening due to cavitation at virgin loading. A typical softening path has occurred during unloading, which can be attributed to the classical Mullins effect. However, it was interesting to observe that pronounced healing in the material occurred during all reloading paths, which has not yet been observed to this extent in the literature. Another interesting observation could be made by the analysis of the nano-structure of TSSA, in which a finite porosity in the percentage range could be determined based on TEM images and subsequent image evaluation. Until now, it has always been assumed that rubbers and rubber-like materials have porosities of almost zero, as they are generally incompressible. However, this could not be confirmed.

In conclusion, it can be said that the structural behaviour and failure of TSSA was determined for homogeneous and inhomogeneous loading scenarios with the aid of experimental characterization. Based on the provided results, further material models or further concepts can be used in the future to describe the failure.

## **Chap. 5 Development of Constitutive Models of Poro-Hyperelastic Materials**

In the chapter on the constitutive description of TSSA, material models have been developed separately for isochoric and volumetric deformations, analysed and validated on the basis of the experimental results and compared with classical models in order to show their necessity. Besides the development of a very adaptive isochoric hyperelastic Helmholtz free energy function, which is excellently suited for the approximation of silicone adhesives, a volumetric Helmholtz free energy function has been developed on the basis of the Nelder function, which is able to effectively represent isotropic void growth of poro-hyperelastic materials. In order to obtain physically plausible material responses for any deformation or stress states, the internally developed volumetric Helmholtz free energy function was transferred into the context of pseudo-elasticity. This showed that even in the case of isochoric deformations, physical results could be obtained. Since the approach of pseudo-elasticity can be extended to describe other effects, the isochoric and volumetric models were additionally equipped with an extension to describe the Mullins effect and purely volumetric healing. In order to show the quality of the presented novel material models, the uniaxial, biaxial tension and pancake tension test were simulated, whereby the results showed a very good approximation of the experiments. It has even been possible to simulate the cavitation effect for three pancake tension tests with dif-

ferent diameters, which has not yet been demonstrated to this extent in literature. Furthermore, it was possible to verify the stress softening due to the Mullins effect as well as healing by the extensions of the pseudo-elastic cavitation model. Therefore, the cyclic uniaxial tensile tests and the cyclic pancake tension tests were simulated for validation. During the numerical calculation of the cyclic pancake tension tests, numerical problems occurred with the explicit representation of the healing effect, so that within this thesis the healing effect could only be shown numerically based on a so-called one-element test. In contrast, the isochoric Mullins effect could be simulated without problems using three-dimensional FE calculations of the dumbbell test sample.

In conclusion, the newly developed material models allowed the structural behaviour of a structural silicone with finite porosity to be approximated for the first time, taking into account the cavitation effect. In addition, a significant improvement in the approximation of the isochoric material behaviour of silicones compared to classical hyperelastic material formulations was shown. This makes it possible to calculate silicone adhesive joints more accurately, not only providing a more accurate verification format but also enabling new designs of adhesive joints in façade construction. This allows the creation of new construction forms and connection types.

## **Chap. 6 Development of Failure Criteria for Poro-Hyperelastic Materials**

Based on the experimental results, general failure criteria for a transparent silicone adhesive were specifically developed. On the one hand, the so-called stretch-based PBP criterion (distortional failure criterion) succeeded in approximating the measured isochoric failure of TSSA very well. On the other hand, it was necessary to find a criterion that could describe the occurrence of cavitation under any triaxial stress state. For this purpose, classical stress-based cavitation criteria were compared with a specially developed criterion in order to proof the quality of the internally developed failure formulation. It turned out that the new approach includes classical cavitation criteria, i.e. it can predict cavitation under the assumption of a porosity of  $f_0 = 0\%$ . The stress-based cavitation criterion was extended by the porosity  $f_0$  in order to be able to represent cavitation at finite porosity. This allows to approximate numerically determined cavitation failure data points in three-dimensional stress space for different finite porosities. Furthermore, a stretch-based cavitation criterion was presented which shows a very simple representation, is extremely efficient in the determination of only one parameter, and

approximates cavitation at finite porosity very well. In addition, the presentation of the stretch-based cavitation criterion, which is also denoted as dilatation failure, offers the advantage that it can be coupled with the stretch-based distortional failure criterion. For validation, the coupled stretch-based distortional-dilatational failure criterion was applied to predict failure in the uniaxial and biaxial tensile tests as well as three pancake tension tension tests with different diameters. The prognosis of the cavitation failure and the description of the final distortional failure correspond to the experimentally determined failure points. As a result, the failure criteria developed are ideally suited to calculate the failure of TSSA under any load.

### **Chap. 7 Design Methods for Structural Silicone Adhesives**

In this chapter, the gained knowledge was summarized schematically. Here, an attempt was made to present the essential findings in a simple and understandable way in order to make the developed mechanical models accessible for engineering offices, façade planners and architects. The course provides assistance with regard to necessary experiments for the characterization of silicone adhesives. Furthermore, tips are given regarding the material parameter identification for hyperelastic material models. In addition, the applicability of the developed hyperelastic material models was presented, including the extension to model cavitation, the effect and healing of Mullins, differentiating between cavitation-insensitive and cavitation-sensitive adhesive joints. Furthermore, simple engineering tools have been presented to decide whether a cavitation-sensitive adhesive joint is present and which material models and failure hypotheses can be used for the calculation. Finally, a design concept for flat-bonded adhesive joints has been presented, which showed that the load bearing capacity could be increased to more than 500 % compared to conventional design methods, only due to the application of improved material models and failure formulations.

## **8.2 Future Research**

Since structural bonding is still a rather new field of research in civil engineering compared to concrete or steel related research, but new applications are constantly being developed with regard to load-bearing adhesive joints, such as load-bearing paper-glass laminated beams (Lübke et al., 2018), cast threaded rods in timber constructions Schober et al. (2012); Schober et al. (2013); Schober et al. (2014); Drass et al. (2014) and laminated joints in structural glass construction (Santar-

siero, 2015; Bedon and Santarsiero, 2018), it is essential to have a basic understanding of the adhesive to be used. In the context of this thesis, however, silicone adhesives have been experimentally investigated and mechanically characterized under quasi-static boundary conditions. Since polymers in general have a strong dependency on temperature, rate of loading and humidity, it is important for future research to capture these effects mechanically correctly and to transfer them into design concepts. Furthermore, there is a considerable need for research in the field of cyclic fatigue of silicone-bonded components, since the question of the reduction of a characteristic strength as a result of cyclic loading has not yet been clarified. Furthermore, open questions arise regarding the coupling between cyclic fatigue and external influences such as temperature and humidity, to which so far only general consideration has been given according to the ETAG concept, but a valid statement regarding the coupling of the individual effects cannot be made. Further questions will deal with the topics of numerical calculation of adhesive joints using spring models vs. three-dimensional volume elements, since a fast calculation progress is essential for large construction projects, but this is extremely slowed down by complex FE simulations. Finally, it should be noted that the description of the failure of polymers is still a current part of research, especially with regard to strength properties and fracture toughness as a function of humidity and temperature influence as well as on aged or cyclically fatigued samples. Accordingly, the research and development work for adhesive joints in the building industry, and especially in façade constructions, is far from finished, so that this work could hopefully make a small contribution to extending the body of knowledge of silicone adhesives, but there are still enough topics that have not been considered and will hopefully find comments in future work.

# Bibliography

## Own Publications

- Drass, M., V. A. Kolupaev, P. L. Rosendahl, J. Schneider, and W. Becker (2018a). “Generalized cavitation criterion for poro-hyperelastic materials”. In: *Forschungskolloquium 2018 Grasellenbach*. Ed. by J. Schneider and N. Kiziltoprak. Wiesbaden: Springer Fachmedien Wiesbaden, pp. 20–23.
- Drass, M., J. Schneider, and S. Kolling (2018b). “Novel volumetric Helmholtz free energy function accounting for isotropic cavitation at finite strains”. In: *Materials & Design* 138, pp. 71–89.
- Drass, M., N. Bartels, J. Schneider, and D. Klein (2019a). “Pseudo-Elastic Cavitation Model - Part II: Extension to Cyclic Behavior of Transparent Silicone Adhesives”. In: *Glass Structures & Engineering*.
- Drass, M., P. A. Du Bois, J. Schneider, and S. Kolling (2019b). “Pseudo-Elastic Cavitation Model - Part I: Finite Element Analyses on Thin Silicone Adhesives in Façades”. In: *Glass Structures & Engineering*.
- Drass, M., V. A. Kolupaev, J. Schneider, and S. Kolling (2018c). “On cavitation in transparent structural silicone adhesive: TSSA”. In: *Glass Structures & Engineering* 3.2, pp. 237–256.
- Drass, M., J. Muth, J. Schneider, and C. Louter (2019c). “Stress Whitening Effects in Transparent Structural Silicone Adhesives”. In: *Glass Structures & Engineering*.
- Drass, M., J. Schneider, and U. Knaack (2018d). “New Technologies and the Future of Glass in Building Constructions”. In: ed. by U. Knaack and B. Horn. Messe Düsseldorf GmbH. Chap. Visions - Glass Technology Live: The Hub @ Glasstec 2018, pp. 10–23.
- Drass, M., J. Schneider, and S. Kolling (2017a). “Damage effects of adhesives in modern glass façades: a micro-mechanically motivated volumetric damage model for poro-hyperelastic materials”. In: *International Journal of Mechanics and Materials in Design*.
- Drass, M., K.-U. Schober, and M. Kuechler (2014). “Advancement of glued-in rods using polymer concrete as composite material”. In: *Proceedings of the 13th World Conference on Timber Engineering (WCTE 2014)*.

- Drass, M., M. Schuster, and J. Schneider (2017b). "Comparison of unconventional testing methods for mechanical characterization of polymeric materials in modern glass structures". In: *IABSE Symposium Report*. Vol. 109. 27. International Association for Bridge and Structural Engineering, pp. 2370–2377.
- Drass, M., G. Schwind, J. Schneider, and S. Kolling (2018e). "Adhesive connections in glass structures—part I: experiments and analytics on thin structural silicone". In: *Glass Structures & Engineering* 3.1, pp. 39–54.
- Drass, M., G. Schwind, J. Schneider, and S. Kolling (2018f). "Adhesive connections in glass structures—part II: material parameter identification on thin structural silicone". In: *Glass Structures & Engineering* 3.1, pp. 55–74.
- Gade, J., R. Kemmler, M. Drass, and J. Schneider (2018). "Enhancement of a meso-scale material model for nonlinear elastic finite element computations of plain-woven fabric membrane structures". In: *Engineering Structures* 177, pp. 668–681.
- Kelleter, C., M. Drass, W. Haase, and J. Schneider (2016). "Aspekte experimenteller und numerischer Untersuchungen von Klemmhalterungen im Glasbau". In: *Stahlbau* 85.1, pp. 183–195.
- Lübke, J., M. Wetzlaufer, N. Kiziltoprak, M. Drass, J. Schneider, and U. Knaack (2018). "Honeycomb-Paperboard Glass Composite Beams". In: *Engineered Transparency* 2.5-6, pp. 57–69.
- Rosendahl, P. L., M. Drass, J. Felger, J. Schneider, and W. Becker (2019). "Equivalent strain failure criterion for multiaxially loaded incompressible hyperelastic elastomers". In: *International Journal of Solids and Structures* 166, pp. 32–46.
- Rosendahl, P. L., M. Drass, J. Schneider, and W. Becker (2018). "Crack nucleation in hyperelastic adhesive bonds". In: *Engineered Transparency* 2.5-6, pp. 409–425.
- Schober, K.-U., W. Becker, and M. Drass (2012). "Advanced interface interaction in timber engineering joints with dowel-type fasteners embedded in high-performance ceramic fillers". In: *Proceedings of the 12th World Conference on Timber Engineering (WCTE 2012)*.
- Schober, K.-U., W. Becker, M. Drass, and J. Weber (2014). "High-performance timber composite joints for spatial round wood truss structures". In: *Proceedings of the 13th World Conference on Timber Engineering (WCTE 2014)*.
- Schober, K.-U., M. Drass, and W. Becker (2013). "Adhesive strength of timber joints with unconventional glued-in steel rods". In: *Proceedings of Wood Adhesives*.
- Silvestru, V. A., M. Drass, O. Englhardt, and J. Schneider (2018a). "Performance of a structural acrylic adhesive for linear glass-metal connections under shear and tensile loading". In: *International Journal of Adhesion and Adhesives* 85, pp. 322–336.

## Standards

- ASTM C1401 (2002). *Standard Guide for Structural Sealant Glazing*.
- ASTM D638 - 02a (2003). *Tensile testing for Thermoplastics*.
- ASTM D732 - 10 (2010). *Standard Test Method for Shear Strength of Plastics by Punch Tool*.
- BS903-A14 (1992). *Physical testing of rubber. Method for determination of modulus in shear or adhesion to rigid plates. Quadruple shear method*.
- DIBt Concept (2012). *Vorschlag: Zeitstandnachweis für geklebte lastabtragende Verbindungen*.
- DIN EN ISO 291 (2008). *Plastics - Standard atmospheres for conditioning and testing*.
- EN 1900 (2002). *Eurocode - Basis of structural design*.
- ETAG 002 (2012). *Guideline for European Technical Approval for Structural Sealant Glazing Kits*.
- ISO 1827 (2011). *Rubber, vulcanized or thermoplastic – Determination of shear modulus and adhesion to rigid plates – Quadruple-shear methods*.
- ISO 37 (2011). *Rubber, vulcanized or thermoplastic — Determination of tensile stress-strain properties*.
- ISO 7743 (2011). *Rubber, vulcanized or thermoplastic – Determination of compression stress-strain properties*.
- Lieb, K. and M. Mutter (2011). *Testing of a Structural Glazing-Bonding*.

## Bibliography

- Alexander, H. (1968). "A constitutive relation for rubber-like materials". In: *International Journal of Engineering Science* 6.9, pp. 549–563.
- Altenbach, H. and A. Zolochevsky (1995). "Erweiterte Deformationsmodelle und Versagenskriterien der Werkstoffmechanik. Stuttgart, Deutscher Verlag für Grundstoffsindustrie". In: *ZAMM - Journal of Applied Mathematics and Mechanics / Zeitschrift für Angewandte Mathematik und Mechanik* 77.7, pp. 502–502.
- Altenbach, H. (2015). *Kontinuumsmechanik: Einführung in die materialunabhängigen und materialabhängigen Gleichungen*. Springer-Verlag.
- Ansarifar, A. and B. Y. Lim (2006). "Reinforcement of silicone rubber with precipitated amorphous white silica nanofiller-effect of silica aggregates on the rubber properties". In: *Journal of Rubber Research* 9.3, pp. 140–158.
- Arruda, E. M. and M. C. Boyce (1993). "A three-dimensional constitutive model for the large stretch behavior of rubber elastic materials". In: *Journal of the Mechanics and Physics of Solids* 41.2, pp. 389–412.

- Avril, S. et al. (2008). "Overview of identification methods of mechanical parameters based on full-field measurements". In: *Experimental Mechanics* 48.4, pp. 381–402.
- Ayatollahi, M., M. Heydari-Meybodi, M. Dehghany, and F. Berto (2016). "A New Criterion for Rupture Assessment of Rubber-Like Materials under Mode-I Crack Loading: The Effective Stretch Criterion". In: *Advanced Engineering Materials* 18.8, pp. 1364–1370.
- Baaser, H., C. Hopmann, and A. Schobel (2013). "Reformulation of strain invariants at incompressibility". In: *Archive of Applied Mechanics* 83.2, pp. 273–280.
- Baker, M. and J. L. Erickson (1954). "Inequalities restricting the form of the stress-deformation relations for isotropic elastic solids and Reiner-Rivlin fluids". In: *Journal of the Washington Academy of Sciences* 44.2, pp. 33–35.
- Bakshi, S., A. Kulshreshtha, B. Singh, and J. Anand (1988). "Stress-whitening of polypropylene block copolymer in impact tests and its measurement". In: *Polymer Testing* 8.3, pp. 191–199.
- Ball, J. M. (1982). "Discontinuous equilibrium solutions and cavitation in nonlinear elasticity". In: *Philosophical Transactions of the Royal Society of London A: Mathematical, Physical and Engineering Sciences* 306.1496, pp. 557–611.
- Bartels, N. (2018). "Experimental and numerical investigation considering cyclic, volumetric damage of structural silicones". Master thesis. Technische Universität Darmstadt.
- Bascom, W. D. and D. L. Hunston (1989). "Fracture of Elastomer-Modified Epoxy Polymers". In: *Rubber-Toughened Plastics*. Ed. by C. K. Riew. American Chemical Society. Chap. 6, pp. 135–172.
- Beatty, M. F. (2008). "On Constitutive Models for Limited Elastic, Molecular Based Materials". In: *Mathematics and Mechanics of Solids* 13.5, pp. 375–387.
- Becker, F. (2009). "Entwicklung einer Beschreibungsmethodik für das mechanische Verhalten unverstärkter Thermoplaste bei hohen Deformationsgeschwindigkeiten". Doctoral Thesis. Martin-Luther-Universität Halle-Wittenberg.
- Beda, T. (2007). "Modeling hyperelastic behavior of rubber: A novel invariant-based and a review of constitutive models". In: *Journal of Polymer Science Part B: Polymer Physics* 45.13, pp. 1713–1732.
- Bedon, C. and M. Santarsiero (2018). "Transparency in Structural Glass Systems Via Mechanical, Adhesive, and Laminated Connections - Existing Research and Developments". In: *Advanced Engineering Materials* 20.5, p. 1700815.
- Behnke, R. (2015). "Thermo-mechanical Modeling and Durability Analysis of Elastomer Components under Dynamic Loading". Doctoral thesis. Technische Universität Dresden.

- Belytschko, T., W. K. Liu, B. Moran, and K. Elkhodary (2013). *Nonlinear finite elements for continua and structures*. John wiley & sons.
- Benveniste, Y. (1987). "A new approach to the application of Mori-Tanaka's theory in composite materials". In: *Mechanics of Materials* 6.2, pp. 147–157.
- Bigoni, D. and A. Piccolroaz (2004). "Yield criteria for quasibrittle and frictional materials". In: *International Journal of Solids and Structures* 41.11, pp. 2855–2878.
- Bischoff, J. E., E. M. Arruda, and K. Grosh (2001). "A New Constitutive Model for the Compressibility of Elastomers at Finite Deformations". In: *Rubber Chemistry and Technology* 74.4, pp. 541–559.
- Bishop, J. F. W. and R. Hill (1951). "XLVI. A theory of the plastic distortion of a polycrystalline aggregate under combined stresses". In: *The London, Edinburgh, and Dublin Philosophical Magazine and Journal of Science* 42.327, pp. 414–427.
- Blanchard, A. F. and D. Parkinson (1952). "Breakage of Carbon-Rubber Networks by Applied Stress". In: *Industrial & Engineering Chemistry* 44.4, pp. 799–812.
- Bonet, J. and R. Wood (2008). *Nonlinear Continuum Mechanics for Finite Element Method*.
- Bonet, J., A. J. Gil, and R. Ortigosa (2015). "A computational framework for polyconvex large strain elasticity". In: *Computer Methods in Applied Mechanics and Engineering* 283, pp. 1061–1094.
- Bonet, J., A. J. Gil, and R. Ortigosa (2016). "On a tensor cross product based formulation of large strain solid mechanics". In: *International Journal of Solids and Structures* 84, pp. 49–63.
- Bouasse, H. and Z. Carrière (1903). "Sur les courbes de traction du caoutchouc vulcanisé". fr. In: *Annales de la Faculté des sciences de Toulouse : Mathématiques* 2e série, 5.3, pp. 257–283.
- Boyce, M. C., K. Kear, S. Socrate, and K. Shaw (2001). "Deformation of thermoplastic vulcanizates". In: *Journal of the Mechanics and Physics of Solids* 49.5, pp. 1073–1098.
- Buddenberg, S., P. Hof, and M. Oechsner (2016). "Climate loads in insulating glass units: comparison of theory and experimental results". In: *Glass Structures & Engineering* 1.1, pp. 301–313.
- Budiansky, B. (1965). "On the elastic moduli of some heterogeneous materials". In: *Journal of the Mechanics and Physics of Solids* 13.4, pp. 223–227.
- Bueche, F. (1960). "Molecular basis for the mullins effect". In: *Journal of Applied Polymer Science* 4.10, pp. 107–114.
- Busse, W. F. (1938). "Physics of Rubber as Related to the Automobile". In: *Journal of Applied Physics* 9.7, pp. 438–451.
- Cantournet, S., K. Layouni, L. Laiarinandrasana, and R. Piques (2014). "Experimental investigation and modelling of compressibility induced by damage in

- carbon black-reinforced natural rubber". In: *Comptes Rendus Mécanique* 342.5. Frontiers of micro and nanomechanics of materials: Soft or amorphous matter, surface effects, pp. 299–310.
- Chaves, E. W. (2013). *Notes on continuum mechanics*. Springer Science & Business Media.
- Chen, W.-F. and D.-J. Han (2007). *Plasticity for structural engineers*. J. Ross Publishing.
- Chenal, J.-M., C. Gauthier, L. Chazeau, L. Guy, and Y. Bomal (2007). "Parameters governing strain induced crystallization in filled natural rubber". In: *Polymer* 48.23, pp. 6893–6901.
- Cristiano, A., A. Marcellan, R. Long, C.-Y. Hui, J. Stolk, and C. Creton (2010). "An experimental investigation of fracture by cavitation of model elastomeric networks". In: *Journal of Polymer Science Part B: Polymer Physics* 48.13, pp. 1409–1422.
- Crocker, L. and B. Duncan (2001). *Measurement Methods for Obtaining Volumetric Coefficients for Hyperelastic Modelling of Flexible Adhesives*. National Physical Laboratory. Great Britain, Centre for Materials Measurement and Technology.
- Dal, H., B. Cansiz, and C. Miehe (2018). "A three-scale compressible micro-sphere model for hyperelastic materials". In: *International Journal for Numerical Methods in Engineering* 0.ja.
- D'Ambrosio, P., D. D. Tommasi, D. Ferri, and G. Puglisi (2008). "A phenomenological model for healing and hysteresis in rubber-like materials". In: *International Journal of Engineering Science* 46.4, pp. 293–305.
- Danielsson, M., D. Parks, and M. Boyce (2004). "Constitutive modeling of porous hyperelastic materials". In: *Mechanics of Materials* 36.4, pp. 347–358.
- Danielsson, M., D. M. Parks, and M. C. Boyce (2007). "Micromechanics, macromechanics and constitutive modeling of the elasto-viscoplastic deformation of rubber-toughened glassy polymers". In: *Journal of the Mechanics and Physics of Solids* 55.3, pp. 533–561.
- Dasari, A., J. Rohrmann, and R. D. K. Misra (2003). "Surface microstructural modification and fracture behavior of tensile deformed polypropylene with different percentage crystallinity". In: *Materials Science and Engineering: A* 360.1, pp. 237–248.
- de Boer, R. (1982). *Vektor- und Tensorrechnung für Ingenieure*. Hochschultext. Berlin: Springer-Verlag Berlin Heidelberg.
- Deam, R. T. and S. F. Edwards (1976). "The theory of rubber elasticity". In: *Philosophical Transactions of the Royal Society of London A: Mathematical, Physical and Engineering Sciences* 280.1296, pp. 317–353.

- Descamps, P., V. Hayez, and M. Chabih (2017). "Next generation calculation method for structural silicone joint dimensioning". In: *Glass Structures & Engineering* 2.2, pp. 169–182.
- Diani, J., M. Brieu, and P. Gilormini (2006). "Observation and modeling of the anisotropic visco-hyperelastic behavior of a rubberlike material". In: *International Journal of Solids and Structures* 43.10, pp. 3044–3056.
- Diani, J., B. Fayolle, and P. Gilormini (2009). "A review on the Mullins effect". In: *European Polymer Journal* 45.3, pp. 601–612.
- Dias, V., C. Odenbreit, O. Hechler, F. Scholzen, and T. B. Zineb (2014). "Development of a constitutive hyperelastic material law for numerical simulations of adhesive steel–glass connections using structural silicone". In: *International Journal of Adhesion and Adhesives* 48, pp. 194–209.
- Dispersyn, J., S. Hertelé, W. D. Waele, and J. Belis (2017). "Assessment of hyperelastic material models for the application of adhesive point-fixings between glass and metal". In: *International Journal of Adhesion and Adhesives* 77, pp. 102–117.
- Doi, M. and S. F. Edwards (1988). *The theory of polymer dynamics*. Vol. 73. oxford university press.
- Dorfmann, A. and R. Ogden (2003). "A pseudo-elastic model for loading, partial unloading and reloading of particle-reinforced rubber". In: *International Journal of Solids and Structures* 40.11, pp. 2699–2714.
- Dorfmann, A. and R. Ogden (2004). "A constitutive model for the Mullins effect with permanent set in particle-reinforced rubber". In: *International Journal of Solids and Structures* 41.7, pp. 1855–1878.
- Drucker, D. C. (1957). *A definition of stable inelastic material*. Tech. rep. Brown University Providence.
- Edwards, S. F. and T. A. Vilgis (1988). "The tube model theory of rubber elasticity". In: *Reports on Progress in Physics* 51.2, p. 243.
- Ehlers, W. and G. Eipper (1998). "The simple tension problem at large volumetric strains computed from finite hyperelastic material laws". In: *Acta Mechanica* 130.1, pp. 17–27.
- Ehret, A. E. (2015). "On a molecular statistical basis for Ogden's model of rubber elasticity". In: *Journal of the Mechanics and Physics of Solids* 78, pp. 249–268.
- Eshelby, J. D. (1957). "The determination of the elastic field of an ellipsoidal inclusion, and related problems". In: *Proceedings of the Royal Society of London A: Mathematical, Physical and Engineering Sciences* 241.1226, pp. 376–396.
- Euchler, E., K. Schneider, G. Heinrich, S. Wiessner, R. Bernhardt, S. V. Roth, and T. Tada (2018). "Failure of rubber vulcanizates - An exploration of the failure behavior of rubber vulcanizates subjected to constraint tensile strain via x-ray experiments". In: *Tire Technology International Annual Review*, pp. 100–103.

- Evesque, P. and F. Adjémian (2002). "Stress fluctuations and macroscopic stick-slip in granular materials". In: *The European Physical Journal E* 9.3, pp. 253–259.
- Fahlbusch, N.-C., V. A. Kolupaev, and W. Becker (2016). "Generalized Limit Surfaces—With an Example of Hard Foams". In: *Advanced Methods of Continuum Mechanics for Materials and Structures*. Springer, pp. 337–365.
- Felger, J., N. Stein, and W. Becker (2017). "Mixed-mode fracture in open-hole composite plates of finite-width: An asymptotic coupled stress and energy approach". In: *International Journal of Solids and Structures* 122-123, pp. 14–24.
- Felger, J., N. Stein, C. Frey, and W. Becker (2019). "Scaling laws for the adhesive composite butt joint strength derived by finite fracture mechanics". In: *Composite Structures* 208, pp. 546–556.
- Feyel, F. (1999). "Multiscale FE2 elastoviscoplastic analysis of composite structures". In: *Computational Materials Science* 16.1–4, pp. 344–354.
- Feyel, F. (2003). "A multilevel finite element method (FE2) to describe the response of highly non-linear structures using generalized continua". In: *Computer Methods in Applied Mechanics and Engineering* 192.28. Multiscale Computational Mechanics for Materials and Structures, pp. 3233–3244.
- Feyel, F. and J.-L. Chaboche (2000). "FE2 multiscale approach for modelling the elastoviscoplastic behaviour of long fibre SiC/Ti composite materials". In: *Computer Methods in Applied Mechanics and Engineering* 183.3–4, pp. 309–330.
- Flory, P. J. (1961). "Thermodynamic relations for high elastic materials". In: *Trans. Faraday Soc.* 57.0, pp. 829–838.
- Fried, I. and A. R. Johnson (1988). "A note on elastic energy density functions for largely deformed compressible rubber solids". In: *Computer Methods in Applied Mechanics and Engineering* 69.1, pp. 53–64.
- Ganczarski, A. W. and J. J. Skrzypek (2015). "General Concept of Limit Surfaces—Convexity and Normality Rules, Material Stability". In: *Mechanics of Anisotropic Materials*. Ed. by J. J. Skrzypek and A. W. Ganczarski. Cham: Springer International Publishing, pp. 133–157.
- Gent, A. N. (1996). "A new constitutive relation for rubber". In: *Rubber chemistry and technology* 69.1, pp. 59–61.
- Gent, A. N. and P. B. Lindley (1959). "Internal Rupture of Bonded Rubber Cylinders in Tension". In: *Proceedings of the Royal Society of London A: Mathematical, Physical and Engineering Sciences* 249.1257, pp. 195–205.
- Gent, A. N., J. B. Suh, and S. G. K. III (2007). "Mechanics of rubber shear springs". In: *International Journal of Non-Linear Mechanics* 42.2. Special Issue in Honour of Dr Ronald S. Rivlin, pp. 241–249.

- Ghosh, S., K. Lee, and S. Moorthy (1995). "Multiple scale analysis of heterogeneous elastic structures using homogenization theory and voronoi cell finite element method". In: *International Journal of Solids and Structures* 32.1, pp. 27–62.
- Ghosh, S., K. Lee, and S. Moorthy (1996). "Two scale analysis of heterogeneous elastic-plastic materials with asymptotic homogenization and Voronoi cell finite element model". In: *Computer Methods in Applied Mechanics and Engineering* 132.1, pp. 63–116.
- Ghosh, S. and S. Moorthy (1995). "Elastic-plastic analysis of arbitrary heterogeneous materials with the Voronoi Cell finite element method". In: *Computer Methods in Applied Mechanics and Engineering* 121.1, pp. 373–409.
- Glüge, R. and S. Bucci (2017). "Does convexity of yield surfaces in plasticity have a physical significance?" In: *Mathematics and Mechanics of Solids* 0.
- Gracia, L. A., E. Peña, J. M. Royo, J. L. Pelegay, and B. Calvo (2009). "A comparison between pseudo-elastic and damage models for modelling the Mullins effect in industrial rubber components". In: *Mechanics Research Communications* 36.7, pp. 769–776.
- Gromov, M. (1991). "Sign and geometric meaning of curvature". In: *Rendiconti del Seminario Matematico e Fisico di Milano* 61.1, pp. 9–123.
- Gunel, E. M. and C. Basaran (2010). "Stress Whitening Quantification of Thermoformed Mineral Filled Acrylics". In: *Journal of Engineering Materials and Technology* 132.3, pp. 031002-031002-11.
- Gusev, A. A. (1997). "Representative volume element size for elastic composites: A numerical study". In: *Journal of the Mechanics and Physics of Solids* 45.9, pp. 1449–1459.
- Hagl, A. (2016). "Development and test logics for structural silicone bonding design and sizing". In: *Glass Structures & Engineering* 1.1, pp. 131–151.
- Hamdi, A., M. N. Abdelaziz, N. A. Hocine, P. Heuillet, and N. Benseddiq (2006). "A fracture criterion of rubber-like materials under plane stress conditions". In: *Polymer Testing* 25.8, pp. 994–1005.
- Hamdi, A., M. N. Abdelaziz, N. A. Hocine, P. Heuillet, and N. Benseddiq (2007). "A new generalized fracture criterion of elastomers under quasi-static plane stress loadings". In: *Polymer Testing* 26.7, pp. 896–902.
- Hamdi, A. and H. Mahjoubi (2015). "Design criterion for rubbery parts under biaxial loading". In: *Theoretical and Applied Fracture Mechanics* 78, pp. 51–55.
- Hamdi, A., S. Guessasma, and M. N. Abdelaziz (2014). "Fracture of elastomers by cavitation". In: *Materials & Design* 53, pp. 497–503.
- Hanson, D. E., M. Hawley, R. Houlton, K. Chitanvis, P. Rae, E. B. Orler, and D. A. Wroblewski (2005). "Stress softening experiments in silica-filled polydimethylsiloxane provide insight into a mechanism for the Mullins effect". In: *Polymer* 46.24, pp. 10989–10995.

- Hartmann, S. and P. Neff (2003). "Polyconvexity of generalized polynomial-type hyperelastic strain energy functions for near-incompressibility". In: *International journal of solids and structures* 40.11, pp. 2767–2791.
- Hart-Smith, L. J. (1966). "Elasticity parameters for finite deformations of rubber-like materials". In: *Zeitschrift für angewandte Mathematik und Physik ZAMP* 17.5, pp. 608–626.
- Harwood, J. A. C., L. Mullins, and A. R. Payne (1965). "Stress softening in natural rubber vulcanizates. Part II. Stress softening effects in pure gum and filler loaded rubbers". In: *Journal of Applied Polymer Science* 9.9, pp. 3011–3021.
- Hashin, Z. and S. Shtrikman (1963). "A variational approach to the theory of the elastic behaviour of multiphase materials". In: *Journal of the Mechanics and Physics of Solids* 11.2, pp. 127–140.
- Heinrich, G., E. Straube, and G. Helmis (1988). "Rubber elasticity of polymer networks: Theories". In: *Polymer Physics*. Berlin, Heidelberg: Springer Berlin Heidelberg, pp. 33–87.
- Hencky, H. (1933). "The Elastic Behavior of Vulcanized Rubber". In: *Rubber Chemistry and Technology* 6.2, pp. 217–224.
- Heyden, S., S. Conti, and M. Ortiz (2015). "A nonlocal model of fracture by crazing in polymers". In: *Mechanics of Materials* 90, pp. 131–139.
- Hill, R. (1952). "The Elastic Behaviour of a Crystalline Aggregate". In: *Proceedings of the Physical Society. Section A* 65.5, p. 349.
- Hill, R. (1965). "A self-consistent mechanics of composite materials". In: *Journal of the Mechanics and Physics of Solids* 13.4, pp. 213–222.
- Hill, R. (1970). "Constitutive inequalities for isotropic elastic solids under finite strain". In: *Proceedings of the Royal Society of London A: Mathematical, Physical and Engineering Sciences* 314.1519, pp. 457–472.
- Hill, R. (1972). "On constitutive macro-variables for heterogeneous solids at finite strain". In: *Proceedings of the Royal Society of London A: Mathematical, Physical and Engineering Sciences* 326.1565, pp. 131–147.
- Hippe, J. (2015). "Investigations of the material behavior of glued connections with TSSA". MA thesis. Technical University Darmstadt.
- Hocine, N. A., A. Hamdi, M. N. Abdelaziz, P. Heuillet, and F. Zaiři (2011). "Experimental and finite element investigation of void nucleation in rubber-like materials". In: *International Journal of Solids and Structures* 48.9, pp. 1248–1254.
- Hohe, J. and W. Becker (2003). "Effective mechanical behavior of hyperelastic honeycombs and two-dimensional model foams at finite strain". In: *International Journal of Mechanical Sciences* 45.5, pp. 891–913.
- Holzapfel, G. A. (2000). *Nonlinear solid mechanics*. Vol. 24. Wiley Chichester.

- Horgan, C. O. and J. G. Murphy (2010). "Simple Shearing of Incompressible and Slightly Compressible Isotropic Nonlinearly Elastic Materials". In: *Journal of Elasticity* 98.2, pp. 205–221.
- Horgan, C. O. and M. G. Smayda (2012). "The importance of the second strain invariant in the constitutive modeling of elastomers and soft biomaterials". In: *Mechanics of Materials* 51, pp. 43–52.
- Horgan, C. O. and G. Saccomandi (2006). "Phenomenological Hyperelastic Strain-Stiffening Constitutive Models for Rubber". In: *Rubber Chemistry and Technology* 79.1, pp. 152–169.
- Hou, H.-S. and R. Abeyaratne (1992). "Cavitation in elastic and elastic-plastic solids". In: *Journal of the Mechanics and Physics of Solids* 40.3, pp. 571–592.
- Houwink, R. (1956). "Slipping of Molecules during the Deformation of Reinforced Rubber". In: *Rubber Chemistry and Technology* 29.3, pp. 888–893.
- Ioannidou-Kati, A., M. Santarsiero, P. de Vries, S. Teixeira de Freitas, R. Nijssse, and C. Louter (2018). "Mechanical behaviour of Transparent Structural Silicone Adhesive (TSSA) steel-to-glass laminated connections under monotonic and cyclic loading". In: *Glass Structures & Engineering*.
- Itskov, M., E. Haberstroh, A. Ehret, and M. Vohringer (2006). "Experimental observation of the deformation induced anisotropy of the Mullins effect in rubber". In: *KGK-Kautschuk Gummi Kunststoffe* 59.3, pp. 93–96.
- James, H. M. and E. Guth (1943). "Theory of the Elastic Properties of Rubber". In: *The Journal of Chemical Physics* 11.10, pp. 455–481.
- Johnson, M. A. and M. F. Beatty (1993). "The mullins effect in uniaxial extension and its influence on the transverse vibration of a rubber string". In: *Continuum Mechanics and Thermodynamics* 5.2, pp. 83–115.
- Kakavas, P. A. and W. V. Chang (1991). "Acoustic emission in bonded elastomer discs subjected to uniform tension. II". In: *Journal of Applied Polymer Science* 42.7, pp. 1997–2004.
- Kaliske, M. and G. Heinrich (1999). "An Extended Tube-Model for Rubber Elasticity: Statistical-Mechanical Theory and Finite Element Implementation". In: *Rubber Chemistry and Technology* 72.4, pp. 602–632.
- Kambour, R. P. (1973). "A review of crazing and fracture in thermoplastics". In: *Journal of Polymer Science: Macromolecular Reviews* 7.1, pp. 1–154.
- Kanit, T., S. Forest, I. Galliet, V. Mounoury, and D. Jeulin (2003). "Determination of the size of the representative volume element for random composites: statistical and numerical approach". In: *International Journal of Solids and Structures* 40.13, pp. 3647–3679.
- Kassnel-Henneberg, B. (2018). *SWISSRAILING: Komplettsysteme für Geländer und Brüstungen*. Tech. rep. Glas Trösch AG SWISSLAMEX.

- Kawabata, S. (1973). "Fracture and mechanical behavior of rubber-like polymers under finite deformation in biaxial stress field". In: *Journal of Macromolecular Science, Part B* 8.3-4, pp. 605–630.
- Kazina, E., O. Starkova, and A. Aniskevich (2011). "Volume changes in filled rubber under uniaxial cyclic loading". In: *Materials Science* 17.3, pp. 271–275.
- Kearsley, E. A. (1989). "Note: Strain Invariants Expressed as Average Stretches". In: *Journal of Rheology* 33.5, pp. 757–760.
- Khajehsaeid, H., J. Arghavani, and R. Naghdabadi (2013). "A hyperelastic constitutive model for rubber-like materials". In: *European Journal of Mechanics - A/Solids* 38, pp. 144–151.
- Khiêm, V. N. and M. Itskov (2016). "Analytical network-averaging of the tube model:: Rubber elasticity". In: *Journal of the Mechanics and Physics of Solids* 95, pp. 254–269.
- Khiêm, V. N. and M. Itskov (2018). "Analytical network-averaging of the tube model: Strain-induced crystallization in natural rubber". In: *Journal of the Mechanics and Physics of Solids* 116, pp. 350–369.
- Kiziltoprak, N. (2016). "Development of a Nano-Mechanical-Model to account for the Cavitation-Effect in Rubber-like Materials". MA thesis. Technical University Darmstadt.
- Kłosowski, J. and A. T. Wolf (2016). *Sealants in construction*. CRC Press.
- Klüppel, M. and J. Schramm (2010). "A generalized tube model of rubber elasticity and stress softening of filler reinforced elastomer systems". In: *Macromolecular Theory and Simulations* 9.9, pp. 742–754.
- Knauss, W. G. (1967). "An upper bound of failure in viscoelastic materials subjected to multiaxial stress states". In: *International Journal of Fracture Mechanics* 3.4, pp. 267–277.
- Kolling, S., P. A. D. Bois, D. J. Benson, and W. W. Feng (2007). "A tabulated formulation of hyperelasticity with rate effects and damage". In: *Computational Mechanics* 40.5, pp. 885–899.
- Kolupaev, V. A. (2017). "Generalized Strength Criteria as Functions of the Stress Angle". In: *Journal of Engineering Mechanics* 143.9, p. 04017095.
- Kolupaev, V. A., M.-H. Yu, H. Altenbach, and A. Bolchoun (2018). "Comparison of Strength Criteria Based on the Measurements on Concrete". In: *Journal of Engineering Mechanics* 144.6, p. 04018028.
- Kolupaev, V. A. (2018). *Equivalent Stress Concept for Limit State Analysis*. Vol. 86. Springer International Publishing.
- Kraus, G., C. W. Childers, and K. W. Rollmann (1966). "Stress softening in carbon black-reinforced vulcanizates. Strain rate and temperature effects". In: *Journal of Applied Polymer Science* 10.2, pp. 229–244.

- Kraus, M. A., M. Schuster, J. Kuntsche, G. Siebert, and J. Schneider (2017). "Parameter identification methods for visco- and hyperelastic material models". In: *Glass Structures & Engineering* 2.2, pp. 147–167.
- Kuhn, W. (1934). "Über die Gestalt fadenförmiger Moleküle in Lösungen". In: *Kolloid-Zeitschrift* 68.1, pp. 2–15.
- Kuhn, W. (1936). "Gestalt und Eigenschaften fadenförmiger Moleküle in Lösungen (und im elastisch festen Zustand)". In: *Angewandte Chemie* 49.48, pp. 858–862.
- Kuna-Ciskał, H. and J. J. Skrzypek (2004). "CDM based modelling of damage and fracture mechanisms in concrete under tension and compression". In: *Engineering Fracture Mechanics* 71.4. Fracture and Damage Mechanics, pp. 681–698.
- Kuntsche, J. (2015). "Mechanisches Verhalten von Verbundglas unter zeit-abhängiger Belastung und Explosionsbeanspruchung". Doctoral thesis. Technische Universität Darmstadt.
- Lahellec, N., F. Mazerolle, and J. Michel (2004). "Second-order estimate of the macroscopic behavior of periodic hyperelastic composites: theory and experimental validation". In: *Journal of the Mechanics and Physics of Solids* 52.1, pp. 27–49.
- Lazopoulos, K. A. and R. Ogden (1998). "Nonlinear Elasticity Theory with Discontinuous Internal Variables". In: *Mathematics and Mechanics of Solids* 3.1, pp. 29–51.
- Le Cam, J.-B. (2010). "A review of volume changes in rubbers: the effect of stretching". In: *Rubber chemistry and technology* 83.3, pp. 247–269.
- Li, J., D. Mayau, and F. Song (2007). "A constitutive model for cavitation and cavity growth in rubber-like materials under arbitrary tri-axial loading". In: *International Journal of Solids and Structures* 44.18, pp. 6080–6100.
- Lindsey, G. H. (1967). "Triaxial Fracture Studies". In: *Journal of Applied Physics* 38.12, pp. 4843–4852.
- Lopez-Pamies, O. and P. P. Castañeda (2007a). "Homogenization-based constitutive models for porous elastomers and implications for macroscopic instabilities: II—Results". In: *Journal of the Mechanics and Physics of Solids* 55.8, pp. 1702–1728.
- Lopez-Pamies, O. and P. P. Castañeda (2007b). "Homogenization-based constitutive models for porous elastomers and implications for macroscopic instabilities: II—Results". In: *Journal of the Mechanics and Physics of Solids* 55.8, pp. 1702–1728.
- Lopez-Pamies, O. (2010). "A new I1-based hyperelastic model for rubber elastic materials". In: *Comptes Rendus Mécanique* 338.1, pp. 3–11.

- Lopez-Pamies, O., M. I. Idiart, and T. Nakamura (2011a). "Cavitation in elastomeric solids: I—A defect-growth theory". In: *Journal of the Mechanics and Physics of Solids* 59.8, pp. 1464–1487.
- Lopez-Pamies, O., T. Nakamura, and M. I. Idiart (2011b). "Cavitation in elastomeric solids: II—Onset-of-cavitation surfaces for Neo-Hookean materials". In: *Journal of the Mechanics and Physics of Solids* 59.8, pp. 1488–1505.
- Machado, G., G. Chagnon, and D. Favier (2010). "Analysis of the isotropic models of the Mullins effect based on filled silicone rubber experimental results". In: *Mechanics of Materials* 42.9, pp. 841–851.
- Machado, G., D. Favier, and G. Chagnon (2012). "Membrane Curvatures and Stress-strain Full Fields of Axisymmetric Bulge Tests from 3D-DIC Measurements. Theory and Validation on Virtual and Experimental results". In: *Experimental Mechanics* 52.7, pp. 865–880.
- Mansouri, M. and H. Darijani (2014). "Constitutive modeling of isotropic hyperelastic materials in an exponential framework using a self-contained approach". In: *International Journal of Solids and Structures* 51.25, pp. 4316–4326.
- Mao, Y., B. Talamini, and L. Anand (2017). "Rupture of polymers by chain scission". In: *Extreme Mechanics Letters* 13, pp. 17–24.
- Marckmann, G. and E. Verron (2006). "Comparison of Hyperelastic Models for Rubber-Like Materials". In: *Rubber Chemistry and Technology* 79.5, pp. 835–858.
- Marlow, R. (2003). "A general first-invariant hyperelastic constitutive model". In: *Constitutive Models for Rubber*, pp. 157–160.
- Miehe, C. (1994). "Aspects of the formulation and finite element implementation of large strain isotropic elasticity". In: *International Journal for Numerical Methods in Engineering* 37.12, pp. 1981–2004.
- Miehe, C., S. Göktepe, and F. Lulei (2004a). "A micro-macro approach to rubber-like materials—Part I: the non-affine micro-sphere model of rubber elasticity". In: *Journal of the Mechanics and Physics of Solids* 52.11, pp. 2617–2660.
- Miehe, C. and A. Koch (2002). "Computational micro-to-macro transitions of discretized microstructures undergoing small strains". In: *Archive of Applied Mechanics* 72.4, pp. 300–317.
- Miehe, C., M. Lambrecht, and E. Gürses (2004b). "Analysis of material instabilities in inelastic solids by incremental energy minimization and relaxation methods: evolving deformation microstructures in finite plasticity". In: *Journal of the Mechanics and Physics of Solids* 52.12, pp. 2725–2769.
- Miehe, C. and J. Keck (2000). "Superimposed finite elastic-viscoelastic-plastoelastic stress response with damage in filled rubbery polymers. Experiments, modelling and algorithmic implementation". In: *Journal of the Mechanics and Physics of Solids* 48.2, pp. 323–365.

- Miehe, C. and L.-M. Schänzel (2014). "Phase field modeling of fracture in rubbery polymers. Part I: Finite elasticity coupled with brittle failure". In: *Journal of the Mechanics and Physics of Solids* 65, pp. 93–113.
- Miehe, C., J. Schröder, and M. Becker (2002). "Computational homogenization analysis in finite elasticity: material and structural instabilities on the micro- and macro-scales of periodic composites and their interaction". In: *Computer Methods in Applied Mechanics and Engineering* 191.44, pp. 4971–5005.
- Mihai, L. A. and A. Goriely (2011). "Positive or negative Poynting effect? The role of adscititious inequalities in hyperelastic materials". In: *Proceedings of the Royal Society A: Mathematical, Physical and Engineering Science* 467.2136, pp. 3633–3646.
- Misra, R. D. K., R. Hadal, and S. J. Duncan (2004). "Surface damage behavior during scratch deformation of mineral reinforced polymer composites". In: *Acta Materialia* 52.14, pp. 4363–4376.
- Mooney, M. (1940). "A Theory of Large Elastic Deformation". In: *Journal of Applied Physics* 11.9, pp. 582–592.
- Moreira, D. C. and L. C. S. Nunes (2013). "Comparison of simple and pure shear for an incompressible isotropic hyperelastic material under large deformation". In: *Polymer Testing* 32.2, pp. 240–248.
- Mori, T. and K. Tanaka (1973). "Average stress in matrix and average elastic energy of materials with misfitting inclusions". In: *Acta Metallurgica* 21.5, pp. 571–574.
- Mullins, L. (1948). "Effect of Stretching on the Properties of Rubber". In: *Rubber Chemistry and Technology* 21.2, pp. 281–300.
- Mullins, L. (1949). "Permanent Set in Vulcanized Rubber". In: *Rubber Chemistry and Technology* 22.4, pp. 1036–1044.
- Mullins, L. and N. R. Tobin (1965). "Stress softening in rubber vulcanizates. Part I. Use of a strain amplification factor to describe the elastic behavior of filler-reinforced vulcanized rubber". In: *Journal of Applied Polymer Science* 9.9, pp. 2993–3009.
- Muth, J. (2018). "Development of hypotheses concerning the stress-whitening effect in structural silicones based on midget-tension tests". Bachelor thesis. Technische Universität Darmstadt.
- Nakamura, T. and O. Lopez-Pamies (2012). "A finite element approach to study cavitation instabilities in non-linear elastic solids under general loading conditions". In: *International Journal of Non-Linear Mechanics* 47.2. Nonlinear Continuum Theories, pp. 331–340.
- Neff, P., I.-D. Ghiba, and J. Lankeit (2015). "The exponentiated Hencky-logarithmic strain energy. Part I: Constitutive issues and rank-one convexity". In: *Journal of Elasticity* 121.2, pp. 143–234.

- Nelder, J. A. (1966). "Inverse polynomials, a useful group of multi-factor response functions". In: *Biometrics* 22.1, pp. 128–141.
- Nemat-Nasser, S. and M. Hori (2013). *Micromechanics: Overall Properties of Heterogeneous Materials*. Vol. 37. Elsevier.
- Nunes, L. C. S. and D. C. Moreira (2013). "Simple shear under large deformation: Experimental and theoretical analyses". In: *European Journal of Mechanics - A/Solids* 42, pp. 315–322.
- Ogden, R. (1972). "Large Deformation Isotropic Elasticity: On the Correlation of Theory and Experiment for Compressible Rubberlike Solids". In: *Proceedings of the Royal Society of London A: Mathematical, Physical and Engineering Sciences* 328.1575, pp. 567–583.
- Ogden, R. and D. G. Roxburgh (1999). "A pseudo-elastic model for the Mullins effect in filled rubber". In: *Proceedings of the Royal Society of London. Series A: Mathematical, Physical and Engineering Sciences* 455.1988, pp. 2861–2877.
- Ogden, R., G. Saccomandi, and I. Sgura (2004). "Fitting hyperelastic models to experimental data". In: *Computational Mechanics* 34.6, pp. 484–502.
- Ohno, N., D. Okumura, and H. Noguchi (2002). "Microscopic symmetric bifurcation condition of cellular solids based on a homogenization theory of finite deformation". In: *Journal of the Mechanics and Physics of Solids* 50.5, pp. 1125–1153.
- Ozbas, B., S. Toki, B. S. Hsiao, B. Chu, R. A. Register, I. A. Aksay, R. K. Prud'homme, and D. H. Adamson (2012). "Strain-induced crystallization and mechanical properties of functionalized graphene sheet-filled natural rubber". In: *Journal of Polymer Science Part B: Polymer Physics* 50.10, pp. 718–723.
- Pence, T. J. and K. Gou (2015). "On compressible versions of the incompressible neo-Hookean material". In: *Mathematics and Mechanics of Solids* 20.2, pp. 157–182.
- Peng, S. T. J. and R. F. Landel (1975). "Stored energy function and compressibility of compressible rubberlike materials under large strain". In: *Journal of Applied Physics* 46.6, pp. 2599–2604.
- Piccolroaz, A. and D. Bigoni (2009). "Yield criteria for quasibrittle and frictional materials: A generalization to surfaces with corners". In: *International Journal of Solids and Structures* 46.20, pp. 3587–3596.
- Pindera, M.-J., H. Khatam, A. S. Drago, and Y. Bansal (2009). "Micromechanics of spatially uniform heterogeneous media: A critical review and emerging approaches". In: *Composites Part B: Engineering* 40.5, pp. 349–378.
- Plagge, J. and M. Klüppel (2017). "A physically based model of stress softening and hysteresis of filled rubber including rate- and temperature dependency". In: *International Journal of Plasticity* 89, pp. 173–196.
- Podgórski, J. (1984). "Limit state condition and the dissipation function for isotropic materials". In: *Archives of Mechanics* 36.3, pp. 323–342.

- Ponte Castañeda, P. and P. M. Suquet (1995). "On the effective mechanical behavior of weakly inhomogeneous nonlinear materials". In: *European journal of mechanics. A. Solids* 14.2, pp. 205–236.
- Poulain, X., V. Lefèvre, O. Lopez-Pamies, and K. Ravi-Chandar (2017). "Damage in elastomers: nucleation and growth of cavities, micro-cracks, and macro-cracks". In: *International Journal of Fracture* 205.1, pp. 1–21.
- Poynting, J. H. (1909). "On Pressure Perpendicular to the Shear Planes in Finite Pure Shears, and on the Lengthening of Loaded Wires When Twisted". In: *Proceedings of the Royal Society of London. Series A* 82.557, pp. 546–559.
- Pucci, E. and G. Saccomandi (2002). "A Note on the Gent Model for Rubber-Like Materials". In: *Rubber Chemistry and Technology* 75.5, pp. 839–852.
- Rastak, R. and C. Linder (2018). "A non-affine micro-macro approach to strain-crystallizing rubber-like materials". In: *Journal of the Mechanics and Physics of Solids* 111, pp. 67–99.
- Reuss, A. (1929). "Berechnung der Fließgrenze von Mischkristallen auf Grund der Plastizitätsbedingung für Einkristalle". In: *ZAMM - Journal of Applied Mathematics and Mechanics / Zeitschrift für Angewandte Mathematik und Mechanik* 9.1, pp. 49–58.
- Rivlin, R. S. (1948). "Large Elastic Deformations of Isotropic Materials. IV. Further Developments of the General Theory". In: *Philosophical Transactions of the Royal Society of London. Series A, Mathematical and Physical Sciences* 241.835, pp. 379–397.
- Rosendahl, P. L., P. Weißgraebel, N. Stein, and W. Becker (2017). "Asymmetric crack onset at open-holes under tensile and in-plane bending loading". In: *International Journal of Solids and Structures* 113-114, pp. 10–23.
- Santarsiero, M. (2015). "Laminated Connections for Structural Glass Applications". Doctoral thesis. Swiss Federal Institute of Technology.
- Santarsiero, M., C. Bedon, and C. Louter (2018a). "Experimental and numerical analysis of thick embedded laminated glass connections". In: *Composite Structures* 188, pp. 242–256.
- Santarsiero, M., C. Louter, and A. Nussbaumer (2016). "The mechanical behaviour of SentryGlas ionomer and TSSA silicon bulk materials at different temperatures and strain rates under uniaxial tensile stress state". In: *Glass Structures & Engineering* 1.2, pp. 395–415.
- Santarsiero, M., C. Louter, and A. Nussbaumer (2018b). "A novel triaxial failure model for adhesive connections in structural glass applications". In: *Engineering Structures* 166, pp. 195–211.
- Sarkawi, S. S., W. K. Dierkes, and J. W. M. Noordermeer (2015). "MORPHOLOGY OF SILICA-REINFORCED NATURAL RUBBER: THE EFFECT OF

- SILANE COUPLING AGENT". In: *Rubber Chemistry and Technology* 88.3, pp. 359–372.
- Sasso, M., G. Palmieri, G. Chiappini, and D. Amodio (2008). "Characterization of hyperelastic rubber-like materials by biaxial and uniaxial stretching tests based on optical methods". In: *Polymer Testing* 27.8, pp. 995–1004.
- Schneider, J., J. Kuntsche, S. Schula, F. Schneider, and J.-D. Wörner (2016). *Glasbau: Grundlagen, Berechnung, Konstruktion*. Springer-Verlag.
- Schreyer, H. L. (1989). "Smooth Limit Surfaces for Metals, Concrete, and Geotechnical Materials". In: *Journal of Engineering Mechanics* 115.9, pp. 1960–1975.
- Schröder, J. and P. Neff (2010). *Poly-, Quasi-and Rank-One Convexity in Applied Mechanics*. CISM International Centre for Mechanical Sciences, Vol. 516.
- Schröder, J. and P. Neff (2003). "Invariant formulation of hyperelastic transverse isotropy based on polyconvex free energy functions". In: *International Journal of Solids and Structures* 40.2, pp. 401–445.
- Selvadurai, A. and M. Shi (2012). "Fluid pressure loading of a hyperelastic membrane". In: *International Journal of Non-Linear Mechanics* 47.2. Nonlinear Continuum Theories, pp. 228–239.
- Shariff, M. H. B. M. (2000). "Strain Energy Function for Filled and Unfilled Rubberlike Material". In: *Rubber Chemistry and Technology* 73.1, pp. 1–18.
- Sikora, S. P. (2014). "Materialcharakterisierung und -modellierung zur Simulation von Klebverbindungen mit Polyurethansklebstoffen". Doctoral thesis. Universität Paderborn.
- Silvestru, V. A., O. Englhardt, and J. Schneider (2018b). "Linear adhesive connections at the edge of laminated glass panes: an experimental study under tensile, compressive and shear loading". In: *Glass Structures & Engineering*.
- Simo, J. C. and R. L. Taylor (1982). "Penalty function formulations for incompressible nonlinear elastostatics". In: *Computer Methods in Applied Mechanics and Engineering* 35.1, pp. 107–118.
- Simo, J. C., R. L. Taylor, and K. S. Pister (1985). "Variational and projection methods for the volume constraint in finite deformation elasto-plasticity". In: *Computer Methods in Applied Mechanics and Engineering* 51.1, pp. 177–208.
- Sitte, S., M. Brasseur, L. Carbay, and A. Wolf (2011). "Preliminary Evaluation of the Mechanical Properties and Durability of Transparent Structural Silicone Adhesive (TSSA) for Point Fixing in Glazing". In: *Journal of ASTM International* 10.8, pp. 1–27.
- Smith, T. L. and J. A. Rinde (1969). "Ultimate tensile properties of elastomers. V. Rupture in constrained biaxial tensions". In: *Journal of Polymer Science Part A-2: Polymer Physics* 7.4, pp. 675–685.
- Staudt, Y. (2017). "Proposal of a Failure Criterion of Adhesively Bonded Connections with Silicone". Doctoral thesis. University of Luxembourg.

- Staudt, Y., C. Odenbreit, and J. Schneider (2018). "Failure behaviour of silicone adhesive in bonded connections with simple geometry". In: *International Journal of Adhesion and Adhesives* 82, pp. 126–138.
- Stein, N., P. Weißgraebner, and W. Becker (2015). "A model for brittle failure in adhesive lap joints of arbitrary joint configuration". In: *Composite Structures* 133, pp. 707–718.
- Steinmann, P., M. Hossain, and G. Possart (2012). "Hyperelastic models for rubber-like materials: consistent tangent operators and suitability for Treloar's data". In: *Archive of Applied Mechanics* 82.9, pp. 1183–1217.
- Stommel, M., M. Stojek, and W. Korte (2011). "Dimensionierung von Kunststoff- und Elastomerbauteilen". In: *FEM zur Berechnung von Kunststoff- und Elastomerbauteilen*. Carl Hanser Verlag GmbH & Co. KG, pp. 121–194.
- Stoughton, T. B. and J. W. Yoon (2006). "Review of Drucker's postulate and the issue of plastic stability in metal forming". In: *International Journal of Plasticity* 22.3, pp. 391–433.
- Suquet, P. M. (1987). "Elements of homogenization for inelastic solid mechanics". In: vol. 272. Lecture Notes in Physics. Springer Verlag. Chap. n.a. Pp. 193–278.
- Thomas, R., D. Yumei, H. Yuelong, Y. Le, P. Moldenaers, Y. Weimin, T. Czigan, and S. Thomas (2008). "Miscibility, morphology, thermal, and mechanical properties of a DGEBA based epoxy resin toughened with a liquid rubber". In: *Polymer* 49.1, pp. 278–294.
- Tibolt, M. (2015). "Design of Point Fitted Insulating Glass Units". Doctoral thesis. University of Luxembourg.
- Timoshenko, S. P. (1953). *History of Strength of Materials: With a Brief Account of the History of Theory of Elasticity and Theory of Structure*. New York: McGraw-Hill.
- Toki, S., T. Fujimaki, and M. Okuyama (2000). "Strain-induced crystallization of natural rubber as detected real-time by wide-angle X-ray diffraction technique". In: *Polymer* 41.14, pp. 5423–5429.
- Treloar, L. R. G. (1943). "The elasticity of a network of long-chain molecules. I". In: *Trans. Faraday Soc.* 39 (0), pp. 36–41.
- Treloar, L. R. G. (1975). *The physics of rubber elasticity*. Oxford University Press, USA.
- Truesdell, C. and W. Noll (2004). "The non-linear field theories of mechanics". In: *The non-linear field theories of mechanics*. Ed. by S. Antman. Springer, pp. 1–579.
- Tschoegl, N. W. (1971). "Failure surfaces in principal stress space". In: *Journal of Polymer Science Part C: Polymer Symposia* 32.1, pp. 239–267.

- Valanis, K. C. and R. F. Landel (1967). "The Strain-Energy Function of a Hyperelastic Material in Terms of the Extension Ratios". In: *Journal of Applied Physics* 38.7, pp. 2997–3002.
- Van den Bogert, P. and R. De Borst (1994). "On the behaviour of rubberlike materials in compression and shear". In: *Archive of Applied Mechanics* 64.2, pp. 136–146.
- Villarino, M. B. (2005). "Ramanujan's Perimeter of an Ellipse". In: *ArXiv Mathematics e-prints*.
- Voigt, W. (1889). "Ueber die Beziehung zwischen den beiden Elasticitätsconstanten isotroper Körper". In: *Annalen der Physik* 274.12, pp. 573–587.
- Waffenschmidt, T., C. Polindara, A. Menzel, and S. Blanco (2014). "A gradient-enhanced large-deformation continuum damage model for fibre-reinforced materials". In: *Computer Methods in Applied Mechanics and Engineering* 268, pp. 801–842.
- Wang, M. C. and E. Guth (1952). "Statistical Theory of Networks of Non-Gaussian Flexible Chains". In: *The Journal of Chemical Physics* 20.7, pp. 1144–1157.
- Weißgraeber, P., D. Leguillon, and W. Becker (2016). "A review of Finite Fracture Mechanics: crack initiation at singular and non-singular stress raisers". In: *Archive of Applied Mechanics* 86.1, pp. 375–401.
- Wineman, A. (2009). "Nonlinear Viscoelastic Solids—A Review". In: *Mathematics and Mechanics of Solids* 14.3, pp. 300–366.
- Wolf, A. T. and P. Descamps (2003). "Determination of Poisson's Ratio of Silicone Sealants from Ultrasonic and Tensile Measurements". In: *Performance of exterior building walls*. ASTM International.
- Xiang, C., H.-J. Sue, J. Chu, and K. Masuda (2001). "Roles of additives in scratch resistance of high crystallinity polypropylene copolymers". In: *Polymer Engineering & Science* 41.1, pp. 23–31.
- Yeoh, O. H. (1990). "Characterization of Elastic Properties of Carbon-Black-Filled Rubber Vulcanizates". In: *Rubber Chemistry and Technology* 63.5, pp. 792–805.
- Yerzley, F. L. (1939). "Adhesion of Neoprene to Metal". In: *Industrial & Engineering Chemistry* 31.8, pp. 950–956.
- Yu, M.-H. (2018). *Unified Strength Theory and its Applications, 2nd Edition*. Singapore: Springer.
- Zhang, X., F. Andrieux, and D. Sun (2011). "Pseudo-elastic description of polymeric foams at finite deformation with stress softening and residual strain effects". In: *Materials & Design* 32.2, pp. 877–884.
- Zúñiga, A. E. and M. F. Beatty (2002). "Constitutive equations for amended non-Gaussian network models of rubber elasticity". In: *International Journal of Engineering Science* 40.20, pp. 2265–2294.

- Zwierzynski, M. (2016). "The improved isoperimetric inequality and the Wigner caustic of planar ovals". In: *Journal of Mathematical Analysis and Applications* 442.2, pp. 726–739.
- Zyczkowski, M. (1981). *Combined Loadings in the Theory of Plasticity*. Warszawa: PWN-Polish Scientific Publ.

# Appendix A

## Triaxiality in 3D Stress Space

### A.1 Numerical Examples of Modified Triaxiality

As already mentioned in Section 7.4.1, the so-called modified triaxiality can be evaluated numerically for any structural adhesive joint in order to identify the prevailing stress state in the material. The modified triaxiality is defined as

$$\eta_{\text{mod}} = \left| -3 \frac{p}{\sigma_{vM}} \right|. \quad (\text{A.1})$$

Possible threshold values for uniaxial, biaxial, triaxial and shear deformations have been evaluated and are listed in Tab. 7.3. These limits are useful to illustrate the stress state in bonded silicone joints.

### A.2 Numerical Examples

The illustration of the proposed modified triaxiality for numerical simulations of different test set-ups for the representation of homogeneous and inhomogeneous stress distributions is presented in the following. In particular, the stress states of the experiments carried out are briefly illustrated to show whether a homogeneous or inhomogeneous stress state prevails. Therefore, the numerical simulation of uniaxial tensile and compression tests, the bulge test, shear pancake test and axially pulled pancake test are shown in the Fig. A.1 with evaluation of the triaxiality. It can be clearly seen that, apart from the pancake test, almost homogeneous stress states prevail, so that the first four experiments are well suited to analytically determine material parameters, for example.

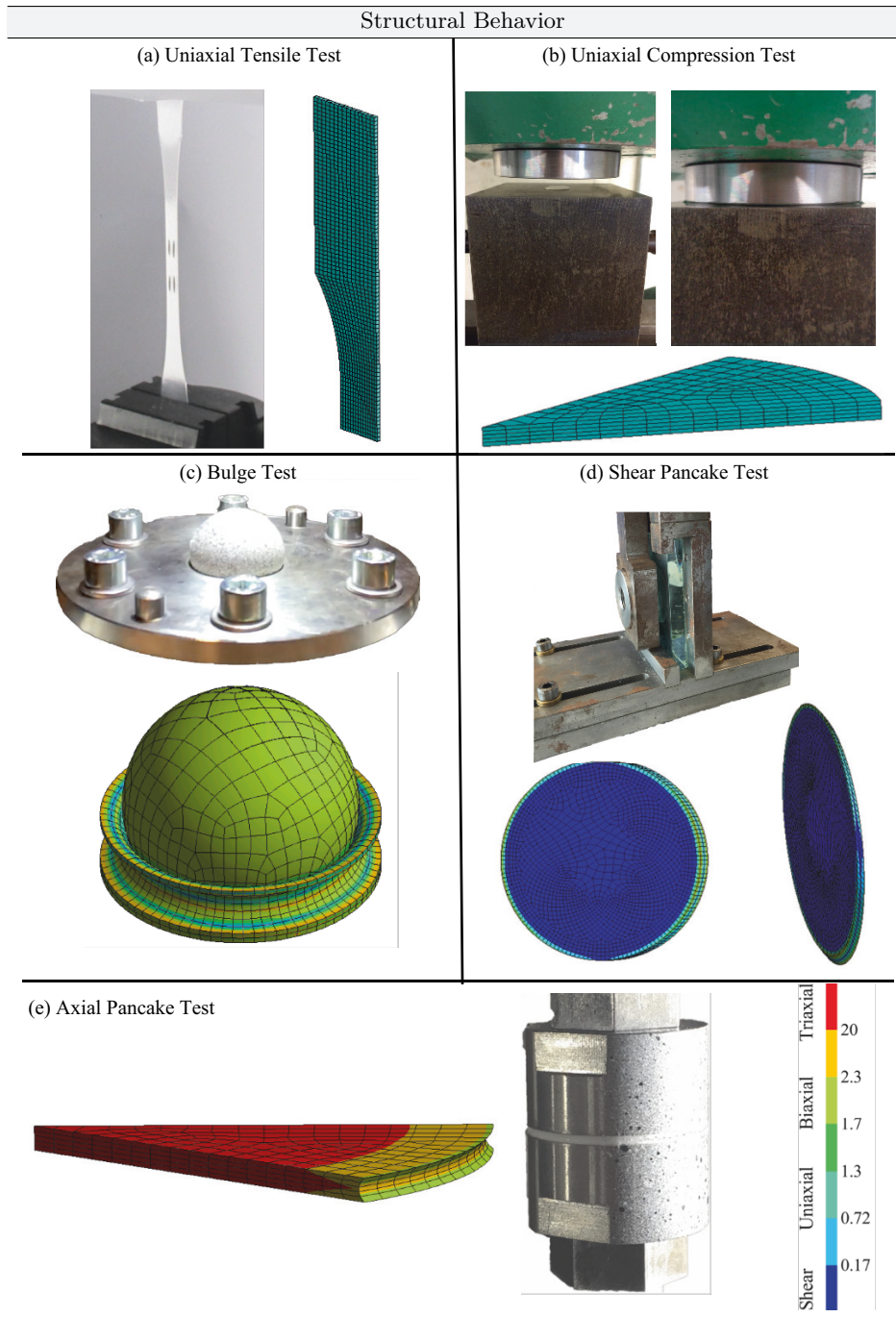


**Figure A.1** Evaluation of modified triaxiality for (a) uniaxial tensile test, (b) uniaxial compression test, (c) bulge test, (d) shear pancake test and (e) axially loaded pancake test

## Appendix B

# Pancake Tension Test under Temperature

Based on the pancake tension tests already presented in Section 4.3.1 at room temperature, the experimental results of the axially loaded pancake samples at a temperature of 80°C and a relative humidity of 50 % are summarized below only for reasons of completeness. The preconditioning of the samples corresponds to the specifications of ETAG 002 (2012), so that the PC-I samples with a diameter of  $d = 50$  mm were stored for 24 hours at a temperature of 80°C and then tested. The local strain in the TSSA was measured optically via DIC. According to the experiments at room temperature, the results at an elevated temperature tend to show the same structural course. Starting with a high initial stiffness, the cavitation effect starts at a critical volumetric strain, resulting in an effective stress softening. It can be

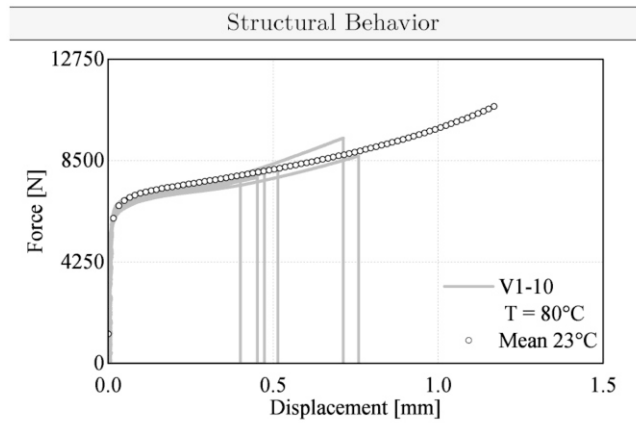


**Figure B.1** Experimental pancake tension test results for TSSA: force vs. local displacement at 80°C

clearly seen in Fig. B.1 that the engineering stresses at failure are noticeably lower than those at room temperature. This shows that the temperature influence has a

decisive effect on the stress that can be sustained in the material. The deviation in the stresses is approximately 40 %.

# Appendix C

## Porosity of TSSA

This section analyses high-resolution TEM images of TSSA to determine the pore content. The method chosen to identify the pore content corresponds to the methodology proposed in Section 4.4.1. Figure C.1 shows five TEM images at dif-

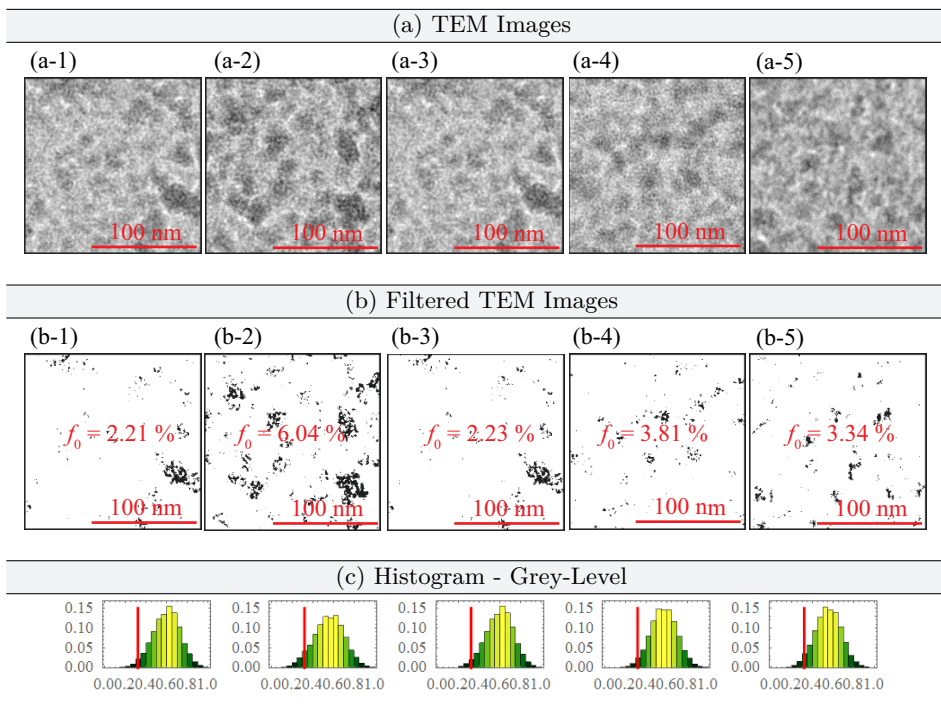


**Figure C.1** (a) TEM images of TSSA at different positions; (b) filtered TEM images with specification of the void fraction; (c) grey-level histogram of the TEM images with indication of the critical grey-scale that still is part of a pore

ferent positions, their binary filtered images including pore content and the grey-

scale histogram. By forming the mean value, a porosity of  $f_0 = 3.35\%$  is obtained for the material TSSA.

## Appendix D

# Engineering Approach Determining Experimental Testing Speed

An engineering approach is introduced, which equals the strain energies of different testing scenarios respectively different testing geometries. The main idea of the following approach is based on Kelleter et al. (2016) and redeveloped under consideration of the individual geometries of the test specimens. The strain energy of a reference experiment (RE), e.g. a dumbbell-shaped test specimen for uniaxial tensile tests, should be equal to the strain energy of any chosen experiment (AE), e.g. cylindrical specimens for uniaxial compression tests, H-shaped specimens for simple shear tests or films for biaxial tensile tests during the test. Equating the inherent strain energies of different test scenarios leads to

$$W_{\text{RE}} \stackrel{!}{=} W_{\text{AE}}. \quad (\text{D.1})$$

The postulation of Eq. (D.1) is based on energetic considerations, where the internal strain energy in an infinitesimal volume element should be equal between a reference and an arbitrary deformation. To satisfy Eq. (D.1) and to obtain a value for a constant testing speed for AE corresponding to the strain energy of the RE, Eq. (D.2) is introduced

$$\dot{\varepsilon}_{\text{AE}} = \dot{\varepsilon}_{\text{RE}} \sqrt{\frac{V_{\text{RE}}}{V_{\text{AE}}}}, \quad (\text{D.2})$$

where  $\dot{\varepsilon}$  describes the strain rate and  $V$  the volume of the AE respectively RE. To calculate the constant testing speed  $v$ ,  $\dot{\varepsilon}$  has to be multiplied with the length of the test specimen  $l_{\text{AE}}$ .

For the derivation of the approach, first the strain energy of the complete test specimen must be calculated by

$$W = V \int_0^{\varepsilon} \sigma(\varepsilon) d\varepsilon. \quad (\text{D.3})$$

To obtain the strain energy per unit volume, one have to divide the total potential by the volume  $V$ , which is also called specific strain energy. By linearisation of the stress strain response at the origin, one obtains a simplified relationship for the infinitesimal strain energy per unit volume as

$$dw = \frac{1}{2}d\sigma(\varepsilon)d\bar{\varepsilon}. \quad (\text{D.4})$$

With the help of the total differential, the infinitesimal energy function can be reformulated by

$$dw = \frac{1}{2}\frac{\partial\sigma(\varepsilon)}{\partial\varepsilon}d\bar{\varepsilon}d\bar{\varepsilon} = \frac{1}{2}Ed\bar{\varepsilon}^2. \quad (\text{D.5})$$

Introducing the strain rate with  $\dot{\varepsilon} = \frac{d\bar{\varepsilon}}{dt} \Leftrightarrow d\bar{\varepsilon} = \dot{\varepsilon}dt$  and applying it into Eq. (D.5), one obtains

$$dw = \frac{1}{2}E\dot{\varepsilon}^2dt^2 \Leftrightarrow \frac{dw}{dt^2} = \frac{1}{2}E\dot{\varepsilon}^2. \quad (\text{D.6})$$

Inserting the relationship of the specific strain energy  $w = \frac{W}{V}$  into Eq. (D.6), one obtains a twofold derivative of the strain energy with respect to the time  $t$  with

$$\frac{d\frac{W}{V}}{dt^2} = \frac{1}{2}E\dot{\varepsilon}^2 \quad \text{or} \quad \frac{dW}{dt^2} = \frac{1}{2}VE\dot{\varepsilon}^2. \quad (\text{D.7})$$

By integrating the strain energy over time and satisfying Eq. (D.1), the linearized strain energy for the initial state must be equal for the RE and the AE. Hence, one can claim that

$$\frac{dW_{\text{RE}}}{dt^2} \stackrel{!}{=} \frac{dW_{\text{AE}}}{dt^2}, \quad (\text{D.8})$$

with the result that one obtains the proposed solution of Eq. (D.2) under utilizing Eq. (D.7).

# Appendix E

## Molecular-Statistical Approaches

### E.1 Gaussian Statistics

As already mentioned, the central challenge in the statistical mechanics of a polymer chain lies in the determination of its entropy  $s$ , which is directly related to the free energy  $\psi$  in purely entropic processes (see Eq. (5.35)). The introduction of the Gaussian statistics, which was proposed by Kuhn (1934); Kuhn (1936), is based on a freely jointed polymer chain where the end-to-end distance  $r$  can never reach the contour length  $L$ . This approach is therefore only valid for moderate deformations or micro-stretches of a free polymer chain. The probability density of an unconstrained polymer single Gaussian chain reads

$$p_s(r) = p_{0,s} \exp\left[-\frac{3}{2}\bar{\lambda}^2\right] \quad \text{with} \quad p_{0,s} = \left(\frac{3}{2}Nl^2\pi\right)^{\frac{3}{2}}, \quad (\text{E.1})$$

where the average micro-stretch  $\bar{\lambda}$  has already been inserted, since in the following only average stretches are assumed according to the approach of Khiêm and Itsakov (2016). Inserting Eq. (E.1) into Eq. (5.34) or Eq. (5.35) respectively, the free energy of a single polymer chain reads

$$\psi_s(\bar{\lambda}) = \frac{3}{2}kT\bar{\lambda}^2 + \psi_0, \quad (\text{E.2})$$

where  $\psi_0$  represents a constant. The average micro-force acting on a polymer chain can be calculated by

$$\bar{f}_s = \frac{d\psi_s}{d\bar{\lambda}} = 3kT\bar{\lambda}. \quad (\text{E.3})$$

Following Treloar (1975), the macroscopic free energy on a continuum scale considering a three-chain model, where the polymer chains are aligned in the principal stretch directions, can be calculated by

$$\Psi = \frac{N}{3} [\psi_s(\lambda_1) + \psi_s(\lambda_2) + \psi_s(\lambda_3)] = \frac{NkT}{2} (\lambda_1^2 + \lambda_2^2 + \lambda_3^2), \quad (\text{E.4})$$

which also corresponds to the solution of Miehe and Schänzel (2014). Eq. (E.4) clearly shows that the Neo-Hookean material model has a molecular-statistical background, as already shown in Section 3.2.4, since the initial shear modulus  $\mu$  is defined as

$$\mu \equiv NkT. \quad (\text{E.5})$$

## E.2 Non-Gaussian Statistics (Langevin Approach)

A main characteristic of a polymer chain is its finite extensibility, which cannot be represented through Gaussian statistics since it describes a linear relationship between the micro-stretch and micro-force (see Eq. (E.3)). In contrast, the non-Gaussian statistical approach is able to consider large stretches up to the limit value of the polymer contour length, where the relationship between micro-stretch and micro-force diverges. Considering this, the work Kuhn and Grün (1942) and James and Guth (1943) was focused to characterize the free energy of an unconstrained single polymer chain accounting for locking stretches. Hence, the non-Gaussian statistics is even applicable for large stretches, while the Gaussian approach is only valid for moderate stretches. The probability density for the non-Gaussian approach reads

$$p_s(\bar{\lambda}) = p_{0,s} \exp \left[ -N \left( \bar{\lambda}_r \beta + \ln \left( \frac{\beta}{\sinh \beta} \right) \right) \right]. \quad (\text{E.6})$$

In this context,  $p_{0,s}$  describes a normalization constant and  $\bar{\lambda}_r = \bar{\lambda}/\sqrt{N}$  gives the average relative stretch of a polymer chain. The parameter  $\beta$  represents the inverse Langevin function  $\mathcal{L}^{-1}(\bar{\lambda}_r)$ , which is an important function in statistical mechanics. Calculating the entropy  $s$  of a single, unconstrained polymer chain by Eq. (5.34) and inserting the result into Eq. (5.35), the free energy reads

$$\psi_s(\bar{\lambda}_r) = NkT \left( \bar{\lambda}_r \mathcal{L}^{-1}(\bar{\lambda}_r) + \ln \frac{\mathcal{L}^{-1}(\bar{\lambda}_r)}{\sinh \mathcal{L}^{-1}(\bar{\lambda}_r)} \right) + \psi_0, \quad (\text{E.7})$$

where  $\psi_0$  represents a constant. Evaluating the inverse Langevin function through Padé approximation given by

$$\mathcal{L}^{-1}(\bar{\lambda}_r) \approx \frac{\bar{\lambda}_r(3 - \bar{\lambda}_r^2)}{(1 - \bar{\lambda}_r^2)}, \quad (\text{E.8})$$

and inserting  $\bar{\lambda}_r = \bar{\lambda}/\sqrt{N}$  into Eq. (E.7), the free energy of a single chain can be written by  $\psi_f(\bar{\lambda})$  only dependent on the average micro-stretch  $\bar{\lambda}$ . Calculating the

average micro-force acting on a single polymer chain, which is dual to the average micro-stretch  $\bar{\lambda}$ , the strain energy of a polymer chain must be differentiated with respect to  $\bar{\lambda}$ :

$$\bar{f}_s = \frac{d\psi_s}{d\bar{\lambda}} = kT\bar{\lambda} \frac{3N - \bar{\lambda}^2}{N - \bar{\lambda}^2}. \quad (\text{E.9})$$

### E.3 Relaxed Langevin Approach

Following the approach of non-Gaussian statistics, the free energy diverges when reaching the average locking stretch  $\bar{\lambda}_m$  due to the segment rigidity assumption. Since the atomic bonds enable a certain deformation, Mao et al. (2017) relaxed this theory by introducing a bond micro-stretch  $\lambda_b$  or an average bond micro-stretch  $\bar{\lambda}_b$  respectively. Based on this assumption, the current segment length can now be calculated by  $l_b = l\bar{\lambda}_b$ . Introducing the change in internal energy  $\hat{\varepsilon}_b(\bar{\lambda})$  related to segment stretching, the free energy of a single polymer chain reads

$$\psi_s(\bar{\lambda}_r) = \hat{\varepsilon}_b N + NkT \left( \frac{\bar{\lambda}_r}{\lambda_b} \mathcal{L}^{-1} \left( \frac{\bar{\lambda}_r}{\bar{\lambda}_b} \right) + \ln \frac{\mathcal{L}^{-1} \left( \frac{\bar{\lambda}_r}{\lambda_b} \right)}{\sinh \mathcal{L}^{-1} \left( \frac{\bar{\lambda}_r}{\lambda_b} \right)} \right) + \psi_0. \quad (\text{E.10})$$

Following Mao et al. (2017),  $\bar{\lambda}_b$  must be calculated by solving an implicit function, to obtain an optimal value, which minimizes the free energy of a single polymer chain. Considering entropic processes, an increase of  $\bar{\lambda}_b$  leads to an increase of free energy while decreasing the entropy at a fixed micro-stretch  $\bar{\lambda} = \text{constant}$ . A conventional approach for the internal energy of continuum models at finite strains reads

$$\hat{\varepsilon}_b(\bar{\lambda}) = \frac{1}{2} E_b (\ln(\bar{\lambda}_b))^2, \quad (\text{E.11})$$

where  $E_b$  represents the bonding stiffness. Inserting Eq. (E.11) into the implicit function, which reads

$$\frac{d\hat{\varepsilon}_b(\bar{\lambda})}{d\bar{\lambda}_b} \bar{\lambda}_b = kT \frac{\bar{\lambda}_r}{\bar{\lambda}_b} \beta, \quad (\text{E.12})$$

the average bond micro-stretch can be calculated dependent on the applied average micro-stretch. By differentiation of Eq. (E.10) with respect to the average micro-stretch  $\bar{\lambda}$  under inserting the result of Eq. (E.12) for  $\bar{\lambda}_b$ , the average micro-force acting on a single polymer chain can be calculated in accordance to Mao et al. (2017) reading

$$\bar{f}_s = \frac{d\psi_s}{d\bar{\lambda}} = \frac{kT}{L} \frac{\beta}{\bar{\lambda}_b}. \quad (\text{E.13})$$

## E.4 Tube Statistics

Since it is not sufficient to consider single polymer chains in a rubber network without an interaction with the surrounding chains and sub-networks, it is assumed that the chain takes a random walk confined by a tube. The free energy from the tube contraction can be calculated by

$$\psi_t(\bar{\nu}) = -kT \ln(p_t(\bar{\nu})), \quad (\text{E.14})$$

which represents a classical formulation (Miehe et al., 2004a). The probability of the tube constraint can be calculated accordingly to Doi and Edwards (1988) with

$$p_t(\bar{\nu}) = p_{0,t} \exp \left[ -\alpha \left( \frac{r_0}{d_0} \right)^2 \bar{\nu} \right], \quad (\text{E.15})$$

where  $\alpha$  characterizes the shape of the cross section of the tube,  $\rho_0$  describes a normalization constant and all other variables have been already introduced. Inserting Eq. (5.33) into Eq. (E.15), the free energy  $\psi_t$  can be calculated in accordance to Eq. (E.14), which reads

$$\psi_t(\bar{\nu}) = \alpha kTN \left( \frac{l}{d_0} \right)^2 \bar{\nu} + \psi_0. \quad (\text{E.16})$$

The average force associated with the increasing or decreasing tube diameter  $d$  reads

$$\bar{f}_t = \frac{d\psi_t(d)}{dd} = -\alpha kTN \frac{l^2}{d^3}, \quad (\text{E.17})$$

which was calculated by inserting Eq. (5.33) in Eq. (E.16) and differentiating the result with respect to  $d$ .

## Appendix F

# User-Defined Material Models in ANSYS FE-Code

In ANSYS FE package, there are two possibilities to implement user-defined hyperelastic constitutive models. The classic way is to write a UserMat subroutine where the six components of the Cauchy stress tensor must be calculated based on the deformation gradient at the current time step  $\mathbf{F}_{n+1}$  (Liu and Sun, 2016). To obtain a quadratic convergence rate during Newton-Raphson iteration, consistent tangent moduli must be calculated and returned to ANSYS to solve incremental nonlinear equations.

An alternative to implementing hyperelastic material models can be realized via UserHyper subroutine. The subroutine considers isotropic, compressible and incompressible hyperelasticity. It is formulated as a total Lagrange approach, where the discrete equations are formulated in relation to the reference configuration. The UserHyper subroutine only requires the initialization of the material parameters and the derivatives of the user-defined Helmholtz function with respect to the invariants  $\bar{I}_1$ ,  $\bar{I}_2$  and  $J$ , i.e.

$$\frac{\partial \Psi}{\partial \bar{I}_1}, \frac{\partial \Psi}{\partial \bar{I}_2}, \frac{\partial \Psi}{\partial J}, \frac{\partial^2 \Psi}{\partial \bar{I}_1^2}, \frac{\partial^2 \Psi}{\partial \bar{I}_1 \partial \bar{I}_2}, \dots \quad (\text{F.1})$$

Baaser et al. (2017) reveals inconsistent material behavior when a compressible hyperelastic material law is implemented in the UserMat environment.

The second more complicated way is to implement a UserMat subroutine. To work with user-defined material models in ANSYS FE-Code, a UserMat subroutine must be implemented and compiled within ANSYS environment, where stresses, the objective rate of stresses and a consistent Jacobian matrix (tangent moduli) must be calculated. In the following, the implementation of a large deformation highly compressible Neo-Hookean UserMat subroutine accounting for cavitation is presented. Considering a Helmholtz free energy function in accordance to

$$\Psi = \Psi_{\text{iso}}(\mathbf{C}) + \Psi_{\text{vol}}(J), \quad (\text{F.2})$$

the second Piola-Kirchhoff stress tensor,  $\mathbf{S} = \mathbf{S}_{\text{iso}} + \mathbf{S}_{\text{vol}}$ , can be calculated by

$$\mathbf{S} = 2 \frac{\partial \Psi(\mathbf{C})}{\partial \mathbf{C}} = 2 \frac{\partial \Psi_{\text{iso}}(\bar{\mathbf{C}})}{\partial \mathbf{C}} + \frac{\partial \Psi_{\text{vol}}(J)}{\partial J} J \mathbf{C}^{-1}. \quad (\text{F.3})$$

Generally speaking for Finite Element Codes, the second Piola-Kirchhoff stress tensor is associated with a total Lagrangian formulation, whereas the Cauchy  $\boldsymbol{\sigma}$  and Kirchhoff stresses  $\boldsymbol{\tau}$  are associated with an updated Lagrangian formulation. In ANSYS FE-Code, the UserMat subroutine is formulated in an updated Lagrangian formulation, hence the Cauchy stresses  $\boldsymbol{\sigma}$  are required by ANSYS. Therefore, the second Piola-Kirchhoff stress tensor is recast by a push-forward operation with  $\boldsymbol{\sigma} = J^{-1} \mathbf{F} \mathbf{S} \mathbf{F}^T$ .

In many commercial FE codes an incremental formulation of the constitutive equations are required. In contrast, considering total form constitutive equations, there exist explicit solutions for stresses, hence they are directly updated using Eq. (F.3) and no integration scheme is needed respectively must be programmed. Furthermore, consistent tangent moduli are required using an objective stress rate to solve incrementally nonlinear equilibrium equations in an UserMat subroutine. Thus, within the UserMat environment the total form constitutive equation and the consistent tangent moduli must be implemented, where rate-integrations of the objective stress rates of the material tangents are internally performed by the program (Nguyen and Waas, 2016).

Considering large deformations in ANSYS FE Code, they must be formulated in a corotated frame given by the rotation  $\mathbf{R}$  from the polar decomposition of the deformation gradient  $\mathbf{F}$ . The rotation of the corotated frame can be expressed as

$$\mathbf{R} = \mathbf{F} \mathbf{U}^{-1}. \quad (\text{F.4})$$

Using the corotated frame formulation, the tangent moduli must be formulated and returned to ANSYS in a rate form. The corotational rate relative to the corotated frame is, in general, the Green-Naghdi rate. Since the Green-Naghdi rate has disadvantages like unsymmetrical tangent moduli, it is recommended to use the Jaumann-Zaremba rate. The Jaumann-Zaremba rate is first of all a convenient approximation of the Green-Naghdi rate, secondly the Jaumann-Zaremba rate is easy to implement into commercial FE-Codes and thirdly it leads to symmetric tangent moduli. A final advantage of the Jaumann-Zaremba rate in comparison to the Green-Naghdi rate lies in a better convergence behaviour for finite strain problems.

Returning to the Helmholtz free energy function in Eq. (F.2) respectively the second Piola-Kirchhoff stress tensor in Eq. (F.3), one obtains the tangent moduli  $\mathcal{C} = \mathcal{C}_{\text{iso}} + \mathcal{C}_{\text{vol}}$  in the Lagrangian configuration (material tangent) by differentiating

the second Piola-Kirchhoff stress tensor  $\mathbf{S}$  with respect to the right Cauchy-Green stretch tensors  $\mathbf{C}$  with

$$\begin{aligned}\mathcal{C} = 2 \frac{\partial S}{\partial \mathbf{C}} = & 4 \frac{\partial^2 \Psi_{\text{iso}}(\bar{\mathbf{C}})}{\partial \mathbf{C} \partial \mathbf{C}} + 2 \frac{\partial}{\partial \mathbf{C}} \left( \frac{\partial \Psi_{\text{vol}}(J)}{\partial J} \right) \otimes J \mathbf{C}^{-1} \\ & + 2 \frac{\partial \Psi_{\text{vol}}(J)}{\partial J} \frac{\partial}{\partial \mathbf{C}} (J \mathbf{C}^{-1}),\end{aligned}\quad (\text{F.5})$$

which represents a fourth-order tensor. In this context,  $\bar{\mathbf{C}}$  describes the isochoric part of the right Cauchy-Green stretch tensor with

$$\bar{\mathbf{C}} = J^{-\frac{2}{3}} \mathbf{C}. \quad (\text{F.6})$$

To obtain the tangent moduli in the spatial configuration  $\mathbf{c}$  (spatial tangent), the Piola transform, which describes a mapping between Eulerian and Lagrangian coordinates in continuum mechanics, can be accomplished by

$$\mathbf{c} = J^{-1} \chi^* (\mathcal{C}), \quad (\text{F.7})$$

where  $\chi^*$  represents indicial manipulations. Since the present paper is focused on the volumetric damage, only the governing equations for the volumetric part of the HELMHOLTZ free energy are presented in the following.

Following the proposal of Holzapfel (2000):p.265, the volumetric spatial tangent  $\mathbf{c}_{\text{vol}}$  can be written directly in the Eulerian configuration by

$$\mathbf{c}_{\text{vol}} = (p + Js) \mathbf{I} \otimes \mathbf{I} - 2p \mathbf{I}, \quad (\text{F.8})$$

where  $Jp$  and  $J^2s$  describe the hydrostatic Kirchhoff stress respectively the corresponding modulus,  $\mathbf{I} \otimes \mathbf{I}$  represents the dyadic product of two second order identity tensors and  $\mathbf{I}$  describes a fourth-order identity tensor. In this context, the hydrostatic Kirchhoff stress and the modulus of it are defined by

$$p = \frac{d\Psi_{\text{vol}}}{dJ} \quad \text{and} \quad s = \frac{d^2\Psi_{\text{vol}}}{dJ^2}, \quad (\text{F.9})$$

which leads to a simple equation to determine the volumetric tangent moduli in the Eulerian configuration (cf. Eq. (F.8)).

As above-mentioned, the spatial tangent must be transferred to ANSYS FE-Code in a rate form using the objective Jaumann-Zaremba stress rate. Therefore,

one has to built the Lie derivative of the Kirchhoff stress respectively the Truesdell rate of the Kirchhoff stress, which is given by

$$\mathcal{L}(\boldsymbol{\tau}) = \dot{\boldsymbol{\tau}} = \dot{\boldsymbol{\tau}} - \mathbf{l}\boldsymbol{\tau} - \boldsymbol{\tau}\mathbf{l}^T = J\dot{\boldsymbol{\sigma}} \quad (\text{F.10})$$

with

$$\mathbf{l} = \dot{\mathbf{F}}\mathbf{F}^{-1} = \mathbf{d} + \mathbf{w} = \frac{1}{2}(\mathbf{l} + \mathbf{l}^T) + \frac{1}{2}(\mathbf{l} - \mathbf{l}^T), \quad (\text{F.11})$$

where the Truesdell rate of the Kirchhoff stress is indicated by  $\dot{\boldsymbol{\tau}}$ , the Truesdell rate of the Cauchy stress is indicated by  $\dot{\boldsymbol{\sigma}}$ . Here, a superposed dot indicates the time derivative of the reference configuration and the rate of deformation tensor  $\mathbf{d}$  respectively and spin tensor  $\mathbf{w}$  are the symmetric and antisymmetric parts of the spatial velocity gradient  $\mathbf{l}$ . Furthermore, rewriting Eq. (F.10) in indicial notation and introducing the Green-Lagrange strain tensor by  $\mathbf{E} = \frac{1}{2}(\mathbf{F}^T\mathbf{F} - \mathbf{I})$ , one obtains

$$\dot{\tau}_{iq} = F_{iM}F_{qI}F_{pK}F_{hL} \frac{\partial S_{MI}}{\partial E_{KL}} d_{ph} \quad (\text{F.12})$$

$$\dot{\tau}_{iq} = c_{iqph} d_{ph}, \quad (\text{F.13})$$

respectively in tensorial notation

$$\dot{\boldsymbol{\tau}} = \mathbf{c} : \mathbf{d}, \quad (\text{F.14})$$

Since the Jaumann-Zaremba stress rate of the Kirchhoff stress is required by ANSYS FE Code, Eq. (F.14) is recast into

$$\overset{\nabla}{\boldsymbol{\tau}} = \dot{\boldsymbol{\tau}} - \mathbf{w}\boldsymbol{\tau} - \boldsymbol{\tau}\mathbf{w}^T = \hat{\mathbf{c}} : \mathbf{d}, \quad (\text{F.15})$$

where  $\hat{\mathbf{c}}$  indicates the Jaumann tangent, which can be expressed in indicial notation by

$$\overset{\nabla}{\tau}_{iq} = F_{iM}F_{qI}F_{pK}F_{hL} \frac{\partial S_{MI}}{\partial E_{KL}} d_{ph} \quad (\text{F.16})$$

$$+ \frac{1}{2}(\tau_{ip}\delta_{qh} + \tau_{qh}\delta_{ip} + \tau_{ih}\delta_{qp} + \tau_{qp}\delta_{ih}) \quad (\text{F.17})$$

$$= \hat{c}_{iqph} d_{ph}. \quad (\text{F.18})$$

Therefore, the relationship between the spatial and the Jaumann tangent considering Kirchhoff stresses can be given by

$$\hat{c}_{iqph} = c_{iqph} + \frac{1}{2} (\tau_{ip}\delta_{qh} + \tau_{qh}\delta_{ip} + \tau_{ih}\delta_{qp} + \tau_{qp}\delta_{ih}), \quad (\text{F.19})$$

whereas considering Cauchy stresses, the Jaumann tangent can be reformulated by

$$\hat{c}_{iqph} = c_{iqph} + \frac{1}{2} J (\sigma_{ip}\delta_{qh} + \sigma_{qh}\delta_{ip} + \sigma_{ih}\delta_{qp} + \sigma_{qp}\delta_{ih}) \quad (\text{F.20})$$

utilizing the relation between the Kirchhoff and Cauchy stress tensor of  $\boldsymbol{\tau} = J\boldsymbol{\sigma}$ .